

Models of radiative neutrino mass and lepton-flavour non-universality

Johnathan Gargalionis

Submitted in total fulfilment
of the requirements of the degree of

Doctor of Philosophy

School of Physics
The University of Melbourne

December 2020

Copyright © 2020 Johnathan Gargalionis

All rights reserved. No part of the publication may be reproduced in any form by print, photoprint, microfilm or any other means without written permission from the author.

Abstract

This thesis presents a series of original studies exploring the space of neutrino-mass models, and the connection that a class of these models might have with the recently purported violations of lepton flavour universality measured in B -meson decays.

We begin by describing and implementing an algorithm that systematises the process of building models of Majorana neutrino mass starting from effective operators that violate lepton number by two units. We use the algorithm to generate computational representations of all of the tree-level completions of the operators up to and including mass-dimension eleven, almost all of which correspond to models of radiative neutrino mass. Our study includes lepton-number-violating operators involving derivatives, updated estimates for the bounds on the new-physics scale associated with each operator, an analysis of various features of the models, and a look at some examples. Accompanying this work we also make available a searchable database containing the catalogue of neutrino-mass models, as well as the code used to find the completions.

The anomalies in B -meson decays have known explanations through exotic scalar leptoquark fields. We add to this work by presenting a detailed phenomenological analysis a particular scalar leptoquark model: that containing $S_1 \sim (3, 1, -\frac{1}{3})$. We find that the leptoquark can accommodate the persistent tension in the ratios $R_{D^{(*)}}$ as long as its mass is lower than approximately 10 TeV, and show that a sizeable Yukawa coupling to the right-chiral tau lepton is necessary for an acceptable explanation. Agreement with the measured $R_{D^{(*)}}$ values is mildly compromised for parameter choices addressing the tensions in the $b \rightarrow s$ transition. The leptoquark can also reconcile the predicted and measured value of the anomalous magnetic moment of the muon, and appears naturally in models of radiative neutrino mass. As a representative example, we incorporate the field into a two-loop neutrino mass model from our database. In this specific case, the structure of the neutrino-mass matrix provides enough freedom to explain the small masses of the neutrinos in the region of parameter space dictated by agreement with the anomalies in $R_{D^{(*)}}$, but not in the $b \rightarrow s$ transition.

In order to address the shortcomings of the S_1 scenario, we construct a non-minimal model containing the scalar leptoquarks S_1 and $S_3 \sim (3, 3, -\frac{1}{3})$ along with a vector-like quark, necessary for lepton-number violation. We find that this new model permits a simultaneous explanation of all of the flavour anomalies in a region of parameter space that also reproduces the measured pattern of neutrino masses and mixing. A

characteristic prediction of our model is a rate of muon–electron conversion in nuclei fixed by the $b \rightarrow s$ anomalies and the neutrino mass. The next generation of muon–electron conversion experiments will thus potentially discover or falsify our scenario.

Finally, we present a general overview from our model database of those minimal radiative neutrino-mass models that contain leptoquarks that are known to explain the anomalies in $R_{D^{(*)}}$ and the $b \rightarrow s$ transition. We hope that our model database can facilitate systematic analyses similar to this, perhaps on both the phenomenological and experimental fronts.

Publications

Refs. [1–5] below are the journal publications, and preprints authored or co-authored during my PhD candidature. The authors are listed alphabetically in all of the titles.

Journal papers and preprints

- [1] R. Foot and J. Gargalionis, *Explaining the 750 GeV diphoton excess with a colored scalar charged under a new confining gauge interaction*, *Phys. Rev. D* **94** (2016), no. 1 011703, [[arXiv:1604.06180](https://arxiv.org/abs/1604.06180)].
- [2] Y. Cai, J. Gargalionis, M. A. Schmidt, and R. R. Volkas, *Reconsidering the One Leptoquark solution: flavor anomalies and neutrino mass*, *JHEP* **10** (2017) 047, [[arXiv:1704.05849](https://arxiv.org/abs/1704.05849)].
- [3] I. Bigaran, J. Gargalionis, and R. R. Volkas, *A near-minimal leptoquark model for reconciling flavour anomalies and generating radiative neutrino masses*, *JHEP* **10** (2019) 106, [[arXiv:1906.01870](https://arxiv.org/abs/1906.01870)].
- [4] J. Gargalionis, I. Popa-Mateiu, and R. R. Volkas, *Radiative neutrino mass model from a mass dimension-11 $\Delta L = 2$ effective operator*, *JHEP* **03** (2020) 150, [[arXiv:1912.12386](https://arxiv.org/abs/1912.12386)].
- [5] J. Gargalionis and R. R. Volkas, *Exploding operators for Majorana neutrino masses and beyond*, [[arXiv:2009.13537](https://arxiv.org/abs/2009.13537)].

Declaration

This is to certify that

1. the thesis comprises only my original work towards the PhD except where indicated in the preface;
2. due acknowledgement has been made in the text to all other material used;
3. the thesis is less than 100,000 words in length, exclusive of tables, maps, bibliographies and appendices.

Johnathan Gargalionis, December 2020

Preface

Particle physics currently finds itself in a strange or exciting place, depending on who you ask. The discovery of a Higgs-like boson at close to 125 GeV has meant both the completion of the Standard Model (SM), and the end of clear signs of new particles at the electroweak scale. Although the Large Hadron Collider (LHC) will continue to collect data well into the next few decades, the mass reach will not increase significantly. The community waits for a new machine, for which there are many candidates and promises, that will continue to push the energy frontier and test theories addressing the many shortcomings of the SM. Time frames for many of these see data taking beginning at the end of my career. If progress is driven by experiment, where do we go from here?

Thankfully, there are already clear signs of new physics in the neutrino sector. The observation of neutrino oscillations, and therefore neutrino masses, is by far the strongest terrestrial evidence demanding an extension of the SM. It is no surprise that a full understanding of the neutrinos has alluded us so far; they are, with the possible exception of the Higgs boson, the most elusive particles currently under laboratory scrutiny. As we move into an era of precision neutrino measurements, now is the right time to take stock of the phenomenologically viable and economic models that explain the pattern of neutrino masses and mixings observed. Armed with the list of possible mechanisms, we can make progress in probing those that are testable and, given that these models are falsified, build circumstantial evidence in favour of those that are not.

Even on the collider front, it is unclear yet that the LHC has left us with the so-called ‘nightmare scenario’ of a lonely Higgs. Perhaps unexpectedly, the most interesting signs of new physics from CERN have come from the *LHCb* experiment. The now famous ‘flavour anomalies’ are a collection of theoretically consistent anomalous measurements indicating a departure from the lepton-flavour universality present in the SM. Are these related to the growing evidence for deviations in leptonic anomalous magnetic moments? Might they be clues to a deeper theory of flavour and mass? The *Belle II* experiment has only just begun taking data, and we wait eagerly for what it has to say on these matters. *LHCb* too will continue to improve its measurements with more collisions; if the anomalies persist, these will be undeniable evidence of physics beyond the SM accessible to the next generation of hadron colliders.

These measurements are tantalising because of their consistency and breadth, but it would not be the first time that physicists have been lead astray, should they disappear

with more statistics. Even so, what is perhaps the central result of my doctoral work will remain unchanged: that deviations from lepton-flavour universality in four-fermion operators may be intimately connected to mass generation in the neutrino sector.

This idea is developed over the six chapters of this thesis, four of which are based on publications and preprints written in collaboration. These are summarised below with a statement of contribution and the publication status of the papers on which the chapters are based.

- Chapter 1 is an original introduction and literature review outlining the background necessary to understand the remaining chapters.
- Chapter 2 is based on the preprint ‘Exploding operators for Majorana neutrino masses and beyond,’ written in collaboration with Raymond R. Volkas [5]. The paper has recently been accepted for publication in JHEP. The calculations, analysis and technical writing in this chapter are largely my own. The ideas motivating the work were developed with Raymond R. Volkas.
- Chapter 3 is based on the publication ‘Reconsidering the One Leptoquark solution: flavor anomalies and neutrino mass,’ written in collaboration with Yi Cai, Michael A. Schmidt and Raymond R. Volkas [2], and ‘A near-minimal leptoquark model for reconciling flavour anomalies and generating radiative neutrino masses,’ written with Innes Bigaran and Raymond R. Volkas [3]. The calculations, analysis and technical writing in this chapter are largely my own. The motivation for this detailed phenomenological analysis of the S_1 leptoquark model stemmed from an idea of Michael A. Schmidt of embedding it into a model of radiative neutrino mass.
- Chapter 4 is based on the publications ‘Reconsidering the One Leptoquark solution: flavor anomalies and neutrino mass,’ written in collaboration with Yi Cai, Michael A. Schmidt and Raymond R. Volkas [2], and ‘A near-minimal leptoquark model for reconciling flavour anomalies and generating radiative neutrino masses,’ written with Innes Bigaran and Raymond R. Volkas [3]. The content of all sections except Sec. 4.4 has been published in one of the aforementioned publications. Sec. 4.3 contains work performed by collaborators, specifically the development of the model and the underlying computational machinery discussed in Sec. 4.3.4. The remaining technical work is largely my own, and the exposition of the model presented here is also my own. The motivation for this work followed from the limited success of the S_1 leptoquark scenario in both the neutrino-mass setting and as a combined explanation of the flavour anomalies. It was the idea of Raymond R. Volkas to combine the two dimension-seven completions containing S_3 and S_1 into the non-minimal model studied in detail in Sec. 4.3.

- Chapter 5 is based on the publication ‘Explaining the 750 GeV diphoton excess with a colored scalar charged under a new confining gauge interaction,’ written in collaboration with Robert Foot [1]. The calculation of the production cross section was my own work, otherwise the work was mostly completed by Robert Foot.
- Chapter 6 provides some concluding comments of my own about the thesis as a whole.

Acknowledgements

This thesis is for me, as perhaps for many, the fulfilment of a childhood goal. I have not arrived here alone, and there are many people I would like to thank.

First and foremost to my supervisor Raymond Volkas, to whom I owe a great debt of gratitude: thank you for accepting me as your student under what were certainly unorthodox circumstances; for all of the opportunities you offered to me in the course of the PhD, especially for work and travel; and for your mentoring in both my personal and professional life. I am deeply grateful to have had the opportunity to study under such a sharp physicist, and such an encouraging friend.

To the other members of my advisory panel, Nicole Bell and Jeff McCallum, thank you for your encouragement and support.

I have been very fortunate to have worked with many dedicated and intelligent collaborators over the course of my doctorate. To Innes Bigaran, Yi Cai, Noel Dawe, Robert Foot, Ayodele Ore and Iulia Popa-Mateiu, working and learning from you has been a pleasure and an invaluable part of my PhD experience. Special mention must go to Matthew Dolan: thank you for your patience and mentoring.

Discussions and interactions with postdocs and other students have helped me greatly in my time as a student. In particular I would like to thank my doctoral contemporaries Leon Friedrich and Tomasz Dutka, for whom, as with me, physics is as much a passion as it is work. I would also like to thank the remaining students with whom I had the pleasure of sharing the theory PhD office at one point or another: Jackson Clarke, Peter Cox, Joshua Ellis, Rebecca Leane, Nick Leerdam, Stephen Lonsdale and Isaac Sanderson.

The encouragement, interest and support of my friends outside of the David Caro building have been a constant source of motivation for me. I thank in particular Dean, Mariah, Mark, Tom and Yianni for their friendship.

Of course, this work would not have been possible without the constant love and support of my family, especially that of my parents. I am indebted to them for encouraging me to pursue my interests, and their unconditional and ready assistance through every step of the journey. My curiosity about the world did not emerge *in vacuo*, and I have my parents and grandparents to thank for instilling in me a love of learning and science. Thank you for these priceless gifts. My time as a PhD student also saw the birth of four children into my life. Thank you to Mary, George, George and Johnny,

who have made these years immeasurably more enjoyable.

Finally to Sabrina, thank you for your understanding, encouragement and patience. I am deeply grateful to have had you next to me for the completion of my doctorate. Thank you for supporting me and keeping me sane in what is all too often a consuming line of work.

Contents

List of Figures	xvii
List of Tables	xxi
1 Introduction	1
1.1 The Standard Model and neutrinos	1
1.2 Massive neutrinos in experiment and theory	3
1.2.1 Neutrino oscillations	3
1.2.2 Other experimental probes	10
1.2.3 Models of neutrino masses	12
1.3 Effective field theory	16
1.3.1 Tree-level matching	17
1.3.2 Effective field theories of the SM	19
1.3.3 Operator redundancy and the Hilbert series	24
1.4 The flavour anomalies and their explanation	30
1.4.1 Neutral-current anomalies	30
1.4.2 Charged-current anomalies	37
1.4.3 Anomalous magnetic moment of the muon	39
1.4.4 Our contention: a connection between neutrino physics and the anomalies	41
2 Neutrino mass <i>ex machina</i>	43
2.1 Introduction	43
2.2 Conventions	45
2.2.1 On operators and tree-level completions	45
2.2.2 Operator taxonomy	49
2.3 Tree-level matching in reverse	51
2.3.1 Tree-level completions of derivative operators	57
2.3.2 An algorithm for model building	64
2.4 Neutrino mass model building	65
2.4.1 Operator closures and neutrino-mass estimates	65
2.4.2 UV considerations	72

2.5	Models	83
2.5.1	Overview	83
2.5.2	Example models	88
2.6	Conclusions	102
3	The S_1 leptoquark as an explanation of the flavour anomalies	103
3.1	Introduction	103
3.2	The scalar leptoquark model	104
3.3	Phenomenological analysis	105
3.3.1	Signals	106
3.3.2	Constraints	112
3.4	Results and discussion	125
3.4.1	Flavour anomalies	127
3.5	Conclusions	134
4	Models of neutrino mass and the flavour anomalies	137
4.1	Introduction	137
4.2	A minimal neutrino-mass scenario with S_1	138
4.3	A non-minimal model: S_1 and S_3	142
4.3.1	The model	143
4.3.2	Neutrino mass	144
4.3.3	Flavour anomalies	146
4.3.4	Constraints	149
4.3.5	Results and discussion	156
4.4	Radiative models explaining the flavour anomalies with leptoquarks	162
4.5	Conclusions	163
5	The two-photon decay of a scalar-quirk bound state	167
5.1	Introduction	167
5.2	The model	168
5.3	Explaining the excess	169
5.4	Conclusions	175
6	Conclusions and Outlook	177
Appendix A	Mathematical notation	181
Appendix B	Table of lepton-number-violating operators	185
Definition of Symbols and Acronyms		195

List of Figures

1.1	The cumulative citation graph for a selection of papers presenting foundational results relevant to the SM.	3
1.2	The figure shows a table taken from the latest global fit to neutrino mass and mixing parameters by the NuFit collaboration [6, 7] in the three-flavour picture.	8
1.3	The figure shows the two-dimensional allowed regions obtained by the latest fit to the neutrino mass and mixing parameters by the NuFit collaboration [6, 7].	9
1.4	The figure shows limits on the effective neutrino mass for different values of m_{lightest} for both normal and inverted mass ordering.	11
1.5	The masses of the SM fermions grouped by generation.	13
1.6	The neutrino self-energy diagrams relevant to the Zee (left) and Zee-Babu (right) models.	15
1.7	The figure shows the measured and predicted values for the differential branching ratio for $B_s \rightarrow \phi \mu \mu$ by bins of q^2	32
1.8	The figure shows the two-dimensional likelihood contours in $\text{Br}(B^0 \rightarrow \mu \mu)$ and $\text{Br}(B_s \rightarrow \mu \mu)$	33
1.9	(top) The measurements of the LFU R_K by LHCb [8], Belle [9] and BaBar [10]. (bottom) The figure shows the experimental situation for R_{K^*} [10–12].	34
1.10	The figure shows the measured values of the P'_5 angular observable in the decays $B \rightarrow K^* \mu \mu$ binned by q^2	35
1.11	The figure shows the results of the global fit conducted in Ref. [13] in the C_9 – C_{10} plane.	36
1.12	The figure shows the combined fit to the available R_D and R_{D^*} data from HFLAV [14].	38
1.13	Individual contributions of the Wilson coefficients of the WET Hamiltonian in different observables ($\Delta X \equiv X - X_{\text{SM}}$): correlation between ΔR_D and ΔR_{D^*} , and $\Delta \mathcal{R}_{D^*}$, $\Delta \mathcal{P}_\tau^{D^*}$ and $\Delta F_L^{D^*}$ as a function of the Wilson coefficients.	40

2.1	(top) Scalar-only and fermion-only topologies which complete dimension-five two-scalar–two-fermion operators, like the Weinberg operator \mathcal{O}_1 . (bottom) The three minimal tree-level completions of \mathcal{O}_1 , each corresponding to a different permutation of the fields on the external lines of the topologies.	53
2.2	The two tree-level topologies relevant to six-fermion operators.	55
2.3	The graph visualises our completion procedure by showing some of the possible ways to explode the operator $\mathcal{O}_{12a\delta} = L^i L^j Q_{ia}^\dagger Q_{jb}^\dagger \bar{u}^{+a} \bar{u}^{+b}$	56
2.4	(a) The diagram shows an example opening of an operator containing at least one derivative. (b) The case where the fermion ψ_1 is heavy, coupling to the light fields ψ_2 and ϕ_2	59
2.5	(a) An intermediate topology representing the operator \mathcal{O}_{D3} with all heavy fields except Δ_1 integrated out. (b) The model with field content $\{\Sigma, \Delta_1 + \bar{\Delta}^\dagger\}$ arises from two similar diagrams, shown here.	63
2.6	The figure shows smoothed histograms of the number of operators that have an estimated upper bound of Λ on the new-physics scale.	70
2.7	For some operators containing $\bar{d}\bar{u}^\dagger$ the operator closure involves a motif like that shown in the figure.	71
2.8	(a) The tree-level topologies relevant for the completions of the four-scalar–two-fermion operator \mathcal{O}'_1 . (b) The two tree-level topologies relevant for the completions of the one-scalar–four-fermion dimension-seven operators in Table B.1.	75
2.9	(a) The figure shows the tree-level topologies relevant to $3s4f$ operators. (b) The two-scalar–four-fermion topologies associated with dimension-nine single-derivative operators in our catalogue.	77
2.10	(a) The $5s2f$ topologies relevant only to the single-derivative operator \mathcal{O}_{D20} . (b) The UV diagrams associated with the $3s2f$ operator \mathcal{O}_{D21}	78
2.11	The tree-level topologies associated with the large class of $2s6f$ dimension-eleven operators in our listing.	79
2.12	The bar chart shows the number of distinct Lagrangians derived from operators of different mass dimension.	85
2.13	(a) The number of filtered models containing different numbers of exotic scalar and fermion fields. (b) The rough upper bound on the new-physics scale Λ shown against the number of exotic fields introduced in the models.	86
2.14	The number of models in which each field appears in the completions shown as a pie chart for scalars and fermions separately.	89
2.15	The graph is a representation of the connectivity between exotic fields in the neutrino-mass models.	91

2.16	(a) The furnishing of the tree-level topology, labelled $2s6f_4$ in our scheme, that generates \mathcal{O}_{62b} at tree level. (b) The neutrino self-energy diagram relevant to the non-genuine completion of \mathcal{O}_{62b}	94
2.17	(a) The tree-level completion diagram for the model derived from exploding \mathcal{O}_{50} and discussed in the main text. (b) One of the neutrino-mass diagrams relevant to the model derived from \mathcal{O}_{50}	95
2.18	(a) The tree-level completion diagram for the model that generates the single-derivative operators $\mathcal{O}_{D10,a,b,c}$ and discussed in the main text. (b) One of the neutrino-mass diagrams relevant to the model generating $\mathcal{O}_{D10a,b,c}$	97
2.19	(a) The figure shows the tree-level completion diagram for the model constructed to address the flavour anomalies and neutrino masses. (b) The self-energy diagram for the same model.	101
3.1	The dependence of the ratio of the tensor and scalar Wilson coefficients evaluated at μ_b in $b \rightarrow c\ell\nu$ as a function of the new-physics scale Λ , at which the ratio is -4	108
3.2	The results of our fit to R_D and R_{D^*} including the new Belle measurement [15].	109
3.3	The box diagrams contributing to $C_{LL}^{S_1}$ and $C_{LR}^{S_1}$ in this scalar leptoquark model.	111
3.4	The 1 and 2σ allowed regions for a_μ in the $y_{23}-z_{23}$ plane for leptoquark masses of $m_{S_1} = 1$ TeV (left) and $m_{S_1} = 5$ TeV (right).	112
3.5	The results of our random scan showing C_{LL} against $R_D^{\mu/e}$ (bottom) and $R_{D^*}^{e/\mu}$ (top) for the parameter choices detailed in Sec. 3.4 for ‘scan I’, in which the leptoquark mass is allowed to vary to values as large as 5 TeV.	118
3.6	The branching ratio $\text{Br}(B_c \rightarrow \tau\nu)$ against R_{D^*} with new physics only in C_S (solid blue) and new physics in both C_S and C_T satisfying $C_S/C_T = -4$ (solid orange) and $C_S/C_T = -7.8$ (dashed orange).	119
3.7	The region allowed by experimental limits on the decay $B \rightarrow K^*vv$ in the $ x_{33} - x_{32} $ plane for $m_{S_1} = 1$ TeV.	121
3.8	The key results probing the extent to which the model can explain the tensions in the $b \rightarrow s$ data.	128
3.9	Slices through the parameter space investigated through scan II.	129
3.10	The solid blue lines represents the dependence of R_D (left) and $R_{D^{(*)}}$ (right) on $ x_{33} $ when all other couplings are set to zero and $m_{S_1} = 1$ TeV.	131
3.11	The results of scan II presented as a scatter plot of R_D against R_{D^*}	132
3.12	Slices through the parameter space of scan II shown against R_{D^*}	133
3.13	A grid plot of the various $b \rightarrow c$ related observables in addition to R_D and R_{D^*} considered in our analysis.	136

4.1	Two loop neutrino mass generation in the model of Ref. [16].	138
4.2	Plots of the relative sizes of the couplings of the leptoquark S_1^1 to the bottom quark and the r th neutrino flavour against θ , the Casas–Ibarra parameter, for $m_f = 25$ TeV, $m_{S_1^2} = 20$ TeV, $m_{S_1^1} = 4$ TeV and $w_3 = 0.003$. We only consider the case $\theta \in \mathbb{R}$ here.	140
4.3	The figure shows the current (solid) and expected [17] (dashed) limits from muon–electron conversion in nuclei in the θ – w_3 plane for normal mass ordering (blue) and inverted ordering (orange).	141
4.4	The one-loop neutrino-mass diagrams in the combined S_1 , S_3 and $\chi_L + \chi_R$ model, shown here in the unbroken phase.	145
4.5	The figure shows the diagram through which the $ Q = 4/3$ component of S_3 mediates the $b \rightarrow s\mu\mu$ decays.	146
4.6	The leading-order diagrams contributing to R_D and R_{D^*} in our model. .	147
4.7	The figure shows the current (solid) and projected (dashed) upper limits on the couplings of the S_3 leptoquark to down-type quarks and charged leptons x_3^{rs}	151
4.8	The figure shows the additional diagrams contributing to $Z \rightarrow e_r e_s$ and $Z \rightarrow \nu_r \nu_s$ involving both χ and S_3 in our model.	154
4.9	Contours of $ \tan \arg x_3^{r3} = \text{Im}(x_3^{r3})/\text{Re}(x_3^{r3}) $ with varying $\arg \zeta$ and Majorana phase α_2	159
4.10	The results of the random scan projected onto $\text{Br}(\mu\text{Au} \rightarrow e\text{Au})$ and $C_9^{\mu\mu}$. .	160
4.11	The other interesting results of our Monte Carlo analysis. (a) The relation between $C_9^{\mu\mu}$ and the Majorana phase α_2 . (b) The results of the random scan projected onto $\text{Br}(D^0 \rightarrow \mu\mu)$ and $C_9^{\mu\mu}$	161
5.1	Tree-level pair production mechanisms for the scalar quirk χ	170
5.2	The cross section $\sigma(pp \rightarrow f \rightarrow \gamma\gamma)$ at 13 TeV for a range of quirkonium masses M_f and charge assignments.	172

List of Tables

1.1	The SM fields and their transformation properties under the SM gauge group G_{SM} and the Lorentz group written as $SU(2)_+ \otimes SU(2)_-$	2
1.2	The table shows the four-fermion operators in the dimension-six SMEFT in the Warsaw basis [18, 19].	22
1.3	The table shows the operators featuring in the Warsaw basis [18, 19] of the dimension-six SMEFT that are not four-fermion operators.	23
2.1	The table shows an assortment of $\Delta L = 2$ operator closures, displaying a number of paradigmatic motifs.	67
2.2	The table shows the topology classes encountered in our operator listing along with related information: the number of pertinent operators, the number of tree-level topologies associated with each topology type, the number of internal lines featuring in the diagrams (given as a range), and the appropriate figure reference in the text.	74
2.3	The table shows the number of unfiltered models in which the seesaw fields appear.	87
2.4	The table shows the pairs of fields that most often appear together in the filtered completions of the $\Delta L = 2$ operators we consider.	90
2.5	The table shows the models in our filtered list that contain fewer than four fields with the estimate of the upper-bound on the new-physics scale Λ in the range $700 \text{ GeV} < \Lambda < 100 \text{ TeV}$	92
3.1	The results of our fit to R_D and R_{D^*} including the new Belle combined measurement [15].	110
3.2	A table summarising the experimental values we take for the various leptonic branching ratios and LFU ratios considered in this section.	115
4.1	Particle content of two radiative models derived from dimension-seven operators identified in our model database [20] that contain S_1 and S_3	142
4.2	The table shows the limits we take on the LFV processes considered in our analysis [21].	153

4.3	The table is a summary of the constraints considered in this section, not also mentioned in Table 4.2.	157
4.4	The table shows the intervals from which the corresponding free parameters are randomly drawn for our Monte Carlo analysis.	160
4.5	The table shows a small sample of the 287 models of radiative neutrino mass that also contain either both of S_3 and R_2 or both of S_3 and S_1 . . .	164
A.1	The SM fields and their transformation properties under the SM gauge group G_{SM} and the Lorentz group.	183
A.2	The table shows the exotic scalars (top) and vectorlike or Majorana fermions (bottom) contributing to the dimension-six SMEFT at tree-level [22].	184
B.1	The table displays our listing of the $\Delta L = 2$ operators along with the number of completions before and after our model-filtering procedure, the number of loops in the neutrino self-energy diagram, and the upper bound on the new-physics scale associated with each operator.	186

1

Introduction

The following is a general introduction to the background topics referred to and assumed in subsequent chapters. This includes a review of popular theories of neutrino mass, the current status of neutrino-oscillation parameters, a general introduction to Effective Field Theory (EFT), the experimental situation relevant to the flavour anomalies, and topics peripheral to all of these.

1.1 The Standard Model and neutrinos

Laboratory experiments to date have firmly established the predictive power of the Standard Model (SM) of particle physics, a combined theory of the electroweak and strong interactions described by the gauge group $G_{\text{SM}} = \text{SU}(3)_c \otimes \text{SU}(2)_L \otimes \text{U}(1)_Y$. It is a model whose probes and predictions span at least 33 orders of magnitude¹ with varying degrees of precision, and these are consistent with almost all known experiments. Although it displays a number of arbitrary features, the dynamics of the theory are mostly fixed by the fundamental principles of gauge theory and Lorentz invariance. Most of this arbitrariness resides in the matter sector of the theory, whose properties (masses, coupling constants, quantum numbers, *etc.*) are not predicted, but are instead motivated on phenomenological grounds. We show the fields of the SM and their defining properties in Table 1.1, according to the mathematical conventions of Appendix A.

¹The interval given is from the distance scales probed at the LHC (roughly 10^{-17} cm) to the average diameter of the galaxy (roughly 10^{23} cm), for which some electromagnetic effects have been tested.

Field	$SU(3)_c \otimes SU(2)_L \otimes U(1)_Y$	$SU(2)_+ \otimes SU(2)_-$
$Q^{\alpha ai}$	$(3, 2, \frac{1}{6})$	$(2, 1)$
$L^{\alpha i}$	$(1, 2, -\frac{1}{2})$	$(2, 1)$
\bar{u}_a^α	$(\bar{3}, 1, -\frac{2}{3})$	$(2, 1)$
\bar{d}_a^α	$(\bar{3}, 1, \frac{1}{3})$	$(2, 1)$
\bar{e}^α	$(1, 1, 1)$	$(2, 1)$
$(G_{\alpha\beta})_b^a$	$(8, 1, 0)$	$(3, 1)$
$(W_{\alpha\beta})_j^i$	$(1, 3, 0)$	$(3, 1)$
$B_{\alpha\beta}$	$(1, 1, 0)$	$(3, 1)$
H^i	$(1, 2, \frac{1}{2})$	$(1, 1)$

Table 1.1: The SM fields and their transformation properties under the SM gauge group G_{SM} and the Lorentz group written as $SU(2)_+ \otimes SU(2)_-$. The final unbolted number in the 3-tuples of the G_{SM} column represents the $U(1)_Y$ charge of the field, normalised such that $Q = I_3 + Y$. For the fermions a generational index has been suppressed. See Appendix A for details about the mathematical notation used here and throughout this work.

The SM inherits the experimental success of the $SU(2) \otimes U(1)$ theory of the weak interactions, first proposed by Glashow [23] in 1961 as a possible underlying structure for Fermi’s theory of beta decay. Before the end of the same decade, Weinberg [24] and Salam [25] had constructed the modern theory of leptons based on the spontaneous breaking of $SU(2)_L \otimes U(1)_Y$ to the electromagnetic symmetry. Interestingly, it seems that these seminal papers went mostly unnoticed (see Fig. 1.1) until the early 1970s, when ’t Hooft proved the renormalisability of spontaneously broken gauge theories [26] as a graduate student working under the supervision of Veltman. By the mid 1970s the framework had been extended to include the quarks [27] and the unbroken chromodynamic group, which was successfully shown to reproduce the Bjorken scaling seen in deep-inelastic-scattering experiments through asymptotic freedom [28].

Despite its successes, the SM cannot be the complete theory of fundamental particles and their interactions. It does not explain phenomena such as the baryon asymmetry present, and the particle spectrum contains no viable candidate for dark matter. The SM cannot explain why the electric dipole moment of the neutron is so small, why there are three generations of matter or, notably in our case, the origin of neutrino oscillations and the implied small but non-zero neutrino masses.

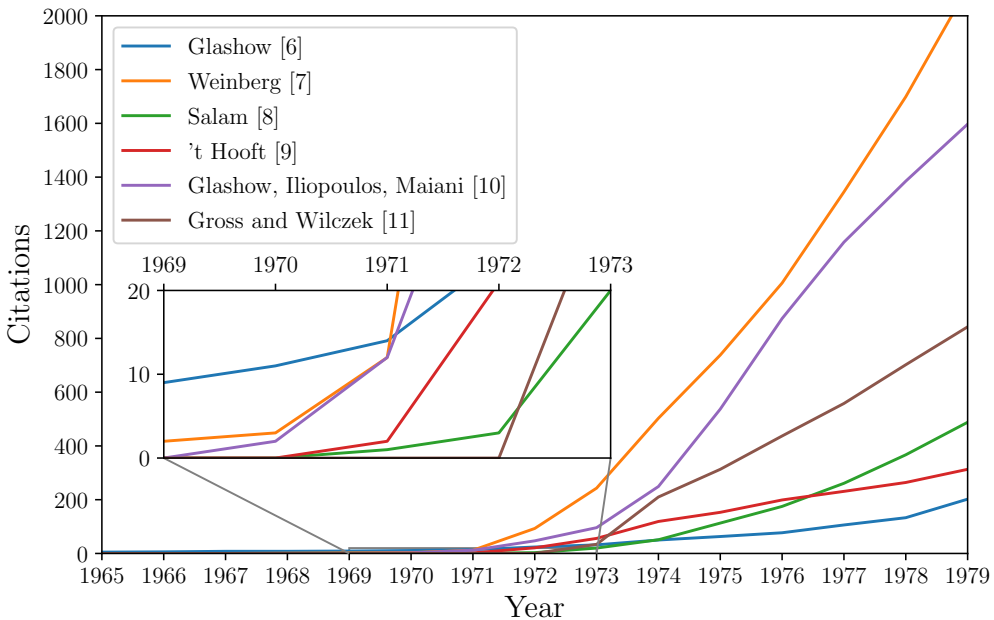


Figure 1.1: The cumulative citation graph for a selection of papers presenting foundational results relevant to the SM. Weinberg’s seminal paper ‘A model of leptons’ (1967) saw an explosion of citations following ’t Hooft’s work on the renormalisability of gauge theories (1971).

1.2 Massive neutrinos in experiment and theory

The minimal SM predicts massless neutrinos, a prediction that today sits in contradiction to a wealth of empirical evidence. This evidence could in principle have come from many kinds of experiments, but currently only neutrino oscillations provide strong signs that the masses are non-zero. Below we discuss the phenomenon of neutrino oscillations in the context of the outstandingly successful three-flavour mixing paradigm. We then move on to other probes of neutrino masses, which currently only provide limits on the mass scale. On the theory side, we summarise some popular and motivated extensions of the SM that accommodate massive neutrinos, placing particular emphasis on the direction we have followed in the novel work presented in this thesis. This includes an overview of tree- and loop-level models of Majorana neutrino mass.

1.2.1 Neutrino oscillations

The neutrino flavour eigenstates $\check{\nu}_i = (\nu_e, \nu_\mu, \nu_\tau)$ are defined as the states that couple at charged-current interaction vertices with the corresponding charged lepton. These

are the states in which the neutrinos are almost always produced in experiments, and certainly always measured. If neutrinos are massive there is no reason to expect these to coincide with the mass eigenstates $\nu_i = (\nu_1, \nu_2, \nu_3)$. In general, the flavour eigenstates will be an admixture of the propagating fields

$$\check{\nu}_i = U_i^j \nu_j , \quad (1.1)$$

where the U_i^j are elements of the unitary Pontecorvo–Maki–Nakagawa–Sakata (PMNS) neutrino mixing matrix [29, 30]. The PMNS matrix is defined such that it diagonalises the neutrino mass matrix:

$$\mathbf{U}^\dagger \mathbf{m}_\nu \mathbf{U}^* = \text{diag}(m_1, m_2, m_3), \quad (1.2)$$

where the m_i are the neutrino masses. Being a 3×3 unitary matrix, \mathbf{U} is in general parametrised by three mixing angles and six phases. Not all of the phases are physical, since the neutrino and charged-lepton fields can be redefined in such a way that five of the phases are removed in the case of Dirac neutrinos. In the presence of a Majorana mass term, only the charged leptons can be rephased. This leaves three physical phases with the two additional ones termed *Majorana phases*. In general

$$\mathbf{U} = \begin{bmatrix} c_{12}c_{13} & s_{12}c_{13} & s_{13}e^{-i\delta_{\text{CP}}} \\ -s_{12}c_{23} - c_{12}s_{23}s_{13}e^{i\delta_{\text{CP}}} & c_{12}c_{23} - s_{12}s_{23}s_{13}e^{i\delta_{\text{CP}}} & s_{23}c_{13} \\ s_{12}s_{23} - c_{12}c_{23}s_{13}e^{i\delta_{\text{CP}}} & -c_{12}s_{23} - s_{12}c_{23}s_{13}e^{i\delta_{\text{CP}}} & c_{23}c_{13} \end{bmatrix} \mathbf{P} , \quad (1.3)$$

where $c_{ij} = \cos \theta_{ij}$, $s_{ij} = \sin \theta_{ij}$ and

$$\mathbf{P} = \begin{cases} \text{diag}(e^{i\alpha_1}, e^{i\alpha_2}, 1) & \text{for Majorana neutrinos} \\ \mathbf{1}_{3 \times 3} & \text{for Dirac neutrinos} \end{cases} . \quad (1.4)$$

The phase δ_{CP} is often called the *Dirac phase*, while $\alpha_{1,2}$ are the Majorana phases discussed above.

Neutrino oscillation experiments typically involve the production of neutrino flavour states from charged-current processes, *e.g.* leptonic pion decays. Each mass eigenstate evolves in time independently according to the Schrödinger equation: *i.e.* $|\check{\nu}_i(t)\rangle = \exp(-iE_i t)|\check{\nu}_i(0)\rangle$, for evolution *in vacuo*. This alters the initial superposition away from being a pure flavour eigenstate:

$$|\check{\nu}_i(t)\rangle = \sum_j U_i^{*j} e^{-iE_j t} |\nu_j\rangle \quad (1.5)$$

$$= \sum_{j,k} U_i^{*j} e^{-iE_j t} U_j^k |\check{\nu}_k\rangle . \quad (1.6)$$

The probability of measuring a specific flavour through the charged-current interaction then oscillates with time:

$$P(\check{\nu}_m \rightarrow \check{\nu}_n) = |\langle \check{\nu}_n | \check{\nu}_m(t) \rangle|^2 = \left| \sum_i U_m^{*i} U_n^i e^{-iE_i t} \right|^2. \quad (1.7)$$

The expression can be expanded and the kinematic factors simplified from the fact that the neutrinos are ultra-relativistic. We follow the usual convention and take $E_i = \sqrt{\mathbf{p}^2 + m_i^2} \approx |\mathbf{p}| + m_i^2/(2E)$ with $E = |\mathbf{p}|$. This gives

$$\begin{aligned} P(\check{\nu}_m \rightarrow \check{\nu}_n) &= \delta_{mn} - 4 \sum_{i < j} \operatorname{Re} (U_m^{*i} U_m^j U_n^{*i} U_n^j) \sin^2 \frac{\Delta m_{ij}^2 L}{4E} \\ &\quad + 2 \sum_{i < j} \operatorname{Im} (U_m^{*i} U_m^j U_n^{*i} U_n^j) \sin \frac{\Delta m_{ji}^2 L}{2E}, \end{aligned} \quad (1.8)$$

where $\Delta m_{ij}^2 \equiv m_j^2 - m_i^2$ are the squared neutrino mass differences and $L = ct$, sometimes called the baseline, is the approximate distance travelled by the particles. To interpret the results of many experiments, it is often sufficient to consider an effective two-flavour oscillation paradigm. In this case, the neutrino-oscillation probabilities are governed by a single squared mass difference Δm^2 and a single angle θ . We note that the CP-violating phase is completely absent from the two flavour formula:

$$P(\check{\nu}_m \rightarrow \check{\nu}_n)_{n_f=2} = \sin^2(2\theta) \sin^2 \frac{\Delta m^2 L}{4E}. \quad (1.9)$$

From the expressions in Eqs. (1.8) and (1.9) a number of properties of the vacuum neutrino oscillations become clear.

1. The neutrino oscillation probabilities depend on the neutrino mass differences, and not on the absolute mass scale. For three flavours, there are only two independent squared mass differences. Typically chosen to be Δm_{21}^2 and Δm_{31}^2 , although often they are referred to with the historical names Δm_{sol}^2 and Δm_{atm}^2 , discussed in detail below.
2. From Eq. (1.8) it is clear that the oscillations only occur if the neutrinos are non-degenerate and the neutrino mixing is non-trivial, *i.e.* if $\Delta m_{ij} \neq 0$ and $\mathbf{U} \neq \mathbf{1}$.
3. The PMNS matrix elements only appear in the combination $U_m^{*i} U_m^j$, to which the Majorana phases contained within the matrix \mathbf{P} do not contribute. This implies that oscillation experiments cannot comment on the Dirac or Majorana nature² of the neutrinos. Oscillations can however probe δ_{CP} .

²Of course, this is already clear from the fact that neutrino oscillations conserve total lepton number, despite breaking the individual familial lepton-number symmetries $L_{e,\mu,\tau}$.

Thus, neutrino oscillations imply that the neutrino masses of at least two of the mass eigenstates are non-degenerate, and therefore only one neutrino could potentially be massless. The largest squared mass difference can therefore be translated into a lower bound on the mass of the heaviest neutrino, which we present later with modern data.

Historically, the effective two-flavour mixing paradigm has provided a good framework for interpreting early indications of neutrino oscillations. Specifically, the solar and atmospheric neutrino puzzles have approximate descriptions in terms of a two-flavour picture. Oscillations $\nu_e \rightarrow \nu_{\text{active}}$, where ν_{active} is a coherent superposition of ν_μ and ν_τ , in both matter and vacuum account for the deficit of electron neutrinos measured from the sun, and $\nu_\mu \rightarrow \nu_\tau$ oscillations *in vacuo* explain the shortage of muon neutrinos from cosmic-ray-induced production in the upper atmosphere. Today, it is understood that the former effect is rather due to non-oscillatory adiabatic flavour conversion [31], although both are consequences of neutrino mixing.

The measurement and resolution of these puzzles is an interesting and exciting chapter in the recent history of physics. Experiments as early as the 1960s had noticed a shortage of electron neutrinos coming from the sun relative to the predictions of solar models [32–35], which themselves were subject to much uncertainty [36]. For detection there were three main approaches: Raymond Davis and collaborators [37] pioneered experiments that measured the solar electron-neutrino flux using Chlorine, the Kamiokande and later Super-Kamiokande collaborations [38, 39] used water Cherenkov detectors, and the experiments GALLEX [40] and SAGE [41] had Gallium as the detecting material. All of these experiments showed a deficit of solar electron neutrinos, although they were sensitive to neutrinos of different energies. The Sudbury Neutrino Observatory gave the final word on the solution to the solar neutrino puzzle with accurate confirmation of the electron-neutrino deficit, along with a measurement of the *total* neutrino flux which was found to be in agreement with the solar models [42, 43].

Atmospheric neutrinos were known to come about from helicity-suppressed pion and kaon decays to muons and muon neutrinos. A zenith-angle and energy-dependent suppression in the flux of atmospheric muon neutrinos was measured by the Kamiokande and Irvine–Michigan–Brookhaven experiments [44, 45] in the early 1990s, and after the upgrade to Super-Kamiokande the deficit was confirmed to high precision with results presented at the ‘Neutrino 1998’ conference [46–49].

The pairs of mixing parameters associated with these two classes of measurements are usually dubbed $\theta_{\text{sol}}, \Delta m_{\text{sol}}^2$ and $\theta_{\text{atm}}, \Delta m_{\text{atm}}^2$. Experimental results find $\Delta m_{\text{sol}}^2 \ll \Delta m_{\text{atm}}^2$ and that both θ_{sol} and θ_{atm} are large compared to any angles found in the Cabibbo–Kobayashi–Maskawa (CKM) matrix, the quark mixing matrix. Interpreted in terms of three-flavour mixing, common convention identifies Δm_{sol}^2 with the squared mass difference between ν_2 and ν_1 , which is known to be positive³ (*i.e.* $\Delta m_{21}^2 > 0$). The solar mixing angle θ_{sol} is then associated with θ_{12} . The atmospheric mixing parameters are

³We note that the sign of Δm_{21}^2 can be known since oscillations in matter are also relevant for the solar squared mass difference, which depart from the simple formula of Eq. (1.9).

identified with $|\Delta m_{31}^2|$ or $|\Delta m_{32}^2|$ and θ_{23} . Of course, three-flavour effects alter the simplistic picture presented here and must be included to interpret measurements of θ_{13} and δ_{CP} , see *e.g.* Ref. [50] and references therein for a more detailed discussion. The picture that emerges from these experiments is then

$$\Delta m_{\text{sol}}^2 \approx \Delta m_{21}^2 \ll |\Delta m_{31}^2| \approx |\Delta m_{32}^2| \approx |\Delta m_{\text{atm}}^2| , \quad (1.10)$$

with which both the *normal mass ordering* $m_1 < m_2 < m_3$ and the *inverted mass ordering* $m_3 < m_1 < m_2$ are consistent.

Neutrino oscillation experiments have continued to probe the squared mass differences and mixing parameters with impressively high precision, see *e.g.* Refs. [6, 51]. Reactor neutrino experiments like KamLAND [52] are sensitive to solar neutrino mixing parameters, while accelerator long-baseline experiments, *e.g.* T2K [53], MINOS [54] and NOvA [55], are sensitive to the atmospheric parameters. The parameter θ_{13} is best measured at short-baseline reactor experiments like Double Chooz [56], RENO [57] and Daya Bay [58]. Today the octant of θ_{12} is certainly known, while θ_{13} is constrained to be close to 0.15. The sign of the atmospheric squared mass difference is still unknown, and therefore so is the mass ordering for the neutrinos. The value of the CP-violating Dirac phase δ_{CP} is less clear, although there is a preference for a value somewhere between π and $3\pi/2$. The extent of CP-violation in the neutrino sector can be represented in a rephasing-invariant way with the leptonic Jarlskog invariant [59]

$$J_{\text{CP}} = \frac{1}{8} \cos \theta_{13} \sin 2\theta_{12} \sin 2\theta_{13} \sin 2\theta_{23} \sin \delta_{\text{CP}} , \quad (1.11)$$

so a value of π would imply no CP-violating effects, while $\delta_{\text{CP}} = 3\pi/2$ would make these maximal. For this work we take the results of the most recent fit to neutrino oscillation data by the NuFit collaboration [6, 7] in the context of the three-flavour paradigm. These results are summarised in Fig. 1.2 separately for the cases of normal and inverted mass ordering. Results including atmospheric neutrino oscillation data from Super-Kamiokande and those not are also distinguished. Two-dimensional projections of the χ^2 fit for the same parameters are shown in Fig. 1.3. These data suggest a leptonic mixing matrix that has a very different form to the CKM matrix, which we call V . We represent this qualitatively by using boxes whose side lengths are scaled to the magnitude of the best-fit values of the parameters in the matrices, the textures are

$$U \sim \begin{pmatrix} \blacksquare & \blacksquare & \cdot \\ \cdot & \blacksquare & \blacksquare \\ \blacksquare & \blacksquare & \blacksquare \end{pmatrix}, \quad V \sim \begin{pmatrix} \blacksquare & \cdot & \cdot \\ \cdot & \blacksquare & \cdot \\ \cdot & \cdot & \blacksquare \end{pmatrix} . \quad (1.12)$$

For the PMNS matrix we take the best fit values for the normal mass ordering including the Super-Kamiokande results, *i.e.* the numbers in the top-left quadrant of Fig. 1.2. The same numbers also imply a lower bound on the mass of the heaviest neutrino at

$$m_{\text{heaviest}} \geq \sqrt{|\Delta m_{\text{atm}}^2|} \approx 0.05 \text{ eV} . \quad (1.13)$$

		NuFIT 5.0 (2020)				
		Normal Ordering (best fit)		Inverted Ordering ($\Delta\chi^2 = 2.7$)		
		bfp $\pm 1\sigma$	3σ range	bfp $\pm 1\sigma$	3σ range	
without SK atmospheric data	$\sin^2 \theta_{12}$	$0.304^{+0.013}_{-0.012}$	$0.269 \rightarrow 0.343$	$0.304^{+0.013}_{-0.012}$	$0.269 \rightarrow 0.343$	
	$\theta_{12}/^\circ$	$33.44^{+0.78}_{-0.75}$	$31.27 \rightarrow 35.86$	$33.45^{+0.78}_{-0.75}$	$31.27 \rightarrow 35.87$	
	$\sin^2 \theta_{23}$	$0.570^{+0.018}_{-0.024}$	$0.407 \rightarrow 0.618$	$0.575^{+0.017}_{-0.021}$	$0.411 \rightarrow 0.621$	
	$\theta_{23}/^\circ$	$49.0^{+1.1}_{-1.4}$	$39.6 \rightarrow 51.8$	$49.3^{+1.0}_{-1.2}$	$39.9 \rightarrow 52.0$	
	$\sin^2 \theta_{13}$	$0.02221^{+0.00068}_{-0.00062}$	$0.02034 \rightarrow 0.02430$	$0.02240^{+0.00062}_{-0.00062}$	$0.02053 \rightarrow 0.02436$	
	$\theta_{13}/^\circ$	$8.57^{+0.13}_{-0.12}$	$8.20 \rightarrow 8.97$	$8.61^{+0.12}_{-0.12}$	$8.24 \rightarrow 8.98$	
	$\delta_{CP}/^\circ$	195^{+51}_{-25}	$107 \rightarrow 403$	286^{+27}_{-32}	$192 \rightarrow 360$	
	$\frac{\Delta m_{21}^2}{10^{-5} \text{ eV}^2}$	$7.42^{+0.21}_{-0.20}$	$6.82 \rightarrow 8.04$	$7.42^{+0.21}_{-0.20}$	$6.82 \rightarrow 8.04$	
with SK atmospheric data	$\frac{\Delta m_{3\ell}^2}{10^{-3} \text{ eV}^2}$	$+2.514^{+0.028}_{-0.027}$	$+2.431 \rightarrow +2.598$	$-2.497^{+0.028}_{-0.028}$	$-2.583 \rightarrow -2.412$	
			Normal Ordering (best fit)			
			bfp $\pm 1\sigma$	3σ range	Inverted Ordering ($\Delta\chi^2 = 7.1$)	
	$\sin^2 \theta_{12}$	$0.304^{+0.012}_{-0.012}$	$0.269 \rightarrow 0.343$	$0.304^{+0.013}_{-0.012}$	$0.269 \rightarrow 0.343$	
	$\theta_{12}/^\circ$	$33.44^{+0.77}_{-0.74}$	$31.27 \rightarrow 35.86$	$33.45^{+0.78}_{-0.75}$	$31.27 \rightarrow 35.87$	
	$\sin^2 \theta_{23}$	$0.573^{+0.016}_{-0.020}$	$0.415 \rightarrow 0.616$	$0.575^{+0.016}_{-0.019}$	$0.419 \rightarrow 0.617$	
	$\theta_{23}/^\circ$	$49.2^{+0.9}_{-1.2}$	$40.1 \rightarrow 51.7$	$49.3^{+0.9}_{-1.1}$	$40.3 \rightarrow 51.8$	
	$\sin^2 \theta_{13}$	$0.02219^{+0.00062}_{-0.00063}$	$0.02032 \rightarrow 0.02410$	$0.02238^{+0.00063}_{-0.00062}$	$0.02052 \rightarrow 0.02428$	
	$\theta_{13}/^\circ$	$8.57^{+0.12}_{-0.12}$	$8.20 \rightarrow 8.93$	$8.60^{+0.12}_{-0.12}$	$8.24 \rightarrow 8.96$	
	$\delta_{CP}/^\circ$	197^{+27}_{-24}	$120 \rightarrow 369$	282^{+26}_{-30}	$193 \rightarrow 352$	
	$\frac{\Delta m_{21}^2}{10^{-5} \text{ eV}^2}$	$7.42^{+0.21}_{-0.20}$	$6.82 \rightarrow 8.04$	$7.42^{+0.21}_{-0.20}$	$6.82 \rightarrow 8.04$	
	$\frac{\Delta m_{3\ell}^2}{10^{-3} \text{ eV}^2}$	$+2.517^{+0.026}_{-0.028}$	$+2.435 \rightarrow +2.598$	$-2.498^{+0.028}_{-0.028}$	$-2.581 \rightarrow -2.414$	

Figure 1.2: The figure shows a table taken from the latest global fit to neutrino mass and mixing parameters by the NuFit collaboration [6, 7] in the three-flavour picture. The results presented in the upper (lower) panel are obtained by excluding (including) the χ^2 data on atmospheric neutrinos provided by the Super-Kamiokande collaboration (SK). The numbers in the 1st (2nd) column are obtained assuming normal (inverted) neutrino mass ordering. See Ref. [7] for more information.

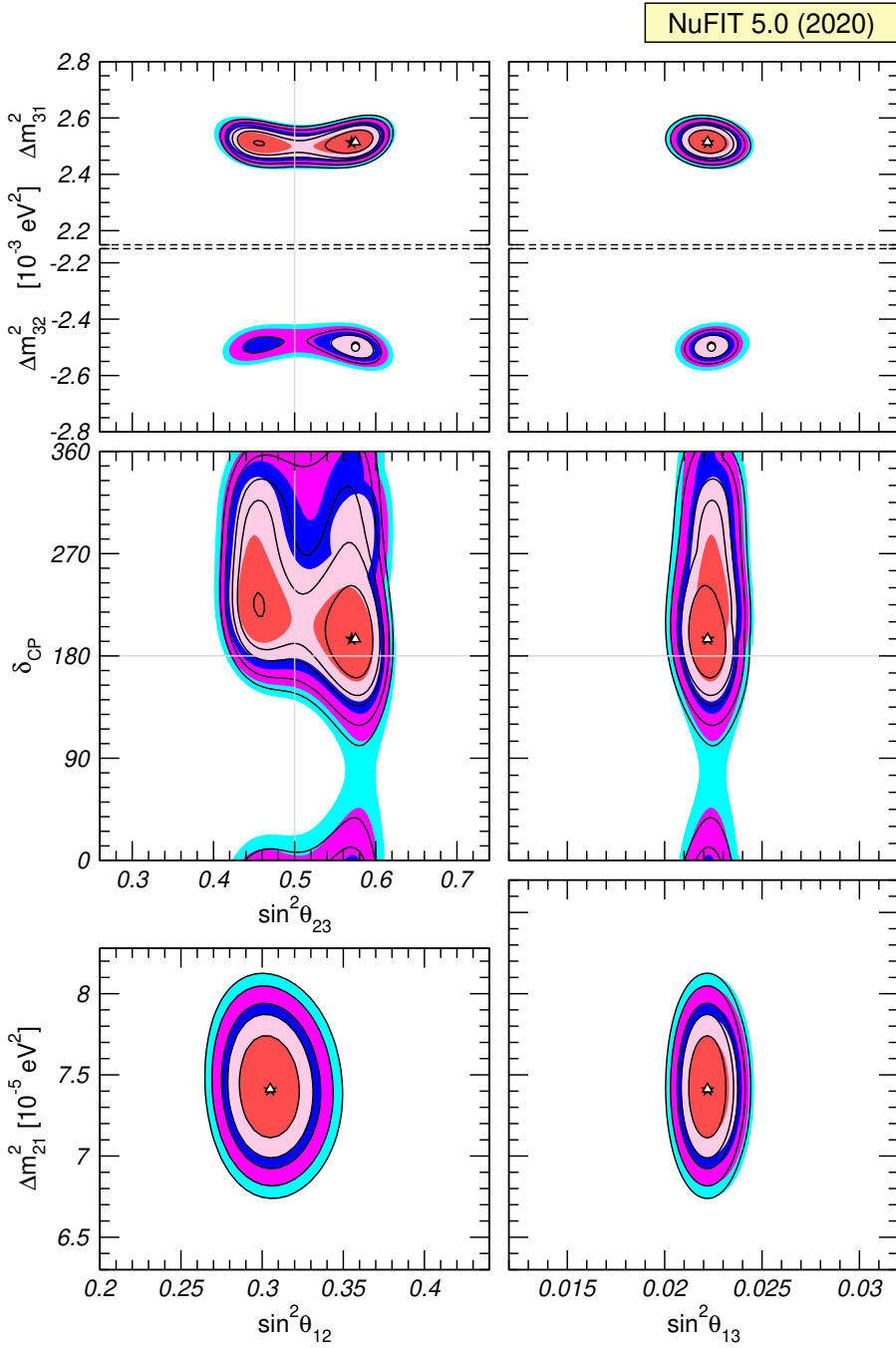


Figure 1.3: The figure shows the two-dimensional allowed regions obtained by the latest fit to the neutrino mass and mixing parameters by the NuFit collaboration [6, 7]. Each plot shows the two-dimensional projection of the allowed region after marginalising with respect to the other parameters. The coloured regions (black contour curves) are obtained by excluding (including) the Super-Kamiomande χ^2 data. The different contours correspond to the two-dimensional allowed regions at 1σ , 90%, 99%, 3σ confidence. See Ref. [7] for more information.

1.2.2 Other experimental probes

Although neutrino oscillations provide a wealth of evidence for non-zero masses for at least two of the neutrino fields, they do not probe the absolute mass scale. There are however kinematic and cosmological probes which bound the neutrino masses, and some of these are mentioned here.

Beta decay

A study of the kinematics of beta-decay experiments shows that differences in the energy distribution of the emitted electron are expected for different values of the neutrino mass. Currently these experiments only provide upper bounds on the effective neutrino mass [60]

$$m_\beta \equiv \sqrt{\sum_i |U_1^i|^2 m_i^2} . \quad (1.14)$$

The best results come from tritium experiments which probe ${}^3\text{H} \rightarrow {}^3\text{He} + e + \bar{\nu}_e$. The KATRIN experiment recently presented the most stringent upper bound [61, 62]

$$m_\beta < 1.1 \text{ eV} , \quad (1.15)$$

at 90% confidence, with a projected limit of $m_\beta < 0.2 \text{ eV}$ with the full dataset.

Another process with the potential to probe the absolute scale of the neutrino masses, as well as the Majorana phases, is neutrinoless double beta decay ($0\nu\beta\beta$). The process requires the violation of lepton-number by two units, and is therefore intimately tied to the neutrinos' possible Majorana nature. If double-beta decay is seen, the *black box theorem* [63–65] guarantees that the neutrinos pick up a radiative Majorana mass, even if the neutrino masses vanish at tree level. Graphically this is easy to understand: a $0\nu\beta\beta$ operator can always be turned into a neutrino self-energy graph with four loops. The amplitude for the process is proportional to

$$\langle m_\nu \rangle_{\beta\beta} = \sum_i (U_1^i)^2 m_i , \quad (1.16)$$

which features both the neutrino masses and the Majorana phases. (Of course it may be that the four-loop contribution to the neutrino mass implied by the double-beta-decay operator represents only a small correction to the neutrino masses, which could arise at lower order.) Current limits on $\langle m_\nu \rangle_{\beta\beta}$ are around 0.2 eV, see e.g. Ref. [66] for a recent review of the experimental status and prospects. Constraints on $\langle m_\nu \rangle_{\beta\beta}$ are usually presented against the mass of the lightest neutrino mass eigenstate. The behaviour of $\langle m_\nu \rangle_{\beta\beta}$ is very sensitive to the neutrino mass ordering, in such a way that the inverted scenario implies a minimum allowed value of $\langle m_\nu \rangle_{\beta\beta}$, which will begin

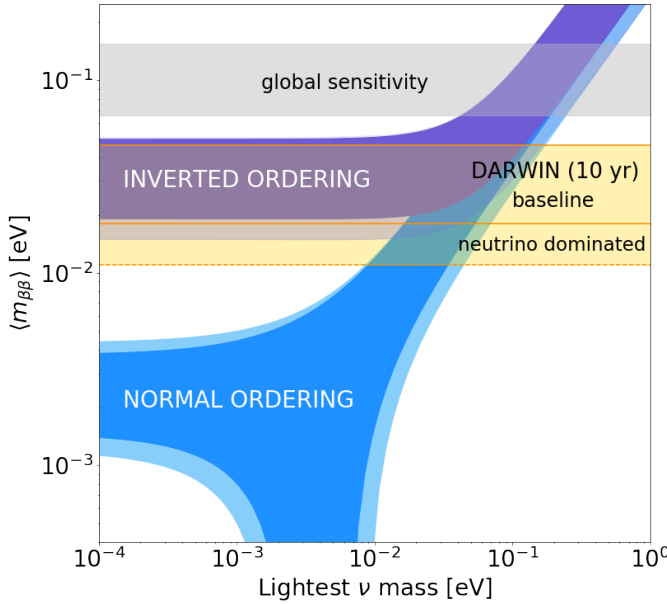


Figure 1.4: The figure shows limits on the effective neutrino mass for different values of m_{lightest} for both normal and inverted mass ordering. The grey region represents the combined sensitivity from a number of leading experiments [68]. The yellow regions are projections for the DARWIN experiment under different background hypotheses. The figure is taken from Ref. [67], and we point the reader there for more information.

to be probed by the next generation of experiments. A combined global limit and the projected sensitivity of the DARWIN experiment [67] are shown in Fig. 1.4, which also illustrates the different behaviour of the inverted and normal neutrino mass orderings in the $\langle m_\nu \rangle_{\beta\beta}$ vs. m_{lightest} plane.

Cosmological limits

The most stringent limits on the sum of the neutrino masses come from cosmology, although they are model-dependent. In the minimal Λ CDM model adjusted for massive neutrinos, the limit implied by the most recent Planck data release [69] is

$$\sum_i m_i < 0.12 \text{ eV}, \quad (1.17)$$

at 95% confidence. This is impressively small, and puts pressure on the inverted-ordering scenario, for which $\sum_i m_i \gtrsim 0.1$ eV. Excitingly, future cosmological probes will likely make a measurement of the sum of the neutrino masses.

1.2.3 Models of neutrino masses

In the SM the neutrino fields appear only within the lepton doublet L , and one cannot write down—in analogy to the up-type Yukawa—a renormalisable operator that leads to neutrino masses because of the absence of the right-handed fields. There is also no isotriplet scalar that couples to LL to provide a tree-level Majorana mass for the left-handed neutrinos. A simple model of neutrino mass then involves introducing a gauge-singlet fermion field $\bar{\nu} \sim (1, 1, 0)_{(2,1)}$, extending the Yukawa sector of the SM accordingly to

$$-\mathcal{L}_Y \supset y_e \bar{e} L H^\dagger + y_d \bar{d} Q H^\dagger + y_u \bar{u} Q H + y_\nu \bar{\nu} L H , \quad (1.18)$$

in a simplified one-flavour picture. This implies Dirac neutrinos with a mass $m_\nu \approx y_\nu v$, and makes mass generation symmetric between the quarks and leptons.

There are a number of problems with this simplistic scenario. First, it is perhaps uncomfortable to suppose that the neutrinos are many orders of magnitude lighter than the charged fermions only because y_ν is a very small number. Indeed, the posited large hierarchy between y_ν and y_u seems to spoil any aesthetic arguments for quark-lepton symmetry in favour of this hypothesis. Although the Yukawa couplings for the other SM fermions span six orders of magnitude, couplings within any one generation are all of similar order. We illustrate this in Fig. 1.5, where the fermion masses are plotted by generation. Whereas one could consider that some underlying theory of flavour may explain, for example, the disparity in scale between the masses of the electron and the top quark, the large mass difference between the electron and the lightest neutrino, although technically natural, seems to cry out for its own explanation.

A second point of criticism with the simple scenario presented above is that it ignores the Majorana mass term for $\bar{\nu}$

$$\mathcal{L} \supset -\frac{1}{2} \mu \bar{\nu} \bar{\nu} + \text{h.c.} \quad (1.19)$$

In order to maintain the Dirac neutrino mass with the relation $m_\nu \approx y_\nu v$, the Majorana mass must be forbidden or else chosen to be negligibly small, assumptions adding layers of contrivance to the theory. A sensible choice for the scale μ is some high scale Λ associated with the breaking of $U(1)_{B-L}$. Taking $\mu \gg y_\nu v$, the neutrino-mass matrix takes on the form

$$\mathbf{m}_\nu = \begin{pmatrix} 0 & y_\nu v \\ y_\nu v & \mu \end{pmatrix} , \quad (1.20)$$

with eigenvalues

$$m_l \approx \frac{y_\nu^2 v^2}{\mu}, \quad m_h \approx \mu . \quad (1.21)$$

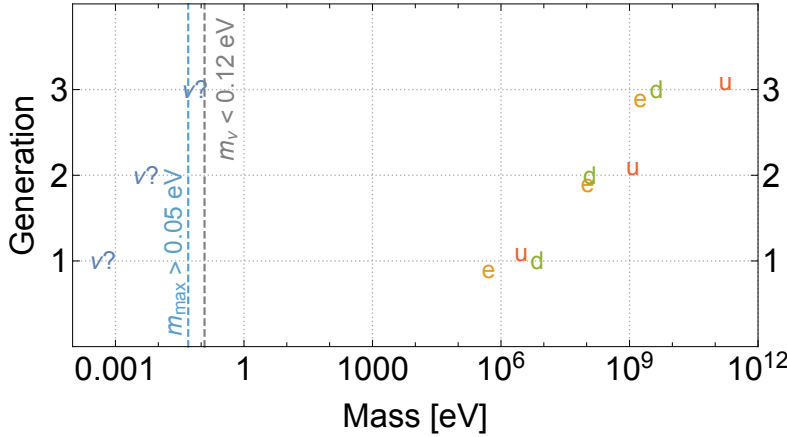


Figure 1.5: The masses of the SM fermions grouped by generation. While the SM Yukawa couplings span a wide range of values, within any specific generation they are all of similar order. The tiny masses of the neutrinos seem to suggest an alternate mass-generation mechanism.

The assumption $\mu \gg y_\nu v$ implies that $m_l \ll y_\nu v$, and the neutrino is successfully arranged to be much lighter than $y_\nu v$, which can now be taken to be on the order of the charged fermion masses. The theory also leaves us with a neutrino whose mass must be significantly larger than the electroweak scale: $m_h \gtrsim 10^{14}$ GeV, assuming $m_l = 0.05$ eV and $y_\nu = 1$. After transforming into the mass-diagonal basis, the physical fields v_l and v_h correspond to Majorana particles. Thus, in the most motivated region of parameter space, the phenomenology of the light neutrinos in even the SM + $\bar{\nu}$ scenario is Majorana. This toy scenario illustrates the mechanism commonly called the *seesaw mechanism*: making the neutrinos very light at the expense of making other fields very heavy. This is discussed more broadly below.

Tree-level models of neutrino mass

The toy seesaw scenario discussed above can be understood more generally by studying the effective theory valid below the scale μ , which does not contain the field $\bar{\nu}$. The leading-order lepton-number-violating (LNV) effects appear at dimension five in the operator

$$\mathcal{L} \supset \frac{\kappa}{\Lambda} (L^i L^j) H^k H^l \cdot \epsilon_{ik} \epsilon_{jl}, \quad (1.22)$$

with κ a dimensionless coefficient. This operator is commonly called the *Weinberg operator*. In the broken phase it gives rise to a Majorana mass for the neutrinos consistent

with the seesaw formula:

$$\mathcal{L} \supset \frac{v^2 \kappa}{\Lambda} \nu \bar{\nu}. \quad (1.23)$$

The SM + $\bar{\nu}$ scenario is not the only simplified model that generates the Weinberg operator at tree-level. A simple diagram-topology analysis suggests there are another two seesaw mechanisms in the UV: a model with a scalar isotriplet field $\Xi_1 \sim (\mathbf{1}, \mathbf{3}, \mathbf{1})_S$, called the type-II mechanism, and another with an isotriplet Majorana fermion $\Sigma \sim (\mathbf{1}, \mathbf{3}, \mathbf{0})_F$, called type-III. Along with the type-I heavy $\bar{\nu}$ model, these are collectively referred to as the canonical seesaw mechanisms [70–80] and have been studied at length in the literature. They are simple models in that they introduce only very few exotic degrees of freedom and free parameters. However, the high seesaw scale makes these models practically untestable at current and future collider experiments.

Models of Majorana neutrino mass can be made more testable if, instead of the suppression of the neutrino masses coming from a large Λ in Eq. (1.23), the coefficient κ were somehow arranged to be small. Although there are a number of mechanisms to achieve this, we concentrate below on radiative models of Majorana neutrino mass, in which κ is made small through loop and coupling suppression.

Radiative models and their classification

It may be the case that the field content of whatever high-energy theory describes the neutrino masses is such that no neutrino self-energy diagram can be drawn at the tree level. Indeed, this will be the case if there is lepton-number violation by two units ($\Delta L = 2$) from interactions other than those present in the canonical seesaw models. Such models are called radiative, since the neutrino masses arise through loop graphs. The historically important Zee [81] and Zee–Babu [82, 83] models have come to be archetypal radiative scenarios in which the neutrinos gain masses through $\Delta L = 2$ the interactions of exotic scalars at one and two loops respectively. In the Zee model, an additional Higgs doublet $\varphi \sim (\mathbf{1}, \mathbf{2}, \frac{1}{2})$ and a charged scalar $\mathcal{S}_1 \sim (\mathbf{1}, \mathbf{1}, \mathbf{1})$ are introduced, while the Zee–Babu model contains \mathcal{S}_1 and the doubly-charged scalar $\mathcal{S}_2 \sim (\mathbf{1}, \mathbf{1}, \mathbf{2})$. The neutrino self-energy diagrams for these models are shown in Fig. 1.6 as examples. The corresponding neutrino-mass matrices are

$$[\mathbf{m}_\nu^{\text{Zee}}]_{rs} = \frac{\mu v^2}{16\pi^2} \sum_t x_{[rt]} I_t [\mathbf{m}_e]_t y_{ts} + (r \leftrightarrow s), \quad (1.24)$$

$$[\mathbf{m}_\nu^{\text{Zee–Babu}}]_{rs} = \frac{\mu' v^2}{(16\pi^2)^2} \sum_{t,u} x_{[rt]} [\mathbf{m}_e]_t z_{\{tu\}} [\mathbf{m}_e]_u x_{[us]} I'_{tu} + (r \leftrightarrow s), \quad (1.25)$$

written in terms of the couplings $x, y, z \in \mathbb{C}$ as shown in Fig. 1.6, and the associated loop functions I and I' . One can see that in these models, the coefficient of the Weinberg

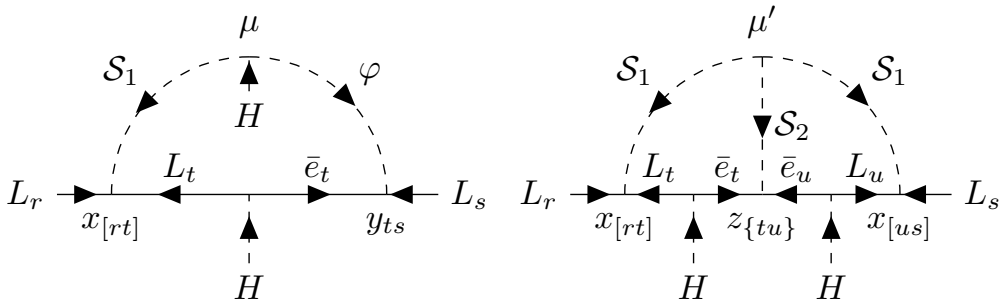


Figure 1.6: The neutrino self-energy diagrams relevant to the Zee (left) and Zee–Babu (right) models.

operator κ is naturally suppressed with respect to the seesaw formula by SM-fermion masses (charged-lepton masses in this case), exotic couplings, and loop factors.

Such models are economic, since they do not require the imposition of *ad hoc* symmetries, and in many cases make a connection to other unsolved problems of the SM such as the nature of dark matter or the matter–antimatter asymmetry of the Universe. They are also elegant, since the smallness of the neutrino masses emerges as a natural consequence, rather than through the imposed requirement of exceedingly small coupling constants. Radiative models are easier to probe experimentally since the additional loop suppression and products of couplings bring down the allowed scale of the new physics, in some cases to LHC-accessible energy ranges [84]. The Zee–Babu model, for example, is non-trivially constrained by same-sign dilepton searches performed by ATLAS [85–87] and CMS [88–90]. Additionally, the predicted dependence of the neutrino-mass matrix on SM parameters, as is clear from Eqs. (1.24) and (1.25), can make these models very predictive as far as neutrino phenomenology is concerned. For example, the minimal version of the Zee model has the charged-lepton masses arising from couplings to φ , allowing for a simplification of the expression Eq. (1.24) such that the leptonic flavour index t must be the same as s . The antisymmetry in the leptonic flavour indices implied by $x_{[rs]}$ must be accounted for by an antisymmetry in the loop integral such that $I \sim I_r - I_s$. The flavour structure then becomes [91]

$$[\mathbf{m}_\nu^{\text{Min. Zee}}]_{rs} \propto x_{[rs]} ([\mathbf{m}_e]_r^2 - [\mathbf{m}_e]_s^2), \quad (1.26)$$

which makes clear predictions relevant to neutrino oscillations that in this case rule out the model. For recent reviews of radiative models see Refs. [92, 93].

The Zee and Zee–Babu scenarios are only two of a very large number of radiative models, none of which are *a priori* more likely to be true than any other. In the context of such a large theory-space, it is useful to have an organising principle to aid in the study and classification of these models, and beginning with $\Delta L = 2$ effective operators has been shown to be an effective strategy.

Draft compiled on 2020/12/17 at 19:21:00

One approach to this model taxonomy involves studying loop-level completions of the Weinberg operator, and its dimension- $(5 + 2n)$ generalisations

$$\mathcal{O}_1^{(n)} = (LL)HH(H^\dagger H)^n.$$

Here, models can be systematically written down by studying the various topologies able to be accommodated by the operator with increasing number of loops. This is done in such a way that models implying lower-order contributions to the neutrino mass can be discarded [94]. Such an approach has been applied to the Weinberg operator up to three loops [95–97] and to its dimension-seven generalisation at one loop [98]. An alternative and complementary method begins by considering all of the gauge-invariant $\Delta L = 2$ operators in the SM effective field theory (SMEFT), first listed in this context by Babu and Leung [99] and extended by de Gouv  a and Jenkins [84]. Supposing that the tree-level coefficient of one of these is non-zero at the high scale, neutrino masses will be generated from loop graphs contributing to the mixing of this operator and the Weinberg-like operators $\mathcal{O}_1^{(n)}$. The process of expanding the operator into a series of UV-complete, renormalisable models that generate the parent operator at tree-level is called *opening up* or *exploding* the operator. The remaining external fields must be looped-off, with additional loops of SM gauge bosons or Higgs fields added as necessary in order to obtain a neutrino self-energy diagram. A model-building formula along these lines has been formulated in Ref. [100], and it has been used to write down all of the minimal, tree-level UV-completions of $\Delta L = 2$ operators at dimension seven [101] corresponding to tree-level and radiative neutrino-mass models. The tree-level completions of the Weinberg-like operators have been written down up to dimension eleven [101–103].

We note that an economic classification scheme, separate from an eft framework, was presented in Ref. [104] based on the number of exotic degrees of freedom by which the SM is extended. There, the method is applied to the case of radiative models with two exotics⁴, and has also been used to study minimal neutrino-mass models compatible with SU(5) unification [105].

1.3 Effective field theory

In the following we introduce EFT in general, and then specialise to those built out of SM fields: the Standard Model EFT (SMEFT) and the Weak Effective Theory (WET). We place particular emphasis on the operators appearing at dimension-six, since these play an important role in phenomenological analyses. Much of the focus of this work is the operators of odd mass-dimension up to dimension eleven, which organise the building of neutrino-mass models in the tradition of Refs. [84, 99–101]. Many of the principles

⁴Including models with one scalar and one Dirac fermion.

introduced here for the dimension-six SMEFT will be directly relevant there. We begin with prefatory comments on the process of tree-level matching, then move on to discuss the SMEFT and some of the intricacies associated with redundancies among operators.

1.3.1 Tree-level matching

Suppose one has a theory with light particle states described by fields π_i and heavy states described by Π_i with a Lagrangian of the form

$$\begin{aligned}\mathcal{L}_{\text{UV}}[\pi, \Pi] &= \mathcal{L}_{\text{kin}}[\pi, \Pi] + \mathcal{L}_{\text{int}}[\pi, \Pi], \text{ with} \\ \mathcal{L}_{\text{int}}[\pi, \Pi] &= \mathcal{L}^l[\pi] + \mathcal{L}^h[\Pi] + \mathcal{L}^{lh}[\pi, \Pi].\end{aligned}\tag{1.27}$$

Below the threshold for Π_i production, an effective description of the theory can be used that involves interactions only between the light fields. This effective theory is described by a Lagrangian $\mathcal{L}_{\text{eff}}[\pi]$ involving interactions between the π_i that correspond to diagrams in the full theory containing only heavy internal propagators and light external states. At the classical level, \mathcal{L}_{eff} can be written down by integrating out the Π_i . Perturbatively this corresponds to expanding the heavy propagators Δ in powers of momenta on the heavy mass scale⁵ Λ , such that

$$\Delta = \begin{cases} -\frac{1}{\Lambda^2} \left(1 + \frac{p^2}{\Lambda^2} + \dots \right) & \text{for } \text{---} \\ -\frac{\delta_\alpha^\beta}{\Lambda} \left(1 + \frac{p^2}{\Lambda^2} + \dots \right) & \text{for } \beta \xrightarrow{\quad} \alpha \\ -\frac{ip \cdot \bar{\sigma}^{\dot{\alpha}\beta}}{\Lambda^2} \left(1 + \frac{p^2}{\Lambda^2} + \dots \right) & \text{for } \beta \xleftarrow{\quad} \dot{\alpha} \end{cases}.\tag{1.28}$$

In this notation, the arrow-preserving propagator corresponds to the part of the regular four-component fermion propagator proportional to momentum, while the arrow-violating one is the part proportional to the fermion mass. Expressions for the fermion propagators with reversed arrows follow from $\bar{\sigma}^\mu \rightarrow \sigma^\mu$ and interchanging dotted and undotted indices (see Ref. [106] Sec. 4.2 for the Lorentz structure).

Equivalently, the integration can be performed using the classical equations of motion (EOM) of the Π_i . For some heavy field Π , the linearised solution to its classical EOM can be used to remove it from the Lagrangian completely. This procedure is mildly different for scalars and fermions, and we briefly outline these separately below. In both cases, we begin with a Lagrangian \mathcal{L}_{UV} for which we imagine that kinetic and mass mixing terms between heavy and light fields have been removed.

⁵We note that some UV scenarios may have more than one characteristic scale. In this case Λ can be understood as an effective scale which may not necessarily correspond to the mass of a specific particle.

There are tree-level contributions to \mathcal{L}^{eff} as long as there are interaction terms linear in Π . For scalar Π , the UV Lagrangian contains the terms

$$\mathcal{L}_{\text{UV}}[\Pi, \pi] \supset \Pi^\dagger (-D^2 - m_\Pi^2) \Pi + \left(\Pi \frac{\partial \mathcal{L}^{lh}}{\partial \Pi} + \text{h.c.} \right), \quad (1.29)$$

where $\partial \mathcal{L}^{lh}/\partial \Pi$ is a function only of light fields, and we are neglecting interactions of the form $\Pi^\dagger \Pi f(\pi)$ for the sake of conciseness. The EOM are

$$(-D^2 - m_\Pi^2) \Pi = -\frac{\partial \mathcal{L}^{lh}}{\partial \Pi^\dagger} + \mathcal{O}(\Pi^2), \quad (1.30)$$

which can be solved for Π^{cl} , the classical field configuration, by inverting the differential operator on the LHS of Eq. (1.30) and expanding in D^2/m_Π^2 :

$$\Pi^{\text{cl}} = -\frac{1}{m_\Pi^2} \left(1 - \frac{D^2}{m_\Pi^2} + \dots \right) \frac{\partial \mathcal{L}^{lh}}{\partial \Pi^\dagger}. \quad (1.31)$$

This solution can be substituted back into Eq. (1.29) to give interactions between light fields in the tree-level effective Lagrangian:

$$\mathcal{L}_{\text{eff}}[\pi] \supset -\frac{\partial \mathcal{L}^{lh}}{\partial \Pi} \frac{1}{m_\Pi^2} \left(1 - \frac{D^2}{m_\Pi^2} + \dots \right) \frac{\partial \mathcal{L}^{lh}}{\partial \Pi^\dagger}. \quad (1.32)$$

Many concrete examples of this procedure can be found in the literature, see e.g. Ref. [107]. The expansion in D^2/m_Π^2 corresponds to the expansion in p^2/Λ^2 in the first case of Eq. (1.28), showing the expansion of the scalar propagator.

Next we sketch out the procedure for a Dirac fermion $\Pi + \bar{\Pi}^\dagger$, where Π and $\bar{\Pi}$ are separate two-component spin- $\frac{1}{2}$ fields transforming oppositely under G_{SM} . In this case, the UV theory is described by a Lagrangian like

$$\mathcal{L}_{\text{UV}}[\Pi, \pi] \supset i\Pi^\dagger \bar{\sigma}^\mu D_\mu \Pi + i\bar{\Pi}^\dagger \bar{\sigma}^\mu D_\mu \bar{\Pi} + \left(\Pi \frac{\partial \mathcal{L}^{lh}}{\partial \Pi} + \bar{\Pi} \frac{\partial \mathcal{L}^{lh}}{\partial \bar{\Pi}} - m_\Pi \bar{\Pi} \Pi + \text{h.c.} \right) \quad (1.33)$$

Varying the action with respect to the heavy fields gives two coupled EOM:

$$i\bar{\sigma}^\mu D_\mu \Pi - m\bar{\Pi}^\dagger + \frac{\partial \mathcal{L}^{lh}}{\partial \Pi^\dagger} = 0, \quad (1.34)$$

$$i\bar{\sigma}^\mu D_\mu \bar{\Pi} - m\Pi^\dagger + \frac{\partial \mathcal{L}^{lh}}{\partial \Pi^\dagger} = 0. \quad (1.35)$$

Substituting Eq. (1.34) into Eq. (1.35) gives a second-order partial differential equation in Π , analogous to Eq. (1.30). Inverting the differential operator in a similar way gives

$$\Pi_\beta^{\text{cl}} = \frac{1}{m_\Pi^2} \left(\epsilon_{\alpha\beta} + \frac{\frac{1}{2} X_{\alpha\beta} - D^2 \epsilon_{\alpha\beta}}{m_\Pi^2} + \dots \right) \left(iD^{\alpha\dot{\alpha}} \frac{\partial \mathcal{L}^{lh}}{\partial \Pi_\dot{\beta}^\dagger} \epsilon_{\dot{\alpha}\dot{\beta}} + m_\Pi \frac{\partial \mathcal{L}^{lh}}{\partial \bar{\Pi}_\alpha} \right), \quad (1.36)$$

where the field-strength tensor comes about from a structure like

$$[\sigma^\mu \bar{\sigma}^\nu]_\alpha^\beta D_\mu D_\nu = \eta^{\mu\nu} D_\mu D_\nu \delta_\alpha^\beta - 2i[\sigma^{\mu\nu}]_\alpha^\beta D_\mu D_\nu \quad (1.37)$$

$$= D^2 \delta_\alpha^\beta - \frac{1}{2} X_\alpha^\beta . \quad (1.38)$$

Here, and later in this section, the replacement $\bar{\Pi} \rightarrow \Pi$ should be understood for Majorana Π . Each contribution corresponds to a particular kind of propagator in the perturbative picture. The first term in the last parenthesis of Eq. (1.36) results from the fermion propagator proportional to momentum: the arrow-preserving fermion propagator shown as the last case of Eq. (1.28). The second term in the same parentheses stems from the fermion propagator proportional to the mass, corresponding to the arrow-violating propagator shown in the middle case of Eq. (1.28). Replacing Π in Eq. (1.33) gives the tree-level effective Lagrangian with the heavy fermion integrated out:

$$\begin{aligned} \mathcal{L}_{\text{eff}}[\pi] &\supset \frac{\partial \mathcal{L}^{lh}}{\partial \Pi_\beta} \frac{1}{m_\Pi^2} \left(\epsilon_{\alpha\beta} + \frac{\frac{1}{2} X_{\alpha\beta} - D^2 \epsilon_{\alpha\beta}}{m_\Pi^2} + \dots \right) i D^{\alpha\dot{\alpha}} \frac{\partial \mathcal{L}^{lh}}{\partial \Pi_\beta^\dagger} \epsilon_{\dot{\alpha}\dot{\beta}} \\ &+ \frac{\partial \mathcal{L}^{lh}}{\partial \Pi_\beta} \frac{1}{m_\Pi^2} \left(\epsilon_{\alpha\beta} + \frac{\frac{1}{2} X_{\alpha\beta} - D^2 \epsilon_{\alpha\beta}}{m_\Pi^2} + \dots \right) \frac{\partial \mathcal{L}^{lh}}{\partial \bar{\Pi}_\alpha} . \end{aligned} \quad (1.39)$$

As shown in Eqs. (1.32) and (1.39), expanding in powers of derivatives on heavy masses leads to a tower of local operators of increasing mass dimension d_i organised as a power series in the inverse heavy scale:

$$\mathcal{L}_{\text{eff}}[\pi] = \mathcal{L}^l[\pi] + \sum_i \frac{C_i}{\Lambda^{d_i-4}} \mathcal{O}_i[\pi]. \quad (1.40)$$

The C_i are dimensionless coefficients which are in general calculable if one knows the high-energy theory.

1.3.2 Effective field theories of the SM

Below we discuss EFTs constructed from SM fields and invariant under SM symmetries. The main theory of study is the SMEFT: the gauge- and Lorentz-invariant EFT built from the fields listed in Table 1.1. We also mention the WET, also known as the LEFT (Low-energy Effective Field Theory), for which invariance under $SU(2)_+ \otimes SU(2)_- \otimes SU(3)_c \otimes U(1)_{\text{EM}}$ is required.

The SMEFT at dimension six

Given the broad experimental success of the SM, it is perhaps a sensible assumption that there should be a sizeable mass gap between the electroweak scale and the mass-scale characterising any new physics. In this context, the SMEFT can be a powerful tool for constraining how this new physics might look in a model-independent way. Indeed, the SMEFT operators at dimension six are already coming to play an increasingly important role in particle phenomenology, and they have become the *de facto* framework for interpreting low-energy constraints on theoretical models and experimental deviations from SM predictions. For an extensive review, we point the reader to Ref. [108].

It has not been easy to write down a complete basis of operators in the SMEFT [18, 19], although this is now a mostly solved problem [109–113]. The lowest-dimensional operator appearing in the EFT is also the only dimension-five operator:

$$\mathcal{L}^{(5)} = [C_5]_{\{rs\}} (L_r^i L_s^j) H^k H^l \epsilon_{ik} \epsilon_{jl} + \text{h.c.}, \quad (1.41)$$

already discussed briefly in Sec. 1.2.3. The matrix of operator coefficients is necessarily symmetric by Fermi–Dirac statistics. The operator violates lepton-number by two units, and usually gives the dominant contribution to the neutrino mass in Majorana models. Ref. [114] shows that operators in the SMEFT of mass-dimension d satisfy

$$\frac{1}{2}(\Delta B - \Delta L) = d \mod 2, \quad (1.42)$$

and thus odd mass-dimension operators must violate $B-L$ by two units, while operators of even mass-dimension cannot violate $B-L$. So, aside from lepton-number-violating effects, the leading-order deviations from the SM appear at dimension six, where there are many more operators.

The dimension-six operators come in eight general classes: X^3 , H^6 , $H^4 D^2$, $X^2 H^2$, $\psi^2 H^3$, $\psi^2 XH$, $\psi^2 H^2 D$ and ψ^4 . (Here, X represents a general field-strength tensor, D is a covariant derivative and ψ is a fermion field.) The ψ^4 -type operators illustrate some of the difficulties encountered when writing down a complete basis of operators, since they can be simplified by Fierz and Schouten identities relating to the spinor, isospin and colour structure. The most common basis found in the literature is the Warsaw basis [18, 19], which tends to prefer vector currents for fermions. Thus, for example, the four-fermion operators with field content L^4 written in this way are

$$[\mathcal{O}_{ll}]_{rstu} = (L_r^\dagger \bar{\sigma}_\mu L_s)(L_t^\dagger \bar{\sigma}_\mu L_u), \quad (1.43)$$

$$[\mathcal{O}_{ll}^{(3)}]_{rstu} = (L_r^\dagger \bar{\sigma}_\mu \tau^I L_s)(L_t^\dagger \bar{\sigma}_\mu \tau^I L_u). \quad (1.44)$$

Here $\mathcal{O}_{ll}^{(3)}$ contracts the $\bar{2} \otimes 2$ of the L^\dagger and L into the triplet representation. Naively there seem to be two operators, however $\mathcal{O}_{ll}^{(3)}$ can be rewritten using the SU(2) Fierz

identity

$$[\tau^I]_j^i [\tau^I]_l^k = 2\delta_m^i \delta_j^k - \delta_j^i \delta_l^k \quad (1.45)$$

and the related identity acting on the spinor structure

$$(\psi_1^\dagger \bar{\sigma}^\mu \psi_2)(\psi_3^\dagger \bar{\sigma}^\mu \psi_4) = (\psi_1^\dagger \bar{\sigma}^\mu \psi_4)(\psi_3^\dagger \bar{\sigma}^\mu \psi_2) \quad (1.46)$$

such that

$$[\mathcal{O}_{ll}^{(3)}]_{rstu} = 2[\mathcal{O}_{ll}]_{ruts} - [\mathcal{O}_{ll}]_{rstu} . \quad (1.47)$$

Thus, the operators $[\mathcal{O}_{ll}^{(3)}]_{rstu}$ can be expressed as linear combinations of the $[\mathcal{O}_{ll}]_{rstu}$, and both operators should not be included in a genuine basis. The situation is slightly more complicated for the four-quark operators, since there is an additional space of indices to handle. In the case of operators with field content Q^4 , there seem to naively be four invariants, which can be written as vector currents

$$(Q^\dagger \bar{\sigma}_\mu \Gamma Q)(Q^\dagger \bar{\sigma}^\mu \Gamma Q) , \quad (1.48)$$

where the possible structures $\Gamma \otimes \Gamma$ can be expressed schematically as

$$1 \otimes 1, \quad \tau^I \otimes \tau^I, \quad \lambda^A \otimes \lambda^A, \quad \tau^I \lambda^A \otimes \tau^I \lambda^A . \quad (1.49)$$

The $SU(2)_L$ and $SU(3)_c$ index contraction can either be internal to the fermion current, or it may connect fermions in adjacent currents. For example, the $SU(2)_L$ contraction is internal for the structures $1 \otimes 1$ and $\lambda^A \otimes \lambda^A$, but external for $\tau^I \otimes \tau^I$ and $\tau^I \lambda^A \otimes \tau^I \lambda^A$. The spinor identity Eq. (1.46) exchanges the Q fields, so it interchanges the isospin and colour indices so that

$$\text{both internal} \leftrightarrow \text{both external}, \quad SU(2)_L \text{ external} \leftrightarrow SU(3)_c \text{ external} . \quad (1.50)$$

This means only two of the four invariants are independent. These are chosen to be $1 \otimes 1$ and $\tau^I \otimes \tau^I$ in the Warsaw basis.

The operators in the Warsaw basis are listed in Tables 1.2 and 1.3. This is the form in which we use the operators throughout the rest of this work. Each operator is given in four-component spinor notation, as is usual in the literature. We refer the reader to Appendix A for the correspondence to the two-component notation we use elsewhere, along with other relevant mathematical notation used in the tables. Our conventions are chosen to comply with those of Ref. [115].

	Operator	Label	Operator	Label
$(\bar{L}L)(\bar{L}L)$	$(\bar{L}\gamma_\mu L)(\bar{L}\gamma^\mu L)$	\mathcal{O}_{ll}		
	$(\bar{Q}\gamma_\mu Q)(\bar{Q}\gamma^\mu Q)$	$\mathcal{O}_{qq}^{(1)}$	$(\bar{Q}\gamma_\mu \tau^I Q)(\bar{Q}\gamma^\mu \sigma^I Q)$	$\mathcal{O}_{qq}^{(3)}$
	$(\bar{L}\gamma_\mu L)(\bar{Q}\gamma^\mu Q)$	$\mathcal{O}_{lq}^{(1)}$	$(\bar{L}\gamma_\mu \sigma^I L)(\bar{Q}\gamma^\mu \sigma^I Q)$	$\mathcal{O}_{lq}^{(3)}$
$(\bar{R}R)(\bar{R}R)$	$(\bar{e}_R \gamma_\mu e_R)(\bar{e}_R \gamma^\mu e_R)$	\mathcal{O}_{ee}		
	$(\bar{u}_R \gamma_\mu u_R)(\bar{u}_R \gamma^\mu u_R)$	\mathcal{O}_{uu}	$(\bar{d}_R \gamma_\mu d_R)(\bar{d}_R \gamma^\mu d_R)$	\mathcal{O}_{dd}
	$(\bar{u}_R \gamma_\mu u_R)(\bar{d}_R \gamma^\mu d_R)$	$\mathcal{O}_{ud}^{(1)}$	$(\bar{u}_R \gamma_\mu \lambda^A u_R)(\bar{d}_R \gamma^\mu \lambda^A d_R)$	$\mathcal{O}_{ud}^{(8)}$
	$(\bar{e}_R \gamma_\mu e_R)(\bar{u}_R \gamma^\mu u_R)$	\mathcal{O}_{eu}	$(\bar{e}_R \gamma_\mu e_R)(\bar{d}_R \gamma^\mu d_R)$	\mathcal{O}_{ed}
$(\bar{L}L)(\bar{R}R)$	$(\bar{L}\gamma_\mu L)(\bar{e}_R \gamma^\mu e_R)$	\mathcal{O}_{le}	$(\bar{Q}\gamma_\mu Q)(\bar{e}_R \gamma^\mu e_R)$	\mathcal{O}_{qe}
	$(\bar{L}\gamma_\mu L)(\bar{u}_R \gamma^\mu u_R)$	\mathcal{O}_{lu}	$(\bar{L}\gamma_\mu L)(\bar{d}_R \gamma^\mu d_R)$	\mathcal{O}_{ld}
	$(\bar{Q}\gamma_\mu Q)(\bar{u}_R \gamma^\mu u_R)$	$\mathcal{O}_{qu}^{(1)}$	$(\bar{Q}\gamma_\mu \lambda^A Q_L)(\bar{u}_R \gamma^\mu \lambda^A u_R)$	$\mathcal{O}_{qu}^{(8)}$
	$(\bar{Q}\gamma_\mu Q)(\bar{d}_R \gamma^\mu d_R)$	$\mathcal{O}_{qd}^{(1)}$	$(\bar{Q}\gamma_\mu \lambda^A Q_L)(\bar{d}_R \gamma^\mu \lambda^A d_R)$	$\mathcal{O}_{qd}^{(8)}$
$(\bar{L}R)(\bar{R}L)$	$(\bar{L}e_R)(\bar{d}_R Q)$	\mathcal{O}_{ledq}		
$(\bar{L}R)(\bar{L}R)$	$(\bar{Q}_i u_R)(\bar{Q}_j d_R) \epsilon^{ij}$	$\mathcal{O}_{quqd}^{(1)}$	$(\bar{Q}_i \lambda^A u_R)(\bar{Q}_j \lambda^A d_R) \epsilon^{ij}$	$\mathcal{O}_{quqd}^{(8)}$
	$(\bar{L}_i e_R)(\bar{Q}_j u_R) \epsilon^{ij}$	$\mathcal{O}_{lequ}^{(1)}$	$(\bar{L}_i \sigma_{\mu\nu} e_R)(\bar{Q}_j \sigma^{\mu\nu} u_R) \epsilon^{ij}$	$\mathcal{O}_{lequ}^{(3)}$
$\Delta B = 1$			$(d_R^a u_R^b)(Q^{ci} L^j) \epsilon_{abc} \epsilon_{ij}$	\mathcal{O}_{duq}
			$(Q^{ai} Q^{bj})(u_R^c e_R) \epsilon_{abc} \epsilon_{ij}$	\mathcal{O}_{qqu}
			$(d_R^a u_R^b)(u_R^c e_R) \epsilon_{abc}$	\mathcal{O}_{duu}
			$(Q^{ai} Q^{bk})(Q^{cl} L^j) \epsilon_{abc} \epsilon_{ij} \epsilon_{kl}$	\mathcal{O}_{qqq}

Table 1.2: The table shows the four-fermion operators in the dimension-six SMEFT in the Warsaw basis [18, 19]. The operators are listed in four-component spinor notation, and a full correspondence to the two-component notation we use elsewhere can be found in Appendix G of Ref. [106]. We remind the reader that we intend combinations like (QQ) stand for $(\bar{Q}^C Q)$, where Q^C is the charge-conjugated spinor. Flavour indices are omitted, and should be understood to label the fermions in the order $\{r, s, t, u\}$ as they appear.

	Operator	Notation	Operator	Notation
X^3	$W_\mu^{I\nu} W_\nu^{J\rho} W_\rho^{K\mu} \epsilon_{IJK}$ $G_\mu^{Av} G_\nu^{B\rho} G_\rho^{C\mu} f_{ABC}$	\mathcal{O}_W \mathcal{O}_G	$\tilde{W}_\mu^{I\nu} W_\nu^{J\rho} W_\rho^{K\mu} \epsilon_{IJK}$ $\tilde{G}_\mu^{Av} G_\nu^{B\rho} G_\rho^{C\mu} f_{ABC}$	$\mathcal{O}_{\tilde{W}}$ $\mathcal{O}_{\tilde{G}}$
H^6	$(H^\dagger H)^3$	\mathcal{O}_H		
$H^4 D^2$	$(H^\dagger H) \square (H^\dagger H)$	$\mathcal{O}_{H\square}$	$H_i^\dagger (D_\mu H)^i \cdot (D^\mu H)_j^\dagger H^j$	\mathcal{O}_{HD}
$\psi^2 H^2$	$(H^\dagger H)(\bar{L}He_R)$ $(H^\dagger H)(\bar{Q}Hd_R)$	\mathcal{O}_{eH} \mathcal{O}_{dH}	$(H^\dagger H)(\bar{Q}\tilde{H}u_R)$	\mathcal{O}_{uH}
$X^2 H^2$	$(H^\dagger H)B_{\mu\nu}B^{\mu\nu}$ $(H^\dagger H)W_{\mu\nu}^I W^{I\mu\nu}$ $(H^\dagger \tau^I H)W_{\mu\nu}^I B^{\mu\nu}$ $(H^\dagger H)G_{\mu\nu}^A G^{A\mu\nu}$	\mathcal{O}_{HB} \mathcal{O}_{HW} \mathcal{O}_{HWB} \mathcal{O}_{HG}	$(H^\dagger H)\tilde{B}_{\mu\nu}B^{\mu\nu}$ $(H^\dagger H)\tilde{W}_{\mu\nu}^I W^{I\mu\nu}$ $(H^\dagger \tau^I H)\tilde{W}_{\mu\nu}^I B^{\mu\nu}$ $(H^\dagger H)\tilde{G}_{\mu\nu}^A G^{A\mu\nu}$	$\mathcal{O}_{H\tilde{B}}$ $\mathcal{O}_{H\tilde{W}}$ $\mathcal{O}_{H\tilde{W}B}$ $\mathcal{O}_{H\tilde{G}}$
$\psi^2 XH$	$(\bar{L}\sigma^{\mu\nu} e_R)HB_{\mu\nu}$ $(\bar{Q}\sigma^{\mu\nu} u_R)\tilde{H}B_{\mu\nu}$ $(\bar{Q}\sigma^{\mu\nu} d_R)HB_{\mu\nu}$ $(\bar{Q}\sigma^{\mu\nu} \lambda^A u_R)\tilde{H}G_{\mu\nu}^A$	\mathcal{O}_{eB} \mathcal{O}_{uB} \mathcal{O}_{dB} \mathcal{O}_{uG}	$(\bar{L}\sigma^{\mu\nu} e_R)\tau^I HW_{\mu\nu}^I$ $(\bar{Q}\sigma^{\mu\nu} u_R)\tau^I \tilde{H}W_{\mu\nu}^I$ $(\bar{Q}\sigma^{\mu\nu} d_R)\tau^I HW_{\mu\nu}^I$ $(\bar{Q}\sigma^{\mu\nu} \lambda^A d_R)HG_{\mu\nu}^A$	\mathcal{O}_{eW} \mathcal{O}_{uW} \mathcal{O}_{dW} \mathcal{O}_{dG}
$\psi^2 H^2 D$	$(H^\dagger i\tilde{D}_\mu H)(\bar{L}\gamma^\mu L)$ $(H^\dagger i\tilde{D}_\mu H)(\bar{e}_R\gamma^\mu e_R)$ $(H^\dagger i\tilde{D}_\mu H)(\bar{Q}\gamma^\mu Q)$ $(H^\dagger i\tilde{D}_\mu H)(\bar{u}_R\gamma^\mu u_R)$ $H^i(iD_\mu H)^j \epsilon_{ij} \cdot (\bar{u}_R\gamma^\mu d_R)$	$\mathcal{O}_{Hl}^{(1)}$ \mathcal{O}_{He} $\mathcal{O}_{Hq}^{(1)}$ \mathcal{O}_{Hu} \mathcal{O}_{Hud}	$(H^\dagger i\tilde{D}_\mu^I H)(\bar{L}\gamma^\mu \tau^I L)$ $(H^\dagger i\tilde{D}_\mu^I H)(\bar{Q}\gamma^\mu \tau^I Q)$ $(H^\dagger i\tilde{D}_\mu^I H)(\bar{d}_R\gamma^\mu d_R)$	$\mathcal{O}_{Hl}^{(3)}$ $\mathcal{O}_{Hq}^{(3)}$ \mathcal{O}_{Hd}

Table 1.3: The table shows the operators featuring in the Warsaw basis [18, 19] of the dimension-six SMEFT that are not four-fermion operators. We point the reader to Appendix G of Ref. [106] for the correspondence between the four-component notation used here and the two-component notation used elsewhere in this work for spinors, while the definition of \tilde{D}^μ can be found in Eq. (A.4). Flavour indices are omitted and should be understood to act on fermions in the order $\{r, s\}$ as they appear in each operator.

The Low-energy or Weak Effective Theory

Many experimental constraints on the SM and its extensions come from low-energy flavour-changing process involving four fermions. These can be accurately described using an effective theory, similar to the Fermi theory of the Weak interactions, in which the electroweak gauge bosons, the physical higgs and the top quark have been integrated out. The dimension six operators in this low-energy EFT [116–119] have been extensively applied to B , K and D meson decays, meson–anti-meson oscillations and leptonic decays, e.g. [120]. They are also an invaluable tool for studying deviations from the SM in a way independent from many of the assumptions underlying SMEFT. The symmetries of the theory are only those of QCD and electromagnetism, and the fermions are the usual quarks and leptons with the top quark excluded from the theory. At dimension six there are 3,631 $\Delta B = \Delta L = 0$ operators [116], and we do not list them all here. Rather, we introduce the pertinent operators within the discussion of each specific phenomenological process we study in this work.

1.3.3 Operator redundancy and the Hilbert series

The previous section introduced some of the difficulties involved with writing down a basis of four-fermion operators for a complex EFT like the SMEFT. Additional redundancy can occur once operators with (covariant) derivatives are included. These include operator relations through integration by parts (IBP) and field redefinitions involving the classical equations of motion [18, 121, 122]. At mass-dimensions larger than six, these come to be a large source of the difficulty in writing down a complete operator basis, but the problem can be addressed through Hilbert-series methods [109–113]. Below, we motivate how the EOM can be used to simplify effective operator bases, and explain how these redundancies can be accounted for through Hilbert series techniques.

Field redefinitions and the equations of motion

It is clear that operators can be simplified using the EOM at lowest order [18, 123–125], since the external legs are put on-shell in the Feynman rules. That is, an operator like

$$(H^\dagger H)(\bar{e}_R i \not{D} e_R) \tag{1.51}$$

can be simplified when it appears in calculations with all legs external. So, any leading-order amplitude involving the operator can be reduced through

$$i \not{D} e_R = y_e H^\dagger L, \tag{1.52}$$

(or equivalently $\mathcal{M} \sim \not{p} u_e = m_e u_e$ by the momentum-space Dirac equation) to \mathcal{O}_{eH} . Surprisingly, this useful result can be extended even to cases involving propagators and

loops by performing field redefinitions. Specifically, field redefinitions that preserve the symmetries of the theory and contain a term linear in the original field allow the EOM to simplify a local effective Lagrangian without affecting the S -matrix [126–132]. We illustrate this with a toy ϕ^4 theory:

$$\mathcal{L} = \frac{1}{2}(\partial_\mu\phi)(\partial^\mu\phi) - \frac{1}{2}m^2\phi^2 - \frac{\lambda}{4!}\phi^4 + \frac{c_1}{\Lambda^2}\phi^6 + \frac{c_2}{\Lambda^2}\phi^3\Box\phi + \mathcal{O}(\Lambda^{-4}). \quad (1.53)$$

Under the field redefinition

$$\phi \rightarrow \phi + \frac{c_2}{\Lambda^2}\phi^3, \quad (1.54)$$

the kinetic term becomes

$$\frac{1}{2}(\partial_\mu\phi)(\partial^\mu\phi) \rightarrow \frac{1}{2}(\partial_\mu\phi)(\partial^\mu\phi) - \frac{c_2}{\Lambda^2}\phi^3\Box\phi + \mathcal{O}(\Lambda^{-4}), \quad (1.55)$$

where the second term comes from integrating $c_2\Lambda^{-2}(\partial_\mu\phi)(\partial^\mu\phi^3)$ by parts. This term cancels the last term in Eq. (1.53), for which the additional operators induced by the field redefinition are all $\mathcal{O}(\Lambda^{-4})$ terms. Performing the field redefinition on the other interaction terms in the Lagrangian leads to an effective redefinition of λ and c_1 , with all other induced operators suppressed by four powers of Λ . Concretely,

$$\begin{aligned} \mathcal{L} &\rightarrow \frac{1}{2}(\partial_\mu\phi)(\partial^\mu\phi) - \frac{1}{2}m^2\phi^2 - \frac{\lambda}{4!}\phi^4 + \frac{c_1}{\Lambda^2}\phi^6 + \frac{c_2}{\Lambda^2}\phi^3\Box\phi \\ &\quad + \frac{c_2}{\Lambda^2}\phi^3 \underbrace{\left(-\Box\phi - m^2\phi - \frac{\lambda}{3!}\phi^3 \right)}_{\equiv E[\phi]} + \dots \\ &= \frac{1}{2}(\partial_\mu\phi)(\partial^\mu\phi) - \frac{1}{2}m^2\phi^2 - \underbrace{\left(\frac{\lambda}{4!} + \frac{c_2}{\Lambda^2}m^2 \right)\phi^4}_{\equiv \lambda'/4!} + \underbrace{\left(\frac{c_1}{\Lambda^2} - \frac{c_2}{\Lambda^2}\frac{\lambda}{3!} \right)\phi^6}_{\equiv c'_1/\Lambda^2} + \mathcal{O}(\Lambda^{-4}). \end{aligned} \quad (1.56)$$

This is guaranteed since in the effective theory all of the operators consistent with the symmetries are already present, so the effects of the additional terms are exclusively to shift the coefficients of the theory around. The appearance of the EOM operator $E[\phi]$ above can be understood on the basis of the nature of the field redefinition Eq. (1.54). The additional terms induced by the field redefinition up to $\mathcal{O}(\Lambda^{-2})$ will be those in which a ϕ or its derivative has been replaced with $c_2\Lambda^{-2}\phi^3$. That is,

$$\begin{aligned} \Delta\mathcal{L} &= \frac{c_2}{\Lambda^2}\phi^3\frac{\partial\mathcal{L}}{\partial\phi} + \frac{c_2}{\Lambda^2}(\partial_\mu\phi^3)\frac{\partial\mathcal{L}}{\partial(\partial_\mu\phi)} + \mathcal{O}(\Lambda^{-4}) \\ &= \frac{c_2}{\Lambda^2}\phi^3 \left[\frac{\partial\mathcal{L}}{\partial\phi} - \partial_\mu\frac{\partial\mathcal{L}}{\partial(\partial_\mu\phi)} \right] + \mathcal{O}(\Lambda^{-4}), \end{aligned} \quad (1.57)$$

where we have integrated the second term by parts in the last step. In order to show that the S -matrix is unaffected, it is not sufficient to show only that the Lagrangian has not changed form (up to order Λ^{-2}). In the path integral picture, the field redefinition Eq. (1.54) will also change the measure of the path integral and the sources \mathcal{J}_i for each of the fields, whose effects we have not considered. These additional changes can be dealt with generically [121]. In short, the Jacobian can be written as a Lagrangian involving ghost fields, similar to the Fadeev–Popov approach taken in Gauge Theory. In this case the ghost fields acquire a mass of order Λ , and are therefore not relevant to the effective theory. The change to the source \mathcal{J}_ϕ does lead to a change in the Green’s functions of the theory, although the S -matrix remains unchanged. We can see this easily in our toy theory. The LSZ reduction formula [133]

$$G^{(n+m)}(q_1, \dots, q_m; p_1, \dots, p_n) \underset{\substack{p_j^2 \rightarrow m^2 \\ q_k^2 \rightarrow m^2}}{\sim} \left(\prod_{j=1}^m \frac{i\sqrt{Z_j}}{p_j^2 - m^2 + i\epsilon} \right) \left(\prod_{k=1}^n \frac{i\sqrt{Z_k}}{q_k^2 - m^2 + i\epsilon} \right) \langle q_1, \dots, q_m | S | p_1, \dots, p_n \rangle, \quad (1.58)$$

relates the poles in the $(m+n)$ -point Green’s function to the S -matrix, up to wavefunction renormalisation factors Z_i . Here momenta p_i label the m incoming particles and q_i label the n outgoing particles. Consider, for example, the four-point Green’s function with all particles taken to be incoming for simplicity:

$$G^{(4)}(p_1, p_2, p_3, p_4) = \left(\prod_{i=1}^4 \int d^4 x_i \cdot e^{-ip_i \cdot x_i} \right) \langle 0 | T\{\phi(x_1)\phi(x_2)\phi(x_3)\phi(x_4)\} | 0 \rangle. \quad (1.59)$$

The effect of the term $c_1 \Lambda^{-2} \mathcal{J}_\phi \phi^3$ is to alter the momentum-space Green’s function to

$$\begin{aligned} & \langle 0 | T\{[\phi(x_1) + c_1 \Lambda^{-2} \phi(x_1)^3] \cdots [\phi(x_4) + c_1 \Lambda^{-2} \phi(x_4)^3]\} | 0 \rangle \\ &= \langle 0 | T\{\phi(x_1)\phi(x_2)\phi(x_3)\phi(x_4)\} | 0 \rangle + \langle 0 | T\{c_1 \Lambda^{-2} \phi(x_1)^3 \phi(x_2)\phi(x_3)\phi(x_4)\} | 0 \rangle \\ &+ \sum_{i=2}^4 (1 \leftrightarrow i) + \mathcal{O}(\Lambda^{-4}), \end{aligned} \quad (1.60)$$

which differs only by the terms like $\langle 0 | T\{c_1 \Lambda^{-2} \phi(x_1)^3 \phi(x_2)\phi(x_3)\phi(x_4)\} | 0 \rangle$ to order Λ^{-2} . These matrix elements do not affect the S -matrix, since the singularity structure is different. In this case, there is no single-particle pole at x_1 , and so there is no contribution to scattering.

In the context of this toy ϕ^4 theory we have motivated that terms in the effective Lagrangian \mathcal{L} that are connected by the EOM are redundant when working to a fixed order in Λ . Such field redefinitions are a powerful tool for simplifying operator bases, and they are often used to eliminate as many operators with derivatives as possible. We proceed to illustrate how such redundancies, along with those from IBP, can be accounted for systematically with the Hilbert series.

The Hilbert series

In the following we discuss the Hilbert series (HS), also known as the Molien or Poincaré function, as a tool for enumerating Lagrangian invariants in a conceptually clean and efficient way. The Hilbert series is a generating function that contains information about the number and structure of the invariants that can be constructed from a set of multiplets. The approach has been used in more formal contexts e.g. [134–136], although it has also been used to count lepton and quark flavour invariants [137, 138] as well as operators in the SMEFT [112]. Our aim here is to illustrate the essential components of the HS approach with examples.

The HS H is a generating function that counts the number of operators with a certain field content, *i.e.*

$$H(\{\chi_j\}) = \sum_i c_i \mathcal{O}_i(\{\chi_j\}), \quad (1.61)$$

where $c_i \in \mathbb{N}$ is the number of independent invariants with field content \mathcal{O}_i , a polynomial in the fields of the theory $\{\chi_j\}$. The c_i and \mathcal{O}_i in the simplified case of a theory with a single field χ transforming under the compact Lie group G can be computed from the general formula for the HS:

$$H(\chi) = \int_G d\mu_G \exp \left[\sum_{r=1}^{\infty} \frac{\Delta(r)\chi^r \chi_R(z_j^r)}{r} \right], \quad (1.62)$$

where $d\mu_G$ is the Haar measure of the group, the invariant measure one can use to integrate over the manifold of G , and $\chi_R(z_j^r)$ is the character function associated with the representation R in which χ transforms under G . The character functions can be found using character generating functions [139] in general, but the functions relevant to the SM representations are listed in Appendix A.1 of Ref. [109]. The function

$$\Delta(r) = \begin{cases} 1 & \chi \text{ bosonic} \\ (-1)^{r+1} & \chi \text{ fermionic} \end{cases}, \quad (1.63)$$

accounts for the fact that χ is anticommuting in the fermionic case [139].

Even redundancies due to IBP and EOM relations can be incorporated into the HS technique. The space of invariants modulo EOM can be organised into representations of the conformal group [112, 113]. Irreducible representations of the conformal group involve a ‘primary operator’ \mathcal{O} and its derivatives, called ‘descendant operators’: $(\mathcal{O}, \partial_\mu \mathcal{O}, \partial_\mu \partial_\nu \mathcal{O}, \dots)$. The invariants can be constructed by decomposing tensor products of these irreps, which accounts for EOM redundancy, and then projecting out the primary operator, which deals with IBP relations. This alters the formula Eq. (1.62) slightly:

$$H(D, \chi) = \int_G d\mu_G \frac{1}{P(D, x_+, x_-)} \exp \left[\sum_{r=1}^{\infty} \frac{\Delta(r)\chi^r \chi_R(z_j^r)}{r D^r} \right] + \Delta H(D, \chi), \quad (1.64)$$

where D is a spurion field representing the (covariant) derivative, d_r is the mass-dimension of the field χ_r and

$$P(D, x_+, x_-) = \frac{1}{(1 - Dx_+x_-)\left(1 - \frac{D}{x_+x_-}\right)\left(1 - \frac{Dx_+}{x_-}\right)\left(1 - \frac{Dx_-}{x_+}\right)}, \quad (1.65)$$

with x_\pm the $SU(2)_\pm$ integration variables. The function ΔH can be obtained from a general formula presented in Ref. [113]. Its role is to cancel unwanted terms (of mass-dimension $d \leq 4$) from the HS that come about because the character functions of the conformal group are not orthonormal [113].

We illustrate the use of Eq. (1.64) with a simple example: the independent invariants built out of the SM Higgs doublet H . The Higgs doublet transforms in the fundamental representation of $SU(2)_L$ and carries hypercharge $Y = \frac{1}{2}$, for which the relevant Haar measures are [140]

$$\int_{SU(2)} d\mu_{SU(2)} = \frac{1}{2\pi i} \oint_{|x|=1} \frac{dx}{x} (1 - x^2), \quad \int_{U(1)} d\mu_{U(1)} = \frac{1}{2\pi i} \oint_{|y|=1} \frac{dy}{y}, \quad (1.66)$$

and the character functions are [109, 141]

$$\chi_{I=\frac{1}{2}}(x) = \frac{1}{x} + x, \quad \chi_{Y=\frac{1}{2}}(y) = y^{1/2}, \quad (1.67)$$

for $x, y \in \mathbb{C}$. This gives [113]

$$\begin{aligned} H(H, \tilde{H}) &= \frac{1}{(2\pi i)^4} \oint_{|x_+|=1} dx_+ \oint_{|x_-|=1} dx_- \cdot \oint_{|x|=1} \frac{dx}{x} (1 - x^2) \cdot \oint_{|y|=1} \frac{dy}{y} \\ &\cdot \exp \left[n_f \sum_{r=1}^{\infty} \frac{H^r}{rD} \left(\frac{1}{x^r} + x^r \right) y^{r/2} \chi_{(0,0)}^r \right] \cdot \exp \left[n_f \sum_{r=1}^{\infty} \frac{\tilde{H}^r}{rD} \left(\frac{1}{x^r} + x^r \right) y^{-r/2} \chi_{(0,0)}^r \right] \\ &\cdot \frac{1}{P(D, x_+, x_-)} + (H^\dagger H D^2 - D^4) \end{aligned} \quad (1.68)$$

for the Hilbert series, where we have accounted for H and its conjugate \tilde{H} separately, and included the possibility of n_f flavours. The last term in parentheses is the relevant part of ΔH in this case, and $\chi_{(0,0)}$ is the scalar character function:

$$\chi_{(0,0)} = DP(D, x_+, x_-)(1 - D^2). \quad (1.69)$$

The contour integrals can be done by expanding the integrand in H and \tilde{H} , and integrating up to the required order [134]. For this example, the dimension-six terms are

$$H(H, \tilde{H}) = \frac{n_f^2}{36} (n_f + 1)^2 (5n_f^2 - 4n_f + 8) H^3 \tilde{H}^3 + n_f^2 (3n_f^2 + 1) H^2 \tilde{H}^2 D^2 + n_f^2 H \tilde{H} D^4, \quad (1.70)$$

where we have allowed for the possibility of n_f Higgs generations.

The HS approach has an attractive modular structure. For example, if one wanted to count the number of invariants while not accounting for IBP and EOM redundancies, one need only remove the Lorentz integrals, character functions and ΔH . Something that is perhaps less clear is that the HS can also be used to construct operators that are not invariants of the symmetry groups in G , but rather violate those symmetries in specific ways.

We work through this point with an even simpler example than the previous one: a scalar ϕ charged only under a U(1) symmetry, motivated by Ref. [109]. In this case, the HS is

$$H(\phi, \phi^*) = \sum_{n=0}^{\infty} (\phi^* \phi)^n \quad (1.71)$$

$$= \frac{1}{1 - \phi^* \phi}, \quad (1.72)$$

where we treat $\phi^* \phi$ as a c-number less than one. This sum can be written as a contour integral, making a more clear connection⁶ to Eq. (1.62):

$$H(\phi, \phi^*) = \frac{1}{2\pi i} \oint_{|z|=1} \frac{dz}{z} \frac{1}{(1 - \phi z)(1 - \phi^* / z)}, \quad (1.73)$$

whose integrand we expand

$$\begin{aligned} \frac{1}{(1 - \phi z)(1 - \phi^* z)} &= [1 + \phi^* \phi + (\phi^* \phi)^2 + \dots] + z[\phi + \phi(\phi^* \phi) + \phi(\phi^* \phi)^2 + \dots] \\ &\quad + z^2[\phi^2 + \phi^2(\phi \phi^*) + \dots] + \dots \end{aligned} \quad (1.74)$$

The invariants sit in the first term, and so are picked out by the contour integral after dividing through by z in Eq. (1.73). Importantly, the terms proportional to z in Eq. (1.74) violate the symmetry by one unit, and so these can be picked out by the contour integral if we divide by z^2 in Eq. (1.73), and similarly for any desired value of charge violation.

The HS provides information about the field content of the invariants and the number of independent operators, but does not tell us exactly how to construct the singlets. This is an important drawback of the approach, although even here there has been much recent progress using on-shell methods, e.g. [142–145].

⁶The integrand can also be written as an exponential like in Eq. (1.62) containing ϕ and ϕ^* :

$$\frac{1}{(1 - \phi z)(1 - \phi^* / z)} = \exp \left[\sum_{r=1}^{\infty} \frac{(\phi z)^r}{r} + \sum_{r=1}^{\infty} \left(\frac{\phi^*}{z} \right)^r \frac{1}{r} \right].$$

1.4 The flavour anomalies and their explanation

In recent years, measurements of a number of processes involving leptons have established a large set of significant and unresolved deviations from SM predictions. Many of these measurements involve semileptonic B -meson decays, and these can be placed into two broad classes:

Neutral-current These involve flavour-changing neutral-current (FCNC) $b \rightarrow s$ transitions and include branching-ratio measurements in final states with muons, anomalous angular observables in $B \rightarrow K^* \mu\mu$, and violations of μ - e LFU in $B \rightarrow K^{(*)}\ell\ell$ processes, where ℓ represents a charged lepton. This class corresponds to hundreds of discrepant measurements in total, and single-operator fits suggest a preference for new-physics at roughly 6σ , e.g. [13].

Charged-current These involve $b \rightarrow c\ell\nu$ transitions and shown apparent deviations from τ - μ and τ - e LFU. The main observables measured in this case are LFU ratios in $B \rightarrow D^{(*)}\ell\nu$, for which the combined deviation from the SM expectation is just over 3σ [14].

Excitingly there is a high-degree of self-consistency between the measurements, both within and across these two classes. That is, the measurements imply coherent and theoretically well-motivated patterns when interpreted in terms of deviations in four-fermion operator coefficients.

In addition to these classes, the most precise measurement of the anomalous magnetic moment of the muon ($g - 2)_\mu$ [146], is in tension with the SM expectation [147] at roughly 3.5σ . More recently, a smaller discrepancy has also been measured in $(g - 2)_e$ [148]. Taken together, these anomalies paint a picture of new-physics coupling to leptons in way that violates the LFU present in the SM. In the following we discuss the experimental situation relevant to each of these classes, and the extent to which new contributions to dimension-six operator coefficients can reconcile the discrepancies.

1.4.1 Neutral-current anomalies

The neutral-current anomalies represent a large family of measurements in tension with SM prediction with a common underlying $b \rightarrow s$ transition at the quark level and usually a $\mu^+ \mu^-$ pair. The measurements come in three main categories: branching ratios, LFU ratios, and angular observables.

There are many discrepancies seen in branching ratio data at dimuon invariant masses below the charmonium threshold. Examples include the branching ratios for the semileptonic decays $B \rightarrow K^{(*)}\mu\mu$ [149] and $B_s \rightarrow \phi\mu\mu$ [150], the leptonic decay $B_s \rightarrow \mu\mu$ [151–154], and the hyperon channels $\Lambda_b \rightarrow \Lambda\mu\mu$ [155]. In all cases, the measured values tend to fall short of the respective SM expectations.

Semileptonic B decays like $B \rightarrow K^{(*)}\mu\mu$ had already been recognised as good probes of new physics even before the start of the LHC, e.g. [156]. This is because, being FCNC processes, they are additionally suppressed in the SM by off-diagonal CKM matrix elements, weak couplings, and a loop factor. The differential decay rate for $B^+ \rightarrow K^+\ell\ell$ is [157]

$$\frac{d\Gamma}{dq^2} = \frac{G_F^2 \alpha^2 |V_{tb} V_{ts}^*|^2}{128\pi^5} |k| \beta \left[\frac{2}{3} |k|^2 \beta^2 |C_{10} f_+(q^2)|^2 + \frac{4m_\ell^2(m_B^2 - m_K^2)^2}{q^2 m_B^2} |C_{10} f_0(q^2)|^2 \right. \\ \left. + |k^2| \left(1 - \frac{1}{3} \beta^2 \right) \left| C_9 f_+(q^2) + 2C_7 \frac{m_b + m_s}{m_B + m_K} f_T(q^2) \right|^2 \right], \quad (1.75)$$

where k is the kaon momentum, $\beta = (1 - 4m_\ell^2 q^{-2})^{1/2}$, and $f_{0,+,\ell T}$ are the $B \rightarrow K$ scalar, vector and tensor form factors. The expression is representative of the structure of the whole class of relevant semileptonic decays. The strongest dependence is on the operator coefficients C_9 and C_{10} in the WET, defined as

$$\mathcal{O}_9 = (\bar{s}\gamma^\mu P_L b)(\bar{\mu}\gamma_\mu \mu), \quad (1.76)$$

$$\mathcal{O}_{10} = (\bar{s}\gamma^\mu P_L b)(\bar{\mu}\gamma_\mu \gamma_5 \mu), \quad (1.77)$$

with the coefficients usually normalised such that

$$\mathcal{L} = \frac{4G_F}{\sqrt{2}} V_{tb} V_{ts}^* \frac{e^2}{16\pi^2} \sum_i C_i \mathcal{O}_i. \quad (1.78)$$

Experimentally, semileptonic process like $B \rightarrow K\mu\mu$ are difficult to separate from the corresponding background processes like $B \rightarrow K\psi(\rightarrow \mu\mu)$, where ψ represents any of the vector charmonium resonances. For this reason, kinematic regions close to the narrow charmonium resonances are excluded from experimental analyses. The most significant single deviation is in the semileptonic decay $B_s \rightarrow \phi\mu\mu$, for which the data depart from the SM prediction by more than 3σ in the $q^2 \in [1, 5] \text{ GeV}^2$ bin [150]. A problematic feature of this and many of these channels is that the SM prediction is plagued by hadronic uncertainties, which can be difficult to calculate. We show the differential branching ratio for $B_s \rightarrow \phi\mu\mu$ measured by LHCb in Fig. 1.7, taken from Ref. [158], along with the SM predictions using different methods to deal with the form factors [159–161]. Both the large uncertainties on the theory side and the apparent suppression of the measured values are clear. The discrepancy with the SM is largest in the aforementioned q^2 bin.

The decay $B_s \rightarrow \mu\mu$ is cleaner than the semileptonic decays on the theory side: the final state is leptonic and the only non-perturbative physics needed is the B_s decay constant, which can be calculated to high precision on the lattice [162]. The measurements performed by ATLAS [154], LHCb [152, 153] and CMS [151] are shown in Fig. 1.8,

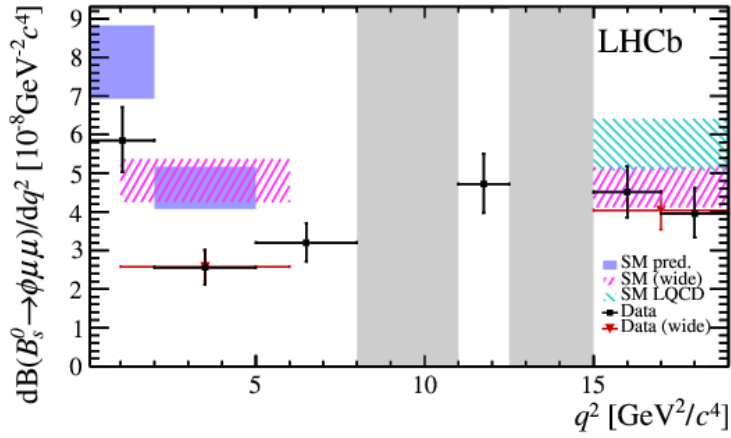


Figure 1.7: The figure shows the measured and predicted values for the differential branching ratio for $B_s \rightarrow \phi \mu \mu$ by bins of q^2 . The data points are the LHCb measurements, while the coloured rectangles are the SM predictions with form factors calculated using light-cone sum rules [159, 160] and lattice QCD [161]. The greyed out regions correspond to charmonium resonances, exluded from the analysis as discussed in the main text. The LHCb data points are generally lower than the SM expectation, especially in the $q^2 \in [1, 5] \text{ GeV}^2$ bin where the discrepancy is larger than 3σ . The plot is taken from Ref. [158].

along with correlated limits on $B^0 \rightarrow \mu\mu$. The combination of the measurements shown is taken from Ref. [13], and suggests a compatibility with the SM at close to 2σ . Currently, measurements of $B_s \rightarrow \mu\mu$ are statistically limited; the branching ratio in the SM is very small because it is chirality suppressed, but this also makes it a promising mode for measuring new-physics effects.

The large theoretical uncertainties featuring in the expressions for the decay rates $\Gamma[B \rightarrow K^{(*)}\mu\mu]$ can be tamed in a more direct way by constructing a ratio with the electronic mode $B \rightarrow K^{(*)}ee$, in which many sources of uncertainty cancel in the regime where new-physics effects are small [163–165]. Interestingly, the LHCb collaboration has measured a suppression in the ratios

$$R_{K^{(*)}} = \frac{\Gamma[B \rightarrow K^{(*)}\mu\mu]}{\Gamma[B \rightarrow K^{(*)}ee]} \quad (1.79)$$

in the $q^2 \in [1, 6] \text{ GeV}^2$ bin. In the SM the prediction of the observables outside of the low- q^2 region is determined by physics which is wholly independent of the flavour of the lepton pair in the final state, making R_K and R_{K^*} finely sensitive to violations of LFU. LHCb finds [8]

$$R_K = 0.846^{+0.060+0.016}_{-0.054-0.014}, \quad (1.80)$$

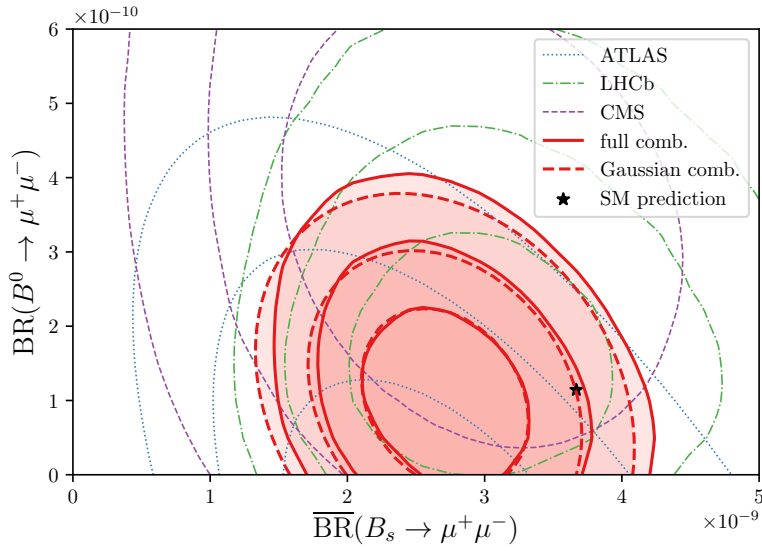


Figure 1.8: The figure shows the two-dimensional likelihood contours in $\text{Br}(B^0 \rightarrow \mu\mu)$ and $\text{Br}(B_s \rightarrow \mu\mu)$. The thin contours are individual measurements, while the thick contours are the combination. A Gaussian approximation to the combined fit is shown with thick dashed contours. For more details see Ref. [13], from where the figure is taken. The SM prediction (shown with a star) is compatible with the combined fit at 2σ .

for dilepton invariant mass squared range $q^2 \in [1.1, 6] \text{ GeV}^2$, while the SM demands $R_K^{\text{SM}} = 1.0003 \pm 0.0001$ [166]. The analysis accounts for systematic differences in the reconstruction of muons and electrons by LHCb by first normalising the decay rates to the $B^+ \rightarrow K^+ J/\psi(\rightarrow \mu\mu/ee)$ rates. The measurement is then a double ratio in which many theoretical and experimental uncertainties cancel. The ratio R_K has also been measured by Belle [9] and BaBar [10] to be suppressed, although with larger uncertainties.

The K^* ratio has also been measured by LHCb [12] to show an approximately 2.5σ discrepancy in the central q^2 bin:

$$R_{K^*} = \begin{cases} 0.660^{+0.110}_{-0.070} \pm 0.024 & \text{for } 0.045 \text{ GeV}^2 < q^2 < 1.1 \text{ GeV}^2 \\ 0.685^{+0.113}_{-0.069} \pm 0.047 & \text{for } 1.1 \text{ GeV}^2 < q^2 < 6 \text{ GeV}^2 \end{cases}. \quad (1.81)$$

The Belle measurement [11] is consistent with the SM prediction at $\lesssim 2\sigma$:

$$R_{K^*} = \begin{cases} 0.90^{+0.27}_{-0.21} \pm 0.10 & \text{for } 0.1 \text{ GeV}^2 < q^2 < 8 \text{ GeV}^2 \\ 1.18^{+0.52}_{-0.32} \pm 0.10 & \text{for } 15 \text{ GeV}^2 < q^2 < 19 \text{ GeV}^2 \end{cases}. \quad (1.82)$$

Although the error bars are large, the central value is still suppressed with respect to the SM prediction in the low- q^2 region. A summary of the experimental situation relevant to R_K and R_{K^*} is presented in Fig. 1.9.

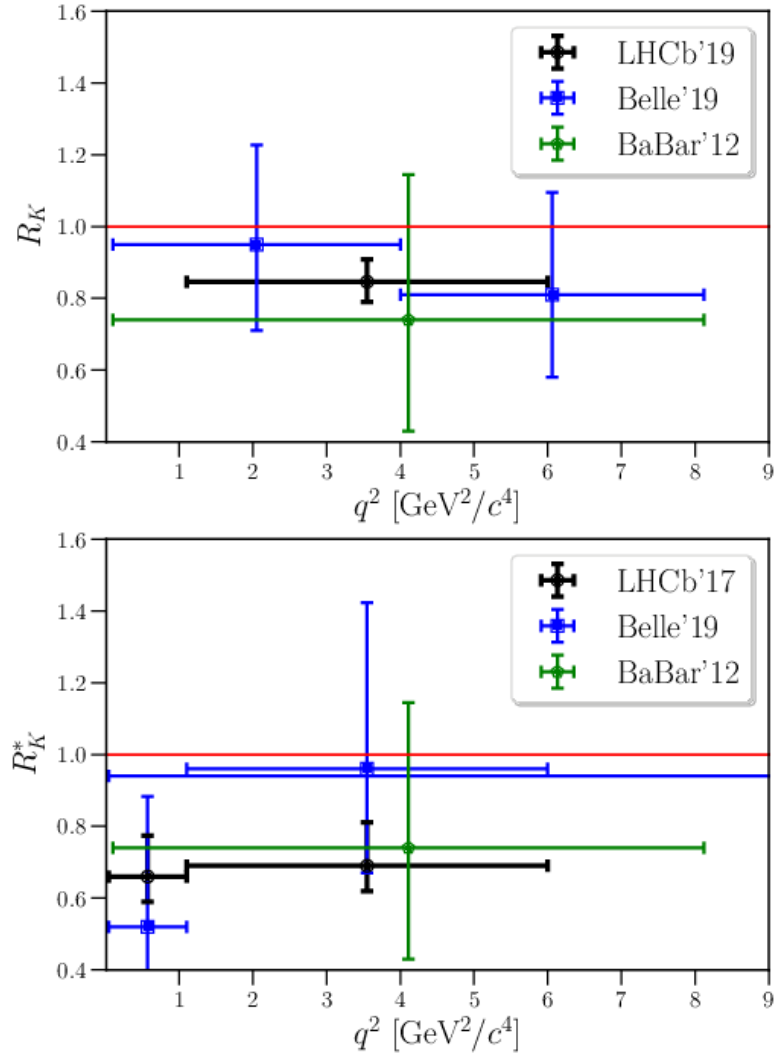


Figure 1.9: (top) The measurements of the LFU R_K by LHCb [8], Belle [9] and BaBar [10]. All measurements are suppressed relative to the SM prediction, shown in red. (bottom) The figure shows the experimental situation for R_{K^*} [10–12]. Like R_K , the measured values are found to be smaller than the SM value, shown in red. Both figures are taken from Ref. [167].

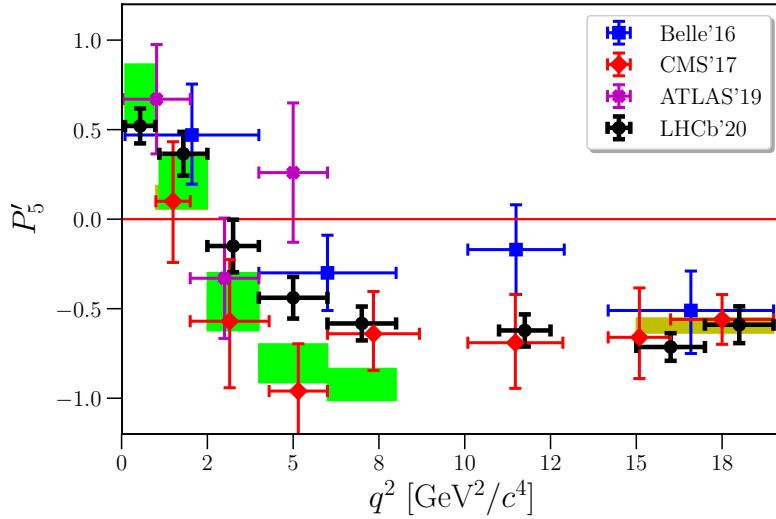


Figure 1.10: The figure shows the measured values of the P'_5 angular observable in the decays $B \rightarrow K^* \mu \mu$ binned by q^2 . With the exception of the CMS measurements, there is an enhancement with respect to the SM prediction (green) around $q^2 \sim 5 \text{ GeV}^2$. The plot is taken from Ref. [167].

The distribution of final-state particles in the semileptonic decays $B \rightarrow K^* \mu \mu$ define a number of angular observables, some of which have also been measured to be in disagreement with SM predictions. The P'_5 asymmetry [168–170] is constructed as a ratio of angular observables to minimise form-factor uncertainties. Measurements show a significant deviation from the SM at around $q^2 \sim 5 \text{ GeV}^2$ [171–174] as shown in Fig. 1.10, although the CMS measurement [175] is consistent with the SM prediction [159, 160, 176, 177] in this region. The hadronic uncertainties are still sizeable in this case.

Fits

The picture of the neutral-current anomalies given above is still only a small cross-section of the several hundred observables that are in tension with the SM predictions. A large number of global-fit analyses have been conducted in which these anomalies are interpreted in terms of deviations in the operators C_9 and C_{10} , introduced above in Eq. (1.76). These analyses are all in mutual agreement, and generally find that a sizeable negative value for C_9 is preferred over the SM value at between 4 and 7σ [13, 178–180]. (This was first pointed out in Ref. [181], which analysed the 2013 data.) This wide range is largely due to differences in dealing with uncertainties in the semileptonic decays. Importantly, no large deviation in the electronic modes is necessary for a good fit. An example of one of the recent global fits [13] to C_9 and C_{10} is shown in Fig. 1.11. The

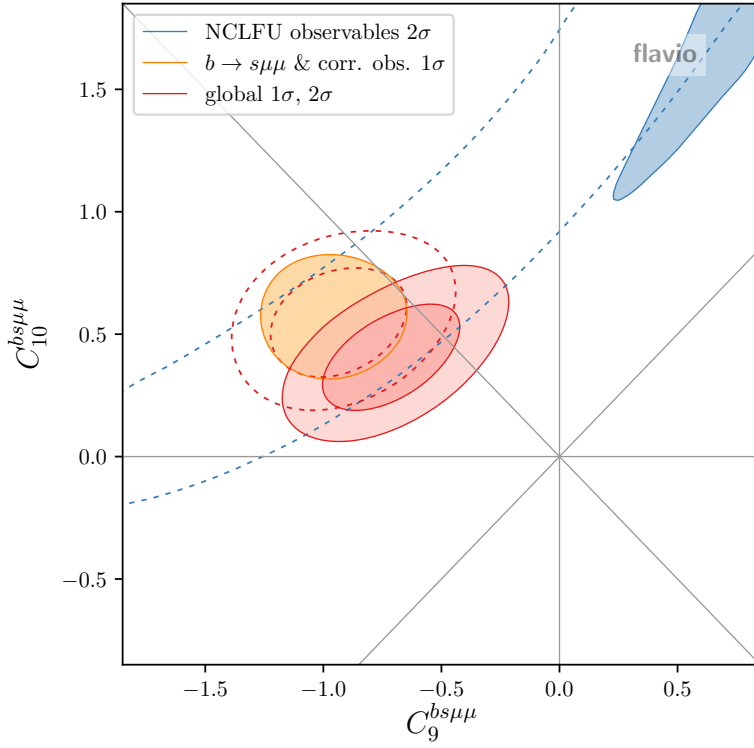


Figure 1.11: The figure shows the results of the global fit conducted in Ref. [13] in the C_9 – C_{10} plane. The fit to just the LFU ratios is shown in blue, while that for the other $b \rightarrow s$ data is shown in yellow, with the combined fit shown in red. The $SU(2)_L$ -invariant direction $C_9 = -C_{10}$ gives a good fit to the data, and any acceptable fit requires a sizeable negative value for C_9 . The plot is taken from Ref. [13].

authors find the single-operator best-fit scenario to be in the $SU(2)_L$ -invariant direction $C_9 = -C_{10}$, with $C_9 = -C_{10} = -0.53$ giving a pull from the SM of 6.6σ . We note that following the updated measurements of R_K [8] and R_{K^*} [11] presented at the 2019 Moriond conference, there is a slight tension between explaining the LFU ratios and the rest of the $b \rightarrow s$ data. We point the reader to Ref. [13] for a more detailed discussion on this point.

That much of the tension is driven by a deviation in C_9 also allows for an explanation of many of the anomalies in a way that does not require the introduction of new physics. The deviation in C_9 necessary to explain much of the anomalous $b \rightarrow s$ data can be mimicked by non-perturbative effects associated with loops of charm quarks, e.g. [158], and the data seem to be currently consistent with both hypotheses [182, 183]. Such effects cannot account for the violation of LFU seen in the ratios $R_{K^{(*)}}$, again highlighting their importance in understanding the potential role of new physics in

explaining the neutral-current anomalies.

1.4.2 Charged-current anomalies

The class of charged-current anomalies in the $b \rightarrow c$ transition consists of a smaller number of measurements and processes. The primary observables of interest are the LFU ratios

$$R_{D^{(*)}} = \frac{\text{Br}[B \rightarrow D^{(*)}\tau\nu]}{\text{Br}[B \rightarrow D^{(*)}\ell\nu]}, \quad (1.83)$$

where ℓ denotes one of the light leptons: $\ell \in \{e, \mu\}$. The ratio has been measured by BaBar [184, 185], Belle [15, 186–188] and LHCb [189–191], with combined values from HFLAV given by [14]

$$R_D = 0.340 \pm 0.027 \pm 0.013 \quad \text{and} \quad R_{D^*} = 0.295 \pm 0.011 \pm 0.008. \quad (1.84)$$

These combinations are in tension with the SM predictions [192–195] as averaged by HFLAV:

$$R_D^{\text{SM}} = 0.299 \pm 0.003 \quad \text{and} \quad R_{D^*}^{\text{SM}} = 0.258 \pm 0.005 \quad (1.85)$$

at approximately 3σ . We note that BaBar and Belle use the average of the electronic and muonic modes in the denominator, while LHCb uses only the muonic mode. The tension was significantly decreased following the most recent Belle measurement presented at the Moriond 2019 conference [15]; this combined measurement is consistent with the SM prediction at 1.2σ . A summary of the measurements of $R_{D^{(*)}}$ is shown in Fig. 1.12. BaBar [185] and Belle [186] have measured the q^2 distributions of the tau-mode decay rate, which has proven to be a powerful model discriminator, e.g. [196].

Although the ratios $R_{D^{(*)}}$ are our primary concern in this work, we also introduce a number of other observables relevant to the charged current process. The first of these is the LFU ratio $R_{J/\psi}$:

$$R_{J/\psi} = \frac{\text{Br}(B_c \rightarrow J/\psi\tau\nu)}{\text{Br}(B_c \rightarrow J/\psi\mu\nu)}, \quad (1.86)$$

which has recently been measured by LHCb to be $R_{J/\psi} = 0.71 \pm 0.17 \pm 0.18$ [197]. Although the ratio is also measured to be enhanced with respect to the SM prediction $R_{J/\psi}^{\text{SM}} \approx 0.25\text{--}0.29$ [198–210], the central value of the measurement shows a very large effect that cannot be well-accommodated with BSM contributions [211], although the error bars are very large. The observable $f_L^{D^*}$, the longitudinal polarisation of the D^* in $B \rightarrow D^*\tau\nu$, also differs from the SM expectation by $\sim 1.6\sigma$:

$$f_L^{D^*} = 0.60 \pm 0.08 \pm 0.04, \quad (1.87)$$

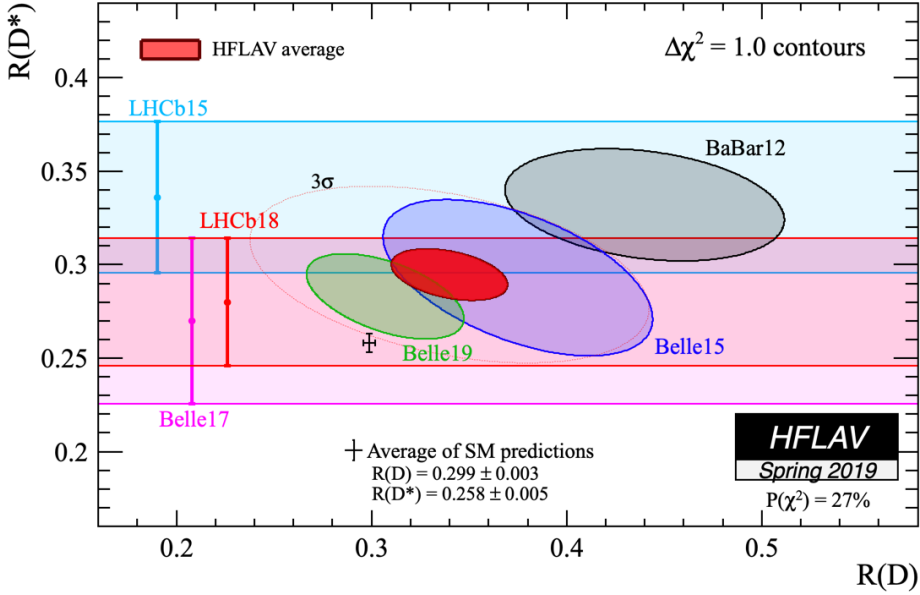


Figure 1.12: The figure shows the combined fit to the available R_D and R_{D^*} data from HFLAV [14]. The combination is shown in red, just over 3σ away from the SM prediction (black data point). Both ratios are measured to be enhanced compared to the SM value.

as measured by the Belle collaboration [212], and has been shown to have good discriminating power for BSM explanations of $R_{D^{(*)}}$. The third class of observables we consider are tau polarisation asymmetries {see Ref. [213] for a detailed discussion in the context of explaining $R_{D^{(*)}}$ }. The polarisation asymmetry in the longitudinal direction of the τ in the D^* mode has also recently been measured by Belle [187]:

$$\mathcal{P}_\tau^* = -0.38 \pm 0.51^{+0.21}_{-0.16}. \quad (1.88)$$

Although the errors are large, the projected Belle II sensitivity at 50 ab^{-1} for the same observable in the D mode is estimated at about 3% [214], and we expect the \mathcal{P}_τ^* to be measured even more precisely at Belle II.

The leptonic decays of the charmed B meson have not been measured yet, although measurements of its lifetime may imply serious constraints on models attempting to explain the discrepancies in R_D and R_{D^*} with new physics. A number of groups have inferred a wide variety of limits

$$\text{Br}(B_c \rightarrow \tau\nu) < [0.1, 0.6] \quad (1.89)$$

using differing theoretical arguments [215–219]. The range of limits is so wide because it is sensitive to the ratio of hadronisation probabilities of the charm and up quarks:

f_c/f_u . The range of values given for the limit in Eq. (1.89) corresponds only to a change in f_c/f_u of a factor of five [219].

Fits

The charged-current $b \rightarrow c$ anomalies can be interpreted in terms of deviations from dimension-six operator coefficients in the WET. The pertinent Hamiltonian for $b \rightarrow c\ell_r v_s$ is

$$H_{\text{eff}}^{b \rightarrow c} = \frac{4G_F}{\sqrt{2}} V_{cb} \sum_{rs} [(S^{rs} + C_{V_L}^{rs}) \mathcal{O}_{V_L}^{rs} + C_{V_R}^{rs} \mathcal{O}_{V_R}^{rs} + C_{S_L}^{rs} \mathcal{O}_{S_L}^{rs} + C_{S_R}^{rs} \mathcal{O}_{S_R}^{rs} + C_T^{rs} \mathcal{O}_T^{rs}] + \text{h.c.} \quad (1.90)$$

where

$$\mathcal{O}_{V_X}^{rs} = (\bar{c}\gamma^\mu P_X b)(\bar{\ell}_r \gamma_\mu P_L v_s), \quad \mathcal{O}_{S_X}^{rs} = (\bar{c}P_X b)(\bar{\ell}_r P_L v_s), \quad \mathcal{O}_T^{rs} = (\bar{c}\sigma^{\mu\nu} P_X b)(\bar{\ell}_r \sigma_{\mu\nu} P_L v_s), \quad (1.91)$$

and $X \in \{L, R\}$. The left-handed vector operator is the same one generated in the SM, while the scalar and tensor operators can provide large enhancements to the decay rate, since they lift the helicity-suppression.

A number of analyses have considered interpreting the measurements of R_D and R_{D^*} in the context of these operators, usually restricting to single-operator fits, *e.g.* [196, 207, 211, 220–223]. In Fig. 1.13 we present a plot taken from Ref. [211] in which the effects of each of the operators on the observables of interest are explored. The plot indicates that a number of single-operator solutions exist that reconcile the predicted and measured values for both R_D and R_{D^*} , although single-operator resolutions of the mild tension in $f_L^{D^*}$ are disfavoured by the limits on the B_c lifetime, discussed above.

1.4.3 Anomalous magnetic moment of the muon

The most precise measurement of the anomalous magnetic moment of the muon

$$a_\mu \equiv \frac{(g-2)_\mu}{2} \quad (1.92)$$

shows a sizeable tension with the SM prediction. The difference between the measured value [147, 224] and the SM prediction [225] is

$$\Delta a_\mu = a_\mu^{\text{exp}} - a_\mu^{\text{SM}} = (286 \pm 63 \pm 43) \cdot 10^{-11}, \quad (1.93)$$

corresponding to a 3.6σ discrepancy. More recently, the measured value a_e , the anomalous magnetic moment of the electron, has also been found to disagree with the SM value at 2.5σ [148].

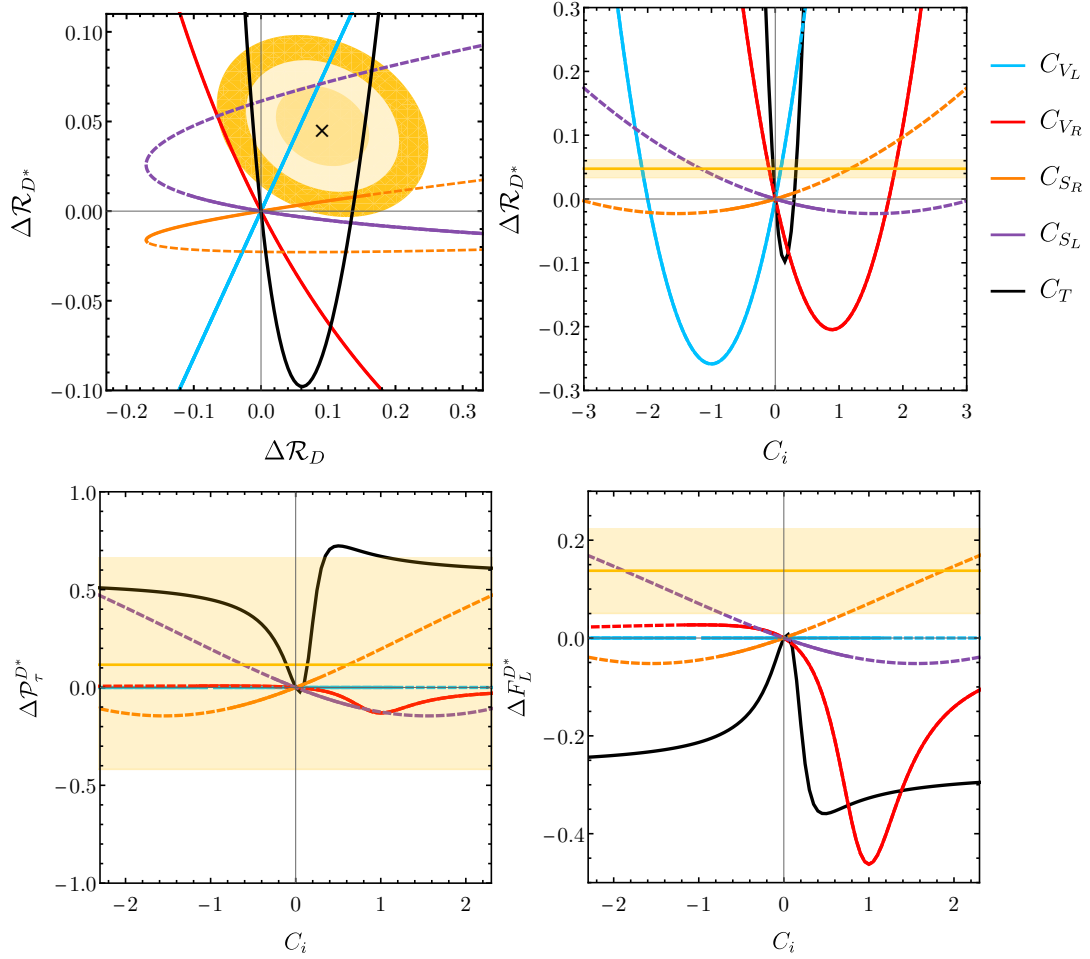


Figure 1.13: The figure shows the contributions of the coefficients of the operators presented in Eq. (1.91) in different observables, where $\Delta X = X - X_{SM}$. (top left) The directions implied by contributions to the operator coefficients in $\Delta R_D - \Delta R_{D^*}$ space. The experimental central value is denoted by a black cross and the 1σ , 2σ and 3σ uncertainties by yellow contours. (top right and bottom) Similar directions for ΔR_{D^*} , $\Delta \mathcal{P}_\tau^{D^*}$ and $\Delta f_L^{D^*}$. The experimental central values are displayed by a solid yellow line and their 1σ uncertainty by a yellow band. Dashed lines indicate regions excluded by the constraint $\text{Br}(B_c \rightarrow \tau\nu) < 0.1$. The figure is taken from Ref. [211].

1.4.4 Our contention: a connection between neutrino physics and the anomalies

The flavour anomalies together present an interesting case for new physics violating lepton flavour universality. This new physics should live at less than 40 TeV, and many of the simplest models in the literature generate the appropriate pattern of dimension-six operators required to explain them through scalar leptoquark fields, *e.g.* [222, 226, 227]. In the remainder of this thesis, we suggest that there may be some connection between the physics underlying mass generation in the neutrino sector and the flavour anomalies, since, as we show in the next chapter, the landscape of minimal Majorana neutrino mass models is dominated by scalar leptoquarks.

2

Neutrino mass *ex machina*

This chapter is based on the publication ‘Exploding operators for Majorana neutrino masses and beyond,’ written in collaboration with Raymond R. Volkas [5]. We describe and implement an algorithm for ‘exploding’ operators: taking an effective operator and deriving from it renormalisable models that generate the operator at the low scale. We systematise this model-building procedure in a way that is easy to automate, and our methods are implemented in our publicly available example code [228]. We use the algorithm to generate computational representations of all of the tree-level completions of the $\Delta L = 2$ operators in the SMEFT up to and including mass-dimension eleven. Almost all of these correspond to models of radiative neutrino mass. Our work includes operators involving derivatives, updated estimates for the bounds on the new-physics scale associated with each operator, an analysis of various features of the models, and a look at some examples. We also make available a searchable database containing all of our results [20].

2.1 Introduction

We saw in Sec. 1.2.3 that the space of neutrino-mass models can be organised in various ways. One way we call the loop-level-matching paradigm, in which graphs of various loop orders are matched onto the Weinberg operator. Thorough analyses have been conducted in this framework, studying the Weinberg operator and its dimension-seven generalisation [95–98] up to three and one loop, respectively. An alternative approach to neutrino-mass model taxonomy is to start with the $\Delta L = 2$ operators in the SMEFT and consider what field content generates these operators at tree-level in the UV [84, 99–101]. As discussed briefly in Sec. 1.2.3, this approach has been applied up to dimension-

seven [101] to systematically write down a large class of simple models of neutrino mass.

Our analysis continues in the tradition of the latter methodology, but where appropriate we make a connection to the results from loop-level matching for completeness. We consider that there is complementary insight to be gained from thorough and complete analyses involving both approaches. Building models from tree-level completions of the $\Delta L = 2$ operators allows for a direct connection to be made between the neutrino-mass mechanism and other lepton-number-violating phenomena. The models derived in this way are also minimal in the sense that they involve the fewest number of exotic fields required to furnish a given loop-level topology, since the neutrino self-energy graphs always involve some SM fields. This has a number of important implications. First, the neutrino masses depend on SM parameters, and their rough scale can therefore be readily estimated from the effective operator alone. Second, neutrino-mass mechanisms containing SM gauge bosons are included automatically, and these constitute a large fraction of the models. Finally, it also means that our approach never produces models that contain loops of only exotic fields, although these can be added easily (see, for example, section IV.C of Ref. [100]). The appeal of these models notwithstanding, a benefit of giving up heavy loops is that the transformation properties of the beyond-the-standard-model particle content of each model are now uniquely determined, and therefore the total number of minimal models is finite. Minimal exotic particle content, in the aforementioned sense, is an attractive feature of this approach. Indeed, there are many examples of operators whose insertion and closure lead to neutrino masses at dimension nine and higher, but for which the number of exotic degrees of freedom introduced are not more than those of a garden-variety model generating the Weinberg operator at the low scale. The consideration of such equally simple models in the loop-level matching paradigm would require a detailed analysis of the dimension-seven and dimension-nine analogues of the Weinberg operator¹ up to a large number of loops.

Here, we sharpen the model building prescription developed in Ref. [100] and extend it to the case of operators involving field-strength tensors and derivatives. This procedure is automated and applied to all $\Delta L = 2$ operators in the SMEFT up to dimension eleven. We classify the neutrino-mass topologies, completions and their exotic fields. We also make available a database containing our main results and example code used to generate the operators along with their completions and Lagrangians [228]. We emphasise that the usefulness of these methods and tools extends beyond the study of neutrino mass and lepton-number-violating phenomena. To illustrate this point we reproduce some recent results of work listing completions of SMEFT operators [22].

The remainder of the paper is structured as follows. Sec. 2.2 sets out some conventions. Sec. 2.3 contains a description of the methods we use to find the tree-level

¹One can always generate the dimension-five Weinberg operator from its analogues at dimensions seven, nine and eleven with additional Higgs loops, but these models usually contain more than three loops.

completions of the operators. Neutrino mass model building is described in Sec. 2.4, while Sec. 2.5 presents a preliminary analysis of the models along with some examples.

2.2 Conventions

In this section we establish the conventions we employ throughout the rest of the paper: our operational semantics and the classification of the lepton-number-violating operators on which our analysis is based. We highlight that this classification differs mildly from that found in earlier work, since our list includes additional structures as well as operators containing derivatives. We find the operators containing field-strength tensors to be uninteresting from the perspective of model building — a point justified in detail in Sec. 2.3.1 — and choose not to include them in our classification in this section. We remind the reader that our mathematical and notational conventions can be found in Appendix A, and these are drawn on heavily in this chapter.

2.2.1 On operators and tree-level completions

Below we discuss our use of the terms operator and completion. We establish naming conventions of types of operators that we use throughout the paper, and illustrate the sense in which we talk about models as completions of operators with the use of a simple example from the dimension-six SMEFT.

The term operator is used in the literature to loosely denote one of three² things:

1. A gauge- and Lorentz-invariant product of fields of specified flavour and their derivatives. Understood in this sense, the Weinberg ‘operator’

$$\mathcal{O}_1^{\{rs\}} = (L_r^i L_s^j) H^k H^l \epsilon_{ik} \epsilon_{jl} \quad (2.1)$$

is really $n_f(n_f + 1)/2$ complex operators for n_f SM-fermion generations.

2. A gauge- and Lorentz-invariant product of fields of unspecified flavour and their derivatives. According to this definition, $\mathcal{O}_1^{\{rs\}}$ is counted as a single operator.
3. A collection of fields and their derivatives whose product contains a Lorentz- and gauge-singlet part. In this sense, the string of fields $LLHH$ could be called an operator. In this category we also include operators of an intermediate type for which some gauge or Lorentz structure is specified but the rest is implied. For example, a term like³ $\mathcal{O}_{3a} = L^i L^j Q^k \bar{d} H^l \epsilon_{ij} \epsilon_{kl}$, for which colour and Lorentz structure are implicit.

²These correspond to *operators*, *terms* and (roughly) *types of operators* in the convention of Ref. [229].

³Although the colour structure is unique here, this is not true of the Lorentz structure.

The catalogues of $\Delta L = 2$ operators are lists of operators of type 3 in the above sense, since they are only distinguished on the basis of field content and $SU(2)_L$ structure. Thus, the operators \mathcal{O}_{3a} and $\mathcal{O}_{3b} = L^i L^j Q^k \bar{d} H^l \epsilon_{ik} \epsilon_{jl}$, for example, are understood to stand in for a large family of operators of types 1 and 2. In this case these differ in Lorentz structure (since the colour contraction is unique), and almost all of them are linearly dependent. They are related to each other by Fierz and $SU(2)$ -Schouten identities, and can in general be related to other dimension-seven operators such as $(\bar{d}L)(LD\bar{u}^\dagger)$ and $(LL)H\Box H$ through field redefinitions involving the EOM of SM-fermion and Higgs fields. The total number of independent operators of type 1 can be found using Hilbert-series techniques [109–113], which give $2n_f^4$ independent operators with field content $L^2 Q \bar{d} H$ with the methods of Ref. [112]. These can be arranged into two terms with the Lorentz structure of the operators chosen such that the flavour indices don't have any permutation symmetries [230]:

$$\mathcal{O}_{3a}^{(LQ)(Ld)}_{rstu} = (L_r^i Q_t^k)(L_s^j \bar{d}_u) H^l \epsilon_{ij} \epsilon_{kl}, \quad (2.2a)$$

$$\mathcal{O}_{3b}^{(LQ)(Ld)}_{rstu} = (L_r^i Q_t^k)(L_s^j \bar{d}_u) H^l \epsilon_{ik} \epsilon_{jl}. \quad (2.2b)$$

From the perspective of $\Delta L = 2$ phenomenology, the $SU(2)_L$ structure of the operators is most important. This can be seen in the following way: given a non-zero value for the coefficient of such an operator, the $SU(2)_L$ structure is sufficient to tell at how many loops the neutrino self-energy or neutrinoless-double-beta-decay diagrams will arise, and what they will look like. Considering the example of operators \mathcal{O}_{3a} and \mathcal{O}_{3b} introduced above, it is clear that no component of \mathcal{O}_{3a} contains two neutrino fields. Therefore, the Weinberg operator will be generated by one-loop graphs involving W bosons, which are additionally suppressed by powers of the weak coupling g . This coupling and loop suppression leads to inferred values of the new-physics scale characterising the operators \mathcal{O}_{3a} and \mathcal{O}_{3b} that differ by three orders of magnitude. On the other hand, predictions for the neutrino-mass scale from operators with different Lorentz structures differ only by $\mathcal{O}(1)$ factors [84].

Thus, our main goal is to find particle content in the UV that generates particular $SU(2)_L$ structures of $\Delta L = 2$ operators at the low scale through tree graphs. In this way, we organise the catalogue of radiative neutrino-mass models by the number of loops in the neutrino self-energy diagram, or equivalently, by the implied scale of the new physics. In this sense, exploding the operator \mathcal{O}_{3a} , for instance, means finding the combinations of heavy field content that generate an operator of type 2 with $SU(2)_L$ structure 3a. This generated operator will not in general be $\mathcal{O}_{3a}^{(LQ)(Ld)}$ of Eq. (2.2), but will be expressible as a linear combination of $\mathcal{O}_{3a}^{(LQ)(Ld)}$ and $\mathcal{O}_{3b}^{(LQ)(Ld)}$, or any other chosen spanning set of operators.

This last point highlights the importance of the operator basis in talking about the

completions of operators. A completion of an operator \mathcal{O} is a model generating a non-zero value for the operator coefficient $C_{\mathcal{O}}$ at the high scale. Even a change of basis that leaves \mathcal{O} unchanged will in general change $C_{\mathcal{O}}$, so one cannot talk about the completions of \mathcal{O} *in vacuo*, apart from the other operators which together constitute the EFT. Restricting to the case of tree-level matching, after eliminating the heavy fields through their EOM, a UV model will generate some structure organically, which we call the *organic* operator, and this must then be matched onto the operator basis to extract coefficients. Our goal here is not to perform this matching onto a complete set of operators. Instead, we work with an implicitly overcomplete set of operators and define a convention that allows us to speak unambiguously about the UV models that might give rise to an operator in the set.

The existing catalogues of $\Delta L = 2$ operators enumerate operators of type 3 with definite $SU(2)_L$ -structure. The different isospin contractions are constructed by contracting indices in all possible ways with the invariant ϵ tensor. Operators with symmetric combinations of indices [which come about from non-trivial exotic irreps of $SU(2)_L$] generate organic operators in general expressible as many linear combinations of different operators in the spanning set. One such combination is sufficient for our purposes, and we choose the one implied by the convention that non-trivial irreps never give rise to fields contracted with an ϵ symbol. We now illustrate this with an example from the dimension-six SMEFT below.

An overcomplete spanning set of two-Higgs–two-derivative operators is

$$\mathcal{O}_{H^2 D^2}^{(1)} = \tilde{H}^i \tilde{H}^j \square H^k H^l \epsilon_{ik} \epsilon_{jl}, \quad (2.3a)$$

$$\mathcal{O}_{H^2 D^2}^{(2)} = \tilde{H}^i H^j \square \tilde{H}^k H^l \epsilon_{ij} \epsilon_{kl}, \quad (2.3b)$$

$$\mathcal{O}_{H^2 D^2}^{(3)} = \tilde{H}^i H^j \square \tilde{H}^k H^l \epsilon_{ik} \epsilon_{jl}, \quad (2.3c)$$

$$\mathcal{O}_{H^2 D^2}^{(4)} = \tilde{H}^i H^j \square \tilde{H}^k H^l \epsilon_{il} \epsilon_{jk}. \quad (2.3d)$$

The renormalisable UV models of interest are a scalar $SU(2)_L$ triplet with unit hypercharge $\Xi_1 \sim (1, 3, 1)_S$, as well as a triplet and a singlet with vanishing hypercharge: $\Xi \sim (1, 3, 0)_S$ and $\mathcal{S} \sim (1, 1, 0)_S$. We envisage integrating these out from an interaction Lagrangian like

$$-\mathcal{L} \supset \tilde{H}^i H^j (x \mathcal{S} \epsilon_{ij} + y \Xi^{\{kl\}} \epsilon_{ik} \epsilon_{jl}) + (z H^i H^j \tilde{\Xi}_1^{\{kl\}} \epsilon_{ik} \epsilon_{jl} + \text{h.c.}), \quad (2.4)$$

with couplings $x, y, z \in \mathbb{C}$. They will generate organic operators that can be written as

linear combinations of the operators listed above

$$\mathcal{S} : \frac{x^2}{M_{\mathcal{S}}^2} \mathcal{O}_{H^2 D^2}^{(2)}, \quad (2.5a)$$

$$\Xi : \frac{y^2}{M_{\Xi}^2} \left[\mathcal{O}_{H^2 D^2}^{(3)} + \mathcal{O}_{H^2 D^2}^{(4)} \right], \quad (2.5b)$$

$$\Xi_1 : \frac{|z|^2}{M_{\Xi_1}^2} \mathcal{O}_{H^2 D^2}^{(1)}, \quad (2.5c)$$

up to $\mathcal{O}(1)$ factors. Of course, these can then be matched onto a genuine basis of operators like

$$\mathcal{O}_{\phi \square} = \mathcal{O}_{H^2 D^2}^{(2)} = \tilde{H}^i H^j \square \tilde{H}^k H^l \epsilon_{ij} \epsilon_{kl}, \quad (2.6a)$$

$$\mathcal{O}_{\phi D} \stackrel{\text{IBP}}{\sim} \mathcal{O}_{H^2 D^2}^{(3)} = \tilde{H}^i H^j \square \tilde{H}^k H^l \epsilon_{ik} \epsilon_{jl}, \quad (2.6b)$$

but this is unnecessary for our purposes. (Note here that IBP stands for integration by parts.) The construction of the organic operator is in general not unique, since we work with an overcomplete set of operators. Here, for example, $\mathcal{O}_{H^2 D^2}^{(3)} + \mathcal{O}_{H^2 D^2}^{(4)} = 2\mathcal{O}_{H^2 D^2}^{(3)} - \mathcal{O}_{H^2 D^2}^{(2)}$, indicating clearly the redundancy of one of the operators. The convention that non-trivial representations never give rise to fields contracted with an ϵ symbol implies $\mathcal{O}_{H^2 D^2}^{(2)}$ should not be chosen to feature in Eq. (2.5b). Thus, we call Ξ a completion of operators $\mathcal{O}_{H^2 D^2}^{(3)}$ and $\mathcal{O}_{H^2 D^2}^{(4)}$, even though the operator it generates can also be expressed as a linear combination of $\mathcal{O}_{H^2 D^2}^{(2)}$ and $\mathcal{O}_{H^2 D^2}^{(3)}$. This convention allows us to talk unambiguously about completions of the $\Delta L = 2$ operators in a way that makes their implications for neutrino mass most clear, while avoiding constructing a complete basis all the way up to dimension eleven.

We remark that this discussion can be extended to operators of type 3 with explicit $SU(3)_c$ -structure with minor modifications. Here, irreducible representations are furnished by traceless tensors with raised and lowered symmetrised indices, which can be written as sums of operators in which contractions between raised and lowered indices are written with the δ symbol. The tracelessness condition can be enforced by additionally allowing contractions with the three-index ϵ symbol, and choosing that non-trivial representations never give rise to fields contracted with a δ , *i.e.* always choosing $[\lambda^A]_c^a [\lambda^A]_d^b = \frac{4}{3} \delta_d^a \delta_c^b - \frac{2}{3} \epsilon_{cde} \epsilon^{abe}$ over $[\lambda^A]_c^a [\lambda^A]_d^b = 2\delta_d^a \delta_c^b - \frac{2}{3} \delta_c^a \delta_d^b$. Explicit examples involving non-trivial colour contractions are presented in Sec. 2.3 and in the publicly available notebook we introduce in Sec. 2.3.2, which contains complete matching calculations for some of the dimension-six operators in the SMEFT.

2.2.2 Operator taxonomy

The list of gauge-invariant, $\Delta L = 2$ operators first provided by BL runs from \mathcal{O}_1 to \mathcal{O}_{60} [99]. Each numbered operator is distinguished on the basis of field content, although each in general corresponds to a family of operators differing in $SU(2)_L$ -, Lorentz-, and flavour-structure. The operators are constructed from SM fermion fields and Higgs fields only and no internal global symmetries are imposed on the operators aside from baryon number. To violate lepton number by two units, each operator must contain at least one $\Delta L = 2$ fermion bilinear: one of $\{LL, L\bar{e}^\dagger, \bar{e}^\dagger\bar{e}^\dagger\}$. The operators enter the list at odd mass dimension [114] and only up to dimension eleven, since it was thought that higher dimensional operators generally imply neutrinos insufficiently heavy to meet the atmospheric lower bound. (It seems that a truly exhaustive treatment requires operators of higher mass-dimension [4], and this is discussed in detail in Sec. 2.4.1.) An additional 15 operators (acknowledged by BL, but left implicit) of mass dimension nine and eleven were added to the list by dGJ, increasing the total number to 75. These are constructed as products of lower-dimensional operators with the dimension-four Yukawa operators of the SM. Thus, they have the same field content as other operators in the list but carry different numerical labels. Latin subscripts were introduced by the same authors to distinguish different $SU(2)_L$ contractions. The number of type-3 operators counted in this way is 129. Inclusion of the *all-singlets* operator $\bar{e}^\dagger\bar{e}^\dagger\bar{u}^\dagger\bar{u}^\dagger\bar{d}\bar{d}$, whose tree-level completions were recently written down [231], brings the tally to 130. Even in the extended dGJ scheme, product operators of the form $\mathcal{O} \cdot H_i^\dagger H^i$ are left implicit.

Here we work with a modified classification scheme which differs mildly from those used in the previous analyses. We list all operators explicitly, including product operators built from lower-dimensional ones and SM Yukawas or $H^\dagger H$, and enforce that operators with the same field content carry the same numerical labels. We adopt the convention of labelling $SU(2)_L$ -structures with an additional Latin subscript⁴. We have a greater number of such structures for each numbered operator than the other catalogues because we include product-type operators and new structures which may have been missed previously. We attempt to ensure that these new operators have labels that do not break compatibility with these and other previous works using lepton-number violating operators. A small exception is the case where only one structure is listed by BL and dGJ. In such situations this corresponds to operator a in our classification.

We find some new non-product operators not appearing in previous classifications even implicitly. These include new $SU(2)_L$ -structures but also new numbered operators. Dimension-eleven product-type operators built from a lower-dimensional operator and factors of $H^\dagger H$ that are not given numerical labels in the previous catalogues are given primed labels here, a common convention in the literature. In cases where a number of such operators carry the same field content, we prefer to use a new numerical label.

⁴We note that this introduces a notational ambiguity with colour indices, the resolution of which must be based on context.

For example, operators $\mathcal{O}'_{5a} = \mathcal{O}_{5a}(H^\dagger H)$ and $\mathcal{O}''_{3a} = \mathcal{O}_{3a}(H^\dagger H)^2$ have the same field content. They appear in our list as different $SU(2)_L$ -structures of the new numbered operator \mathcal{O}_{80} .

This means that the 75 numbered type-3 operator classes presented by dGJ now correspond to 82 classes and additional $SU(2)_L$ -structures $\{a, b, c, \dots\}$. We present our list of $\Delta L = 2$ operators containing SM fermion and Higgs fields in Table B.1, located in Appendix B. Product operators as presented in our tables must be read with care. This is just a convenient shorthand to represent the field-content of an operator and illustrate that isospin indices are internally contracted. For example, by writing $\mathcal{O}_{5b} = \mathcal{O}_1 Q^i \bar{d} \tilde{H}^j \epsilon_{ij}$, we do not mean to suggest that Lorentz indices must be contracted internally to \mathcal{O}_1 and the down-type Yukawa. We discuss the additional information presented in Table B.1 as it is introduced throughout the paper.

The table also includes a list of $\Delta L = 2$ operators involving derivatives up to dimension nine. The pertinent operators at dimension seven were mentioned in Ref. [99] and listed in the context of a complete basis of operators for the dimension-seven SMEFT in Ref. [230]. The operators of higher dimension were excluded from the earlier catalogues of $\Delta L = 2$ operators on the basis that they may be less important for neutrino-mass model building, although they have appeared recently [145]. We find that opening up these operators does yield novel neutrino-mass models, although this is not clear at dimension seven. The derivative operators are also interesting from a broader phenomenological perspective, for example in the study of lepton-number-violating hadron decays, see *e.g.* Ref. [232]. The procedure we use for identifying these operators draws from the earlier $\Delta L = 2$ catalogues, Hilbert series techniques [109–113] as well as more recent automated approaches [229, 233–237].

Although operators related by field redefinitions through the classical EOM lead to identical S -matrix elements, we do not account for these redundancies in our catalogue of operators containing derivatives. This is done for two reasons: (1) we are ultimately interested in comparing Green’s functions in the effective theory to those in various compatible UV theories; and (2) we are only interested in tree-level completions of effective operators, and EOM redundancies may relate operators generated from tree graphs to those generated by loops [238, 239]. Redundancies arising from integration by parts are also not accounted for, and it should be understood that derivatives act on the operators listed in Table B.1 in all possible ways. In our listing, we prefer to act them in whichever way maximises the number of non-vanishing $SU(2)_L$ structures, so that they can all be labelled. Often this means that derivatives will be carried by Higgs fields.

2.3 Tree-level matching in reverse

In this section we outline the procedure we use for opening up operators of the sort introduced in Sec. 2.2.1 and Sec. 2.2.2 for the purpose of exploratory model building. We refer back to the prefatory comments made in Sec. 1.3.1 on tree-level matching for scalars and fermions, and include a discussion of the tree-level completions of operators containing derivatives and field-strength tensors. We highlight that the results of this section are not specific to $\Delta L = 2$ physics, and the model-building prescription can be applied (high-dimensional) operators in other EFTs. To illustrate the point, we apply the methods to an EFT unrelated to neutrino masses: the SMEFT at dimension-six.

The model-building framework introduced and used in Ref. [240] assumes that the new heavy fields introduced in the UV completions are only scalars, vector-like Dirac fermions or Majorana fermions. This particle content ensures the models are genuinely UV complete in the sense that their predictions can be extrapolated to arbitrarily high energies. Chiral fermions will in general introduce gauge anomalies, and the generation of their masses may introduce unnecessary complications. This treatment of exotic fermion fields is also used in Ref. [22], where a tree-level dictionary of the dimension-six SMEFT is written down. Exotic Proca fields will still need to be interpreted in the context of some larger UV framework (e.g. an extended gauge group), and so these are not introduced in our approach. Thus for the remainder of the paper we limit the discussion of building UV-complete models to those containing only scalars and non-chiral fermions.

In Sec. 1.3.1 we introduced the process of matching a UV Lagrangian onto an effective theory. In this case, we are interested in the case where the UV theory is unknown. Here, the EFT is a useful way to encapsulate the effects of the entire class of possible UV theories in a model-agnostic way. We advocate that it is also a practical model-building tool, since the operators provide information about the types of UV models from which the EFT may arise. Subject to a number of assumptions, the possible UV models implied by an effective operator can be enumerated by building all possible tree graphs with an external-leg structure reflecting that of the operator. The quantum numbers of the heavy propagators can then be read off by imposing Lorentz- and gauge-invariance at every vertex, starting with vertices with two or three (for scalars) external edges. This is equivalent to exploring all of the possible ways the light fields may have been grouped into terms in $\mathcal{L}[\pi, \Pi]$ and distributed in the products of Eqs. (1.32) and (1.39). In the following we develop this picture into a precise algorithm.

Exploding operators

As an introductory example we use the Weinberg operator $\mathcal{O}_1 = (L^i L^j) H^k H^l \epsilon_{ik} \epsilon_{jl}$, whose minimal tree-level completions are the canonical seesaw models: $N \sim (\mathbf{1}, \mathbf{1}, 0)_{(2,1)}$, $\Xi_1 \sim$

$(1, 3, 1)_S$ and $\Sigma \sim (1, 3, 0)_{(2,1)}$. These can be derived by considering the allowed ways of decorating the two tree-level two-scalar–two-fermion topologies with the field content of the operator. These topologies are shown in Fig. 2.1 along with the possible ways of furnishing the topologies into Feynman diagrams, each corresponding to a seesaw model. As discussed above, this is equivalent to grouping fields together as they may have arisen in the partial derivatives of Eqs. (1.32) and (1.39). For the Weinberg operator, these groupings are:

$$\boxed{L^i L^j H^k H^l} \epsilon_{ik} \epsilon_{jl} \Rightarrow \frac{\partial \mathcal{L}^{lh}}{\partial N_\alpha} \supseteq x_r L_r^{\alpha i} H^k \epsilon_{ik} \sim N, \quad (2.7a)$$

$$\boxed{L^i L^j H^k H^l} \epsilon_{ik} \epsilon_{jl} \Rightarrow \frac{\partial \mathcal{L}^{lh}}{\partial \Xi_{1\alpha}^{kl}} \supseteq [y_{rs}(L_r^i L_s^j) + \kappa \tilde{H}^i \tilde{H}^j] \epsilon_{ik} \epsilon_{jl} \sim \Xi_1^\dagger, \quad (2.7b)$$

$$\boxed{L^i L^j H^k H^l} \epsilon_{ik} \epsilon_{jl} \Rightarrow \frac{\partial \mathcal{L}^{lh}}{\partial \Sigma_\alpha^{kj}} \supseteq z_r L_r^{\alpha i} H^l \epsilon_{ik} \epsilon_{jl} \sim \Sigma, \quad (2.7c)$$

where we use \sim to mean ‘transforms as’ under $SU(2)_+ \otimes SU(2)_- \otimes G_{SM}$. Each pattern of contractions corresponds to a topology, with each individual grouping of the fields corresponding to a vertex, or equivalently, a term in the $\Delta L = 2$ UV Lagrangian. The explicit form of these terms can be written down by keeping track of the isospin indices as in Eq. (2.7), and expanding implicit index structures in all possible ways (*i.e.* decomposing products of fields into irreducible representations), consistent with our model building assumptions. (In our case this means keeping only scalar and fermion Lorentz irreps.) In Eq. (2.7c), the indices i, l are symmetrised since this is the only way the component $L^i H^l$ (with i, l not antisymmetric under exchange) can appear in the Yukawa interaction $L\Sigma H$. Note that we adopt the convention that the conjugate exotic field couples to the contracted fields in the operator. This means that Ξ_1^\dagger transforms like $L^i L^j$, as implied in Eq. (2.7b), but the renormalisable term in the UV theory which corresponds to the vertex is $L\Xi_1 L$. For Majorana fermions there is only one state which can couple in both cases, while for a Dirac fermion $\psi + \bar{\psi}^\dagger$ we arbitrarily choose $\bar{\psi}$ to couple to the contracted fields.

This process of grouping fields into renormalisable interaction terms can be conveniently expressed with the following replacement rules:

$$\boxed{\psi_1^\alpha \psi_{2\alpha}} \rightarrow \Phi^\dagger, \quad \boxed{\phi_1 \phi_2} \rightarrow \Phi^\dagger, \quad \boxed{\phi_1 \phi_2 \phi_3} \rightarrow \Phi^\dagger, \quad \boxed{\phi \psi^\alpha} \rightarrow \bar{\Psi}^\alpha, \quad \boxed{\psi_1^\alpha \psi_2^\dagger} \rightarrow \mathbf{X}, \quad (2.8)$$

with free raised or lowered gauge-indices (suppressed above) of the same type always symmetrised on the right-hand side. We are using Φ and $\bar{\Psi}$ to represent a heavy scalar and fermion; while the lowercase ϕ_i and ψ_i represent scalar and fermion fields that may be light or heavy. Note that $\bar{\Psi} = \Psi$ for a Majorana fermion. The mark \mathbf{X} signals that the completion should be discarded, in this case because it represents a model involving a

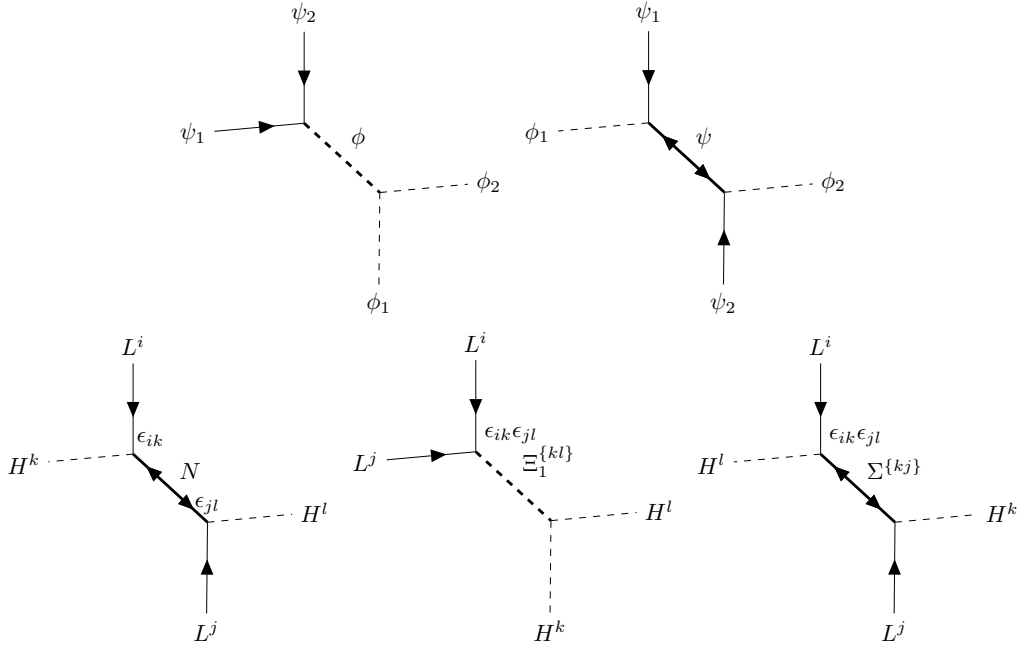


Figure 2.1: (top) Scalar-only and fermion-only topologies which complete dimension-five two-scalar–two-fermion operators, like the Weinberg operator \mathcal{O}_1 . (bottom) The three minimal tree-level completions of \mathcal{O}_1 , each corresponding to a different permutation of the fields on the external lines of the topologies. These are traditionally called (read from left to right) the type-I, type-II and type-III seesaw models. The $SU(2)_L$ indices are included explicitly to distinguish type-I and type-III, while making a more clear connection to Eq. (2.7). The exotic propagators are shown in bold.

heavy vector field. The repeated application of these rules allows us to build explicit computational representations of the $\Delta L = 2$ Lagrangian and diagram topology for a completion.

We move on with a more involved example that also involves colour structure: a completion of $\mathcal{O}_{12} = LLQ^\dagger Q^\dagger \bar{u}^\dagger \bar{u}^\dagger$. According to Table B.1 there are two $SU(2)$ structures. Both of these structures need to be opened up to enumerate all of the completions, and models will in general generate sums of these with a specific Lorentz structure, as per the discussion in Sec. 2.2.1. We choose to look at

$$\mathcal{O}_{12a} = \sum_{rstuvw} L^i L^j \tilde{Q}^k \tilde{Q}^l \bar{u}^\dagger \bar{u}^\dagger \epsilon_{ik} \epsilon_{jl} \quad (2.9)$$

and begin with some preliminary comments. There are only two topologies that accommodate tree-level completions for six-fermion operators. A scalar-only topology (shown in Fig. 2.2a), where pairs of fermions are contracted into scalars which meet at

a trilinear vertex, and a scalar-plus-fermion topology (shown in Fig. 2.2b) in which two exotic scalars come about by fermion contractions and each meets another SM fermion. Since we are not interested in introducing exotic vector fields, contractions between fermions must come about by grouping only fields with dotted or undotted indices, *i.e.* from $(2, 1) \otimes (2, 1)$ or $(1, 2) \otimes (1, 2)$ contracted into a $SU(2)_\pm$ -scalar representation with an epsilon tensor. These contractions fix the Lorentz-structure of the generated type-2 operator. For \mathcal{O}_{12a} it is clear that all scalar-only completions will contain the triplet scalar Ξ_1 , since the two L fields in the operator are the only fermions carrying undotted indices, making the contraction

$$\Xi_1^\dagger \sim (1, 3, -1) \\ L^i L^j \tilde{Q}^k \tilde{Q}^l \bar{u}^\dagger \bar{u}^\dagger \epsilon_{ik} \epsilon_{jl} \quad (2.10)$$

unique. For the quark fields there are a number of choices to be made. First, the choice of grouping. There are only two choices for how to group the quark fields: as $(\tilde{Q}\tilde{Q})(\bar{u}^\dagger \bar{u}^\dagger)$ or $(\tilde{Q}\bar{u}^\dagger)^2$. The second choice is of the colour representations. These can be explored recursively, or all invariants can be constructed and each opened up separately, following the conventions of Sec. 2.2.1. We opt for the latter case, and enumerate the colour contractions

$$\mathcal{O}_{12ae} = L^i L^j \tilde{Q}_a^k \tilde{Q}_b^l \bar{u}^\dagger \bar{u}^\dagger \epsilon_{ik} \epsilon_{jl} \epsilon^{abe} \epsilon_{cde}, \quad (2.11a)$$

$$\mathcal{O}_{12a\delta} = L^i L^j \tilde{Q}_a^k \tilde{Q}_b^l \bar{u}^\dagger \bar{u}^\dagger \epsilon_{ik} \epsilon_{jl} \delta_c^a \delta_d^b. \quad (2.11b)$$

The colour sextet combinations $Q_{\{a}^\dagger Q_{b\}}^\dagger \bar{u}^\dagger {}^a \bar{u}^\dagger {}^b$ come about as a sum of flavour permutations of the left-handed quark doublets in $\mathcal{O}_{12a\delta}$, and the octet combinations $(Q^\dagger \lambda^A \bar{u}^\dagger)^2$ as a linear combination of $\mathcal{O}_{12a\delta}$ and \mathcal{O}_{12ae} . Thus, we understand contractions like $Q_a^\dagger Q_b^\dagger \delta_c^a \delta_d^b$ as coming about from colour-sextet scalars, and $Q_a^\dagger \bar{u}^\dagger {}^b \delta_c^a \delta_d^b$ or $Q_a^\dagger \bar{u}^\dagger {}^b \epsilon_{bce} \epsilon^{ade}$ as coming about from octets.

Finding all of the completions of \mathcal{O}_{12a} involves contracting all fields in all possible ways for each colour contraction. We work through the example of a particular scalar-only completion of $\mathcal{O}_{12a\delta}$ in Fig. 2.3. Each step follows the grouping of fields into a vertex, the Lagrangian term this grouping corresponds to, and the evolving topology of the completion under the replacement rules of Eq. (2.8). At intermediate stages in the explosion of the operator, the theory described is still effective because some vertices still correspond to irrelevant operators⁵. The procedure stops once all vertices have mass-dimension $d \leq 4$. We replace the contracted fields in the operator with the irreducible representation that, following the restrictions described in Sec. 2.2.1, could give

⁵We note that one can make a connection here to the framework of Ref. [241], where neutrino-mass models are classified and studied in the context of single-field extensions of the SM, corresponding to the first intermediate step in our completions procedure. Similar approaches to SMEFT extensions have also been considered elsewhere in the literature, *e.g.* [242].

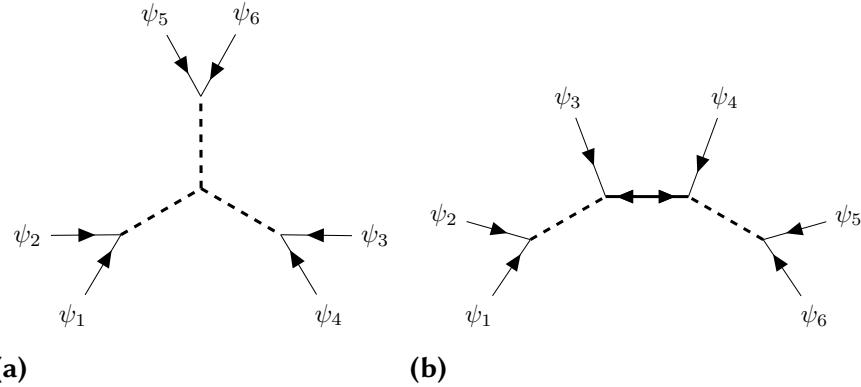


Figure 2.2: The two tree-level topologies relevant to six-fermion operators. For some operators, some fermion arrows may be reversed. The exotic propagators are shown in bold. (a) The scalar-only topology. (b) The scalar-plus-fermion or central-fermion topology.

rise to the contraction. This will in general require the addition of other structures⁶, although this is not the case here. The operator generated by the model highlighted in Fig. 2.3 is

$$(L_r^{\{i} L_s^{j\}})(Q_{t a}^\dagger Q_{u b}^\dagger)(\bar{u}_v^{\dagger\{a} \bar{u}_w^{\dagger b\}}) = \mathcal{O}_{rstuvw} + \mathcal{O}_{stuvwxyz} + \mathcal{O}_{rsuvwxyz} + \mathcal{O}_{sruvwxyz}, \quad (2.12)$$

with the same Lorentz structure carried through $\mathcal{O}_{12a\delta}$. The relevant part of the $\Delta L = 2$ Lagrangian of the model can be read directly off each contraction

$$\begin{aligned} -\mathcal{L}_{\Delta L=2} \supseteq & x_{\{rs\}}(L_r^i L_s^j)\Xi_{1\{ij\}} + y_{\{tu\}}(\tilde{Q}_t^k \tilde{Q}_u^l)Y_{\{kl\}}^{\{ab\}} + z_{[vw]}(\bar{u}_v^{\dagger a} \bar{u}_w^{\dagger b})\Omega_{4\{ab\}} \\ & + \kappa\Xi_{1\{ij\}}Y_{\{kl\}}^{\{ab\}}\Omega_{4\{ab\}}\epsilon_{ik}\epsilon_{jl} + \text{h.c.}, \end{aligned} \quad (2.13)$$

although the generation of the entire Lagrangian implied by the field content requires a program implementing group-theory methods, spin-statistics and tensor algebra (see Sec. 2.3.2). This particular model inherits the high level of symmetry in the effective operator. This introduces symmetries in the Yukawa couplings of the model, reducing the total number of free parameters.

Given an effective operator, we have established a simple rule for reducing it to a renormalisable interaction through a processes of contracting fields into each other, corresponding diagrammatically to pairing the fields off into Yukawa or scalar interaction vertices according to a system of rewrite rules. Applying these groupings in all

⁶The organic operator of the model can be written as a linear combination of these other operators and the operator being opened up, and all of these share the model as a completion in our sense.

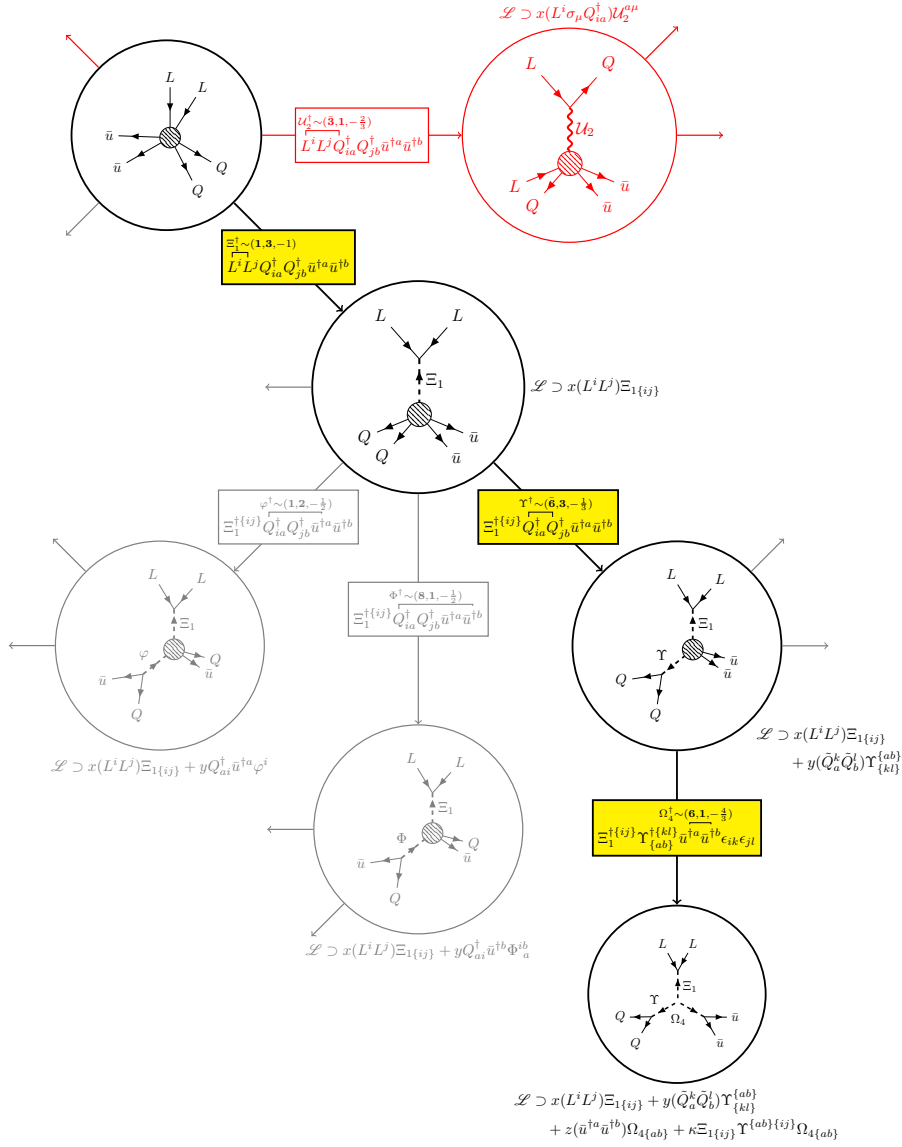


Figure 2.3: The graph visualises our completion procedure by showing some of the possible ways to explode the operator $\mathcal{O}_{12a\delta} = L^i L^j Q_{ia}^\dagger Q_{jb}^\dagger \bar{u}^{ta} \bar{u}^{tb}$. The options are only followed to a fully UV-complete model on one branch, shown in bold with yellow edge labels. In each step groups of fields are contracted at a vertex, fixing the properties of the exotic field as well as the structure of the term describing the interaction, shown alongside each diagram. The effective operator is gradually opened up until each vertex in the diagram corresponds to a term with mass-dimension $d \leq 4$. Opening up the operator fully requires repeating this procedure for all possible contractions. In this case this includes other scalar-only completions and scalar-plus-fermion models. We also show steps that we choose to forbid in our approach in red, like the vector contraction giving rise to the vector leptoquark \mathcal{U}_2 in the figure. Flavour indices have been suppressed.

possible ways and following quantum numbers through index structure allows one to efficiently write down not only the particle content generating the operator at tree-level, but also the pertinent interaction terms in the Lagrangian. In the next section, we discuss how to expand this rule to reducing operators containing derivatives.

2.3.1 Tree-level completions of derivative operators

In the following we broaden the discussion to exploratory model building through effective operators containing (covariant) derivatives and field-strength tensors. We begin by summarising the main results of this section. We argue that (if only scalars and fermions are introduced) a large class of such operators do not contribute new completions to the pool of models. That is, models derived from these operators could be found by opening up operators without derivatives and field strengths. With notable exceptions, it is usually sufficient to study only single-derivative operators. Some of the derivative operators also admit fermion-only completions, which are otherwise only found for the Weinberg-like operators [103]. The completion of operators containing derivatives has been studied before in the context of $\Delta L = 2$ physics [243–245], and our work expands on this.

Exploding derivative operators

In our setup, derivatives in effective operators arise at tree-level by the expansions given in Eqs. (1.39) and (1.32). It is clear that derivatives occur in one of two ways: (1) in pairs as D^2 or X from next-to-leading order terms in the EFT expansion, or (2) as single derivatives contracted with fermions (\not{D} in traditional notation) coming about from arrow-preserving fermion propagators. The job of finding the completions of operators containing derivatives is therefore equivalent to enumerating all possible tree graphs with the appropriate external-leg structure including arrow-preserving propagators proportional to momentum for heavy fermion fields and taking powers of momentum from past the leading order in the expansion of all propagators. As in the non-derivative case, the quantum numbers of the heavy fields can then be deduced by imposing Lorentz and gauge invariance at each vertex.

It is not always guaranteed that a tree-level topology with internal fermion and scalar lines exists for an effective operator containing derivatives. This is in contrast to the non-derivative case, where this is guaranteed for all operators of mass dimension larger than four. For example, at dimension seven there are $\Delta L = 2$ effective operators like $\bar{d}_\alpha \bar{u}_{\dot{\alpha}}^\dagger L^{i\beta} D^{\alpha\dot{\alpha}} L_\beta^i \epsilon_{ij}$ containing four fermions: three with undotted indices and one with a dotted index. In this case there is no tree-level topology that allows a arrow-preserving fermion propagator to give rise to the derivative, and so the operator can

only be generated with loops. We call such operators *non-explosive*. This distinction between tree and loop operators has been discussed in the literature in the context of the dimension-six operators of the SMEFT, see *e.g.* [22, 238, 239], and more recently for the dimension-eight operators [246].

The derivatives originating from arrow-preserving fermion propagators in the UV theory enter the effective Lagrangian through the first term in Eq. (1.39). Here, the derivative acts on an object with which it shares a contracted index, *i.e.* it is contracted as $(2, 2) \otimes (1, 2) = (2, 1)$ with the object carrying the index $\dot{\beta}$. This object must be a $(1, 2)$ -fermion if it comes from a renormalisable interaction, which in our case is uniquely a Yukawa interaction. Thus,

$$\frac{\partial \mathcal{L}^{lh}}{\partial \Pi_{\dot{\beta}}^{\dagger}} = \sum_i \psi_i^{\dagger \dot{\beta}} \phi_i, \quad (2.14)$$

with ψ_i and ϕ_i defined as in Eq. (2.8). For example, a structure like $D^{\alpha\dot{\alpha}} \psi_1^{\dagger \dot{\beta}} \phi_1 \epsilon_{\dot{\alpha}\dot{\beta}}$ could enter an effective operator by integrating out a heavy fermion Π that couples through $\mathcal{L} \supset \Pi^{\dagger} \psi_1^{\dagger} \phi_1$. For clarity, the effective Lagrangian looks like

$$\mathcal{L}_{\text{eff}}[\pi] \supset \frac{\partial \mathcal{L}^{lh}}{\partial \Pi_{\beta}} \frac{1}{m_{\Pi}^2} D^{\alpha\dot{\alpha}} \frac{\partial \mathcal{L}^{lh}}{\partial \Pi_{\dot{\beta}}^{\dagger}} \epsilon_{\alpha\beta} \epsilon_{\dot{\alpha}\dot{\beta}} + \dots \quad (2.15)$$

$$= \frac{\partial \mathcal{L}^{lh}}{\partial \Pi_{\beta}} \frac{1}{m_{\Pi}^2} D^{\alpha\dot{\alpha}} \left(\psi_1^{\dagger \dot{\beta}} \phi_1 + \dots \right) \epsilon_{\alpha\beta} \epsilon_{\dot{\alpha}\dot{\beta}} \quad (2.16)$$

in this case. The fields ϕ_i and ψ_i need not be light, and could have arisen from the contraction of fields in a complicated way. For example, ϕ_1 may have come from the contraction of two light fermions $\phi_1 \sim \xi_1 \xi_2$. This situation is visualised diagrammatically in Fig. 2.4a. The figure shows the ξ_i fermions coupling to the heavy ϕ propagator, which in turn couples to ψ_1^{\dagger} leading to the arrow-preserving fermion propagator for the heavy Π carrying momentum $k^{\alpha\dot{\alpha}}$. It is clear from Eq. (2.16) that the derivative acts on both the fermion and the scalar, reflecting the fact that in the diagram k is the sum of the ψ and ϕ momenta. So, derivatives acting on fermions or scalars can be grouped off into a Yukawa interaction in this way, leaving a arrow-preserving fermion propagator in their wake. This corresponds to the replacement rules

$$D^{\alpha\dot{\alpha}} (\psi_{\dot{\alpha}}^{\dagger}) \phi \rightarrow \Pi^{\alpha}, \quad D^{\alpha\dot{\alpha}} (\psi_{\dot{\alpha}}^{\dagger} \phi) \rightarrow \Pi^{\alpha}, \quad D^{\alpha\dot{\alpha}} (\phi) \psi_{\dot{\alpha}}^{\dagger} \rightarrow \Pi^{\alpha}. \quad (2.17)$$

We highlight that the arrow-preserving propagator implies that only one chirality of the Dirac fermion Π is necessary for LNV in these models. However, we still only work with vector-like fermions in our completions to guarantee anomaly cancellation and straightforwardly give them large masses.

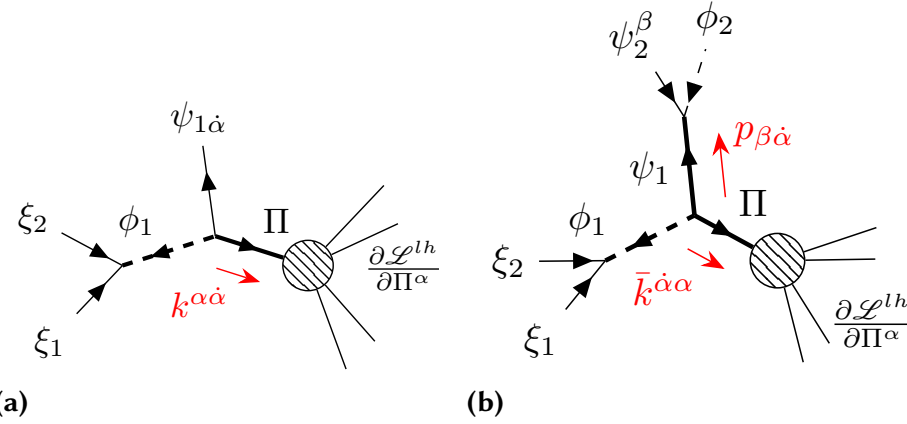


Figure 2.4: (a) The diagram shows an example opening of an operator containing at least one derivative. The derivative can be understood as arising from the leading-order term in the expansion of the arrow-preserving fermion propagator, emphasised in the diagram. As shown, the fields ξ_i and ψ_1 are external and therefore light, but in general they could themselves be heavy propagators. (b) The case where the fermion ψ_1 is heavy, coupling to the light fields ψ_2 and ϕ_2 . The σ -matrix structure of the propagators is in accordance with the conventions of Ref. [106]. Here, the Lorentz structure is such that the momenta are contracted, which arises from contractions of derivatives which share one contracted index.

In an effective operator the derivative may act on a fermion with which it does not share a contracted index. For example, in the model shown in Fig. 2.4a, the effective operator at the low scale looks something like

$$D^{\betā̄}(\xi_1^\alpha \xi_{2\alpha} \psi_1^\dagger) \frac{\partial \mathcal{L}^{lh}}{\partial \Pi^\beta} = D^{\betā̄}(\xi_1^\alpha) \xi_{2\alpha} \psi_1^\dagger \frac{\partial \mathcal{L}^{lh}}{\partial \Pi^\beta} + \dots \quad (2.18)$$

although as long as the operator is generated at tree-level, the term with the derivative acting on ψ^\dagger will always also be present as long as it is not removed by a field redefinition involving its classical EOM. Our approach is the following: act the derivative in all possible ways on the fields constituting the effective operator and discard the topologies in which a contraction like $(D^{\alphā̄} \psi_1^\dagger) \phi$ is made. After a UV-complete model is derived, the operator it implies will still have the form of the one on the left-hand side of Eq. (2.18), so no information is lost. This implies the rules

$$(D^{\alphā̄} \psi_1^\dagger) \phi \rightarrow X, \quad (D^{\alphā̄} \psi_1^\dagger \phi) \rightarrow X, \quad (D^{\alphā̄} \phi) \psi_1^\dagger \rightarrow X, \quad (D^{\alphā̄} \phi_1) \phi_2 \rightarrow X. \quad (2.19)$$

The first parentheses of Eqs. (1.39) and (1.32) contribute powers of D^2 or X to oper-

ators in the effective Lagrangian. They contribute the rules

$$\begin{aligned} (D^{\alpha\dot{\alpha}}\psi_1^\beta)(D_{\alpha\dot{\alpha}}\psi_{2\beta}) &\rightarrow \Phi^\dagger, & (D^{\alpha\dot{\alpha}}\phi_1^\beta)(D_{\alpha\dot{\alpha}}\phi_2) &\rightarrow \Phi^\dagger \\ (D^{\alpha\dot{\alpha}}\psi_1^\beta)(D_{\alpha\dot{\alpha}}\phi) &\rightarrow \Psi^\beta, & (D^{\alpha\dot{\alpha}}\phi_1^\beta)(D_{\alpha\dot{\alpha}}\phi_2)\phi_3 &\rightarrow \Phi^\dagger \end{aligned} \quad (2.20)$$

to those discussed previously. We intend these to stand in for similar rules like *e.g.*

$$\boxed{\phi_1 \square \phi_2}$$

as well. For the field-strength contractions, there is the additional requirement that one or both of the fields in the contraction be charged under the corresponding gauge interaction, but these cannot be contracted into a gauge singlet, since the field-strength tensor comes about from the anticommutator of the covariant derivatives acting on the exotic fermion. These rules are

$$\boxed{\psi_i^\alpha X_{\alpha j}^{i\beta} \phi} \rightarrow \bar{\Psi}_j^\beta, \quad \boxed{\phi X_\alpha^\beta \phi} \rightarrow \mathbf{x}, \quad \boxed{\psi_i^\alpha X_{\alpha j}^{i\beta} \phi^j} \rightarrow \mathbf{x}, \quad (2.21)$$

where i and j stand in for fundamental indices of $SU(2)_L$, $SU(3)_c$, or no indices at all for the field-strength tensor of $U(1)_Y$.

Operators with derivatives coming about as this way, *i.e.* as D^2 or X , are often redundant from the perspective of model discovery, since they imply the existence of the leading-order operator in which these derivatives do not appear. Thus, the tree-level completions of these operators can be found by studying the lower-dimensional operators without those derivatives or field-strength tensors. It may however be the case that the leading-order operator is absent, in which case these operators may be important. For the $n_f = 3$ SMEFT with one Higgs doublet, we conjecture this can only come about from operators with a structure like

$$\mathcal{O}^\mu H^i \partial_\mu H^j \epsilon_{ij}, \quad (2.22)$$

which vanishes when the derivative is removed. (Similar structures like $L_r^i L_s^j \epsilon_{ij}$ are non-vanishing since there is an additional space of flavour indices to carry the anti-symmetry.) This exception does not apply to the case of field-strength tensors, since $[X^{\mu\nu}, H] = 0$ for all field strengths X . This is the justification for our earlier comments that operators containing field-strength tensors are not interesting from the perspective of model discovery.

The replacement rules given in Eq. (2.20) do not exhaust the possible Lorentz structures for two derivatives, scalars and fermions. The additional structures involve single indices contracted between the derivatives, and others contracted into fermions. Diagrammatically, we find that these combinations come about from fermion lines containing two arrow-preserving propagators, each contributing a factor of momentum.

This would be the case, for example, if ψ in Fig. 2.4 were a heavy arrow-preserving propagator, as shown in Fig. 2.4b. Here the rules are

$$(D^{\alpha\dot{\alpha}}\overline{\psi}_{1\alpha})(D^{\beta\dot{\beta}}\overline{\psi}_{2\beta})\epsilon_{\dot{\alpha}\dot{\beta}} \rightarrow \Phi^\dagger, \quad (D^{\alpha\dot{\alpha}}\overline{\psi})(D^{\beta\dot{\beta}}\overline{\phi})\epsilon_{\dot{\alpha}\dot{\beta}} \rightarrow \bar{\Psi}^\beta, \quad \text{other combinations} \rightarrow X. \quad (2.23)$$

In summary, exploding derivative operators can lead to novel models that would not be found by exploding non-derivative operators. We have already seen that this happens when a structure such as Eq. (2.22) is present in the operator. It can also happen when the presence of an odd number of derivatives allows new topologies with novel chirality structures. The presence of an even number of derivatives implies either that the derivatives arose as D^2 or X , which usually do not contribute new models, or else from the contractions of structures like those in Eq. (2.23). It is clear from Fig. 2.4b that in such cases, the two arrow-preserving fermion propagators can be replaced with arrow-violating propagators, and indeed these will generically be present since we work with vector-like fermions. So, with the exception of operators with structures like Eq. (2.22), studying single derivative operators is sufficient for model discovery.

Derivative operator examples

Among the simplest derivative operators in the $\Delta L = 2$ SMEFT is the dimension seven operator

$$\mathcal{O}_{D3} = L_\alpha^i \bar{e}_\beta^\dagger H^j (DH)^{\alpha\dot{\beta}k} H^l \epsilon_{ij} \epsilon_{kl} \quad (2.24)$$

which we use as a paradigm for showing how single-derivative operators can be opened up. We note that the operator's tree-level completions have also been discussed in Ref. [244]. The placement of the derivative on the Higgs field is enforced by the unique $SU(2)_L$ contraction. This is not generally true, and the derivative should be acted in all possible ways if it can be. The contraction of (DH) into another Higgs is forbidden by Eq. (2.19). Thus, the (DH) must be contracted into a fermion. The options are

$$\overline{L}_\alpha^i (DH)^{\alpha\dot{\beta}k} \epsilon_{ij} \epsilon_{kl} \sim \Sigma_{jl}^{\dot{\alpha}\dot{\beta}} \quad \text{and} \quad \overline{\bar{e}}_{\dot{\beta}}^\dagger (DH)^{\alpha\dot{\beta}k} \sim \bar{\Delta}_1^{\alpha k} \quad (2.25)$$

with the Dirac fermion $\Delta_1 + \bar{\Delta}_1^\dagger \sim (1, 2, -\frac{1}{2})$ transforming like L under G_{SM} . The field Σ is the protagonist in the type-III seesaw model, and further contractions on the resulting operator $\Sigma_{jl}^{\dot{\alpha}\dot{\beta}} \bar{e}^\dagger H^j H^l$ lead to the models $\{\Sigma, \Delta_1 + \bar{\Delta}_1^\dagger\}$ (from $\bar{e}^\dagger H$) and $\{\Sigma, \Xi_1\}$ (from $H H$) in that case. The second option in Eq. (2.25) leads to the operator $L^i \bar{\Delta}_1^k H^j H^l \epsilon_{ij} \epsilon_{kl}$, which is the Weinberg operator with the second L replaced with the exotic vector-like lepton.

This contraction is illustrated diagrammatically in Fig. 2.5a. It thus implies the same completions⁷ as \mathcal{O}_1 , each along with $\Delta_1 + \bar{\Delta}_1^\dagger$. This is expected since $\tilde{e}^\dagger(DH)$ transforms like L . There are then a total of five completions, but four models, since two have the same particle content: $\{\Sigma, \Delta_1 + \bar{\Delta}_1^\dagger\}$. In Fig. 2.5b we show how this can be seen as coming about from the fact that the chirality structure of the diagram allows two positions for the arrow-preserving fermion propagator. Note that this is not the case for the completion with the singlet fermion N . Interestingly, there are two fermion-only models found: $\{N, \Delta_1 + \bar{\Delta}_1^\dagger\}$ and $\{\Sigma, \Delta_1 + \bar{\Delta}_1^\dagger\}$. Both of them contain seesaw fields, which is consistent with the proof of Ref. [104] that models containing two exotic fermion fields must contain one of N or Σ if they violate lepton-number by two units. Since the structure of the operator \mathcal{O}_{D3} is unique, there is no work to be done in writing down the organic operator generated by these models at the low scale.

We move on to a two-derivative operator example by studying a completion of

$$\mathcal{O}_{18d} = L^i L^j H^k H^l (D^\mu H)^m (D_\mu \tilde{H})^n \epsilon_{ij} \epsilon_{km} \epsilon_{ln}, \quad (2.26)$$

which has the property that it vanishes when the derivatives are removed. (Note that, comparing to the operator in Table B.1, the first derivative has been moved onto a Higgs field.) Applying the only allowed replacement rule on the derivatives first implies the presence of the real triplet scalar⁸ $\Xi \sim (\mathbf{1}, \mathbf{3}, 0)_S$ in the theory

$$L^i L^j H^k H^l (D^\mu H)^m (D_\mu \tilde{H})^n \epsilon_{ij} \epsilon_{km} \epsilon_{ln} \rightarrow L^i L^j H^k H^l \Xi^{mn} \epsilon_{ij} \epsilon_{km} \epsilon_{ln}. \quad (2.27)$$

From here there are a number of choices. We choose to look at a particular scalar-only completion involving the unit-hypercharge isosinglet scalar present in the Zee model $\mathcal{S}_1 \sim (\mathbf{1}, \mathbf{1}, \mathbf{1})$:

$$L^i L^j H^k H^l \Xi^{mn} \epsilon_{ij} \epsilon_{km} \epsilon_{ln} \rightarrow \mathcal{S}_1^\dagger H^k H^l \Xi_{kl}^\dagger, \quad (2.28)$$

implying the interaction Lagrangian

$$\mathcal{L}_{\text{int}} \supset x_{[rs]} L_r L_s \mathcal{S}_1 + \kappa H^i \tilde{H}^j \Xi_{\{ij\}} + \lambda \mathcal{S}_1 \Xi^{ij} H_i^\dagger H_j^\dagger + \text{h.c.} \quad (2.29)$$

This model was studied in Ref. [247] and identified as the simplest neutrino mass model according to their assumptions. It has remarkably few free parameters since the scalar Ξ does not have Yukawa couplings to SM fermions, and the couplings of \mathcal{S}_1 to leptons are antisymmetric in flavour. As in the minimal Zee–Wolfenstein scenario [91] (see Eq. (1.26) and surrounding discussion), this model implies a neutrino-mass matrix

⁷This phenomenon is discussed in more detail in Sec. 2.4.2.

⁸We remind the reader that this is not the seesaw field present in the type-II scenario, which has unit hypercharge.

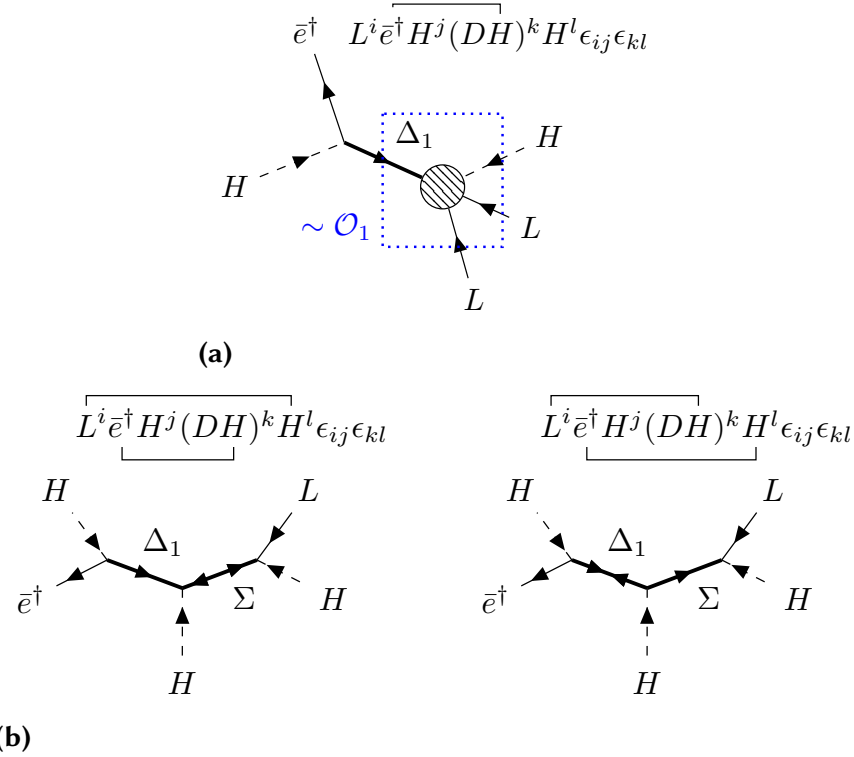


Figure 2.5: (a) An intermediate topology representing the operator \mathcal{O}_{D3} with all heavy fields except Δ_1 integrated out. The contraction $\bar{e}^\dagger H \sim \Delta_1^\dagger$ gives rise to an effective operator similar to the Weinberg operator \mathcal{O}_1 , shown in blue. This branch of the completion tree therefore involves models featuring Δ_1 along with one of the seesaw fields. (b) The model with field content $\{\Sigma, \Delta_1 + \bar{\Delta}^\dagger\}$ arises from two similar diagrams, shown here. These correspond to the two ways the arrow-preserving and arrow-violating fermion propagators can be placed in the graphs for this furnishing of the topology.

with zeros down the diagonal and is therefore incompatible with neutrino oscillation data [248]. It is, however, a good example of how interesting models can be missed when overlooking operators with derivatives in this model-building framework. The model generates the following combination of basis operators at the low scale

$$\mathcal{O}_{\mathcal{S}_1+\Xi}^{[rs]} = (L_r^i L_s^j) H^k H^l \square (H^m \tilde{H}^n) \epsilon_{ij} \epsilon_{km} \epsilon_{ln}. \quad (2.30)$$

Note that the operator is already symmetric under the interchange $m \leftrightarrow n$, so another structure need not be added.

2.3.2 An algorithm for model building

With our basic completion recipe established, in the following we outline the procedures we use to build the UV models that generate the operators listed in Table B.1, along with relevant metadata: the tree-level diagrams and the models' Lagrangians. The methods are presented as they are implemented in our example code [228].

We use a computational representation for tensors representing fields transforming as irreducible representations of $SU(2)_+ \otimes SU(2)_- \otimes G_{\text{SM}}$ built on top of the SymPy package [249] for symbolic computation in Python, as well as BasisGen [234] for group-theory functionality. The code implements the Butler–Portugal algorithm [250, 251] for obtaining the canonical form of tensorial expressions, which we use to simplify operators and compare them for equality. Strings of fields and their derivatives representing gauge- and Lorentz-invariant effective operators are dressed with ϵ and δ tensors to form all possible invariants. In our specific case, the content of these operators is constructed directly by taking the product of all field combinations and keeping only those that contain a singlet part in the decomposition. We checked this against results from the Hilbert series, projecting out the $\Delta L = 2$ component for the pertinent operators by the method described in Sec. 1.3.3 and removing the spurions accounting for redundancies from field redefinitions involving the classical EOM and IBP. For our study of the $\Delta L = 2$ operators, since we are interested in model discovery, we excluded derivative operators that are non-explosive along with those that contain field-strength tensors and contracted pairs of derivatives that do not lead to a vanishing structure upon removal.

In practice we start with a template pattern of contractions corresponding to the topologies that can accommodate the field content of the operators at tree-level. These are generated using FeynArts [252] through Mathematica, and filtered for isomorphism with graph-theory tools [253–256]. These templates provide the order and pattern of contractions for classes of operators based on the number of scalars and fermions they contain. Since no distinction is made at this level between $(2, 1)$ - and $(1, 2)$ -fermions, for some operators only a subset of these templates will be relevant for our purposes, since some contractions may always imply Proca fields. These templates are used to open up the operator with the assumptions and methods presented in Sec. 2.3. Every time a replacement rule is applied, the Feynman graph information is updated and a Lagrangian term is generated as described in Sec. 2.3. After the procedure is finished, the full Lagrangian of the model can be generated in the same way as the input effective operators, described above.

We keep track of the quantum numbers of the heavy fields so as to be economic with exotic degrees of freedom, while still providing some flexibility in the model database. Concretely, if a field arises from a contraction whose corresponding term has already appeared in the Lagrangian, the two associated exotic fields are identified. If two fields come about from different contractions but share the same quantum numbers they are

distinguished, since it may be possible that some symmetry would forbid one term but not the other. The choice to identify fields not only reduces the number of fields in each model, but may also reduce the total number of completions for a given operator. This is due to couplings between exotic fields that vanish in the absence of some exotic generational structure. For example, $\phi^i \phi^j \epsilon_{ij} = 0$ for some exotic isodoublet ϕ , or $\eta^a \eta^b \eta^c \epsilon_{abc} = 0$ for a colour-triplet η .

We have attempted to validate our example code against many results in the literature. We have been able to reproduce the results of Refs. [22, 101, 231, 244, 245], which give systematic listings of models that generate effective operators at tree-level. Ref. [22] provides a UV dictionary for the dimension-six SMEFT. Validation of these results first required the adaptation of the dimension-six operators to something analogous to the overcomplete spanning set of type-3 operators used here. The entire process in this case—including generating the set of operators, finding the completions and matching examples back onto the Warsaw basis—is provided as an interactive notebook accompanying our example code. We note that such matching calculations can also be automated with the help of automated tools [257, 258]. For the other studies mentioned, we provide our validation of their results along with our example code.

2.4 Neutrino mass model building

Up until now we have tried to keep the discussion of exploding operators general, but in this and following sections we specialise to the case of opening up operators to build radiative models of Majorana neutrino mass. We discuss the process of turning $\Delta L = 2$ operators into neutrino self-energy graphs, the tree-level topologies of the operators, and the methods we use to ensure a given model’s contribution to the neutrino mass is the dominant one.

2.4.1 Operator closures and neutrino-mass estimates

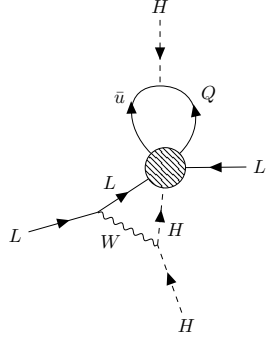
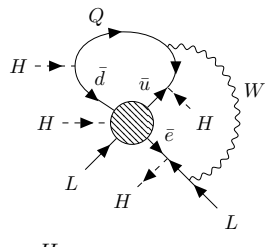
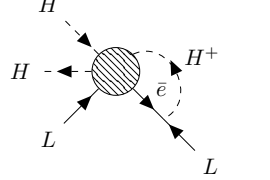
For operators other than the Weinberg-like ones, neutrino masses are necessarily generated at loop level. The fields of the $\Delta L = 2$ operator need to be looped off using SM interactions in such a way that a Weinberg-like operator is generated after the SM fields are integrated out. We call this the operator *closure* and it represents the mixing between the $\Delta L = 2$ operator and the Weinberg-like ones. Examples of $\Delta L = 2$ operator closures are given in Table 2.1, and these are referred to throughout this section. The closure provides enough information to know the number of loops in the neutrino self-energy graph (since the $\Delta L = 2$ operator is generated at tree level) and to estimate the scale of the new physics underlying the operator. We automate the operator-closure

process by applying the methods discussed below through a pattern-matching algorithm [259, 260]. The program is a part of our public example-code repository.

Current neutrino oscillation data provide a lower bound on the mass of the heaviest neutrino, coming from the measured atmospheric mass-squared difference $\Delta m_{\text{atm}}^2 \approx (0.05 \text{ eV})^2$ [7, 261]. We take the neutrino-mass scale $m_\nu \approx 0.05 \text{ eV}$, so that the new-physics scale is bounded above by the implied scale we estimate for each operator. This is derived by estimating the loop-level operator closure diagrams. In our case we are interested in estimating the scale of the neutrino mass in the UV models generating the operator, rather than the calculable loop-level contributions to the neutrino mass in the EFT. We associate a factor of $(16\pi^2)^{-1} \approx 6.3 \cdot 10^{-3}$ with each loop and assume unit operator coefficients for the non-renormalisable $\Delta L = 2$ vertices. We take the SM Yukawa couplings to be diagonal and include factors of $g \approx 0.63$ appropriately for interaction vertices involving W bosons. Neutrino-mass matrices proportional to Yukawa couplings will be dominated by the contributions from the third generation of SM fermions in the absence of any special flavour hierarchy in the new-physics couplings. For this reason, we consider only the effects of third-generation SM fermions in our estimates, but mention that our program can be straightforwardly extended to accommodate the general case where light-fermion Yukawas and off-diagonal CKM matrix elements appear in the neutrino-mass matrix. For derivative-operator closures, we can include the W boson from the covariant derivative if it is present and necessary to correctly close off the diagram. Otherwise, the vertex should come with an additional factor of momentum. We work in the Feynman gauge to avoid spurious factors of Λ in the neutrino-mass estimates [244]. The overall scale-suppression of the neutrino mass is determined by the Weinberg-like operator generated at the low scale. In most cases, this is the dimension-five operator \mathcal{O}_1 , which implies $m_\nu^{\mathcal{O}_1} \sim v^2/\Lambda$. Closures leading to the loop-level generation of \mathcal{O}'_1 and \mathcal{O}''_1 can also be found, and these naively imply a significant suppression of the neutrino mass compared to the \mathcal{O}_1 case: $m_\nu^{\mathcal{O}'_1} \sim v^4/\Lambda^3$ and $m_\nu^{\mathcal{O}''_1} \sim v^6/\Lambda^5$. However, a diagram with additional Higgs loops can always be drawn to recover the Weinberg operator at the low scale. Despite the additional loop suppression, these diagrams will dominate over those generating \mathcal{O}'_1 and \mathcal{O}''_1 as long as $\Lambda \gtrsim 4\pi v \approx 2.2 \text{ TeV}$ [84, 99].

It is still true that higher-dimensional operators typically imply smaller neutrino masses. There are two main reasons for this. First, the number of loops required for the closure of the operator generally increases with increasing mass dimension. Second, operators containing more fields imply neutrino self-energy diagrams containing more couplings. Many of these are SM Yukawas which (with the exception of y_t) are small and tend to suppress the neutrino mass, despite the contributions being dominated by the third generation. Non-minimal choices such as small exotic Yukawa couplings or hierarchical flavour structures in the operator coefficients can also lead to additional suppression of the neutrino mass, and in turn of the implied scale of the new physics.

Table 2.1: The table shows an assortment of $\Delta L = 2$ operator closures, displaying a number of paradigmatic motifs. We represent flavour indices in a sans-serif typeface here to avoid confusion with subscripts labelling the Yukawa couplings. The expressions given for m_ν^{rs} needs to be symmetrised in rs, something we do not explicitly indicate in the table. These expressions carry flavour indices in alphabetical order on the fields as they appear in Table B.1. Here κ represents the operator coefficient, V is the CKM matrix and $y_{e,u,d}^r$ are the diagonal electron, up-type and down-type Yukawa couplings in the SM. A number of operators require an external electron to be converted into a neutrino. This often necessitates the introduction of a W boson or an unphysical charged Higgs H^+ . Operator \mathcal{O}_8 generates the dimension-seven analogue of the Weinberg operator with the two-loop diagram shown. (There is a lower order diagram with an H^+ in place of the W that happens to vanish [262].) A three-loop diagram in which two of the external Higgs lines are looped off leads to mixing with the Weinberg operator. Operator \mathcal{O}_{76} generates the dimension-nine operator $LLHH(H^\dagger H)^2$, and hence five- and six-loop diagrams are also implied. There is usually more than one choice about where to attach the W boson if one is present in a diagram, and the additional diagrams with the W connecting in other possible ways are left implicit.

Op.	Diagram	m_ν^{rs}
4b		$\kappa_{[\text{rs}]\text{tt}} \frac{g^2 y_u^t}{(16\pi^2)^2} \frac{v^2}{\Lambda}$
8		$\kappa_{rstu} V_{tu} \frac{g^2 y_e^s y_u^t y_d^u}{(16\pi^2)^2} \frac{v^2}{\Lambda} \left(\frac{v^2}{\Lambda^2} + \frac{1}{16\pi^2} \right)$
D3		$\kappa_{rs} \frac{y_e^s}{16\pi^2} \frac{v^2}{\Lambda}$

Op.	Diagram	m_ν^{rs}
11b		$\kappa_{\text{rstutu}} \frac{y_d^t y_d^u}{(16\pi^2)^2} \frac{v^2}{\Lambda}$
76		$\kappa_{\text{rstuvw}} V_{tv} V_{uw} \frac{g^4 y_e^r y_e^s y_u^t y_u^u y_d^v y_d^w}{(16\pi^2)^4} \frac{v^2}{\Lambda} \left(\frac{v^2}{\Lambda^2} + \frac{1}{16\pi^2} \right)^2$
47a		$\kappa_{\text{rstuvw}} \frac{1}{(16\pi^2)^2} \frac{v^2}{\Lambda}$
56		$\kappa_{\text{rstvvv}} \frac{y_e^s y_d^t}{(16\pi^2)^3} \frac{v^2}{\Lambda}$

In Fig. 2.6 we show the new-physics scales Λ associated with neutrino-mass generation from the $\Delta L = 2$ operators in the SMEFT up to dimension 13, assuming unit operator coefficients and the dominance of third-generation couplings. We separate single-derivative operators from those that contain no derivatives, and choose not to include operators containing more than one derivative in the figure. This is because these operators most often arise at next-to-leading order in the EFT expansion, and therefore usually imply a neutrino-mass scale identical to that of lower-dimensional operators. The dimension-eleven operators with derivatives as well as the dimension-13 operators are constructed only as products of lower-dimensional ones, making the set of operators incomplete. We highlight that similar kinds of product operators at dimensions eleven and nine do not imply special values for the estimated neutrino-mass scale or Λ , and therefore we expect the results to be representative of the situation up to dimension 13. From the figure, it is clear that there is a trend towards smaller values of Λ with increasing mass dimension. By dimension 13, the implied new-physics scale is between 1 and 100 TeV for most operators. It seems to be the case that the most constrained closures are generally those of non-derivative operators.

We note that at dimension eleven it begins to become clear that the neutrino-mass

estimates associated with a category of operators remain large. These operators include \mathcal{O}_{47a} , whose closure is shown in Table 2.1, and 44 others like it which have loops that contain no connecting Higgs, and therefore no additional suppression from SM Yukawa couplings⁹. These operators have the form

$$\mathcal{O}_1 \cdot \prod_{i=1}^n \psi_i^\dagger \psi_i, \quad (2.31)$$

where ψ_i are SM fermion fields, and imply

$$m_\nu \sim \kappa \frac{1}{(16\pi^2)^n} \frac{v^2}{\Lambda}, \quad (2.32)$$

with κ the operator coefficient. The loop suppression becomes too great to meet the atmospheric bound at $n = 6$. Although five loops are viable in the absence of any other suppression, the operators $\mathcal{O}_1 \cdot \prod_{i=1}^5 (\psi_i^\dagger \psi_i)$ cannot form a Lorentz-singlet without a derivative. This suggests that dimension-21 operators of the form

$$LLH(\partial^\mu H) \cdot (\psi_0 \sigma_\mu \psi_0^\dagger) \prod_{i=1}^4 \psi_i^\dagger \psi_i \quad (2.33)$$

are the highest-dimensional operators leading to phenomenologically viable neutrino masses. They require new physics below ~ 6 TeV. All of the tree-level topologies associated with the structure in Eq. (2.33) imply that the neutrino mass depends on the product of nine or more dimensionless couplings. It is clear from Fig. 2.6 that these operators are outliers, and the associated new-physics scale is already heavily constrained by dimension 13 for most.

Estimates for the neutrino mass for the majority of the $\Delta L = 2$ operators without derivatives have been given previously in Ref. [84]. Those that we present here differ in two ways:

1. We aim to estimate the contribution to the neutrino mass implied by the completions of the operator, not the operator alone. This means, for example, that we do not need more loops of gauge bosons to provide additional factors of momentum on fermion loops with no mass insertions, since it is implicit that the appropriate factors of momentum will arise at higher orders in the EFT expansion. Such arrow-preserving loops, as shown in the closures of \mathcal{O}_{47a} and \mathcal{O}_{56} in Table 2.1, vanish by even-odd parity arguments absent these higher-order contributions [84]. Indeed, in UV models built from these operators the additional

⁹A UV example of such a model was presented and studied in Ref. [4] for \mathcal{O}_{47j} . A number of other examples were also mentioned in Ref. [263], including a two-loop model generating a dimension-13 operator at tree level.

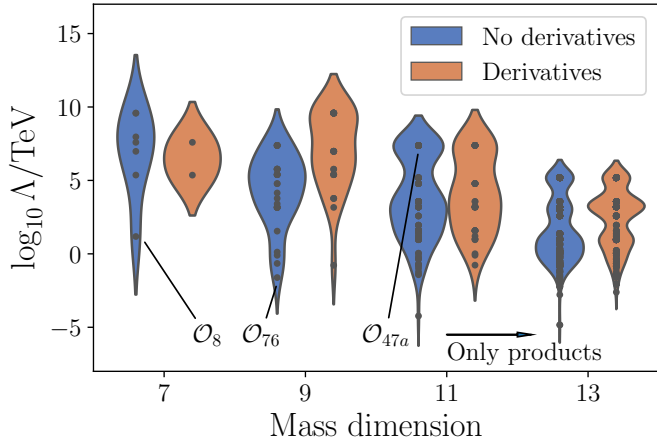


Figure 2.6: The figure shows smoothed histograms of the number of operators that have an estimated upper bound of Λ on the new-physics scale. Black dots generally represent more than one operator. The strips are broken up by mass dimension and whether the operators contain derivatives or not. We assume unit operator coefficients and the dominance of third-generation SM-fermion contributions in the closure diagrams. Operators containing no derivatives (blue) are separated from those containing one derivative (orange). Those containing more than one derivative are not included in the figure, since in most cases these come about at next-to-leading order in the EFT expansion, and therefore imply the same Λ values as the lower-dimensional operator with two fewer derivatives. The dimension-eleven operators containing one derivative and all of the dimension-13 operators shown are constructed from the lower-dimensional operators in our listing only as products. This means that the set of operators plotted above that do not feature in Table B.1 are incomplete. However, we do not find that similar product-type operators at dimensions nine and eleven give special estimates for the neutrino mass or Λ , and so we expect these results to be representative of the true situation up to mass-dimension 13. The general decrease in Λ with increasing operator mass dimension is evident in the figure. The most suppressed closures tend to be of non-derivative operators. By mass-dimension eleven it becomes clear that a class of operators, those with the structure shown in Eq. (2.31), are less suppressed than the rest.

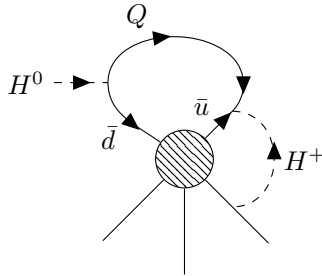


Figure 2.7: For some operators containing $\bar{d}\bar{u}^\dagger$ the operator closure involves a motif like that shown in the figure. There is always an additional diagram with the roles of the unphysical Higgs and H^0 interchanged. Both diagrams are proportional to $y_u y_d$ but related by a negative sign coming from the couplings of H^+ to up- and down-type quarks as shown in Eq. (2.34), and therefore their sum vanishes.

gauge-boson loops are not necessary [4, 240]. This means that for operators such as \mathcal{O}_{47a} and \mathcal{O}_{56} , our neutrino-mass estimates are enhanced with respect to those presented in Ref. [84] by $16\pi^2/g^2$.

2. In some cases, operators containing a factor of $\bar{u}^\dagger \bar{d}$ require a closure with W bosons rather than H^+ , since the sum of the diagrams with the unphysical Higgs fields vanishes [262]. The situation is shown in Fig. 2.7 for a general one-loop case of this phenomenon. Ultimately this comes from the relative negative sign in the Lagrangian between the up- and down-type Yukawa interactions:

$$\mathcal{L}_{\text{Yuk}} \supset y_u^r V_{rl} d_t \bar{u}_r H^+ - y_d^r V_{tr} \bar{d}_t^\dagger u_t^\dagger H^+. \quad (2.34)$$

As shown in the Fig. 2.7, the fermion loop requires a mass insertion on the quark line to which the H^+ does not connect, making both loops proportional to $y_u y_d$ but with differing signs. Care must be taken to ensure that the loop functions are also necessarily the same in cases where this property is used.

It might be possible that, in a similar way to (2) above, the sum of diagrams with different W placements or of the neutrino-flavour-symmetrised diagrams might also lead to additional cancellations which further decrease the upper bound on the new-physics scale. This is not a possibility we explore in detail here, but note that similar cancellations have been noted in the literature [4].

Our estimates for the neutrino mass are provided as symbolic mathematical expressions in our model database. Where possible these have been checked against more detailed calculations and UV models in the literature generating the operators to ensure acceptable agreement [4, 16, 82, 83, 101, 244, 262, 264, 265]. The predictions for the new-physics scale associated with each operator are provided in Table B.1, along with the number of loops in the closure. Operators for which a range is given for the number of

loops are those that generate the dimension-seven or dimension-nine analogues of the Weinberg operator. As touched on above, the additional Higgs fields in these closures can always be closed off, adding more loops to the neutrino self-energy diagram while reducing the overall scale suppression. The contribution with the highest number of loops will dominate for scales $\Lambda \gtrsim 4\pi v$.

We note that in some cases, more insights can be made about the structure of the neutrino-mass matrix from the nature of the operator, even in the general form with which they appear in our classification. For example, there is only one independent Lorentz-structure associated with \mathcal{O}_{4b} : $\kappa_{rstt}^{\mathcal{O}_{4b}}(L_r^i L_s^j \epsilon_{ij})(Q_{tk}^\dagger \bar{u}_t^\dagger)H^k$, from which it can be seen that the operator coefficient must be antisymmetric in rs from Fermi–Dirac statistics. It is clear from the diagram associated with the operator in Table 2.1 that the loop integral will depend on an external lepton flavour, and this dependence can only come from charged-lepton masses, *i.e.* $I(m_e^r)$. Then the complete expression for the estimated neutrino mass will be something like

$$m_\nu^{\{rs\}} \sim \sum_t \frac{g_2^2 y_u^t}{(16\pi^2)^2} \frac{v^2}{\Lambda} [\kappa_{[rs]tt} I(m_e^r) + \kappa_{[sr]tt} I(m_e^s)] \quad (2.35)$$

$$= \sum_t \frac{g_2^2 y_u^t}{(16\pi^2)^2} \frac{v^2}{\Lambda} \kappa_{[rs]tt} [I(m_e^r) - I(m_e^s)], \quad (2.36)$$

which implies a neutrino-mass matrix with zeros down the diagonal, similar to that following from the Lagrangian in Eq. (2.29). Such a texture is disfavoured by neutrino oscillation data. Studying the structure of the neutrino-mass matrices implied by a complete basis of $\Delta L = 2$ operators would allow more, similar conclusions to be drawn in a model-independent way. Recently, a complete basis of operators in the SMEFT at dimension nine has been written down [145], and this could facilitate such an effort.

2.4.2 UV considerations

We now turn to the UV structure of the operators: their completion topologies, the associated neutrino self-energy graphs, and the nature of the exotic fields that feature therein. Central to our study of neutrino mass is the requirement that a model represent the leading contribution to the neutrino mass, a condition we impose through a process of model filtering, also discussed in the present section.

Tree-level completion topologies

The tree-level UV topologies depend on the number of fermions and scalars in the operator, and this is how we choose to label them. Thus, a dimension-eleven operator

with two scalars and six fermions has topologies labelled $2s6f_i$. We do not distinguish between $(2, 1)$ - and $(1, 2)$ -fermions in this classification, and some of these topologies will therefore always imply the existence of heavy vector particles in the completions. In our analysis these models are not considered, but the topologies are still presented here in general. Each topology corresponds to a pattern of contractions in the language of Sec. 2.3, and sometimes we use this perspective.

We present the different topology types in Table 2.2 along with peripheral information relating to these. The number of propagators in the diagrams represents an inclusive upper bound on the number of exotic fields allowed in the completions of the associated operators, counting Dirac fermions as one exotic field. In many cases, repetition in the operator's field content can lead to fewer fields furnishing the internal lines of the diagram, since we identify fields with the same quantum numbers. To avoid clutter we keep the complete gallery of tree-level diagrams in our online example-code repository, and instead only show some of the graphs here. For some topology types the relevant diagrams have already appeared in earlier parts of the paper, and these figures are referenced in the table. We make more specific comments about the topology types by operator mass dimension below.

Dimension seven At dimension seven there are three broad classes of $\Delta L = 2$ operators by field-content: $0s4f$, $1s4f$ and $4s2f$ in our classification scheme. Operator \mathcal{O}_{D1} is one of only two $0s4f$ operators in the entire listing, both of which are non-explosive¹⁰. The Weinberg-like \mathcal{O}'_1 is the only $4s2f$ operator at dimension seven, while there are six $4s2f$ operators: \mathcal{O}_2 , $\mathcal{O}_{3a,b}$, $\mathcal{O}_{4a,b}$ and \mathcal{O}_8 . The UV topologies relevant for the dimension-seven operators are presented in Fig. 2.8. There are only two tree-level topologies associated with the $1s4f$ operators. One involves two exotic scalars, the other an exotic scalar and a heavy fermion with an arrow-violating propagator line. There are ten topologies associated with the $4s2f$ class, for which the only pertinent operator is \mathcal{O}'_1 . Only topology $4s2f_3$ is associated with a model that does not contain seesaw fields. Topology $4s2f_6$ accommodates up to three exotic scalars and $4s2f_8$ allows up to three exotic fermions. Such fermion-only models are expected only for the Weinberg-like operators, in the absence of derivatives. The remaining topologies allow all other combinations up to three fields for the number of exotic scalars and fermions introduced. Radiative neutrino mass from the dimension-seven operators without derivatives was also studied in Ref. [101].

Dimension nine At dimension nine there are 79 operators in our catalogue. There are 16 operators containing six fermions, these are \mathcal{O}_9 through to \mathcal{O}_{20} as well as \mathcal{O}_{76} . The relevant tree-level topologies are presented in Fig. 2.2. There are 15 $3s4f$ operators,

¹⁰We note that although \mathcal{O}_{D1} is non-explosive, one-loop completions exist that lead to three-loop neutrino mass models.

Topology type	Operators	Topologies	Propagators	Figure
$0s4f$	2	1	1	↪
$0s6f$	16	2	3	2.2
$1s4f$	16	2	2	2.8b
$2s2f$	7	1	1	2.1
$2s4f$	29	8	2,3	2.9b
$2s6f$	137	35	4,5	2.11
$3s2f$	3	4	1,2	2.10b
$3s4f$	15	23	3,4	2.9a
$4s2f$	8	10	2,3	2.8a
$5s2f$	1	24	2,3,4	2.10a
$5s4f$	15	264	4,5,6	↪
$6s2f$	1	66	3,4,5	↪

Table 2.2: The table shows the topology classes encountered in our operator listing along with related information: the number of pertinent operators, the number of tree-level topologies associated with each topology type, the number of internal lines featuring in the diagrams (given as a range), and the appropriate figure reference in the text. Although there is one $0s4f$ topology, all of the pertinent operators in our listing are non-explosive because they contain derivatives. The symbol \hookrightarrow indicates that we do not present these topologies in this paper; instead, we point the interested reader to our online database and example code for the relevant diagrams. We highlight that although the topologies are labelled only by their field content, the pertinent operators may include one or more derivatives. We point the reader to the main text for a detailed breakdown by mass-dimension of the topologies that are relevant to each operator.

most of which have the form $\mathcal{O}_1 \cdot \mathcal{O}_{\text{SM}} \text{ Yukawa}$ or $H^\dagger H$ times a $1s4f$ dimension-seven operator. These are operators \mathcal{O}_5 through to \mathcal{O}_7 as well as \mathcal{O}_{61} , \mathcal{O}_{71} , \mathcal{O}_{77} , \mathcal{O}_{78} and \mathcal{O}'_8 . These topologies are shown in Fig. [2.9a](#). There is a single $6s2f$ operator: the Weinberg-like \mathcal{O}''_1 . The remaining 47 operators contain derivatives. Those that contain an even number share topologies with dimension-five or dimension-seven operators. These include \mathcal{O}_{D19} , a $2s2f$ operator, \mathcal{O}_{D18} and \mathcal{O}_{D22} which are $4s2f$ operators with associated topologies shown in Fig. [2.8a](#), as well as \mathcal{O}_{D4} , \mathcal{O}_{D7} , \mathcal{O}_{D13} and \mathcal{O}_{D15} for which the $1s4f$ topologies of Fig. [2.8b](#) are relevant. The remaining operators contain an odd number of derivatives. The operators \mathcal{O}_{D5} , \mathcal{O}_{D6} , $\mathcal{O}_{D8} - \mathcal{O}_{D10}$, \mathcal{O}_{D12} , \mathcal{O}_{D14} , \mathcal{O}_{D16} and \mathcal{O}_{D17} are of type $2s4f$, implying entirely new topologies, shown in Fig. [2.9b](#). To these we add the $5s2f$ operator \mathcal{O}_{D20} and the $3s2f$ operator \mathcal{O}_{D21} , which also have novel structure. Fig. [2.10a](#) and Fig. [2.10b](#) are relevant in this case. For the operators that contain an odd number of derivatives, only the topologies allowing at least one arrow-preserving

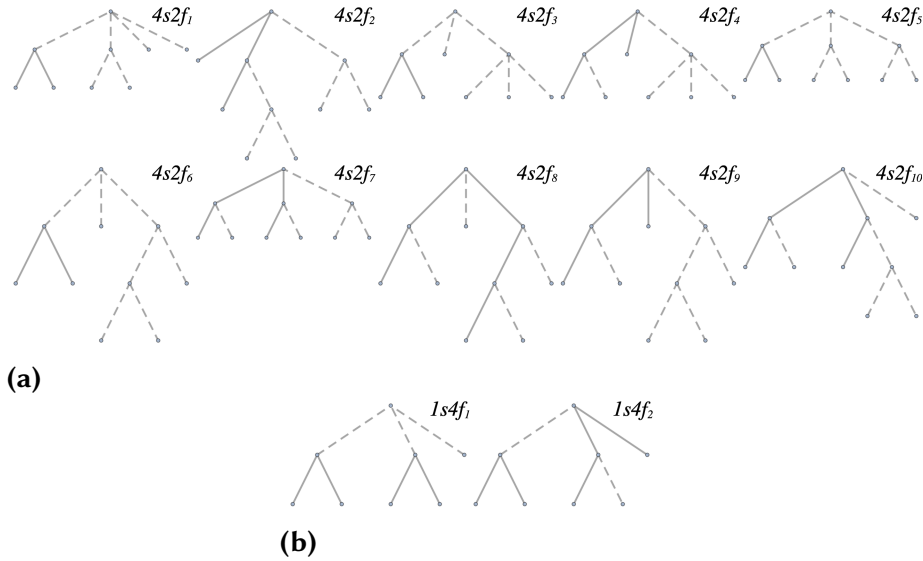


Figure 2.8: (a) The tree-level topologies relevant for the completions of the four-scalar–two-fermion operator \mathcal{O}'_1 . Only topology $4s2f_3$ leads to a novel completion that does not feature a seesaw field. We point out that topology $4s2f_8$ permits fermion-only completions, which are expected only for the Weinberg-like operators in the absence of derivatives. (b) The two tree-level topologies relevant for the completions of the one-scalar–four-fermion dimension-seven operators in Table B.1. The internal fermion line on $1s4f_2$ must be arrow-violating for all of the operators we consider.

fermion propagator do not contain exotic Proca fields. Some $3s4f$ and $5s2f$ topologies have the interesting property that they involve exotic fields that couple only to other exotic fields in the diagram. These are the lowest-dimensional operators in our listing having this feature, although this becomes more common at dimension eleven.

We note that the tree-level topologies can also be important in telling which derivative operators might provide novel completions. As discussed in Sec. 2.3.1, many operators containing more than one derivative have no model-discovery utility. These are operators generated past the leading order in the expansion of the heavy propagators in the UV theory, and their completions are always found by exploding the lower-dimensional operators with an even number of fewer derivatives. One way to diagnose such a situation is to check how many arrow-preserving fermion lines are present in the tree-level topologies associated with an operator. If all of the graphs contain fewer such propagators than the number of derivatives in the operator, then any model generating this operator will also generate the corresponding lower-dimensional one. At dimension nine there are seven operator classes that fall into this category. The four operator families \mathcal{O}_{D4} , \mathcal{O}_{D7} , \mathcal{O}_{D13} and \mathcal{O}_{D15} each contain two derivatives. These opera-

tors are identified above as fitting into the $1s4f$ topology class. It is clear from Fig. 2.8b that no two-fermion completions are relevant to this class, and the Lorentz structure of these operators is such that the internal fermion can only by arrow-violating. This suggests that models generating these operators at tree-level will always also generate the derivative-free dimension-seven operators \mathcal{O}_2 , \mathcal{O}_3 , \mathcal{O}_4 and \mathcal{O}_8 , respectively. There are two three-derivative operators: \mathcal{O}_{D21} , of topology class $3s2f$, and \mathcal{O}_{D11} , a $0s4f$ operator. The latter is non-explosive and therefore not relevant to a discussion of tree-level model building. The $3s2f$ class admits completions that contain one and two fermions: those associated with topologies $3s2f_4$ and $3s2f_2$, respectively. In both cases we find that the operator's structure allows for only a single arrow-preserving propagator in each diagram. As before, this suggests that \mathcal{O}_{D21} is not interesting for model discovery, and its completions will be found by studying \mathcal{O}_{D3} . Finally, there is also one four-derivative operator at dimension nine: the $2s2f$ operator \mathcal{O}_{D19} whose completions coincide with those of the Weinberg operator \mathcal{O}_1 . This means that the only two-derivative operators in our listing that could contribute new completions to the pool of neutrino-mass models are \mathcal{O}_{D18} and \mathcal{O}_{D22} . Operator \mathcal{O}_{D22} has the feature that the removal of the derivatives causes the operator to vanish, while this is not true for all of the $SU(2)_L$ structures associated with \mathcal{O}_{D18} .

Dimension eleven By far the largest class of operators at dimension eleven is the $2s6f$ topology type, for which the topologies are presented in Fig. 2.11. These operators are mostly formed as products of $0s6f$ dimension-nine operators with $H^\dagger H$, or $1s4f$ dimension-seven operators with SM Yukawa couplings. They are operators \mathcal{O}_{21} through to \mathcal{O}_{65} , excluding the structures associated with \mathcal{O}_{61} , as well as \mathcal{O}_{75} , \mathcal{O}'_{76} and \mathcal{O}_{82} . The only other major class relevant to the derivative-free dimension-eleven operators is $5s4f$ for which there are 264 tree-level topologies. These are presented with our example code, along with the topologies relevant to the single $6s2f$ operator \mathcal{O}_1''' . This dimension-eleven generalisation of the Weinberg operator has already received some attention in the literature [103].

Model filtering

The completions constructed by exploding the $\Delta L = 2$ operators are not all automatically guaranteed to provide the leading-order contribution to the neutrino mass. The same $\Delta L = 2$ Lagrangian may, for example, inevitably imply another, larger contribution. Alternatively, the dominant contribution may come from other LNV combinations of couplings in the model's full Lagrangian. The relative importance of different mechanisms may also depend on the assumptions of the model builder. Some neutrino-mass diagrams will dominate over others only in certain regions of parameter space. Are these regions accessible without large hierarchies in exotic couplings? Are such

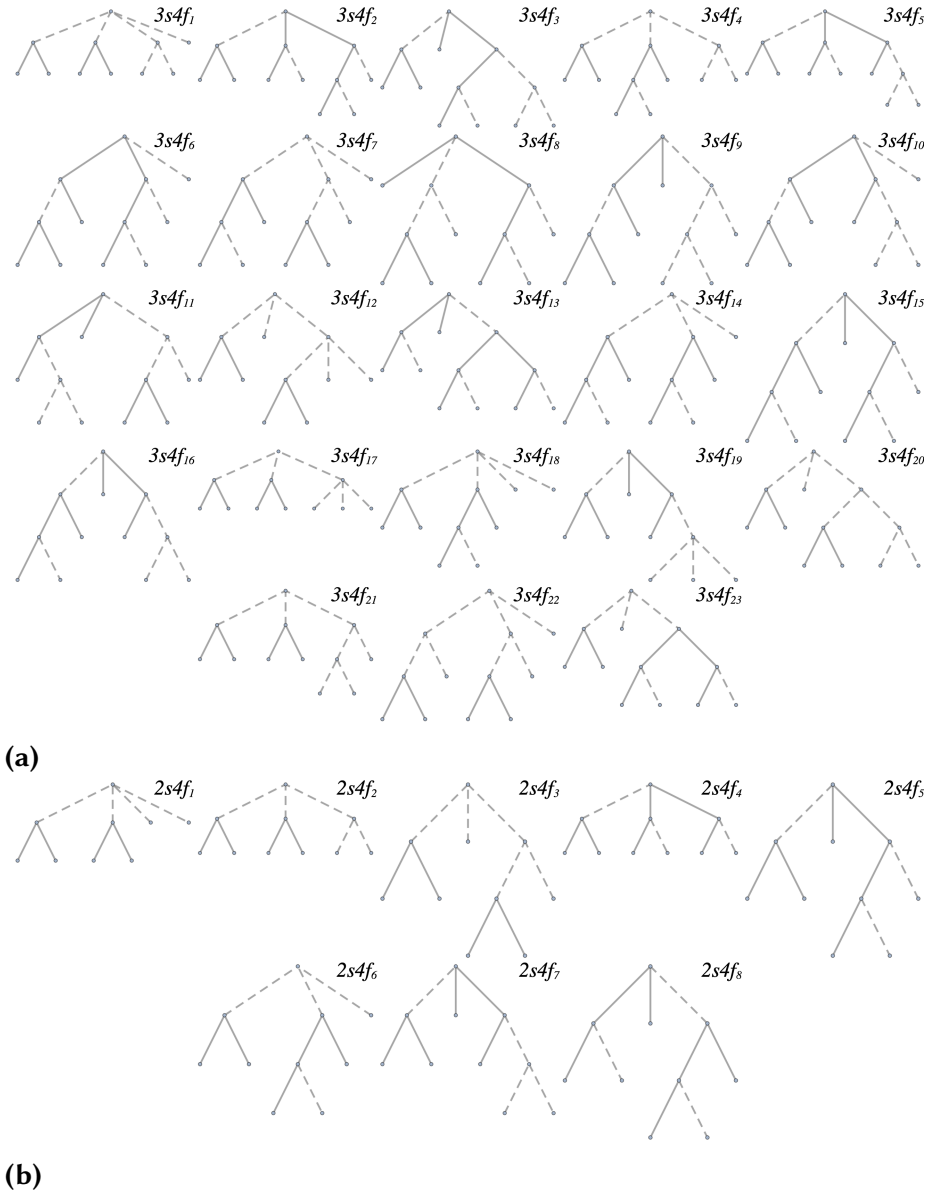


Figure 2.9: (a) The figure shows the tree-level topologies relevant to $3s4f$ operators. Topologies $3s4f_3$, $3s4f_{13}$, $3s4f_{20}$ and $3s4f_{23}$ imply one exotic field that couples only to other exotics in the diagram. This topology class is relevant to a large number of dimension-nine operators, and these are the lowest-dimensional examples of operators containing this property in our listing. (b) The two-scalar–four-fermion topologies associated with dimension-nine single-derivative operators in our catalogue. Since only single-derivative operators furnish these graphs, only those topologies containing at least one arrow-preserving internal fermion line are relevant. These are topologies $2s4f_4$ – $2s4f_8$; the other fermion propagator in $2s4f_4$ and $2s4f_5$ must be arrow violating. Topologies $2s4f_1$ – $2s4f_3$ each give rise to completions involving exotic Proca fields.

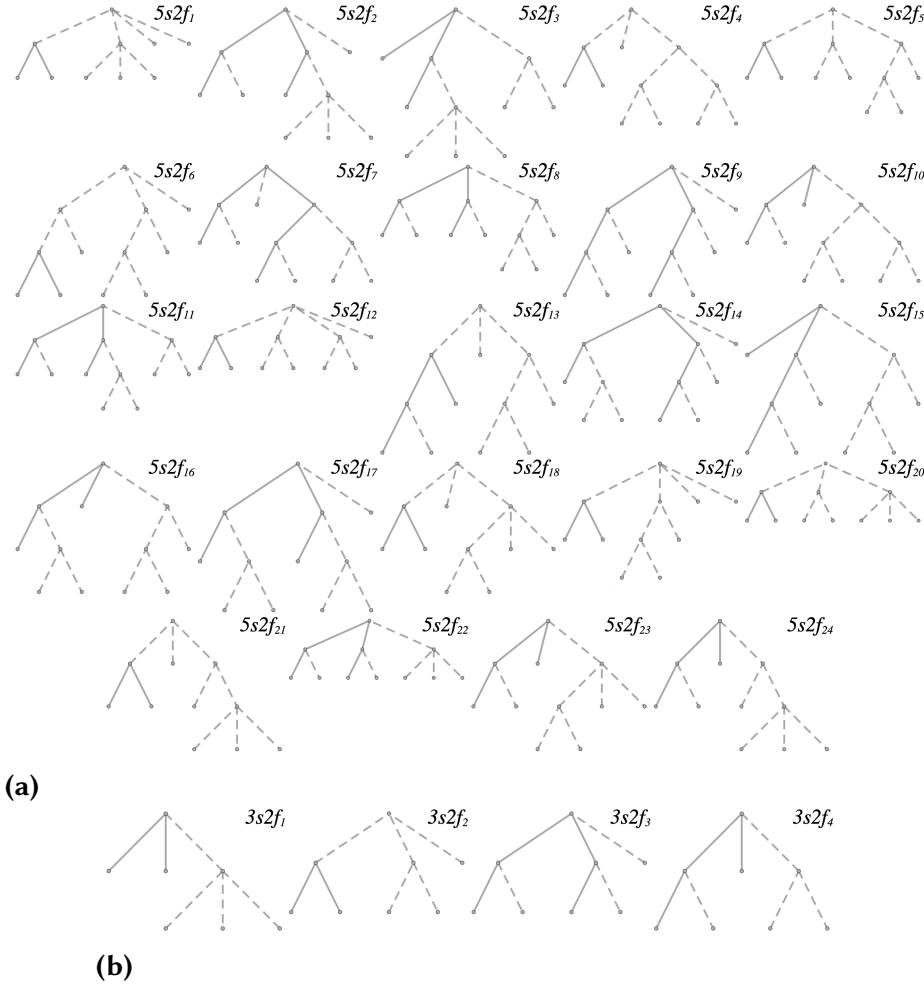


Figure 2.10: (a) The $5s2f$ topologies relevant only to the single-derivative operator \mathcal{O}_{D20} . Only those topologies allowing one arrow-preserving internal fermion line give completions allowed in our framework. Topologies $5s2f_4$, $5s2f_7$ and $5s2f_{10}$ contain heavy fields that couple only to other exotics in the diagram. (b) The UV diagrams associated with the $3s2f$ operator \mathcal{O}_{D21} . Only the last two diagrams can generate the operator under our model-building assumptions.

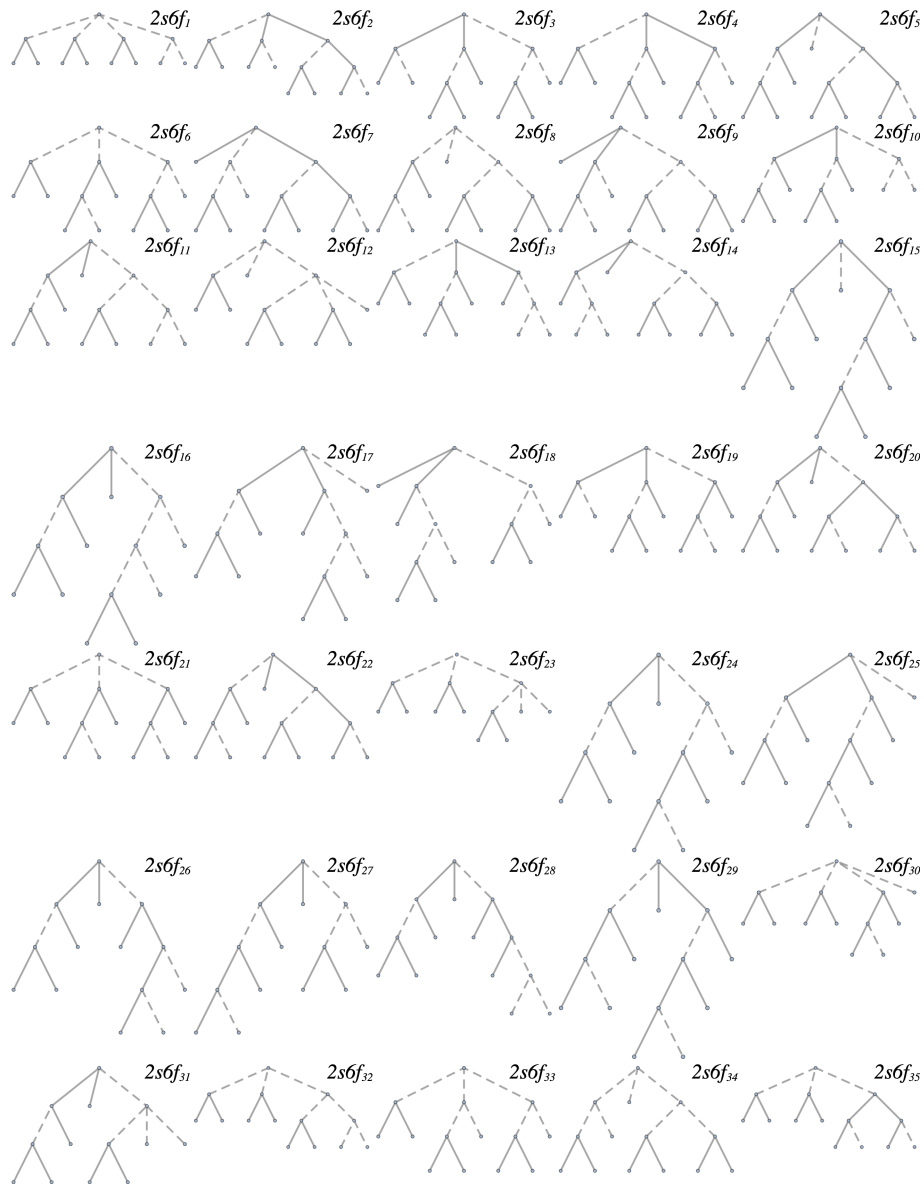


Figure 2.11: The tree-level topologies associated with the large class of $2s6f$ dimension-eleven operators in our listing. A number of graphs display the feature — less common at dimension nine — that an exotic field in the diagram couples only to other internal lines.

hierarchies acceptable, if necessary to render a mechanism dominant? What about exotic flavours or additional symmetries? Model filtering is the process of removing those models that, under some set of assumptions, do not provide the leading-order contribution to the neutrino mass. Our approach to filtering neutrino mass models is contrasted against other possible approaches below, and we also make more general comments about model filtering in other contexts. We mention that the following discussion of filtering is similar in intent to that of ‘genuineness’ in the loop-level matching paradigm [94–97]. We sometimes adopt this notation as well, and call models ‘genuine’ if they represent the dominant contribution to the neutrino mass.

Filtering criterion We begin by noting that model filtering is ubiquitous when considering tree-level effects. Here, the filtering criterion is unambiguously the operator dimension, since higher-dimensional operators are inevitably suppressed compared to lower-dimensional ones. With regard to the $\Delta L = 2$ EFT, such a dimension-focused criterion is useful for thinking about LNV scattering events, for example. As discussed in Sec. 2.4.1, the operator dimension is also a rough indication of the predicted neutrino-mass scale, and therefore has some utility in anticipating which models will dominate the neutrino mass.

We point out that this approach to model filtering allows for the immediate rejection of some models, already during the process of opening up the operator. This can happen, for example, when a contraction introduces an exotic particle transforming like a SM field. Taking \mathcal{O}_2 as an example, contractions like

$$\begin{aligned} \varphi^\dagger &\sim (1, 2, \frac{1}{2}) \\ L^i L^j L^k \bar{e} H^l \epsilon_{ij} \epsilon_{kl} &\rightarrow L^i L^k \tilde{\varphi}^j H^l \epsilon_{ij} \epsilon_{kl}, \end{aligned} \tag{2.37}$$

with $\tilde{\varphi}$ a second Higgs doublet, always imply that further contractions will produce seesaw fields, since the RHS of Eq. (2.37) has the same structure as the Weinberg operator. We note that for fermions the situation is more subtle because of the Lorentz structure. Specifically, although $H\bar{u}$ transforms like Q^\dagger under G_{SM} , the Lorentz transformation properties are different. The derivative contraction $(D^{\alpha\dot{\alpha}} H)\bar{u}_\alpha$ does transform like Q under $SU(2)_+ \otimes SU(2)_- \otimes G_{\text{SM}}$ and that makes a number of such contractions forbidden if one is interested in only dominant contributions according to the mass-dimension criterion. This is the same phenomenon as that seen in the paradigmatic opening of the derivative operator \mathcal{O}_{D3} given in Sec. 2.3.1, where an exotic field transforming like L [see Eq. (2.25)] lead to a similar Weinberg-like operator at an intermediate stage in the completion procedure. We note that this does not completely rule out exotic copies of SM fields featuring in radiative neutrino mass models. Using \mathcal{O}_2 again as an example:

$$\begin{aligned} \varphi^\dagger &\sim (1, 2, \frac{1}{2}) \\ L^i L^j L^k \bar{e} H^l \epsilon_{ij} \epsilon_{kl} &\rightarrow L^i L^j \tilde{\varphi}^k H^l \epsilon_{ij} \epsilon_{kl} \end{aligned} \tag{2.38}$$

is allowed, since the $SU(2)_L$ structure of this operator differs to that of the Weinberg operator. Similarly, vector-like quarks and leptons are extensively found in completions of both derivative and non-derivative operators after the filtering procedure, but their SM and Lorentz quantum numbers are interchanged with respect to their SM counterparts. For example, a particular completion of \mathcal{O}_{3a} is

$$\begin{array}{ccc} U \sim (3,1; \frac{2}{3}) & & \mathcal{S}_1^\dagger \sim (1,1,-1) \\ L^i L^j Q^k \bar{d} H^l \epsilon_{ij} \epsilon_{kl} \rightarrow L^i L^j U \bar{d} \epsilon_{ij} \epsilon_{kl} \rightarrow \mathcal{S}_1^\dagger U \bar{d}, \end{array} \quad (2.39)$$

which contains the vector-like quark $U + \bar{U}^\dagger$. Note however that U transforms like \bar{u}^\dagger under G_{SM} , but oppositely under the Lorentz group. It is true that \bar{U} , the vector-like partner of U , does transform like \bar{u} , but this plays no role in the operator.

Since we are most interested in radiative neutrino mass, a more direct and relevant filtering criterion in our case is the neutrino-mass estimate from the closure graph of the operator. This is the metric we use to compare and filter models in the results we present in Sec. 2.5. Whichever filtering criterion is chosen, the conditions for generating the lower-dimensional operator or the dominant neutrino self-energy graph still depend on the filtering philosophy.

Filtering philosophy The filtering criterion defines a hierarchy among the effective operators. If one is interested in tree-level effects, then operators of low dimension have a high priority in the sense that their effects are dominant over those of high-dimensional operators, whose influence is suppressed by additional powers of Λ . Similarly, the operators whose closure graphs imply large contributions to the neutrino mass have a higher priority than those implying small contributions.

One could take the view that it is sufficient for a subset of the field content associated with a completion of a high-priority operator to be present in that of a lower-priority one for it to be filtered out, even if the relevant diagrams depend on entirely different couplings and interactions. We call this perspective *democratic*, in the sense that it treats all allowed couplings and interactions fairly and ignores possible hierarchies in free parameters. A democratic approach would then filter out all completions of $\Delta L = 2$ operators of mass dimension larger than five containing one of the seesaw fields, for example, since these always imply a dominant contribution from the dimension-five Weinberg operator. Even if the same couplings are not present in both diagrams, there is no reason, on this view, for one coupling to be very much larger than another, making the tree-level contribution dominant.

An alternative approach might be to filter out only those completions that necessarily lead to subdominant contributions to the neutrino mass in all regions of parameter space. Naively it seems that neutrino-mass mechanisms involving different couplings would all survive the filtering process in this case, since the relative ordering of the

contributions from each diagram depends on the chosen values of the coupling constants. This is in general only guaranteed if a symmetry is recovered in the Lagrangian when one coupling is turned off, so that the forbidden coupling is not generated at some higher order in perturbation theory. We call this approach *stringent filtering*, since the conditions for removing a model are more difficult to satisfy.

For our results in Sec. 2.5 we take an intermediate view, leaning more towards the democratic side. We filter on the basis of particle content, but always keep track of the baryon-number assignment of the field. We then keep models with identical SM quantum numbers if the baryon-number assignments of the fields differ. With a concrete example, we treat $\zeta^{(\prime)} \sim (\bar{3}, 1, \frac{1}{3})$ in $x(L^i Q^j) \zeta^{\{kl\}} \epsilon_{ik} \epsilon_{jl}$ and $y(Q^i Q^j) \zeta'^{\{kl\}} \epsilon_{ik} \epsilon_{jl}$ as different fields.

In practice, we enumerate the completions of the operators in order of their estimated contribution to the neutrino mass. We associate a prime number with each exotic field encountered, including baryon-number as a distinguishing property. Models then correspond to products of prime numbers. As we explode each operator in order, we remove models from the list of completions if their characteristic number is divisible by that of any models already seen. In this way, we remove those mechanisms that are subdominant contributions to the neutrino mass in the democratic sense.

We emphasise that this procedure is not sufficient to fully ensure that the remaining models are genuinely dominant contributions to the neutrino mass. For example, it may be the case that the Weinberg operator is generated by loops of a subset of the exotic particles in one of our models. We are not sensitive to these models since we are concerned only with tree-level completions of the operators. One-loop contributions to the neutrino mass from heavy loops can be diagnosed easily on topological grounds. For example, topology T-3 of Ref. [102] will come about whenever the neutrinos in the diagram are connected by a single exotic fermion [240]. At two-loops, one could check the full gauge- and Lorentz-invariant Lagrangian for each model against Table 1 of Ref. [96], for example. We do not include this in our default filtering procedure, since it would require generating the full Lagrangian of each model. This is a computationally prohibitive task, especially since Table 2.2 suggests that the completions of some operators can contain up to six exotic fields. Should any model from our database be chosen for further study, the full Lagrangian can be generated with the functions in our example code and studied for the presence such heavy loops. We note that sometimes the presence of a heavy loop can be diagnosed from the neutrino self-energy graph, or even the tree-level topology, and we give a detailed example of such a case in Sec. 2.5.2. An additional filter on the models that goes beyond our initial tree-level filtering analysis is the possibility of exotic fields gaining vacuum expectation values. In this case, diagrams may exist that imply larger contributions to the neutrino mass than that suggested by our approach, and we are not sensitive to these since they generate exotic operators other than the Weinberg operator at the low scale. Examples are presented in Refs. [266, 267], where in both cases a two-loop completion of the Weinberg operator

also generates the exotic operator $LLH^\dagger\Theta_3$, where $\Theta_3 \sim (1, 4, \frac{3}{2})_S$.

We note that our model database [20] contains both the unfiltered completions of the operators in Table B.1, as well as the models filtered according to the above method. Our example code also includes functions for filtering on interactions rather than fields, and finding U(1) symmetries present in models' Lagrangians. Thus, the results presented in Sec. 2.5 and Table B.1 can be readily reproduced with alternative filtering criteria, philosophies or approaches.

2.5 Models

In this section we present the radiative models derived by exploding the $\Delta L = 2$ operators catalogued in Table B.1. We give an overview of the models, and explore their particle content and the effects of the partial model-filtering method we present in Sec. 2.4.2. We do not provide the entire listing of models here because there are very many, but instead give some examples. We point the interested reader to our database for the full searchable listing.

We distinguish the terms ‘model’ and ‘neutrino-mass mechanism’ or ‘ $\Delta L = 2$ Lagrangian’ in this section. By model we mean a collection of particle content. Those same multiplets may have many combinations of couplings that violate lepton-number by two units, leading to many neutrino-mass mechanisms, or $\Delta L = 2$ Lagrangians. We use the word ‘completion’ here to mean a neutrino-mass mechanism derived from a particular effective operator. Used in this way, the same $\Delta L = 2$ Lagrangian may be shared by two completions, but they correspond to the same model. We also remind the reader that we use the words ‘field’ and ‘multiplet’ interchangeably.

We note here that the following analysis does not include the dimension-eleven generalisation of the Weinberg operator \mathcal{O}_1''' , since the operator has an unwieldy number of topologies and the relevant tree-level completions have already been studied in the literature [103].

2.5.1 Overview

The models are generated by running the algorithm summarised in Sec. 2.3.2, as found in our example code, on our catalogue of the $\Delta L = 2$ operators. The results for the number of completions before and after filtering are presented in Table B.1. In the language of Sec. 2.4.2, we use the democratic filtering procedure with the neutrino-mass scale as the filtering criterion for these data. We note again that this leaves us with an overestimate of the actual number of genuine neutrino-mass models. Even so, one can see that 54 operators end up with no completions after filtering, ruling them out as

possibly playing a dominant role in generating the neutrino masses, at least according to our model-building assumptions. The complete list of unfiltered $\Delta L = 2$ Lagrangians and tree-level completion diagrams is compiled in our database, and the documentation provides information for how to perform different kinds of filtering on the models.

The database contains 430,810 inequivalent $\Delta L = 2$ Lagrangians before filtering. Counted democratically (*i.e.* by particle content) these correspond to 141,989 unfiltered models. Of the distinct Lagrangians, only around 3% (11,483) survive democratic filtering with the neutrino-mass criterion. This corresponds to 11,216 distinct models. In our filtering analysis we also incorporate information from the one-loop study of the Weinberg operator¹¹ done in Ref. [95]. We generate a listing of the models from Tables 2 and 3 of Ref. [95] with hypercharges that are multiples of $1/6$ in the range $[-3, 3]$ and ranges for the $SU(3)_c$ and $SU(2)_L$ representations that cover those of the exotic fields featuring in our models. We remove the completions in our listing that contain a subset of these fields and imply neutrino masses suppressed by more than one loop factor, since the models presented in Ref. [95] generate the Weinberg operator at one loop.

We visualise the number of models with democratic and no filtering in Fig. 2.12 broken down by mass dimension. After filtering there are three models at dimension five, 16 models at dimension seven, 244 models at dimension nine and 10,969 models at dimension eleven¹². It is clear that the number of filtered neutrino-mass models grows with operator dimension, which is perhaps unintuitive. For any high dimensional operator, there are competing effects influencing the number of viable completions. First, the large number of models derived already from lower-dimensional operators means that the chances some model will be filtered out are larger. Second, high dimensional operators involve more fields, meaning that there are more combinations of contractions that can be made, and therefore more completions expected. Despite the increased filtering odds, evidently the combinatorial explosion of different models wins.

In Fig. 2.13 we present data relevant to the number of fields present in the models. Fig. 2.13a shows the number of exotic scalars and fermions present in the completions. Despite the fact that the UV topologies associated with some derivative operators allow completions containing no scalars, we find that only the Weinberg-like operators keep their fermion-only models after the democratic filtering procedure. By far the most common kinds of models contain five heavy fields, especially three fermions and two scalars, or two fermions and three scalars. This is due to the fact that, as is clear from Fig. 2.12, most of the models generate dimension-eleven operators. In Fig. 2.13b we show the estimated new-physics scale Λ against the number of fields featuring in the models. With the exception of one model with two fields, those required to lie at

¹¹We anticipate the number of models in our database generating the Weinberg operator with exotic loops at higher-loop order to be small. Such models would need to contain upwards of four exotic fields, and it becomes increasingly less likely that a model will contain a subset of these fields to be filtered out.

¹²We note that the sum of these numbers is not 11,216 since one model can generate multiple operators of different mass dimension in a way consistent with our neutrino-mass filtering criterion.

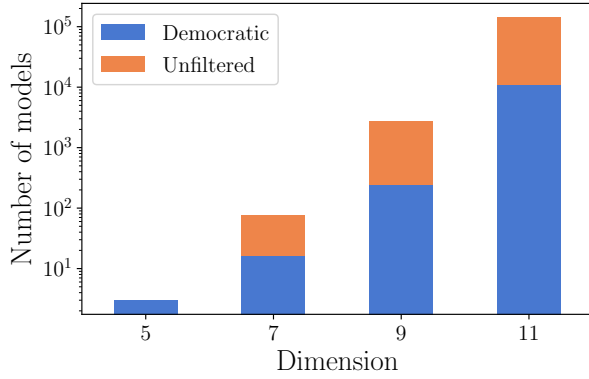


Figure 2.12: The bar chart shows the number of distinct Lagrangians derived from operators of different mass dimension. The orange bars show the number of distinct unfiltered models. The blue bars show the number after democratic filtering. The number of filtered completions grows with mass dimension.

collider-accessible energies contain three or more fields. Models with few fields that imply suppressed neutrino masses, or equivalently a low new-physics scale, have a kind of selection pressure acting against them: since there are few fields, it is likely they will arise in the completion of other operators, that generally will filter out the former and imply a larger value of Λ . At dimension-seven, for example, \mathcal{O}_8 is generated by models featuring two fields and predicts that these should not be heavier than about 15 TeV. However, of its four tree-level completions, only one survives the filtering procedure. This is the outlier two-field model evident in the figure. It was first derived¹³ in Ref. [101] and later in Ref. [104]. The model contains the fields $\Pi_1 \sim (3, 1, \frac{1}{6})_S$ and $Q_7 \sim (3, 2, \frac{7}{6})_F$. We list the models containing three exotic fields that are required to lie below 100 TeV in Sec. 2.5.2.

Of the unfiltered 430,810 models, close to 67% (290,492) contain at least one of the seesaw fields: $N \sim (1, 1, 0)_F$, $\Xi_1 \sim (1, 3, 1)_S$ or $\Sigma \sim (1, 3, 0)_F$. We present the exact breakdown by the interactions involved in the models in Table 2.3. These are by far the most common fields appearing in the list of unfiltered models. Since our default filtering philosophy in this analysis is democratic, all of these are absent from the filtered list of models, and they only appear in completions of the Weinberg operator and \mathcal{O}_{D2} .

The distinct exotic fields appearing in the completions number 171, although five fields are completely removed following filtering. These are $(\bar{6}, 1, \frac{7}{6})_S^{1/3}$, $(\bar{6}, 3, \frac{5}{3})_S^{1/3}$, $(1, 3, 3)_S^0$, $(1, 5, 2)_F^0$ and $(\bar{6}, 1, \frac{5}{3})_S^{1/3}$, where the superscript represents the B assignment of the field. There are 83 different scalar fields and 83 different fermion species. We

¹³We note that the other completion of \mathcal{O}_8 listed in Ref. [101] also generates \mathcal{O}_{50a} through a diagram which dominates the neutrino mass.

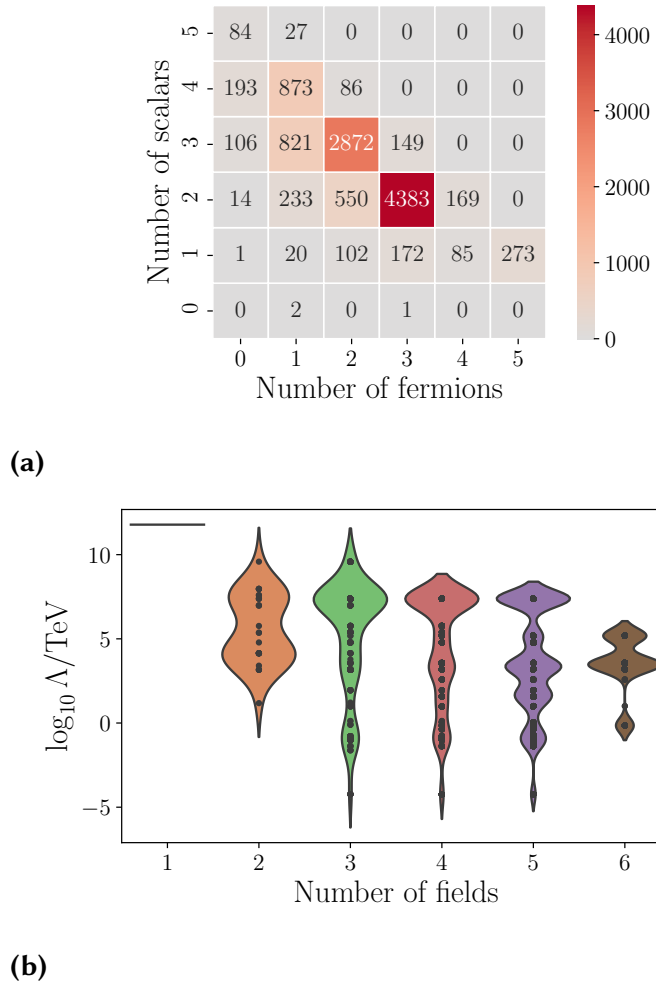


Figure 2.13: (a) The number of filtered models containing different numbers of exotic scalar and fermion fields. Most models contain five fields, with the most common combination being three fermions and two scalars. The fermion-only models are associated only with Weinberg-like operators. (b) The rough upper bound on the new-physics scale Λ shown against the number of exotic fields introduced in the models. The black dots show the upper bound on the scale of the new physics for each model. A given black dot generally denotes more than one model. Each strip is a smoothed histogram of the number of models having a given Λ as the new-physics upper bound for the specified number of fields. A sizeable class of models are testable at current or future collider experiments.

Field	Interactions	$\Delta L = 2$ Lagrangians	Models
$N \sim (1, 1, 0)_F$	LHN	51,245 (11.9%)	17,139 (17.1%)
	Other	12,433 (2.9%)	
$\Sigma \sim (1, 3, 0)_F$	$LH\Sigma$	87,535 (20.3%)	31,629 (31.5%)
	Other	28,157 (6.5%)	
$\Xi_1 \sim (1, 3, 1)_S$	$LL\Xi_1$	59,791 (13.0%)	51,576 (51.4%)
	$HH\Xi_1^\dagger$	95,410 (22.1%)	
	Both	10,323 (2.4%)	
	Other	30,761 (7.1%)	

Table 2.3: The table shows the number of unfiltered models in which the seesaw fields appear. The category ‘other’ includes interactions such as $L\varphi N$, where one of the SM fields in the interaction has been replaced with an exotic copy, as well as couplings involving other exotic fields whose quantum numbers are unrelated to those of SM fields.

distinguish three broad classes of scalars on the basis of their interaction with the SM fermions: leptoquarks, diquarks and dileptons. For exotic fermions we differentiate between those arising from contractions between the Higgs and a SM quark (vectorlike quarks), and the Higgs and a SM lepton (vectorlike leptons). The relative frequencies with which these field classes appear in the filtered completions are shown in Fig. 2.14 as pie charts. The wedges represent the number of Lagrangians in which the field couples as a leptoquark, diquark, dilepton, vectorlike quark or vectorlike lepton. We label fields coupling in all other ways as ‘other’ in the figure. The most represented family of scalars are leptoquarks, with the most common field being $\Pi_7 \sim (3, 2, \frac{7}{6})_S$, commonly called R_2 in the literature [268]. This leptoquark appears in simplified models of $R_{D^{(*)}}$ and the neutral-current flavour anomalies like $R_{K^{(*)}}$, see e.g. Refs. [220, 222, 266, 269, 270]. It was recently shown to be able to reconcile the discrepant measurements in the anomalous magnetic moments of both the muon and the electron [271, 272]. The second most common scalar appearing in our neutrino-mass models is $\zeta \sim (3, 3, \frac{1}{3})_S$, frequently referred to as S_3 . This leptoquark is a popular explanation of the neutral-current $b \rightarrow s$ anomalies such as $R_{K^{(*)}}$, see e.g. [222, 273–276]. The most frequently encountered fermions are vectorlike quarks, with the most common being $T_2 \sim (3, 3, \frac{2}{3})_F$. It contains components that mix with both the up- and down-type SM quarks. We emphasise that the plots and numbers presented here are directly related to our filtering and model-counting conventions. In Fig. 2.14 for example, we do not count fields just by their quantum numbers, but also include coupling information as discussed above. Additionally, we count independent Lagrangians as different models rather than just counting distinct sets of fields, which is perhaps more in line with our ‘democratic’ approach to filter-

ing. We note that the qualitative features discussed here are all relatively robust against these different conventions. We encourage the interested reader to explore our model database to see how different approaches to filtering and counting can answer specific questions they may have of the data.

We are also interested in the connectivity between fields as they feature in the models. To explore this we study a graph in which each vertex represents one of the 163 exotic fields introduced in the completions that contain at least two fields, and an edge is drawn between fields featuring together in a model. The graph is shown in Fig. 2.15. The exterior sectors at each node represent the number of degree of the node. The edges in the graph are weighted by the number of times the corresponding pair of fields appears in the models; this is shown with a linear colour scaling in the figure. There are 3036 edges in the graph, and the average node degree is approximately 37. About a fifth of all possible connections in the graph are realised. The ten most heavily weighted edges, representing the ten most common pairs of fields appearing in the models, are shown in Table 2.4. Many of these correlations can be understood on the basis of common contractions in the derivation of the models, especially those involving H or L . There is a propensity for scalars and fermions with the same gauge quantum numbers to appear in models together. This seems to come about from the fact that $H \otimes L$ is a gauge singlet but transforms like $(2, 1)$ under $SU(2)_+ \otimes SU(2)_-$. We note that all of the fields in the table have $|B| = \frac{1}{3}$, and so this edge cannot come about from $(3, 2, \frac{5}{6})_F \otimes \bar{d} \sim (3, 2, \frac{7}{6})_S$.

2.5.2 Example models

In this section we present some example neutrino-mass models, illustrating use cases of the model database, aspects to be careful of in its use, and representative features of the novel models derived from dimension-eleven and dimension-nine operators.

Simple models at the TeV scale

We are particularly interested in models that are simple, in the sense that they involve few exotic fields, and testable, in that they predict new physics at currently or nearly accessible energy ranges. We query our model database to return models featuring three fields or fewer with the estimated upper bound on the new-physics scale required to be between 700 GeV and 100 TeV. The results of the query are presented in Table 2.5. There are twelve¹⁴ models listed, only one of which has explicitly appeared before in the

¹⁴We note that there are technically more models: those for which the colour-sextet fields in Table 2.5 are replaced with colour triplets, with a corresponding baryon-number assignment such that the same interactions as the sextet are picked out.

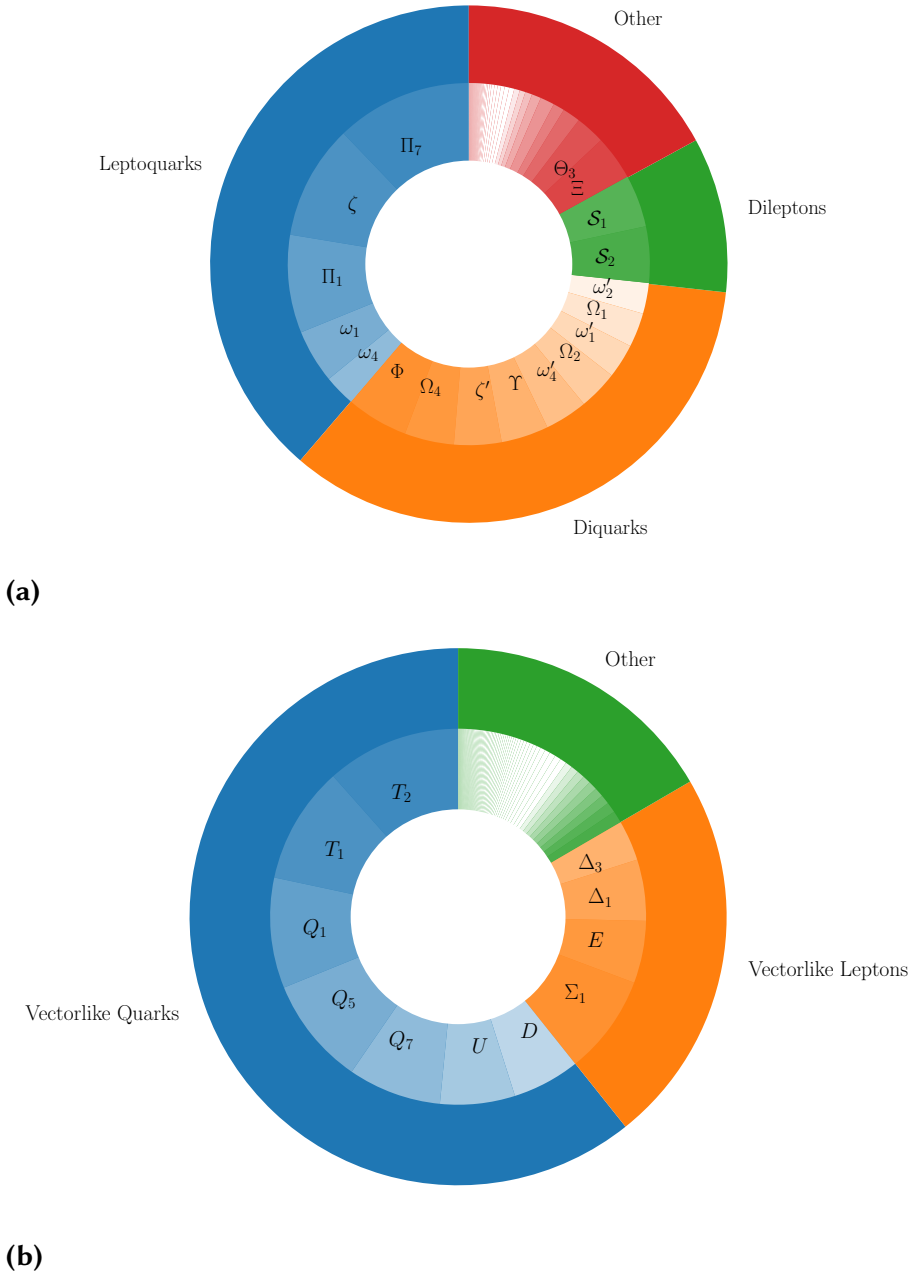


Figure 2.14: The number of models in which each field appears in the completions shown as a pie chart for scalars and fermions separately. The exotics are distinguished by their couplings to SM fields. (a) The pie chart of scalar fields appearing in the completions. Primed fields represent leptoquarks whose baryon-number assignment allows only the diquark couplings. (b) The pie chart of fermion fields appearing in the completions. See Table A.2 or Ref. [22] for the convention used for the field names.

Rank	Edge
1	$(3, 3, \frac{2}{3})_F, (3, 4, \frac{1}{6})_S$
2	$(3, 2, \frac{1}{6})_S, (3, 2, \frac{1}{6})_F$
3	$(3, 3, \frac{2}{3})_S, (3, 2, \frac{7}{6})_S$
4	$(3, 2, \frac{7}{6})_F, (3, 2, \frac{1}{6})_S$
5	$(3, 3, \frac{2}{3})_F, (3, 4, \frac{7}{6})_F$
6	$(\bar{3}, 3, \frac{1}{3})_S, (3, 4, \frac{1}{6})_S$
7	$(3, 2, \frac{1}{6})_F, (3, 3, \frac{2}{3})_S$
8	$(\bar{3}, 3, \frac{4}{3})_F, (\bar{3}, 2, \frac{5}{6})_F$
9	$(3, 2, \frac{1}{6})_S, (3, 3, \frac{2}{3})_S$
10	$(3, 2, \frac{7}{6})_S, (\bar{3}, 2, \frac{5}{6})_F$

Table 2.4: The table shows the pairs of fields that most often appear together in the filtered completions of the $\Delta L = 2$ operators we consider. In the context of the graph of field connections introduced in the main text, these are the top ten edges by edge weight. Many of the connections can be understood on the basis of common couplings to SM fields, especially L and H . For example, $(3, 3, \frac{2}{3})_F \otimes L \sim (3, 4, \frac{1}{6})_S$ and $(3, 3, \frac{2}{3})_S \otimes H \sim (3, 2, \frac{7}{6})_S$. All of the fields in the table have $|B| = \frac{1}{3}$.

literature to our knowledge: the completion of \mathcal{O}_8 discussed in Sec. 2.5.1. It is interesting to note that the scalar leptoquark¹⁵ $\Pi_1 \sim (3, 2, \frac{1}{6})_S$ appears in almost every model listed in the table. This suggests that our general analysis of the frequency of fields appearing in the completions in Sec. 2.5.1 may look different if specific selection criteria are placed on the data. We have checked the full Lagrangians implied by the field content of each model and found that seven of the models listed in the table imply the generation of the Weinberg operator through heavy loops. We emphasise that these non-genuine completions are potentially interesting and new radiative models, although the neutrino self-energy diagram will look different to that implied by the closure of the tree-level graph from which the model was derived. This means that the bound on the implied new-physics scale is in general higher than that suggested by the closure of the original operator. In this class are all of the models for which the upper bound on the new-physics scale is larger than 15 TeV. This means that there are only five models in our database with fewer than four fields for which the upper bound on Λ is between 700 GeV

¹⁵We mention parenthetically that although this leptoquark does not possess diquark couplings, baryon-number violation does occur through a term in the scalar potential. The leading-order contribution is through a dimension-ten operator mediating $p \rightarrow \pi^+ \pi^+ e^- v v$ [277].

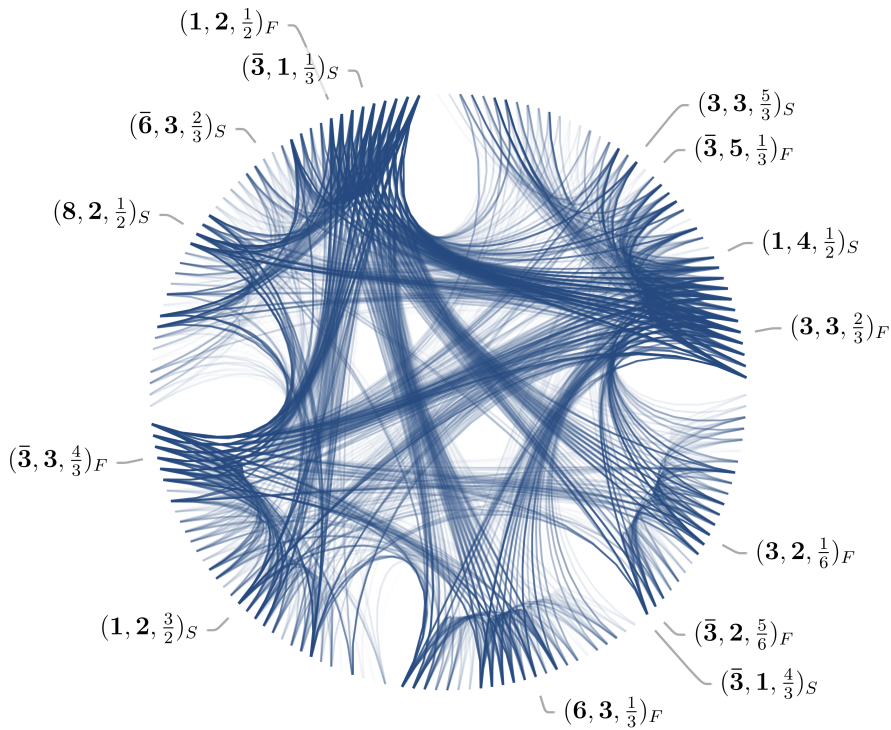


Figure 2.15: The graph is a representation of the connectivity between exotic fields in the neutrino-mass models. Each node represents an exotic field and edges connect fields featuring together in a neutrino-mass model. The colour is an indication of the weight of the edge, *i.e.* the number of times the two nodes appear in models together. The graph is clustered into roughly five communities within which there are many mutual connections. Only a handful of node labels are shown.

and 100 TeV, and they all predict new physics below 15 TeV. In the following we present two example models from the table:

1. We look at one of the models—the one derived from \mathcal{O}_{62b} —that generates the Weinberg operator through a heavy loop. We intend this to be an example of how this phenomenon can appear and how it is easy to diagnose in some cases.
2. We present a brief study of the implications for neutrino mass implied by the model given in the last row.

Model derived from \mathcal{O}_{62b} The model derived from \mathcal{O}_{62b} is especially simple since it does not require the imposition of $U(1)_B$. The exotic fields introduced are $\Delta_1 \sim (1, 2, \frac{1}{2})_F$, $\mathcal{S}_1 \sim (1, 1, 1)_S$ and $\chi \sim (1, 2, \frac{3}{2})_S$. The additional interaction Lagrangian

Field content	Operators	Λ [TeV]	Dominant?
$(3, 2, \frac{1}{6})_S, (3, 2, \frac{7}{6})_F$	$8, D15$	15	Y
$(1, 2, \frac{1}{2})_F, (1, 1, 1)_S, (1, 2, \frac{3}{2})_S$	$62b$	16	N
$(3, 2, \frac{5}{6})_S, (3, 2, \frac{1}{6})_F, (3, 2, \frac{1}{6})_S$	$8'$	1	N
$(3, 1, \frac{1}{3})_S, (\bar{6}, 2, \frac{1}{6})_S, (3, 2, \frac{1}{6})_F$	$24f$	89	N
$(\bar{3}, 3, \frac{1}{3})_F, (\bar{6}, 2, \frac{1}{6})_S, (3, 2, \frac{1}{6})_S$	$24d$	89	N
$(3, 2, \frac{5}{6})_S, (1, 2, \frac{3}{2})_F, (3, 2, \frac{1}{6})_S$	$8'$	1	N
$(\bar{3}, 3, \frac{1}{3})_F, (\bar{6}, 4, \frac{1}{6})_S, (3, 2, \frac{1}{6})_S$	$24f$	89	N
$(\bar{3}, 1, \frac{1}{3})_F, (\bar{6}, 2, \frac{1}{6})_S, (3, 2, \frac{1}{6})_S$	$24d$	89	N
$(\bar{6}, 2, \frac{7}{6})_F, (\bar{8}, 2, \frac{1}{2})_S, (3, 2, \frac{1}{6})_S$	20	0.8	Y
$(\bar{6}, 1, \frac{4}{3})_S, (\bar{6}, 1, \frac{1}{3})_F, (3, 2, \frac{1}{6})_S$	20	0.8	Y
$(\bar{6}, 2, \frac{5}{6})_S, (3, 2, \frac{1}{6})_F, (3, 2, \frac{1}{6})_S$	$50a, b$	10	Y
$(\bar{6}, 2, \frac{1}{6})_S, (\bar{3}, 2, \frac{5}{6})_F, (3, 2, \frac{1}{6})_S$	$50a, b$	10	Y

Table 2.5: The table shows the models in our filtered list that contain fewer than four fields with the estimate of the upper-bound on the new-physics scale Λ in the range $700 \text{ GeV} < \Lambda < 100 \text{ TeV}$. Models containing colour sextet fields can be replaced with the corresponding colour-triplet fields with a different baryon-number assignment. The fields and models are listed in no special order. The scalar lepto-quark $\Pi_1 \sim (3, 2, \frac{1}{6})$ appears in almost all of the models listed. Completions marked as non-dominant may be viable and interesting neutrino-mass models, but the main contribution to the neutrino mass does not come from the closure of the tree-level diagram from which the particle content was derived. This means, among other things, that the upper bound on the scale of the new physics associated with the model will differ to that presented here.

necessary to generate \mathcal{O}_{62b} at tree level is $\Delta\mathcal{L} = \mathcal{L}_Y - \mathcal{V}$, with

$$-\mathcal{L}_Y = m_{\Delta_1} \bar{\Delta}_1 \Delta_1 + x_{[rs]} L_r^i L_s^j \mathcal{S}_1 \epsilon_{ij} + y_r \bar{e}_r \bar{\Delta}_1^i \tilde{H}^j \epsilon_{ij} + z_r \bar{e}_r \tilde{\chi}^i \Delta_1^j \epsilon_{ij}, \quad (2.40)$$

$$\mathcal{V} = m_{\mathcal{S}_1}^2 \mathcal{S}_1^\dagger \mathcal{S}_1 + m_\chi^2 \chi^\dagger \chi + w H^i \chi^j \mathcal{S}_1^\dagger \mathcal{S}_1 \epsilon_{ij}. \quad (2.41)$$

This implies that the neutrino-mass mechanism depends on 13 new parameters: nine Yukawa couplings, w and the three masses; although there are a much larger number of terms present in the full Lagrangian of the model. Importantly, one of these is $x'_r L_r^i \bar{\Delta}_1^j \mathcal{S}_1 \epsilon_{ij}$, which we now show is sufficient to generate the Weinberg operator through a two-loop diagram containing one heavy loop.

The tree-level completion diagram and the neutrino-mass diagram relevant to the model are shown in Fig. 2.16. There are two- and three-loop neutrino self-energies, where the three-loop models arise by connecting the H and H^\dagger lines in Fig. 2.16b in all possible ways. In this case, the first part of the fermion line (highlighted in Fig. 2.16b) can be replaced with the aforementioned $L \bar{\Delta}_1 \mathcal{S}_1$ vertex so that the left loop contains only \mathcal{S}_1 , χ and the Dirac fermion $\Delta_1 + \bar{\Delta}_1^\dagger$. (It can also be noticed from the tree-level opening in Fig. 2.16a that the Δ_1 line can be connected directly to one of the $LL\mathcal{S}_1$ vertices, giving rise to a loop-level completion of \mathcal{O}_2 .) This heavy-loop neutrino-mass diagram, although interesting in its own right, predicts a different mass-scale for the exotic fields (roughly 10^6 TeV), and a different structure for the neutrino-mass matrix.

A genuine low-scale model Below we present a brief exploration of the model derived from \mathcal{O}_{50} that contains the exotic fields $\phi \sim (6, 2, -\frac{1}{6})_F$, $\Pi_1 \sim (3, 2, \frac{1}{6})_S$ and $Q_5 \sim (3, 2, -\frac{5}{6})_F$. The estimate for the neutrino mass derived from the operator closure suggests this model's exotic particle content should live roughly below 10 TeV. The corresponding $\Delta L = 2$ Lagrangian we write again as $\Delta\mathcal{L} = \mathcal{L}_Y - \mathcal{V}$, with

$$-\mathcal{L}_Y = x_{rs} L_r^i \bar{d}_{sa} \Pi_1^{aj} \epsilon_{ij} + y_r \phi^{\{ab\}i} \bar{u}_{ra} \bar{Q}_{5b}^j \epsilon_{ij} + z_r \bar{d}_{ra} H^i Q_5^{aj} \epsilon_{ij} + \text{h.c.} \quad (2.42)$$

$$\mathcal{V} = \lambda \tilde{\Pi}_{1a}^i \tilde{\Pi}_{1b}^j \phi^{\{ab\}k} H^l (\epsilon_{ik} \epsilon_{jl} + \epsilon_{il} \epsilon_{jk}). \quad (2.43)$$

We note that $U(1)_B$ must be imposed on the Lagrangian to prevent terms like $\Pi_1^3 H^\dagger$, $|\phi|^2 \phi^\dagger \Pi_1$ and $|\Pi_1|^2 \Pi_1 \phi$ that destabilise the proton in the presence of the Yukawa interactions of Eq. (2.42). The field ϕ only couples to SM fermions together with Q_5 in this model, and so it generates no dimension-six operators at tree level. The completion graph and one of the neutrino self-energy diagrams are shown in Fig. 2.17. The tree-level topology is again $2s6f_4$, and the neutrino masses are realised at three and four loops, with the additional loop arising from the connection of an H and H^\dagger . One of the loops involves a W boson, and so the diagram does not fit into existing topological classifications. The three-loop diagram is similar to the topology D_9^M of Ref. [97], with one of the scalar lines replaced with a vector boson. The W boson line must connect to Q in

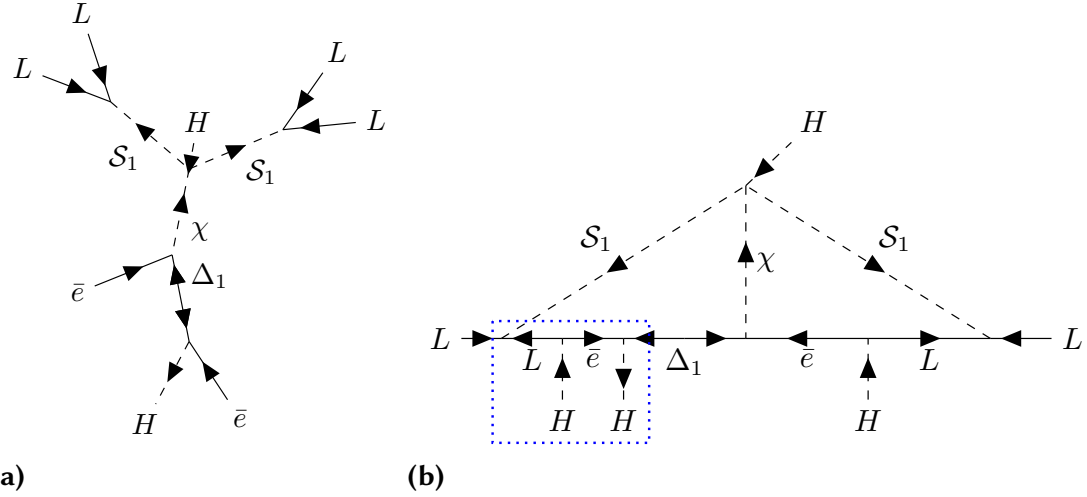


Figure 2.16: (a) The furnishing of the tree-level topology, labelled $2s6f_4$ in our scheme, that generates \mathcal{O}_{62b} at tree level. The interactions allowed in the theory are such that the Δ_1 line can be connected straight into one of the LLS_1 vertices in place of an L , leading to a loop-level completion of \mathcal{O}_2 . (b) The neutrino self-energy diagram relevant to the non-genuine completion of \mathcal{O}_{62b} . It is clear that this diagram does not represent the dominant contribution to the neutrino mass, since the highlighted collection of fields can be replaced with the interaction $\bar{\Delta}_1 L S_1$. This leads to a diagram with heavy loop involving Δ_1 , χ and S_1 , which dominates the neutrino masses. In both cases, the relevant topology is CLBZ-7 in the classification of Ref. [96].

the diagram, but could end on any field with non-trivial $SU(2)_L$ charge. The connection to the L line is shown, since the loop integral then depends on leptonic flavour indices, which can change the structure of the neutrino-mass matrix. There are also several ways of connecting the Higgs lines and only one combination is shown in the figure. The four-loop diagrams will be the dominant contribution to the neutrino masses for exotic fields above $4\pi v \approx 2$ TeV.

The neutrino-mass matrix in this model can be estimated as

$$[\mathbf{m}_\nu]_{rs} = \frac{\lambda g^2}{(16\pi^2)^3} \left(\frac{v^2}{\Lambda^2} + \frac{1}{16\pi^2} \right) \frac{1}{\Lambda} \sum_{t,u,v} x_{rt} z_t^* y_u^* [\mathbf{m}_u]_u V_{uv} [\mathbf{m}_d]_v x_{sv} I_{rstuv} + (r \leftrightarrow s), \quad (2.44)$$

where the V_{rs} are CKM matrix elements, Λ is the generic UV scale, and I_{rstuv} is the loop function. The dependence on the masses of the up- and down-type quarks implies that the largest contributions to the neutrino masses will come from loops containing top and bottom quarks. If the parameters $y_{1,2}$, x_{r1} and x_{r2} play no significant role in the physics of neutrino mass, then the matrix will have rank 1 if the loop function carries no leptonic flavour indices. It may be the case that an additional generation of Q_5 , ϕ or

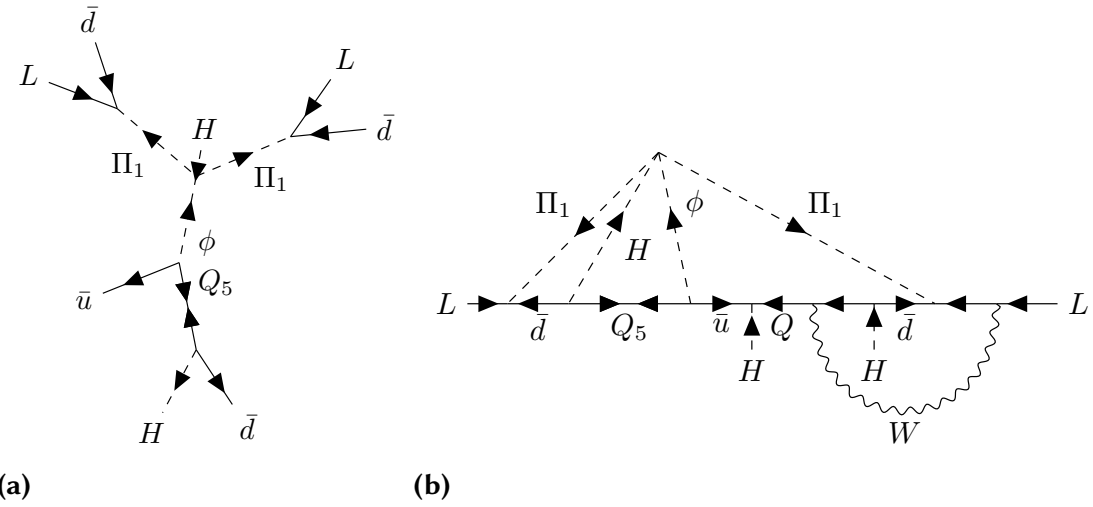


Figure 2.17: (a) The tree-level completion diagram for the model derived from exploding \mathcal{O}_{50} and discussed in the main text. The topology is $2s6f_4$ in our classification scheme. The closure involves an arrow-preserving loop connecting the \bar{d}^\dagger to one of the \bar{d} lines, and the W -boson closure motif discussed in Sec. 2.4.1. (b) One of the neutrino-mass diagrams relevant to the model derived from \mathcal{O}_{50} . There is a three-loop diagram with the H line broken into an H^\dagger, H pair that generates the dimension-seven generalised Weinberg operator. The four-loop diagrams all involve connecting the H^\dagger to each of the three H legs in the diagram. There are also multiple places the W could end in the diagram, although it must couple to the Q line. The four-loop diagrams will give larger contributions to the neutrino mass than the three-loop diagrams for $\Lambda \gtrsim 2$ TeV.

Π_7 is therefore required for the model to successfully reproduce the measured pattern of neutrino masses and mixings.

A model derived from a derivative operator

We move on to discuss a model generating the single-derivative dimension-nine operators $\mathcal{O}_{D10a,b,c}$. The estimated upper-bound on the exotic scale is close to 1.5×10^3 TeV in this case. The model contains the fields $\rho \sim (1, 2, \frac{3}{2})_S$, $Q_5 \sim (3, 2, \frac{5}{6})_F$ and $\Sigma_1 \sim (1, 3, 1)_F$. Such two-fermion–one-scalar models are unique to completions of single-derivative operators at dimension nine.

The part of the Lagrangian relevant to lepton-number violation is

$$-\Delta\mathcal{L} = x_r L_r^i \Sigma_1^{\{jk\}} H_k^\dagger \epsilon_{ij} + y_r L_r^i \rho^j \bar{\Sigma}_1^{\{kl\}} \epsilon_{ik} \epsilon_{jl} + z_r \bar{d}_r a H^i Q_5^{aj} \epsilon_{ij} + w_r \bar{u}_r a \rho^i Q_5^{aj} \epsilon_{ij} + \text{h.c.} \quad (2.45)$$

The only additions to the scalar potential are the expected $|\rho|^2 |H|^2$ and $|\rho|^4$ terms, and

these play no role in the lepton-number violation. Notably, there are no Yukawa couplings involving \bar{Q}_5 , and the field ρ generates no dimension-six operators at tree-level, since the naively expected coupling $H^i H^j H^k \rho_k \epsilon_{ij}$ vanishes. The model also has the nice feature that no baryon-number violating interactions are present.

The tree-level completion diagram and one of the neutrino-mass diagrams are shown in Fig. 2.18. The completion diagram has topology $2s4f_8$, which requires one of the heavy fermions to have an arrow-preserving propagator. The neutrino-mass diagram shown is cocktail-like [278], although there are also two-loop diagrams generating \mathcal{O}'_1 at the low scale, as well as other diagrams with the W and H lines in different places. The topology of the neutrino self-energy diagram is similar to D_{15}^M in Ref. [97].

The flavour structure of the neutrino-mass matrix has the approximate form

$$[\mathbf{m}_\nu]_{rs} = \frac{g^2}{(16\pi^2)^3} \frac{1}{\Lambda} \sum_{t,u} y_r x_s w_t^* z_t [\mathbf{m}_d]_t V_{ut} [\mathbf{m}_u]_u I_{rstu} + (r \leftrightarrow s). \quad (2.46)$$

The dependence on the up- and down-type mass matrices, as in the example presented in Sec. 2.5.2, means that the couplings $w_{1,2}$ and $z_{1,2}$ will not play an important role in generating the observed pattern of neutrino masses and mixings. In this case the matrix has at least rank 2, even if the leptonic-flavour structure of the loop integrals I_{rstu} is flat. Thus, the structure of the neutrino masses and mixing parameters emerges mostly from the six parameters x_r and y_r .

A model of neutrino mass and the flavour anomalies

Here we present a model designed specifically to generate a particular set of dimension-six operators. The example is motivated by the flavour anomalies, discussed in detail in Sec. 1.4. In the following we adhere to the conventions¹⁶ of Ref. [115] relevant to the Warsaw basis for the SMEFT and the flavio basis [279] for the Weak Effective Theory (WET). The leptoquarks $\omega_1 \sim (\bar{3}, 1, \frac{1}{3})_S$ and $\Pi_7 \sim (3, 2, \frac{7}{6})_S$ can provide an explanation of the anomalies in $R_{D^{(*)}}$ with contributions to the SMEFT operators

$$[C_{lequ}^{(1)}]_{3332} = \begin{cases} -4[C_{lequ}^{(3)}]_{3332} & \text{for } \omega_1 \\ 4[C_{lequ}^{(3)}]_{3332} & \text{for } \Pi_7 \end{cases}, \quad (2.47)$$

since they have Yukawa couplings to left- and right-handed SM fields. [We note that Eq. (2.47) holds at the high scale, and the relation between the operators is altered by running.] The Yukawa terms are

$$-\mathcal{L}_{\omega_1} = f_{rs} L_r Q_s \omega_1 + g_{rs} \bar{e}_r^\dagger \bar{u}_s^\dagger \omega_1 + \text{h.c.} \quad (2.48)$$

$$-\mathcal{L}_{\Pi_7} = x_{rs} L_r \bar{u}_s \Pi_7 + y_{rs} \bar{e}_r^\dagger Q_s^\dagger \Pi_7 + \text{h.c.} \quad (2.49)$$

¹⁶These can be accessed easily at <https://flav-io.github.io/docs/operators.html>.

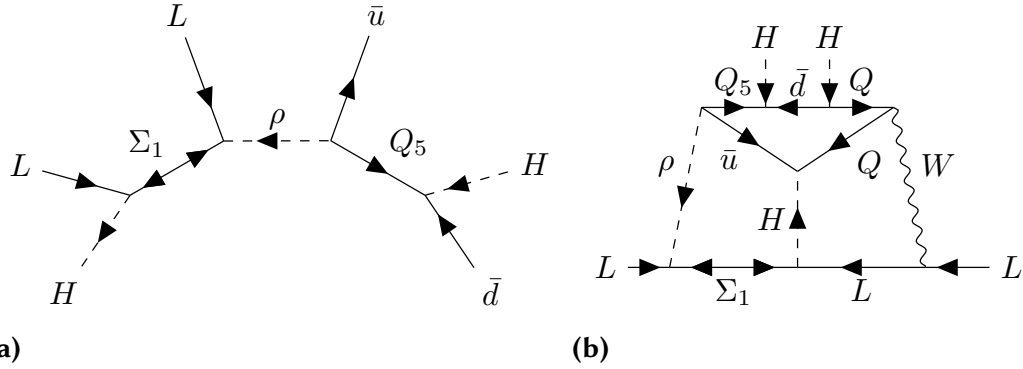


Figure 2.18: (a) The tree-level completion diagram for the model that generates the single-derivative operators $\mathcal{O}_{D10,a,b,c}$ and discussed in the main text. The topology is $2s4f_8$ in our classification scheme. This class of topologies is only relevant to single-derivative operators, and contains an arrow-preserving fermion propagator, that of Q_5 in the diagram. The closure of the diagram involves a W -boson loop, similar to that required in Fig. 2.17. (b) One of the neutrino-mass diagrams relevant to the model generating $\mathcal{O}_{D10,a,b,c}$. The diagram generates the Weinberg operator as drawn, but additional diagrams exist with the central H line cut into an H, H^\dagger pair that generate \mathcal{O}'_1 instead. These diagrams will only be relevant for exotic masses less than about 2 TeV. Additional three-loop diagrams exist in which the Higgs coming from the $\Sigma_1 LH^\dagger$ interaction loops into any of the other external H fields. The W boson must connect to the Q line, but could end on any other field with non-trivial $SU(2)_L$ charge. The topology is cocktail-like [278], and resembles D_{15}^M in Ref. [97].

and these imply

$$[C_{lequ}^{(1)}]_{3332} = \begin{cases} \frac{f_{33}g_{32}^*}{2m_{\omega_1}^2} & \text{for } \omega_1 \\ \frac{x_{32}^*y_{33}}{2m_{\Pi_7}^2} & \text{for } \Pi_7 \end{cases} \quad (2.50)$$

at tree level. A satisfactory explanation of $R_{D^{(*)}}$ requires $\mathcal{O}(1)$ couplings, e.g. [2, 266], and for Π_7 fits are consistent with the operator coefficient being purely imaginary, e.g. [222].

The $b \rightarrow s$ data can be explained by the tree-level exchange of the leptoquark $\zeta \sim (3, 3, \frac{1}{3})_S$, which generates

$$[C_{lq}^{(1)}]_{2223} = 3[C_{lq}^{(3)}]_{2223}, \quad (2.51)$$

relevant for the neutral-current anomalies. We saw in Sec. 1.4.1 that fits are performed to the four-fermion operators $C_9^{bs\mu\mu}$ and $C_{10}^{bs\mu\mu}$ in the WET. For the $b \rightarrow s\ell\ell$ data, a good

fit is given for [13]

$$C_9^{bs\mu\mu} = -C_{10}^{bs\mu\mu} = \frac{1}{2} \left(V_{tb} V_{ts}^* \frac{e^2}{16\pi^2} \frac{4G_F}{\sqrt{2}} \right)^{-1} \left[C_{lq}^{(1)} + C_{lq}^{(3)} \right]_{2232} \approx -0.5 , \quad (2.52)$$

where $C_{9,10}^{bs\mu\mu}$ are referred to simply as $C_{9,10}$ in Sec. 1.4.

It was pointed out in Ref. [13] that there exists a mild tension between the fit to $R_{K^{(*)}}$ and the other anomalous $b \rightarrow s$ data, which can be reconciled with an additional LFU contribution to $C_9^{bs\ell\ell}$ such that

$$C_9^{bs\mu\mu} \approx -0.44 \quad \text{and} \quad C_9^{bs\ell\ell} \approx -0.5 , \quad (2.53)$$

for $\ell \in \{e, \mu, \tau\}$. A potential source of this universal contribution to C_9 is new physics in four-quark operators like [13]

$$[\mathcal{O}_{qu}^{(1)}]_{2322} = (\bar{Q}_2 \gamma_\mu Q_3)(\bar{u}_2 \gamma^\mu u_2) , \quad (2.54)$$

which can be generated, for example, by $\Phi \sim (8, 2, \frac{1}{2})_S$. The relevant Yukawa terms are

$$-\mathcal{L}_\Phi = w_{rs} Q_r^{ai} \bar{u}_{sb} \Phi_a^{bj} \epsilon_{ij} + \text{h.c.} \quad (2.55)$$

and a contribution of about the right size to $C_9^{bs\ell\ell}$ can be generated while avoiding dijet exclusion bounds from the LHC for $m_\Phi \sim 2$ TeV and $|w_{22}|, |w_{32}| \sim 1$ [13].

We construct a UV model that contains ζ and Φ as well as one of ω_1 or Π_7 in an attempt to incorporate this explanation into a model of neutrino mass. We emphasise that our goal here is not to present the most elegant or motivated model of neutrino mass and the flavour anomalies, but rather to show that our database can be used to motivate complex models with a specific structure.

We query the filtered model database for neutrino-mass models that contain the interactions $Q\bar{u}\Phi$, needed to generate $\mathcal{O}_{qu}^{(1)}$; $LQ\zeta$, needed to generate $C_9^{bs\mu\mu} = -C_{10}^{bs\mu\mu}$; and one of ω_1 or Π_7 , required to explain $R_{D^{(*)}}$. Our query returns a number of models, and we choose one to study briefly below. We note that none of the models involve the leptoquark ω_1 , and none feature the interaction $\bar{e}^\dagger Q^\dagger \Pi_7$, implying some freedom in the explanation of $R_{D^{(*)}}$ since the couplings y_{rs} of Eqs. (2.49) and (2.50) will be unrelated¹⁷ to the neutrino mass.

¹⁷Expanding our search criteria, we find no viable models in the database in which both sets of couplings presented in Eqs. (2.48) and (2.49) feature. This can be understood in the following way. Any neutrino self-energy diagram containing both couplings will also imply another where $e^\dagger \bar{u}^\dagger \omega_1$ or $\bar{e}^\dagger Q^\dagger \Pi_7$ is replaced with the corresponding coupling to L , which contains a neutrino field. This generally gives a larger contribution to the neutrino mass, since the closure of the diagram containing the \bar{e} will involve an additional loop with a W boson. Thus, diagrams with both sets of Yukawa interactions to SM fermions relevant to ω_1 and Π_7 are likely to be removed by our filtering procedure. We note that, after studying the unfiltered list of models, we find that some models can be engineered so that a sizeable (but not dominant) contribution to the neutrino masses does come from such diagrams involving both sets of leptoquark–fermion Yukawa couplings.

The model contains the additional fields Φ , ζ , Π_7 and $\eta \sim (8, 1, 1)_S$, necessary for lepton-number violation. It generates \mathcal{O}_{29b} , which implies an upper bound on the new-physics scale of roughly 10^7 TeV. The additional piece of the Lagrangian is $\Delta\mathcal{L} = \mathcal{L}_Y - \mathcal{V}$, with

$$-\mathcal{L}_Y = x_{rs} L_r^i \bar{u}_{sa} \Pi_7^{ja} \epsilon_{ij} + y_{rs} \bar{e}_r^\dagger Q_{sa}^\dagger \Pi_7^{ai} + z_{rs} L_r^i Q_s^j \zeta_a^{\{kl\}} \epsilon_{ik} \epsilon_{jl} + w_{rs} Q_r^{ai} \bar{u}_{sb} \Phi_a^{bj} \epsilon_{ij} + \text{h.c.} \quad (2.56)$$

$$\mathcal{V} = \kappa H^i \Phi_b^{aj} \epsilon_{a\epsilon_{ij}}^{\dagger b} + \lambda H^i \eta_b^a \tilde{\Pi}_{7a}^j \tilde{\zeta}^{b\{kl\}} \epsilon_{ik} \epsilon_{jl} + \text{h.c.} + \dots, \quad (2.57)$$

where we have only shown the part of the scalar potential relevant to lepton-number violation in this model, since the full expression contains a large number of terms. The leptoquark ζ has a diquark coupling which we forbid by imposing $U(1)_B$ on the Lagrangian, assigning baryon numbers of $-\frac{1}{3}$ and $\frac{1}{3}$ to ζ and Π_7 , respectively. (All other exotic fields have $B = 0$.) The model contains 33 free parameters, although not all of them are necessary to address the flavour anomalies and generate viable neutrino masses.

The tree-level completion diagram and the neutrino self-energy diagram are shown in Fig. 2.19. The neutrino mass arises at two loops, and the topology has the feature that no fermion propagators are arrow-violating. This implies that the neutrino masses are not proportional to any SM-fermion masses. This feature has been studied before in the context of a specific UV model in Ref. [4]. The phenomenon is particular to models derived from operators whose closures feature arrow-preserving loops, as discussed in Sec. 2.4.1. From a model-building perspective, one consequence is that the neutrino masses need not be dominated by Yukawa couplings to SM fermions of the third generation. Indeed, motivated by the pattern of operators required to explain the flavour anomalies, we adopt textures for the Yukawa couplings of Eq. (2.56) that imply dominance of the bottom-quark couplings for ζ , but the charm-quark couplings for Π_7 :

$$\mathbf{x} = \begin{pmatrix} 0 & x_{12} & 0 \\ 0 & x_{22} & 0 \\ 0 & x_{32} & 0 \end{pmatrix}, \quad \mathbf{z} = \begin{pmatrix} 0 & 0 & z_{13} \\ 0 & z_{22} & z_{23} \\ 0 & 0 & z_{33} \end{pmatrix}, \quad (2.58)$$

where the additional coupling z_{22} is required to generate the relevant dimension-six operators $[\mathcal{O}_{lq}^{(1,3)}]_{2232}$. Interestingly, the minimal set of couplings w_{rs} that gives viable neutrino masses while incorporating the key ingredients required to generate both $[\mathcal{O}_{lq}^{(1,3)}]_{2232}$ and $[\mathcal{O}_{lequ}^{(1,3)}]_{3332}$ is

$$\mathbf{w} = \begin{pmatrix} 0 & 0 & 0 \\ 0 & w_{22} & 0 \\ 0 & w_{32} & 0 \end{pmatrix}, \quad (2.59)$$

which is exactly the correct set required to also generate the operator given in Eq. (2.54). Thus, there is a natural connection in this model between the explanation of the charged- and neutral-current anomalies through the neutrino masses. With the exception of y_{33} , all of the couplings featuring in the explanation of the flavour anomalies also play a role in the generation of the neutrino masses. The structure of the neutrino-mass matrix is

$$\begin{aligned} [\mathbf{m}_\nu]_{rs} &\simeq \frac{\lambda\kappa}{(16\pi^2)^2} \frac{v^2}{\Lambda^2} \sum_{t,u} [z_{rt} w_{tu} x_{su} + (r \leftrightarrow s)] \\ &= \frac{\lambda\kappa}{(16\pi^2)^2} \frac{v^2}{\Lambda^2} [z_{r2} w_{22} x_{s2} + z_{r3} w_{32} x_{s2} + (r \leftrightarrow s)]. \end{aligned} \quad (2.60)$$

The matrix is rank 2, and so implies an almost massless neutrino. Since there is no suppression of the neutrino-mass scale by SM Yukawa couplings, we distinguish the UV scales Λ and κ so that

$$\Lambda \simeq \max(m_\zeta, m_\Phi, m_\eta, m_{\Pi_7}) \quad (2.61)$$

and consider the region of parameter space in which $\lambda\kappa \ll \Lambda$.

An explanation of the flavour anomalies in this picture can be achieved with $\mathcal{O}(1)$ couplings for Π_7 and Φ at a few TeV, and ζ at tens of TeV. We take η slightly heavier at ~ 50 TeV to decouple its phenomenology and aid in suppressing the neutrino mass. This implies $\lambda\kappa \sim 0.05$ GeV for neutrino masses saturating the atmospheric bound. This choice is technically natural, since in the limit of vanishing λ or κ the Lagrangian regains $U(1)_L$. We rewrite Eq. (2.60) as

$$[\mathbf{m}_\nu]_{rs} = m_0 [x_{s2} (z_{r2} w_{22} + z_{r3} w_{32}) + (r \leftrightarrow s)], \quad (2.62)$$

where $m_0 \approx \lambda\kappa v^2 (16\pi^2)^{-2} m_\eta^{-2}$. This allows for the adoption of a Casas–Ibarra-like parametrisation of the vectors x_{s2} and

$$\mathbf{Z} = \begin{pmatrix} z_{13} w_{32} \\ z_{22} w_{22} + z_{23} w_{32} \\ z_{33} w_{32} \end{pmatrix}, \quad (2.63)$$

so that [101]

$$\begin{aligned} x_{r2} &= \frac{\xi}{\sqrt{2m_0}} (\sqrt{m_2} u_2^* + i\sqrt{m_3} u_3^*) , \\ Z_r &= \frac{1}{\xi\sqrt{2m_0}} (\sqrt{m_2} u_2^* - i\sqrt{m_3} u_3^*) , \end{aligned} \quad (2.64)$$

where the u_i are the i th columns of the PMNS matrix; m_i are the neutrino masses, fixed by the measured squared mass differences and the choice of normal ordering; and ξ is

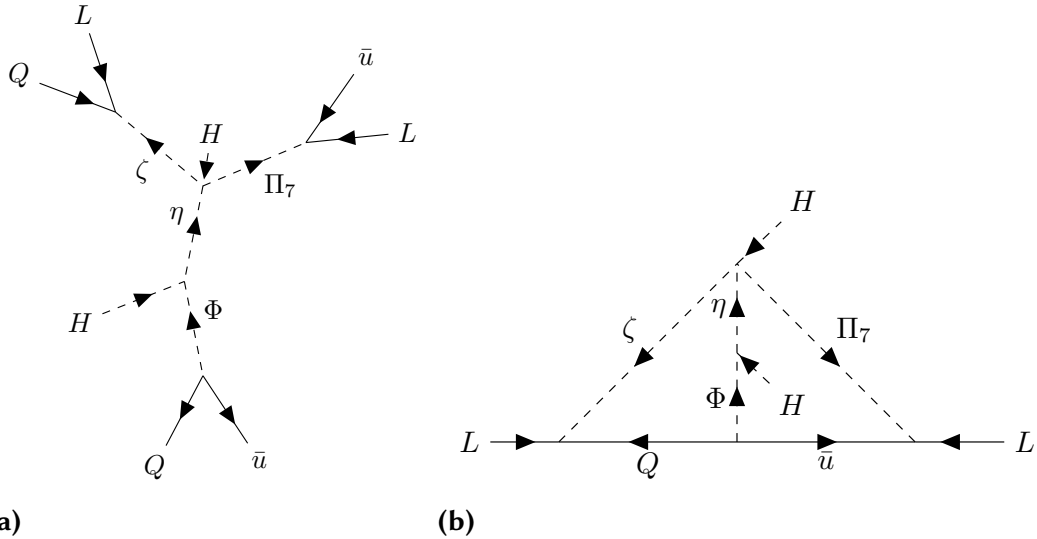


Figure 2.19: (a) The figure shows the tree-level completion diagram for the model constructed to address the flavour anomalies and neutrino masses. The topology is labelled $2s6f_2$ in our scheme. The closure contains two arrow-preserving loops, which arise by looping the \bar{u} into the \bar{u}^\dagger and the Q into the Q^\dagger . (b) The self-energy diagram for the same model. The diagram has a CLBZ-10 topology in the language of Ref. [96]. The neutrino masses are not suppressed by SM-fermion masses on account of the arrow-preserving fermion lines. This feature raises the bound on the new-physics scale relevant to the model, but also allows couplings to the second generation of fermions to play a role in the physics of neutrino mass. This is beneficial in our case since many of these couplings are involved in generating the pattern of dimension-six operators that motivates this example, and so provides for a more intimate connection between the flavour anomalies and neutrino masses.

a free complex parameter. We find, for example, that the choices $m_\Phi = 2 \text{ TeV}$, $m_{\Pi_7} = 1 \text{ TeV}$, $m_\zeta = 15 \text{ TeV}$, $m_\eta = 50 \text{ TeV}$, $\lambda\kappa = 0.05 \text{ GeV}$, $\xi = e^{3i/2}$, $z_{23} = 1$, $w_{22} = -w_{32} = 1$ and $y_{33} = 2e^{2i}$ give approximately the right values to generate the pattern of dimension-six operators discussed and explain the flavour anomalies. This includes the additional lepton-flavour universal contribution to $C_9^{bs\ell\ell}$, discussed in Ref. [13]. Although a more detailed study of the phenomenological implications of the model is beyond the scope of this simple example, we have shown how a specific UV scenario can be embedded into a radiative model in a way consistent with the measured neutrino masses and mixing parameters.

2.6 Conclusions

We have described a procedure for building UV-complete models from effective operators in a way amenable to automation. We have applied the algorithm, as found in our publicly available example code [228], to the $\Delta L = 2$ operators in the SMEFT up to and including dimension eleven, producing just over 11,000 minimal and predictive models of radiative Majorana neutrino mass. We share our complete listing of models, as well as the set reduced by model filtering, in our searchable model database [20].

Our analysis includes new operators that have not appeared in previous catalogues, along with updated estimates for the upper bounds on the new-physics scales associated with these. We performed a preliminary study of the UV models, showing that the most represented exotic fields featuring in the completions are leptoquarks. We find that a number of simple models predict new physics that must live below 100 TeV. Adding the additional requirements that the models contain fewer than four exotic fields and that the new-physics scale should be larger than 700 GeV gives at most five models fitting this description, all of which predict new fields below 15 TeV. One of these models was studied briefly, along with a model derived from a derivative operator, and one that addresses the flavour anomalies.

Our model database is perhaps a good laboratory for experiments in automated phenomenological analysis. Now that the models have been written down and compiled into this computationally accessible format, our hope is that a large number of them can be ruled out in a systematic way through improved model filtering, neutrino oscillation data, or collider constraints. Our results also pave the way for more detailed studies of the models that are currently accessible to experiments. As each model is tested, we will either get very lucky and discover the origin of neutrino masses at low energies, or else falsify these scenarios and build a stronger circumstantial case for those that cannot be tested at collider experiments.

3

The S_1 leptoquark as an explanation of the flavour anomalies

*This chapter is based on the publications ‘Reconsidering the One Leptoquark scenario: flavour anomalies and neutrino mass,’ written in collaboration with Yi Cai, Michael A. Schmidt, and Raymond R. Volkas [2], and ‘A near-minimal leptoquark model for reconciling flavour anomalies and generating radiative neutrino masses,’ written with Innes Bigaran and Raymond R. Volkas [3]. We study the potential of the S_1 leptoquark to explain the flavour anomalies and the anomalous magnetic moment of the muon. Our analysis points to a previously unconsidered region of parameter space for the model, which has now become the *de facto* region in which this scenario is viable. We exclusively use four-component spinor notation in this chapter.*

3.1 Introduction

In Sec. 1.4 we introduced the flavour anomalies: two classes of anomalous measurements in $b \rightarrow c$ and $b \rightarrow s$ transitions. A number of models exist in the literature which purport to explain both anomalies e.g. [196, 220, 226, 227, 270, 273, 274, 280–305] and among these minimal explanations the Bauer–Neubert (BN) model [226] is one of notable simplicity and explanatory power: a TeV-scale scalar leptoquark protagonist mediating $B \rightarrow D^{(*)}\tau\nu$ at tree-level and the $b \rightarrow s$ decays through one-loop box diagrams. The leptoquark transforms under the SM gauge group like a right-handed down-type

quark, and its pattern of couplings to SM fermions can also reconcile the measured and predicted values of the anomalous magnetic moment of the muon. The leptoquark has come to be known as S_1 in the literature, and this is the notation we use as well [268].

Our aim in this chapter is to study the S_1 -leptoquark model in the context of some previously unconsidered constraints and comment more definitely on its viability as an explanation of both the charged- and neutral-current anomalies. The remainder of this chapter is structured as follows. Section 3.2 outlines the scalar leptoquark model in which the phenomenological analysis of Section 3.3 takes place. Within this analysis, we present the regions of parameter space interesting for the flavour anomalies in Section 3.3.1, relevant constraints for the model in Section 3.3.2, and a general discussion of our results in Section 3.4.

3.2 The scalar leptoquark model

The leptoquark S_1 that features in the BN model transforms under the SM gauge group as $S_1 \sim (3, 1, -1/3)$. These transformation properties lead to generalised Yukawa couplings of the leptoquark to SM quarks and leptons as well as baryon number violating diquark couplings, which we choose to turn off to avoid destabilising the proton¹. The part of the Lagrangian relevant to S_1 is²

$$\mathcal{L}_{S_1} = (D_\mu S_1)^\dagger (D^\mu S_1) + m_{S_1}^2 |S_1|^2 - \kappa |H|^2 |S_1|^2 + \hat{x}_{rs} \hat{L}^r \hat{Q}^s S_1^\dagger + \hat{y}_{rs} \hat{e}_R^r \hat{u}_R^s S_1 + \text{h.c.}, \quad (3.1)$$

where interaction eigenstate fields are hatted, $\chi\psi = \overline{\chi}^C \psi$ for spinor fields, and $SU(2)_L$ indices have been suppressed. We move from the interaction to the charged-fermion mass basis through the unitary transformations

$$\begin{aligned} \hat{u}_L^r &= (L_u)^{rs} u_L^s, & \hat{d}_L^r &= (L_d)^{rs} d_L^s, & \hat{u}_R^r &= (R_u)^{rs} u_R^s, \\ \hat{e}_L^r &= (L_e)^{rs} e_L^s, & \hat{\nu}_L^r &= (L_e)^{rs} \tilde{\nu}_L^s, & \hat{e}_R^r &= (R_e)^{rs} e_R^s, \end{aligned} \quad (3.2)$$

where $\mathbf{V} = \mathbf{L}_u^\dagger \mathbf{L}_d$ is the CKM matrix and the PMNS matrix \mathbf{U} rotates the neutrino weak-eigenstate fields $\tilde{\nu}_L^r$ into the mass basis: $\nu_L^r = U^{rs} \tilde{\nu}_L^s$. Applying these transformations, the pertinent parts of the Lagrangian can be written

$$\begin{aligned} \mathcal{L}_{S_1} &\supset x_{rs} \tilde{\nu}_L^r d_L^s S_1^\dagger - [\mathbf{x} \mathbf{V}^\dagger]_{rs} e_L^r u_L^s S_1^\dagger + y_{rs} e_R^r u_R^s S_1^\dagger + \text{h.c.} \\ &\equiv x_{rs} \tilde{\nu}_L^r d_L^s S_1^\dagger - z_{rs} e_L^r u_L^s S_1^\dagger + y_{rs} e_R^r u_R^s S_1^\dagger + \text{h.c.} \end{aligned} \quad (3.3)$$

¹This can be achieved through the imposition of an appropriate symmetry.

²The correspondence between our Yukawa couplings and those of Ref. [226] is $\hat{x}_{rs} = -\lambda_{sr}^L$ and $\hat{y}_{rs} = \lambda_{sr}^{R*}$.

where the Yukawa couplings to the left-handed fermions are related through

$$\mathbf{z} = \mathbf{x}\mathbf{V}^\dagger. \quad (3.4)$$

The x_{rs} and y_{rs} are free parameters in our model, with the z_{rs} fixed through Eq. (3.4). The Yukawa couplings of the leptoquark to the first generation of SM fermions are heavily constrained by a number of processes we discuss in Section 3.3.2. In general, constraints from processes involving the down-quark are more severe for this leptoquark, and for the sake of simplicity we therefore take

$$\mathbf{x} = \begin{pmatrix} 0 & 0 & 0 \\ 0 & x_{22} & x_{23} \\ 0 & x_{32} & x_{33} \end{pmatrix} \quad (3.5)$$

throughout this work. Note that in our notation $x_{22} = x_{\nu_\mu s}$, etc. We emphasise that even with such a texture, non-zero Yukawa couplings to the up-quark cannot be avoided since they are generated through the quark mixing of Eq. (3.4).

Approximate bounds on the mass of the S_1 can be inferred from collider searches. After pair-production, the final states of interest for this work are $\ell\ell jj$, $\ell jj + \cancel{E}_T$ and $jj + \cancel{E}_T$, where $\ell \in \{\mu, \tau\}$. The current most stringent results from these channels are presented here. Experimental limits are usually presented in (m_{LQ}, β) space, where β represents the branching ratio to the charged lepton and quark. The CMS collaboration places an upper limit of 1530 GeV (1285 GeV) on the mass of second generation scalar leptoquarks in the $\mu\mu jj$ channel assuming $\beta = 1(0.5)$ [306]. The most stringent limits on third-generation decays come from ATLAS. Their analysis excludes third generation leptoquark masses below 800 GeV at 95% confidence for $\beta = 0$ and $\beta = 1$, while the exclusion reaches 1 TeV for $\beta = 0.5$ [307]. Ref. [308] finds a lower bound between 400 GeV – 640 GeV for the BN leptoquark, although this range is specific to certain parameter choices.

3.3 Phenomenological analysis

The leptoquark S_1 supports a rich beyond-the-standard-model phenomenology, which includes FCNC interactions as well as the possibility of lepton-flavour violation and non-universality. The primary motivations for this work are charged-current processes in the up-quark sector and FCNCs in the down-quark sector, since these are posited to explain the anomalous measurements in $R_{D^{(*)}}$ and the $b \rightarrow s$ transition, respectively. The new physics essential to explain these anomalies also implies many heavily constrained exotic processes, whose adverse effects on the parameter space available to the model are also computed. Throughout this section, we account for the running of α_s from the leptoquark mass scale to the scale appropriate to the process considered.

For notational convenience, we remove the breve from the neutrino flavour-eigenstate fields, since we work exclusively with these in this section. We also define

$$\hat{m}_{S_1} = \frac{m_{S_1}}{\text{TeV}}. \quad (3.6)$$

3.3.1 Signals

Below we study the ways in which the leptoquark can ameliorate the discrepancies in the charged-current processes $B \rightarrow D\tau\nu$ and $B \rightarrow D^*\tau\nu$ as well as the neutral-current decays associated with the anomalous $b \rightarrow s$ data. We also include the leptoquark's contribution to the anomalous magnetic moment of the muon.

Charged-current processes

The leptoquark's role in decays of the form $b \rightarrow ce_r\nu_s$ can be parameterised by the effective Lagrangian [220]

$$\begin{aligned} \mathcal{L}_{\text{CC}}^{rs} = & -\frac{4G_F}{\sqrt{2}} V_{cb} \left[C_V^{rs} (\bar{c}\gamma^\mu P_L b)(\bar{e}_r \gamma_\mu P_L \nu_s) + C_S^{rs} (\bar{c}P_L b)(\bar{e}_r P_L \nu_s) \right. \\ & \left. + C_T^{rs} (\bar{c}\sigma^{\mu\nu} P_L b)(\bar{e}_r \sigma_{\mu\nu} P_L \nu_s) \right] + \text{h.c.}, \end{aligned} \quad (3.7)$$

with the vector, scalar and tensor contributions generated after Fierz transformation, with Wilson coefficients at the leptoquark mass scale given by

$$C_V^{rs} = \frac{1}{2\sqrt{2}G_F V_{cb}} \frac{z_{r2}^* x_{s3}}{2m_{S_1}^2} + \delta_{rs}, \quad (3.8a)$$

$$C_S^{rs} = \frac{1}{2\sqrt{2}G_F V_{cb}} \frac{y_{r2} x_{s3}}{2m_{S_1}^2}, \quad (3.8b)$$

$$C_T^{rs} = -\frac{1}{4} C_S^{rs}. \quad (3.8c)$$

We note that these are respectively equivalent to C_{V_L} , C_{S_L} and C_T of Eq. (1.90).

The values of these coefficients required for a good fit to the available R_D and R_{D^*} data have been studied in the literature, e.g. [196, 220, 309–312], often under the assumption of lepton-flavour conservation—that is, new physics allowed only in $C_{V,S,T}^{33}$. One of the best-fit points suggested by Ref. [196]:

$$\frac{z_{32}^* x_{33}}{\hat{m}_{S_1}^2} \approx 0.35, \quad \frac{y_{32} x_{33}}{\hat{m}_{S_1}^2} \approx 0, \quad (3.9)$$

is compatible with new physics only in C_V^{33} , and this is the benchmark considered in the original conception of the BN model. The most recent measurements of R_{D^*} [15, 187, 188, 190, 191] could not have been included in their analysis.

We use these results to guide our study but proceed more generally. We evaluate R_D and R_{D^*} by taking an incoherent sum over neutrino flavours in the final state while accounting for the interference between the SM and leptoquark contributions when the flavours of the charged lepton and neutrino coincide. We use the *flavio* software [279] to calculate R_D and R_{D^*} . The ratio R_D is evaluated using recently calculated form factors from lattice QCD [313], and R_{D^*} using form factors [314] extracted from experiments by BaBar [315, 316] and Belle [317–319], since the lattice results are as yet unavailable. We stress that the $B \rightarrow D^*$ form factors are extracted from measurements of the decays $B \rightarrow D^*(e, \mu)\nu$ assuming the SM, and therefore the calculation may become unreliable when the leptoquark effects in the muonic mode are large.

The effects of the running of the strong coupling α_s down from the high scale (Λ) to the b -quark mass scale (μ_b) for the scalar and tensor currents must also be accounted for. The vector coefficient C_V does not run due to the Ward identity of QCD. At leading logarithmic order

$$C_S(\mu_b) = \left[\frac{\alpha_s(m_t)}{\alpha_s(\mu_b)} \right]^{\frac{\gamma_S}{2\beta_0^{(5)}}} \left[\frac{\alpha_s(\Lambda)}{\alpha_s(m_t)} \right]^{\frac{\gamma_S}{2\beta_0^{(6)}}} C_S(\Lambda), \quad (3.10a)$$

$$C_T(\mu_b) = \left[\frac{\alpha_s(m_t)}{\alpha_s(\mu_b)} \right]^{\frac{\gamma_T}{2\beta_0^{(5)}}} \left[\frac{\alpha_s(\Lambda)}{\alpha_s(m_t)} \right]^{\frac{\gamma_T}{2\beta_0^{(6)}}} C_T(\Lambda), \quad (3.10b)$$

where $\gamma_S = -8$, $\gamma_T = 8/3$ and $\beta_0^{(n_f)} = 11 - 2n_f/3$ [320]. We use the *Mathematica* package *RunDec* [321] to run α_s from $\Lambda \sim \text{TeV}$ to $\mu_b = \overline{m_b} = 4.2 \text{ GeV}$. This results in a modification of the relation between the scalar and tensor Wilson coefficients: $C_T(\Lambda) = -\frac{1}{4}C_S(\Lambda)$. Although most of the running occurs at the low scale (between μ_b and m_t), the relationship between these coefficients still depends non-negligibly on the chosen high scale. To illustrate this dependence, we plot the ratio $C_S(\mu_b)/C_T(\mu_b)$ against Λ in Fig. 3.1. Running down to μ_b from higher scales increases the magnitude of the scalar coefficient relative to the tensor one.

We incorporate the new Belle combined measurement [15] into a fit of all measurements of R_D and R_{D^*} using the fitting software *flavio* [279]³. The fit contours are shown in Fig. 3.2, with the fit excluding the new Belle measurement shown with dashed contours to indicate its effect. We find the best-fit point

$$(C_V, C_S) \approx (-0.18, 0.36), \quad (3.11)$$

³We note that our fit does not include the measurements of $f_L^{D^*}$ and $R_{J/\psi}$, since errors here are still large. Instead, we take the central values from our fits and discuss predictions for these observables in section 3.4.

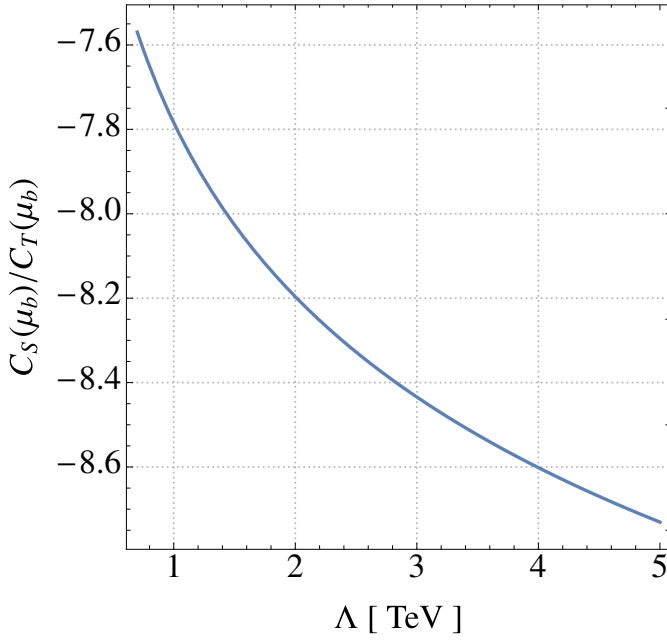


Figure 3.1: The dependence of the ratio of the tensor and scalar Wilson coefficients evaluated at μ_b in $b \rightarrow c\ell\nu$ as a function of the new-physics scale Λ , at which the ratio is -4 . The figure depicts the values down to which the ratio C_S/C_T evolves at μ_b . For example, running from 1 TeV to μ_b implies $C_S/C_T = -7.8$.

for the 2D fit to $\text{Re}C_V$ and $\text{Re}C_S(\Lambda) = -4C_T(\Lambda)$ at $\Lambda = 2$ TeV. We also fit to C_V with $C_S(\Lambda) = 0$ and *vice versa*. These results are summarised in Table 3.1. We comment here that even for S_1 contributing to the direction $C_S(\Lambda) = -4C_T(\Lambda)$, the vector operator will also always be non-zero. This follows from the relation in Eq. (3.4). The leading contribution where only x_{33} is non-zero is suppressed by $|V_{ts}| \approx 0.04$, but this contribution can still be sizeable if x_{33} is chosen to be large.

Neutral-current processes

The physics underlying the neutral-current $b \rightarrow s$ transitions in the model can be described by the effective Lagrangian \mathcal{L}_{NC} :

$$\mathcal{L}_{\text{NC}} = \frac{4G_F}{\sqrt{2}} V_{tb} V_{ts}^* \frac{e^2}{16\pi^2} \sum_{IJ} C_{IJ}^\mu \mathcal{O}_{IJ}^\mu, \quad (3.12)$$

where $I, J \in \{L, R\}$ and the operators in this chiral basis are defined below in terms of $\mathcal{O}_{9,10}$. We note that this is equivalent to Eq. (1.78). Following the matching procedure

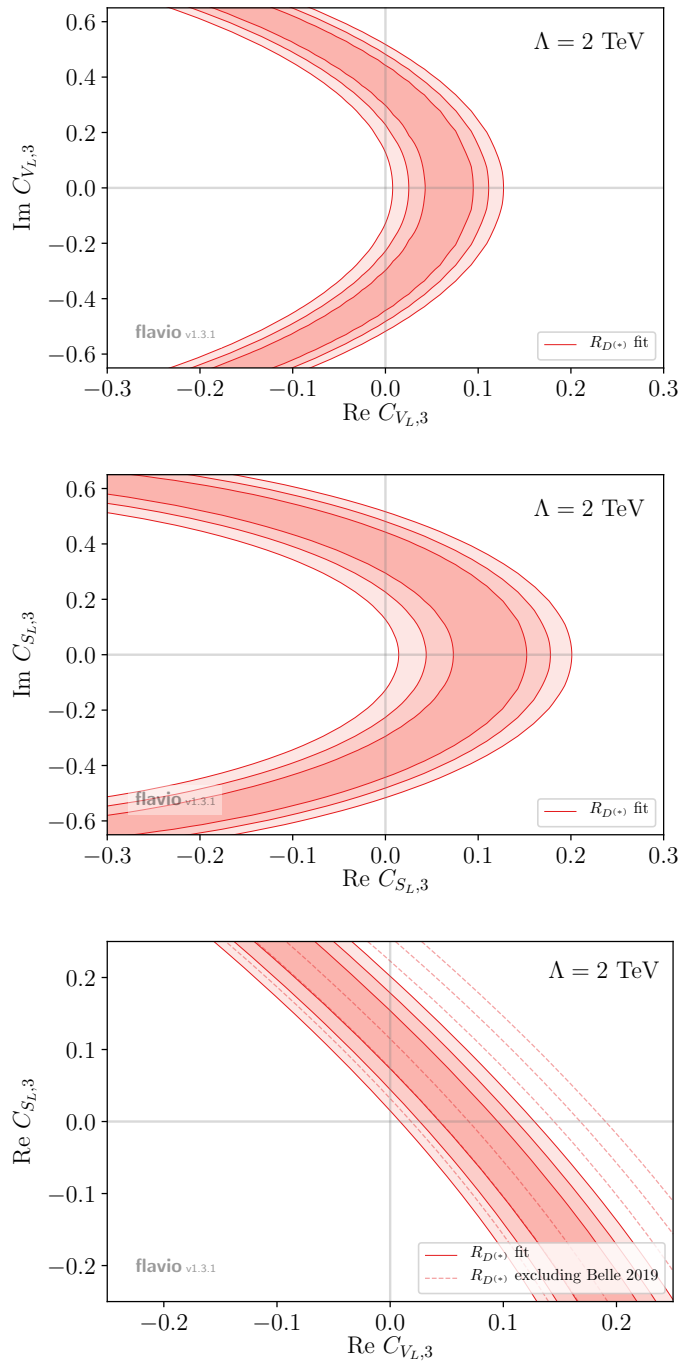


Figure 3.2: The results of our fit to R_D and R_{D^*} including the new Belle measurement [15]. Contours show the 1 , 2 and 3σ regions of the fit, dashed lines show the fit results without the recent Belle measurement. The scalar and tensor coefficients are run to the b -quark mass scale from 2 TeV . See Table 3.1 for central values and the text for more details.

Fit	Best fit	1σ region	2σ region
C_V	0.069	[0.044, 0.094]	[0.026, 0.11]
C_S	0.14	[0.077, 0.15]	[0.047, 0.18]
(C_V, C_S)	(−0.18, 0.36)	—	—

Table 3.1: The results of our fit to R_D and R_{D^*} including the new Belle combined measurement [15]. The first row shows the best fit point and σ -regions fitting to C_V with all other operator coefficients vanishing. The second row shows the same for $C_S(\Lambda) = -4C_T(\Lambda)$ for $\Lambda = 2 \text{ TeV}$ and all other coefficients set to zero. The third row shows the best fit point for a 2D fit to $\text{Re } C_V$ and $\text{Re } C_S(\Lambda) = -4\text{Re } C_T(\Lambda)$, again for $\Lambda = 2 \text{ TeV}$.

performed in Ref. [322], we find that the field S_1 generates the operators

$$\begin{aligned} \mathcal{O}_{LL}^\mu &\equiv \frac{1}{2}(\mathcal{O}_9^\mu - \mathcal{O}_{10}^\mu) = (\bar{s}\gamma^\mu P_L b)(\bar{\mu}\gamma_\mu P_L \mu), \\ \mathcal{O}_{LR}^\mu &\equiv \frac{1}{2}(\mathcal{O}_9^\mu + \mathcal{O}_{10}^\mu) = (\bar{s}\gamma^\mu P_L b)(\bar{\mu}\gamma_\mu P_R \mu) \end{aligned} \quad (3.13)$$

at the one-loop level with coefficients [226]

$$C_{LL}^{S_1, \mu} = \frac{m_t^2}{8\pi\alpha m_{S_1}^2} |z_{23}|^2 - \frac{\sqrt{2}}{64\pi\alpha G_F m_{S_1}^2 V_{tb} V_{ts}^*} \sum_r x_{r3} x_{r2}^* \sum_s |z_{2s}|^2, \quad (3.14a)$$

$$\begin{aligned} C_{LR}^{S_1, \mu} &= \frac{m_t^2}{16\pi\alpha m_{S_1}^2} |y_{23}|^2 \left[\ln \frac{m_{S_1}^2}{m_t^2} - f\left(\frac{m_t^2}{m_W^2}\right) \right] \\ &- \frac{\sqrt{2}}{64\pi\alpha G_F m_{S_1}^2 V_{tb} V_{ts}^*} \sum_r x_{r3} x_{r2}^* \sum_s |y_{2s}|^2, \end{aligned} \quad (3.14b)$$

where

$$f(x) = 1 - \frac{3}{x-1} + \frac{3}{(x-1)^2} \ln x. \quad (3.15)$$

For the rest of the discussion we remove the μ superscript from the Wilson coefficients and operators associated with $b \rightarrow s\mu\mu$, since we only consider new-physics effects in the muonic mode. The dominant contributions are from the box diagrams shown in Fig. 3.3. There are additional lepton flavour universal contributions from γ and Z penguins, however these are subdominant: the Z penguins are suppressed by small neutrino masses and only the small short-range contribution from the γ penguins contributes to $C_9^{S_1}$.

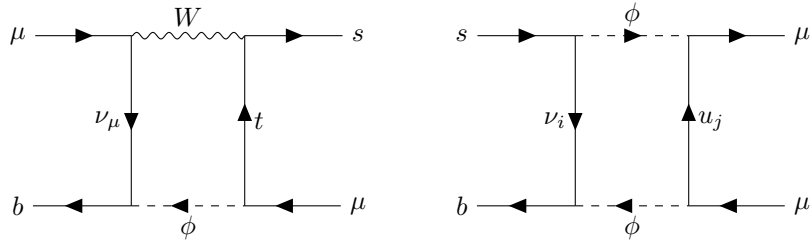


Figure 3.3: The box diagrams contributing to $C_{LL}^{S_1}$ and $C_{LR}^{S_1}$ in this scalar leptoquark model.

The authors of Refs. [13] conduct a global fit of all available experimental data on the $b \rightarrow s$ decays. They find a good fit to the data for the chiral coefficients generated by the leptoquark for

$$C_{LL}^{\text{NP}} \approx -1.0 \text{ and } C_{IJ}^{\text{NP}} \approx 0 \text{ otherwise,} \quad (3.16)$$

where new physics is assumed to significantly alter only the muonic mode and the fit is performed for $C_{IJ} \in \mathbb{R}$. This choice of coefficients results in a significantly improved fit to all of the $b \rightarrow s$ data, with a total 6.6σ pull from the SM. Although a better fit to all of the data can be achieved for $C_{LR}^{\text{NP}} < 0$ (this is clear from Fig. 1.11), the choice $C_{LR}^{\text{NP}} \approx 0$ allows slightly smaller values of C_{LL}^{NP} to explain the $R_{K^{(*)}}$ anomalies. The 2σ region for the fit is $-1.4 \lesssim C_{LL}^{S_1} \lesssim -0.74$ with $C_{LR}^{S_1} = 0$. The condition $C_{LR}^{S_1} \approx 0$ implies a suppression of the Yukawa couplings y_{2r} , while $C_{LL}^{S_1} \approx -1$ requires large leptoquark couplings to the second and third generation of left-handed quarks for the second term in Eq. (3.14a)—corresponding to the second diagram in Fig. 3.3—to dominate over the first, since it alone can be negative.

Anomalous magnetic moment of the muon

The leptoquark also mediates one-loop corrections to the $\gamma\mu\mu$ vertex, contributing to the muon anomalous magnetic moment. In the limit that $m_{S_1}^2 \gg m_t^2$, the contribution of S_1 to $a_\mu = (g - 2)_\mu / 2$ is given by [226, 323–325]

$$a_\mu^{S_1} = \sum_i \frac{m_\mu m_{u_i}}{4\pi^2 m_{S_1}^2} \left(\frac{7}{4} - \ln \frac{m_{S_1}^2}{m_{u_i}^2} \right) \text{Re}(y_{2r} z_{2i}) - \frac{m_\mu^2}{32\pi^2 m_{S_1}^2} \left[\sum_i |z_{2i}|^2 + \sum_i |\gamma_{2i}|^2 \right], \quad (3.17)$$

and the same-chirality terms are suppressed relative to the mixed-chirality term by a factor of the muon mass, leading to the requirement of non-vanishing right-handed couplings for an adequate explanation. We require that the leptoquark contribution account for the measured anomaly, and thus that $a_\mu^{S_1} = (287 \pm 80) \cdot 10^{-11}$ [225].

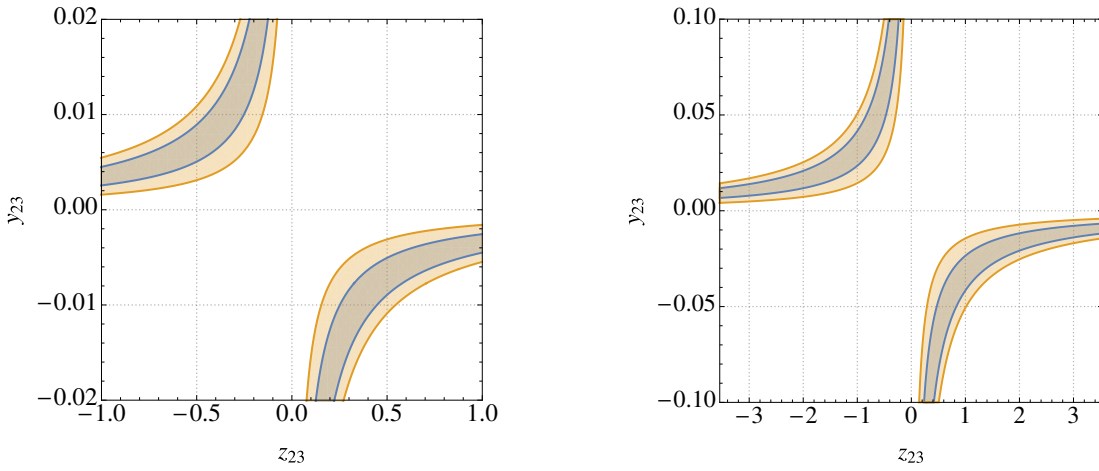


Figure 3.4: The 1 and 2σ allowed regions for a_μ in the y_{23} – z_{23} plane for leptoquark masses of $m_{S_1} = 1$ TeV (left) and $m_{S_1} = 5$ TeV (right). The top-mass enhancement in the first term of Eq. (3.17) allows the model to accommodate a_μ with very small values for $|y_{23}|$ with $z_{23} \neq 0$.

The top-mass enhancement in the first term makes this the dominant contribution in this model, and we illustrate the interesting values of y_{32} and z_{32} in Fig. 3.4 for leptoquark mass values of $m_{S_1} = 1$ TeV and $m_{S_1} = 5$ TeV. Large z_{23} values assist the model’s explanation of the $b \rightarrow s$ anomalies, hence a combined explanation of this and the $(g-2)_\mu$ anomaly prefers a small y_{23} . Explicitly, the condition [226]

$$-20.7(1 + 1.06 \ln \hat{m}_{S_1}) \text{Re}(y_{23} z_{23}) \approx 0.08 \hat{m}_{S_1}^2 \quad (3.18)$$

must be satisfied to meet the central value of the measurements of a_μ in this minimal case.

3.3.2 Constraints

We proceed by studying the constraints important for the leptoquark S_1 in the regions of parameter space dictated by the flavour anomalies. This analysis includes the constraints imposed by B , K and D meson decays, B_s – \bar{B}_s mixing, lepton-flavour violating processes and electroweak measurements.

Many of these processes are studied in the context of an effective-operator framework. Since much of the nomenclature for four-fermion operator coefficients is often only based on the Lorentz-structure of each term, keeping the naming conventions present in the flavour-physics literature for each process can lead to ambiguity. For this

reason we index each effective Lagrangian appearing in this section and retain the common names for each term, with the Lagrangian's index prepended to the label. For example, C_{i,V_L} might correspond to the coefficient of an operator like $(\bar{S}_1 \gamma_\mu P_L \chi)(\bar{\psi} \gamma^\mu P_L \omega)$ in \mathcal{L}_i , where S_1, χ, ψ, ω represent Fermion fields. For clarity we remind the reader that the coefficients of \mathcal{L}_{CC} and \mathcal{L}_{NC} from the previous section are left unindexed.

For the reader's convenience, we signpost the important results of this section below.

Constraints on the left-handed couplings. A feature of the BN model is that the effective operators mediating the $b \rightarrow s\mu\mu$ decays are generated through box diagrams, since S_1 only couples down-type quarks to neutrinos at tree-level. As a consequence, the large Yukawa couplings required to meet the $b \rightarrow s$ measurements will mediate FCNC processes with a neutrino pair in the final state—processes to which they are related by $SU(2)_L$ invariance—at tree level. This makes the $b \rightarrow svv$ decays and $K^+ \rightarrow \pi^+ vv$ very constraining for this model's explanation of the $b \rightarrow s$ anomalies. The former decay is more important, since it involves the combination of left-handed couplings present in Eq. (3.14): $\sum_r x_{r3} x_{r2}^*$, and essential to ensure a negative value for $C_{LL}^{S_1}$. The leptoquark also contributes to $B_s - \bar{B}_s$ mixing through box diagrams similar to those given in Fig. 3.3 with neutrinos running through both internal fermion lines. We find measurements of $B_s - \bar{B}_s$ mixing to be more constraining than those of FCNC decays for leptoquark masses larger than a few TeV. For small leptoquark masses, precision electroweak measurements of the $Z\ell\bar{\ell}$ couplings place upper bounds on the sum of the absolute squares of left-handed couplings, and a relative sign difference between couplings to the third-generation quarks and those to the second implies the possibility of a mild cancellation taming these effects. A very important constraint on the left-handed coupling $|x_{22}|$ can be derived from the meson decay $D^0 \rightarrow \mu\mu$, a large value of which aids the explanation of $R_{K^{(*)}}$ in this scenario. It has also recently been pointed out [227] that the LFU evident in the ratio $R_D^{\mu/e} = \Gamma(B \rightarrow D\mu\nu)/\Gamma(B \rightarrow Dev)$ represents a significant hurdle to the leptoquark's explanation of the $b \rightarrow s$ data, and we discuss this constraint below.

Constraints on the product of left-handed couplings discussed above also frustrate the model's attempts to explain measurements of the ratios R_D and R_{D^*} , specifically in those areas of parameter space suggested by new-physics effects only in C_V^{rs} . This implies the need for non-vanishing right-handed couplings y_{rs} so that the $C_S = -4C_T$ direction is generated.

Constraints on the right-handed couplings. The right-handed couplings y_{rs} are generally less constrained in this leptoquark model, since they mediate interactions involving fewer fermion species. The most stringent limits come from mixed-chirality contributions to tau decays such as $\tau \rightarrow \mu\mu\mu$ and $\tau \rightarrow \mu\gamma$, as well as the precision electroweak measurements mentioned above. Many right-handed couplings also feature in

the model's contributions to B , D , and K decays.

Semileptonic charged-current processes

Leptonic and semileptonic charged-current processes are a sensitive probe of the model we study, since the leptoquark S_1 provides tree-level channels for leptonic pseudoscalar meson decays and semileptonic decays of the tau. In order to describe these processes, we generalise the Lagrangian presented in Eq. (3.7) to

$$\mathcal{L}_1^{rstu} = -\frac{4G_F}{\sqrt{2}}V_{u_r d_s} \left[C_{1,V}^{rstu}(\bar{u}_r \gamma^\mu P_L d_s)(\bar{e}_t \gamma_\mu P_L v_u) + C_{1,S}^{rstu}(\bar{u}_r P_L d_s)(\bar{e}_t P_L v_u) + C_{1,T}^{rstu}(\bar{u}_r \sigma^{\mu\nu} P_L d_s)(\bar{e}_t \sigma_{\mu\nu} P_L v_u) \right], \quad (3.19)$$

where the vector, scalar and tensor Wilson coefficients at the leptoquark mass scale now read

$$C_{1,V}^{rstu} = \frac{1}{2\sqrt{2}G_F V_{u_r d_s}} \frac{z_{ts}^* x_{ur}}{2m_{S_1}^2} + \delta_{tu}, \quad (3.20a)$$

$$C_{1,S}^{rstu} = \frac{1}{2\sqrt{2}G_F V_{u_r d_s}} \frac{y_{ts} x_{ur}}{2m_{S_1}^2}, \quad (3.20b)$$

$$C_{1,T}^{rstu} = -\frac{1}{4}C_{1,S}^{rstu}, \quad (3.20c)$$

in analogy with Eqs. (3.8). The leptonic decay rate for a pseudoscalar meson $P_{rs} \sim \bar{u}_r d_s$ is then given by [227]

$$\Gamma(P_{rs} \rightarrow e_t v_u) = \frac{G_F^2 m_P |V_{u_r d_s}|^2}{8\pi} f_P^2 m_{e_t}^2 \left(1 - \frac{m_{e_t}^2}{m_P^2} \right)^2 \cdot \left| C_{1,V}^{rstu} - C_{1,S}^{rstu} \frac{m_P^2}{m_{e_t}(m_{u_r} + m_{d_s})} \right|^2, \quad (3.21)$$

where f_P is the pseudoscalar meson decay constant. As before, we account for the effect of the running of α_s from the high scale to the scales appropriate for each decay for the scalar operator. We take the relevant scale to be $\mu = \overline{m_c} = 1.27$ GeV for the D meson decays and $\mu = 2$ GeV for the K decays, since this is the matching scale used in Ref. [326], from which we take the decay constants. Explicitly,

$$C_{1,S}(\mu) = \left[\frac{\alpha_s(m_b)}{\alpha_s(\mu)} \right]^{\frac{\gamma_S}{2\beta_0^{(4)}}} \left[\frac{\alpha_s(m_t)}{\alpha_s(m_b)} \right]^{\frac{\gamma_S}{2\beta_0^{(5)}}} \left[\frac{\alpha_s(\Lambda)}{\alpha_s(m_t)} \right]^{\frac{\gamma_S}{2\beta_0^{(6)}}} C_{1,S}(\Lambda), \quad (3.22)$$

Observable	Experimental value
$\text{Br}(K \rightarrow \mu\nu)$	$(63.56 \pm 0.11)\%$
$\text{Br}(D_s \rightarrow \mu\nu)$	$(0.549 \pm 0.016)\%$
$\text{Br}(D_s \rightarrow \tau\nu)$	$(5.55 \pm 0.24)\%$
$\text{Br}(B \rightarrow \mu\nu)$	$(6.46 \pm 2.22 \pm 1.60) \cdot 10^{-7}$ [327]
$\text{Br}(B \rightarrow \tau\nu)$	$(1.09 \pm 0.24) \cdot 10^{-4}$
$\text{Br}(B_c \rightarrow \tau\nu)$	$\lesssim 30\%$ [217]
$r_K^{e/\mu} = \frac{\Gamma(K \rightarrow e\nu)}{\Gamma(K \rightarrow \mu\nu)}$	$(2.488 \pm 0.009) \cdot 10^{-5}$
$R_K^{\tau/\mu} = \frac{\Gamma(\tau \rightarrow K\nu)}{\Gamma(K \rightarrow \mu\nu)}$	$(1.101 \pm 0.016) \cdot 10^{-2}$
$R_{D_s}^{\tau/\mu} = \frac{\Gamma(D_s \rightarrow \tau\nu)}{\Gamma(D_s \rightarrow \mu\nu)}$	$10.73 \pm 0.69^{+0.56}_{-0.53}$ [328]
$R_D^{\mu/e} = \frac{\Gamma(B \rightarrow D\mu\nu)}{\Gamma(B \rightarrow D\nu\nu)}$	$0.995 \pm 0.022 \pm 0.039$ [329]
$R_{D^*}^{e/\mu} = \frac{\Gamma(B \rightarrow D^*\mu\nu)}{\Gamma(B \rightarrow D^*\nu\nu)}$	$1.04 \pm 0.05 \pm 0.01$ [319]

Table 3.2: A table summarising the experimental values we take for the various leptonic branching ratios and LFU ratios considered in this section. Measurements quoted without explicit citation are taken from Ref. [21].

while the running for the scalar operator featuring in the B decays is the same as in Eq. (3.10). Eq. (3.21) is finely sensitive to the Wilson coefficient $C_{1,S}$ since it has the effect of lifting the chiral suppression of the SM due to the charged lepton mass in the denominator of the last term. Recent work [227] has pointed out the importance of considering the decays $B \rightarrow \ell\bar{\nu}$, $K \rightarrow \ell\bar{\nu}$, $D_s \rightarrow \ell\bar{\nu}$ and $B \rightarrow D^{(*)}\ell\bar{\nu}$, to which we also add a discussion of $\tau \rightarrow K\nu$ and $B_c \rightarrow \ell\bar{\nu}$ below. In addition, for each relevant process we calculate a LFU ratio, since in many cases these are well measured quantities which constitute powerful probes of any new-physics attempting to explain $R_{D^{(*)}}$ or $R_{K^{(*)}}$. We summarise the limits and values we take for these decays and their relevant ratios in Table 3.2. All values of the decay constants used throughout this discussion are taken from Ref. [326].

The ratio

$$r_K^{e/\mu} = \frac{\Gamma(K \rightarrow e\nu)}{\Gamma(K \rightarrow \mu\nu)} \quad (3.23)$$

is one of the most precisely measured quantities in weak hadronic physics. As such, the consideration of next-to-leading-order corrections becomes important for our phenomenological analysis of the effects of the leptoquark S_1 on these decays. Electroweak effects contributing to $r_K^{e/\mu}$ have been calculated to order $e^2 p^4$ in chiral perturbation theory, e.g. [330, 331]. Higher order contributions to the quotient Eq. (3.23) are pro-

portional to the lowest order contribution: $r_K^{e/\mu,(0)}$, calculated directly from Eq. (3.21). Including the effects of leading higher-order logarithms through Δ_{LL} , Eq. (3.23) can be written

$$r_K^{e/\mu} = r_K^{e/\mu,(0)} \left(1 + \Delta_{e^2 p^2}^K + \Delta_{e^2 p^4}^K + \dots \right) (1 + \Delta_{LL}) \quad (3.24)$$

and we take $\Delta_{LL} = 0.055\%$, $\Delta_{e^2 p^2}^K = -3.786\%$ and $\Delta_{e^2 p^4}^K = (0.135 \pm 0.011)\%$ [330] in our calculation.

One can extend the study of lepton-flavour universality in leptonic kaon decays by considering the crossed process $\tau \rightarrow K\nu$. More specifically, the ratio

$$R_K^{\tau/\mu} = \frac{\Gamma(\tau \rightarrow K\nu)}{\Gamma(K \rightarrow \mu\nu)} \quad (3.25)$$

can be used to derive constraints on the muon and tau couplings of the leptoquark S_1 , and a similar approach has been taken to constrain the couplings of a vector leptoquark in Ref. [288]. For the numerator, we find

$$\Gamma(\tau \rightarrow K\nu) = \frac{G_F^2 |V_{us}|^2}{8\pi} f_K^2 m_\tau^3 \left(1 - \frac{m_K^2}{m_\tau^2} \right)^2 \sum_r \left| C_{1,V}^{123r} - C_{1,S}^{123r} \frac{m_K^2}{m_\tau(m_u + m_s)} \right|^2, \quad (3.26)$$

and the ratio $R_K^{\tau/\mu}$ is required to lie within 2σ of its experimental value: $(1.101 \pm 0.016) \cdot 10^{-2}$ [21].

Pion leptonic decays have been well-studied in the context of leptoquark models, and measurements of the ratio $R_\pi^{\mu/e} = \Gamma(\pi \rightarrow \mu\nu)/\Gamma(\pi \rightarrow e\nu)$ demand that leptoquark interactions with the electron and first-generation quarks are small⁴ [332, 333]. The electron and down-quark couplings play no role in the anomalies we consider in this work, and we only require that the appropriate couplings are small enough to evade these constraints.

Comments on lepton flavour universality in $B \rightarrow D^{(*)}(e, \mu)\nu$. An additional constraint comes from the observation that LFU is respected in the ratio of decay rates

$$R_{D^{(*)}}^{\mu/e} = \frac{\Gamma(B \rightarrow D^{(*)}\mu\nu)}{\Gamma(B \rightarrow D^{(*)}e\nu)}, \quad (3.27)$$

implying a tension with the purported violation in μ - e universality evident in $R_{K^{(*)}}$. This constraint has been studied in Ref. [227], where it was concluded that the leptoquark model cannot respect this constraint while explaining the suppression of R_K

⁴In the most minimal case, a non-zero x_{21} implies $z_{21} \approx x_{21}$ and these couplings alone are sufficient to mediate the decay $\pi^+ \rightarrow \mu^+\nu$.

in the absence of the right-handed couplings y_{rs} . The ratio has been measured to be $R_D^{\mu/e} = 0.995 \pm 0.022 \pm 0.039$ [329], while the reciprocal is presented for the D^* ratio: $R_{D^*}^{e/\mu} = 1.04 \pm 0.05 \pm 0.01$ [319]. In the case of $R_D^{\mu/e}$, 2σ consistency with the measurement allows for an approximately 10% deviation from the SM prediction, a weaker bound than that presented in Ref. [227], while the recent Belle result for $R_{D^*}^{e/\mu}$ permits only a 4% deviation for contributions to the muonic mode. We find that these constraints become less important for leptoquark masses larger than 1 TeV, permitting sizeable contributions to C_{LL} in this model. We illustrate this point in the top plot of Fig. 3.5, where random points passing all of the constraints presented in our analysis except $R_{D^*}^{e/\mu}$ are presented in the C_{LL} - $R_{D^*}^{\mu/e}$ plane. The parameters and ranges taken in our scan are the same as those of scan I in Sec. 3.4 in which masses are sampled randomly from the range [1, 5] TeV. The complementary set-up for $R_D^{e/\mu}$ is shown in the bottom figure of Fig. 3.5, *mutatis mutandis*.

Comments on $B_c \rightarrow \tau\nu$. The leptonic decays of the charmed B meson have not yet been measured—few B_c mesons are produced at e^+e^- B -factories and the leptonic mode cannot be reliably reconstructed at LHCb. Despite this, measurements of the B_c lifetime have recently been shown to imply serious constraints [215, 217] for models explaining $R_{D^{(*)}}$ with contributions to the operator C_S^{3r} defined in Eq. (3.7). Here, we wish to point out that the $B_c \rightarrow \tau\nu$ rate remains SM-like in this leptoquark model due to the presence of the tensor contribution C_T^{3r} , and thus that measurements of the B_c lifetime do not constitute a serious constraint on the model.

In Fig. 3.6 we plot the branching ratio $\text{Br}(B_c \rightarrow \tau\nu)$ in this leptoquark model against interesting values of R_{D^*} , in the spirit of Fig. 1 of Ref. [217]. The blue curve represents the contribution from only the Wilson coefficient C_S , while the orange curve represents the contribution from the scalar leptoquark S_1 where the scalar and tensor contributions are related through Eq. (3.20c). The presence of both the scalar and tensor contributions results renders the branching ratio sufficiently small in the region of interest.

Lepton flavour violating processes

The lepton-flavour symmetries present in the SM are broken by the Yukawa couplings of the leptoquark to the SM fermions. This implies that S_1 can mediate processes that do not conserve lepton flavour, of which those considered in our analysis are $e_i \rightarrow e_j \gamma$, $e_i \rightarrow e_j e_k e_l$ and muon-electron conversion in nuclei: $\mu_Z^A N \rightarrow e_Z^A N$. We use the expressions for these processes found in the Appendix of Ref. [16], adapted to the case of one leptoquark, and direct the reader there for more details. We impose the following

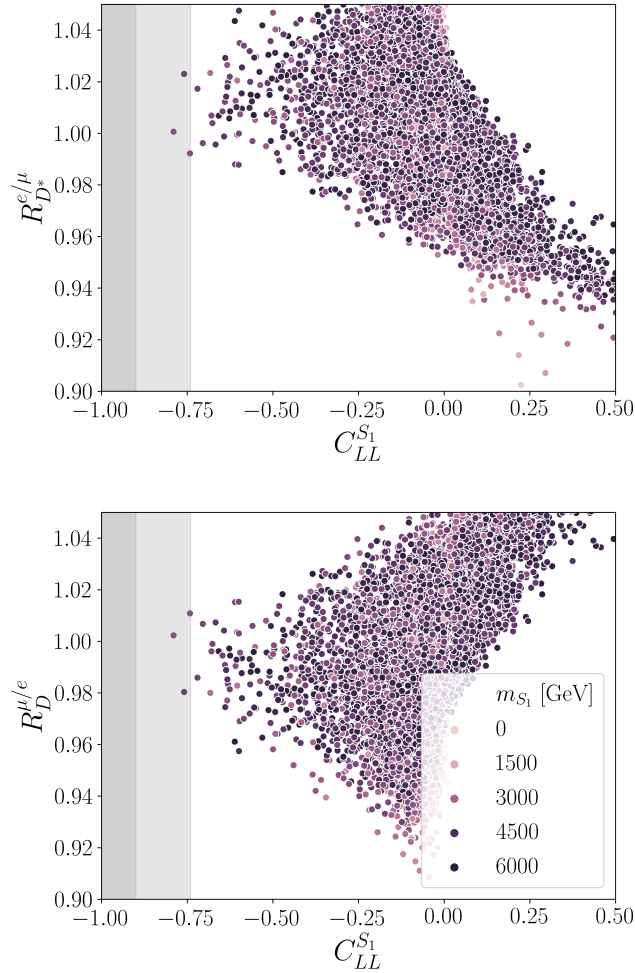


Figure 3.5: The results of our random scan showing C_{LL} against $R_D^{\mu/e}$ (bottom) and $R_{D^*}^{e/\mu}$ (top) for the parameter choices detailed in Sec. 3.4 for ‘scan I’, in which the leptoquark mass is allowed to vary to values as large as 5 TeV. For leptoquark masses between 3 and 5 TeV, the tension in the $b \rightarrow s$ data can be significantly resolved while keeping LFU effects between electron and muon $b \rightarrow c$ modes mild.

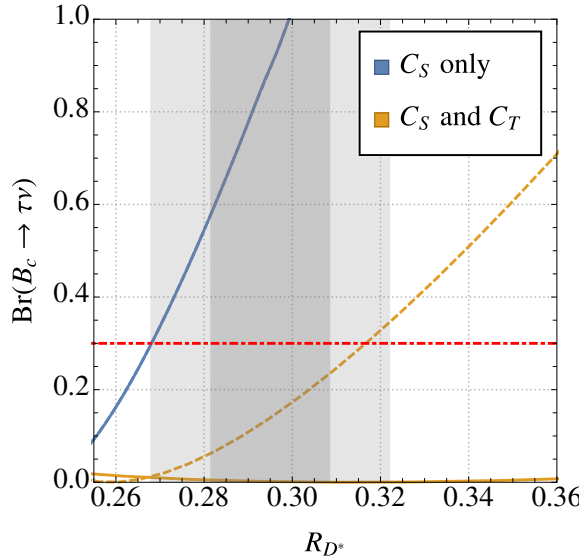


Figure 3.6: The branching ratio $\text{Br}(B_c \rightarrow \tau\nu)$ against R_{D^*} with new physics only in C_S (solid blue) and new physics in both C_S and C_T satisfying $C_S/C_T = -4$ (solid orange) and $C_S/C_T = -7.8$ (dashed orange). The 30% limit is shown in red (dot-dashed). The dark and light grey regions represent the 1 and 2σ regions for $R_{D^{(*)}}$. In this leptoquark model, $\text{Br}(B_c \rightarrow \tau\nu)$ remains $\lesssim 30\%$ in the region of interest.

limits for the constraints:

$$\text{Br}(\tau \rightarrow \mu\gamma) < 4.4 \cdot 10^{-8} \quad [334], \quad (3.28)$$

$$\text{Br}(\tau \rightarrow \mu\mu\mu) < 2.1 \cdot 10^{-8} \quad [335], \quad (3.29)$$

$$\text{Br}(\mu^{197}_{79}\text{Au} \rightarrow e^{197}_{79}\text{Au}) < 7.0 \cdot 10^{-13} \quad [336]. \quad (3.30)$$

In the $\mu \rightarrow e$ transition, we only consider muon–electron conversion since this is the most stringent of the muon’s LFV decay modes that the leptoquark can mediate [16, 101, 262]. The tree-level contributions to muon–electron conversion imply very strong constraints on the coupling combinations involved. Assuming no accidental cancellation between terms, the order-of-magnitude bounds [16]

$$z_{21}y_{11}^*, y_{21}z_{11}^* \lesssim [4 \cdot 10^{-9}, 7 \cdot 10^{-8}] \frac{m_{S_1}^2}{m_W^2}, \quad (3.31)$$

$$z_{21}z_{11}^*, y_{21}y_{11}^* \lesssim [10^{-8}, 10^{-7}] \frac{m_{S_1}^2}{m_W^2}. \quad (3.32)$$

can be evaded with small electron couplings.

Rare meson decays

The most important rare meson decays remain to be mentioned. We group them here and separate their discussion based on the species of lepton in the final state. The decays studied are: (1) $B \rightarrow Kvv$ and $K^+ \rightarrow \pi^+vv$, involving neutrinos, and (2) $D^0 \rightarrow \mu\mu$ and $D^+ \rightarrow \pi^+\mu\mu$, involving charged leptons.

The decays $B \rightarrow K^{(*)}vv$ and $K^+ \rightarrow \pi^+vv$ heavily constrain the combination of Yukawa couplings x_{rs} in this model since the SM contributions proceed at loop-level, while our leptoquark mediates such neutral-current quark decays at tree-level. The physics describing this class of decays is described by the effective Lagrangian [337, 338]

$$\begin{aligned} \mathcal{L}_2^{rstu} = & \frac{8G_F}{\sqrt{2}} \frac{e^2}{16\pi^2} V_{td_r} V_{td_s}^* \left[C_{2,L}^{rstu} (\bar{d}_r \gamma_\mu P_L d_s) (\bar{\nu}_t \gamma^\mu P_L \nu_u) \right. \\ & \left. + C_{2,R}^{rstu} (\bar{d}_r \gamma_\mu P_R d_s) (\bar{\nu}_t \gamma^\mu P_L \nu_u) \right] + \text{h.c.} \end{aligned} \quad (3.33)$$

and operator coefficients

$$C_{2,L}^{rstu} = -\frac{\sqrt{2}\pi^2}{e^2 G_F m_{S_1}^2} \frac{x_{ts}^* x_{ur}}{V_{td_r} V_{td_s}^*} + C_L^{\text{SM}} \delta_{tu}, \quad C_{2,R}^{rstu} = 0, \quad (3.34)$$

where $C_L^{\text{SM}} = -X(m_t^2/m_W^2)/s_w^2$. The SM loop function $X(x)$ is given by [337–340]

$$X(x) = \frac{x}{8} \left[\frac{x+2}{x-1} + \frac{3x-6}{(x-1)^2} \ln x \right], \quad (3.35)$$

and the ratios $R_{K^{(*)}}^{vv} \equiv \Gamma(B \rightarrow K^{(*)}vv)/\Gamma(B \rightarrow Kvv)_{\text{SM}}$ are constrained to satisfy $R_K^{vv} < 3.9$ and $R_{K^*}^{vv} < 2.7$ at 90% C.L. [341]. We find

$$\begin{aligned} R_{K^{(*)}}^{vv} &= \frac{1}{3} \sum_{rs} \frac{|C_{2,L}^{32rs}|^2}{|C_L^{\text{SM}}|^2} \\ &= 1 + \frac{a^2}{3m_{S_1}^4} \sum_{rs} \left| \frac{x_{r2}^* x_{s3}}{V_{tb} V_{ts}^*} \right|^2 - \frac{2a}{3m_{S_1}^2} \sum_r \text{Re} \left(\frac{x_{r2}^* x_{r3}}{V_{tb} V_{ts}^*} \right), \end{aligned} \quad (3.36)$$

where $a = \sqrt{2}\pi^2/(e^2 G_F |C_L^{\text{SM}}|)$. Due to the absence of right-handed currents, our model predicts $R_K^{vv} = R_{K^*}^{vv}$ although the bound on R_K^{vv} is slightly weaker, as is that for the inclusive decay. A conservative limit on the combination $(\sum x_{r2}^* x_{r3})/\hat{m}_{S_1}^2$ can be derived using the Schwartz inequality [226]:

$$-0.05 \lesssim \frac{[\mathbf{x}^\dagger \mathbf{x}]_{23}}{\hat{m}_{S_1}^2} \lesssim 0.1, \quad (3.37)$$

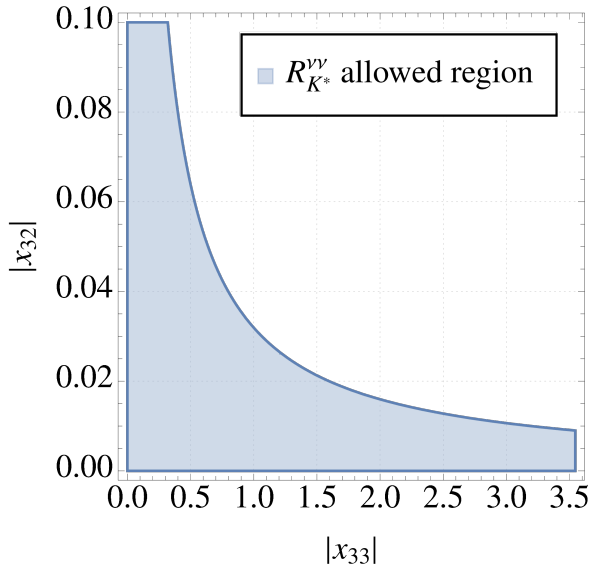


Figure 3.7: The region allowed by experimental limits on the decay $B \rightarrow Kvv$ in the $|x_{33}| - |x_{32}|$ plane for $m_{S_1} = 1$ TeV. All other couplings are switched off. A large value of $|x_{33}|$ is essential to explaining $R_{D^{(*)}}$, and the figure implies that such a requirement keeps $|x_{32}|$ small.

where we have assumed $\text{Arg}(x_{r2}^* x_{r3}) = \text{Arg}(V_{tb} V_{ts}^*)$. We emphasise that this bound represents an insufficient condition for the model to respect the experimental limits. In Fig. 3.7 we present the allowed region for non-zero x_{32} and x_{33} and $m_{S_1} = 1$ TeV—a coupling texture interesting for explaining $R_{D^{(*)}}$, although heavily constrained by $R_{K^*}^{vv}$.

The decay $K^+ \rightarrow \pi^+ vv$ constitutes the most stringent constraint on our model from the kaon sector [342]. We find

$$\begin{aligned} \text{Br}(K^+ \rightarrow \pi^+ vv) = & \frac{1}{3} \sum_{rs} \kappa_+ \left[\left(\text{Im} \frac{V_{ts} V_{td}^* s_w^2 C_{2,L}^{21rs}}{\lambda^5} \right)^2 \right. \\ & \left. + \left(\text{Re} \frac{V_{tb} V_{ts}^* s_w^2 C_{2,L}^{21rs}}{\lambda^5} + P_{(u,c)} \delta_{rs} \right)^2 \right], \end{aligned} \quad (3.38)$$

by adapting Eq. (3.29) of Ref. [337], where the factor $\kappa_+ = (5.27 \pm 0.03) \cdot 10^{-11}$ is due mainly to hadronic matrix elements, λ is the CKM Wolfenstein parameter, $P_{(u,c)} = 0.41 \pm 0.05$ accounts for the effects of light-quark loops, and the small electromagnetic corrections have been neglected. The branching ratio for the decay has most recently been measured by the E949 collaboration to be $\text{Br}(K^+ \rightarrow \pi^+ vv) = (1.73^{+1.15}_{-1.05}) \cdot 10^{-10}$ [343]. A conservative limit can be placed on the combination of new-physics couplings featuring in $C_{2,L}^{21rs}$ by considering only same-flavoured neutrinos in the final state of the

decay. Under the assumptions that the couplings involved are real and that only one combination dominates, we find

$$-9.1 \cdot 10^{-4} < \frac{[\mathbf{x}^\dagger \mathbf{x}]_{21}}{\hat{m}_{S_1}^2} < 4.8 \cdot 10^{-4}. \quad (3.39)$$

This bound can be avoided by considering a suppression of the leptoquark couplings to the first generation of quarks.

In this leptoquark model, the coupling of the c -quark to the charged leptons is essential for the explanation of the $b \rightarrow c\tau\nu$ anomalies. Also, as discussed earlier, the up-quark couplings cannot be entirely avoided due to the stringency of Eq. (3.39) and the mixing of Eq. (3.4). These factors make the physics of operators of the form $\mathcal{O}_{rstu} \sim (u_r \Gamma u_s)(e_t \Gamma e_u)$ an important source of constraint on this model. Additionally, in order to ensure $C_{LL}^{S_1} \approx -1.2$ in the model's original conception, an ansatz for z_{rs} was chosen such that $|z_{22}|$ takes $\mathcal{O}(1)$ values. Constraints from the decays $D^0 \rightarrow \mu\mu$ and $D^+ \rightarrow \pi^+ \mu\mu$ are especially worrying in this case, since the leptoquark mediates these processes at tree-level. Even within the context of vanishing first-generation couplings, one cannot avoid inducing new-physics interactions involving up quarks because of the mixing of Eq. (3.4). The new-physics contributions to decays of the form $u_r \rightarrow u_s e_t e_u$ can be contained within the effective Lagrangian

$$\begin{aligned} \mathcal{L}_3^{rstu} = & \frac{4G_F}{\sqrt{2}} \left[C_{3,V_R}^{rstu} (\bar{u}_r \gamma_\mu P_R u_s) (\bar{e}_t \gamma^\mu P_R e_u) + C_{3,V_L}^{rstu} (\bar{u}_r \gamma_\mu P_L u_s) (\bar{e}_t \gamma^\mu P_L e_u) \right. \\ & + C_{3,T}^{rstu} (\bar{u}_r \sigma_{\mu\nu} P_R u_s) (\bar{e}_t \sigma^{\mu\nu} P_R e_u) + C_{3,S_L}^{rstu} (\bar{u}_r P_L u_s) (\bar{e}_t P_L e_u) \\ & \left. + C_{3,S_R}^{rstu} (\bar{u}_r P_R u_s) (\bar{e}_t P_R e_u) + \text{h.c.} \right], \end{aligned} \quad (3.40)$$

with coefficients $C_{3,r}$ at the leptoquark mass scale given by

$$C_{3,\{V_L, V_R\}}^{rstu} = \frac{1}{2\sqrt{2}G_F} \begin{Bmatrix} z_{ts} z_{lr}^* \\ y_{ts}^* y_{ur} \end{Bmatrix} \frac{1}{2m_{S_1}^2}, \quad (3.41)$$

$$C_{3,\{S_L, S_R\}}^{rstu} = \frac{1}{2\sqrt{2}G_F} \begin{Bmatrix} z_{ts} y_{ur} \\ y_{ts}^* z_{ur}^* \end{Bmatrix} \frac{1}{2m_{S_1}^2}, \quad (3.42)$$

$$C_{3,T}^{rstu} = -\frac{1}{4} C_{3,S_L}^{rstu}. \quad (3.43)$$

For the scalar and tensor operators we account for the running of α_s down to the charm-quark mass scale as in Sec. 3.3.2.

For the leptonic decay, we find

$$\Gamma(D^0 \rightarrow \mu\mu) = \frac{f_D^2 m_D^3 G_F^2}{32\pi} \left(\frac{m_D}{m_c} \right)^2 \beta_\mu \left[\left| C_{3,S_L}^{2122} - C_{3,S_R}^{2122} \right|^2 \beta_\mu^2 + \left| C_{3,S_L}^{2122} + C_{3,S_R}^{2122} - \frac{2m_\mu m_c}{m_D^2} (C_{3,V_L}^{2122} + C_{3,V_R}^{2122}) \right|^2 \right] \quad (3.44a)$$

$$= \frac{f_D^2 m_D^3}{512\pi m_{S_1}^4} \left(\frac{m_D}{m_c} \right)^2 \beta_\mu \left[|y_{22}^* z_{21}^* - z_{22} y_{21}|^2 \beta_\mu^2 \eta^2 + \left| \eta (y_{22}^* z_{21}^* + z_{22} y_{21}) - \frac{2m_\mu m_c}{m_D^2} (z_{22} z_{21}^* + y_{22}^* y_{21}) \right|^2 \right], \quad (3.44b)$$

where $\beta_\mu = (1 - 4m_\mu^2/m_D^2)^{1/2} \approx 0.99$, $f_D = 212(2)$ MeV [326] and $\eta = C_{3,S_L}^{2122}(\overline{m}_c)/C_{3,S_L}^{2122}(m_{S_1})$. In the limit that the left-handed contribution dominates, the bound

$$|x_{22}| < 0.46 \hat{m}_{S_1} \quad (3.45)$$

can be derived from the experimental upper limit $\text{Br}(D^0 \rightarrow \mu\mu) < 7.6 \cdot 10^{-9}$ [344] assuming $x_{23} \ll x_{22}$. One can arrange for a mild cancellation between the same- and mixed-chirality terms in Eq. (3.44) by allowing the right-handed couplings $y_{2(1,2)}$ to take $\mathcal{O}(0.1)$ values, however this creates tensions with other meson decays such as $D_s \rightarrow \mu\nu$, $K \rightarrow \mu\nu$ and $D^+ \rightarrow \pi^+ \mu\mu$, and we find no overlapping allowed region.

For the decay $D^+ \rightarrow \pi^+ \mu\mu$, we implement the calculation of Ref. [345]. The branching ratio

$$\text{Br}(D^+ \rightarrow \pi^+ \mu^+ \mu^-) < 8.3 \cdot 10^{-8}, \quad (3.46)$$

is measured by extrapolating spectra over the resonant region [346], while the bounds on the separate high- and low- q^2 bins are

$$\text{Br}(D^+ \rightarrow \pi^+ \mu^+ \mu^-)_{q^2 \in [1.56, 4.00]} < 2.9 \cdot 10^{-8}, \quad (3.47)$$

$$\text{Br}(D^+ \rightarrow \pi^+ \mu^+ \mu^-)_{q^2 \in [0.0625, 0.276]} < 2.5 \cdot 10^{-8}, \quad (3.48)$$

where q^2 ranges are given in GeV^2 . Both Eq. (3.47) and Eq. (3.48) are imposed in our numerical scans.

Meson mixing

A complementary constraint on the left-handed couplings can be derived from $B_s - \bar{B}_s$ mixing, providing a stronger bound than R_K^{vv} for leptoquark masses larger than a few

TeV. The $\text{UT}fit$ collaboration determines constraints on $\Delta F = 2$ processes in terms of the quotient of the meson mixing amplitude and the SM prediction:

$$C_{B_s} e^{2i\phi_{B_s}} \equiv \frac{\langle B_s | \mathcal{H}^{\Delta F=2} | \bar{B}_s \rangle}{\langle B_s | \mathcal{H}_{\text{SM}}^{\Delta F=2} | \bar{B}_s \rangle}, \quad (3.49)$$

and the current best fit values for these parameters are $C_{B_s} = 1.110 \pm 0.090$ and $\phi_{B_s} = (0.42 \pm 0.86)^\circ$ [347]. In the notation of Ref. [347], our leptoquark only generates the effective operator $Q_1^{rs} = C_1^{bs} (\bar{q}_{ra} \gamma_\mu P_L q_s^a) (\bar{q}_{tb} \gamma^\mu P_L q_u^b)$ through box diagrams with neutrinos and leptoquarks in the loop. The relevant operator coefficient, defined at the high scale Λ , is

$$C_1^{bs,S_1}(\Lambda) = \frac{1}{128\pi^2} \left(\sum_r \frac{x_{r3}^* x_{r2}}{m_{S_1}} \right)^2, \quad (3.50)$$

in the limit of vanishing SM fermion masses. The SM processes involve similar box diagrams with top quarks and W bosons in the loop, inducing the Wilson coefficient (see e.g. [348])

$$C_1^{bs,\text{SM}} = \frac{G_F^2 m_W^2}{4\pi^2} (V_{tb}^* V_{ts})^2 S_0(m_t^2/m_W^2), \quad (3.51)$$

where $S_0(x)$ is the well-known Inami-Lim function [349]:

$$S_0(x) = \frac{x^3 - 11x^2 + 4x}{4(x-1)^2} - \frac{3x^3}{2(x-1)^3} \ln x. \quad (3.52)$$

We account for the effect of the running of α_s down to m_W for the coefficient C_1^{bs,S_1} to compare with the SM result using [117]

$$C_1^{bs,S_1}(m_W) = \left[\frac{\alpha_s(m_t)}{\alpha_s(m_W)} \right]^{\frac{\gamma}{2\beta_0^{(5)}}} \left[\frac{\alpha_s(\Lambda)}{\alpha_s(m_t)} \right]^{\frac{\gamma}{2\beta_0^{(6)}}} C_1^{bs,S_1}(\Lambda), \quad (3.53)$$

where $\gamma = 4$ and $\beta_0^{(n_f)} = 11 - 2n_f/3$. The combination of left-handed couplings in Eq. (3.50) is thus required to satisfy

$$C_{B_s} e^{2i\phi_{B_s}} = 1 + \frac{1}{32G_F^2 m_W^2 S_0(m_t^2/m_W^2)} \left(\frac{\eta'}{V_{tb}^* V_{ts}} \sum_r \frac{x_{r3}^* x_{r2}}{m_{S_1}} \right)^2, \quad (3.54)$$

where $\eta' = C_1^{bs,S_1}(m_W)/C_1^{bs,S_1}(m_{S_1})$.

Precision electroweak measurements

The Yukawa interactions of the leptoquark with both left- and right-handed SM fermions give corrections to many electroweak observables. Precision measurements of these have been translated into bounds on dimension-six operators in the literature, and we proceed by applying the results of a recent fit to the electroweak precision data [350]. Specifically, we consider the way in which the couplings x_{rs} and y_{rs} are constrained by precision electroweak measurements of the $Z\ell\bar{\ell}$ couplings g_L and g_R . These receive corrections from leptoquark loops in our model [226]:

$$\begin{aligned} \delta g_X^{e_r} = & (-1)^{\delta_{XR}} \frac{3}{32\pi^2} \frac{m_t^2}{m_{S_1}^2} \left(\ln \frac{m_{S_1}^2}{m_t^2} - 1 \right) |\lambda_{r3}^X|^2 \\ & - \frac{1}{32\pi^2} \frac{m_Z^2}{m_{S_1}^2} \sum_s^2 |\lambda_{rs}^X|^2 \left[\left(\delta_{XL} - \frac{4s_w^2}{3} \right) \left(\ln \frac{m_{S_1}^2}{m_Z^2} + i\pi + \frac{1}{3} \right) - \frac{s_w^2}{9} \right], \end{aligned} \quad (3.55)$$

where $X \in \{L, R\}$, $\lambda_{rs}^L = z_{rs}$ and $\lambda_{rs}^R = y_{rs}$. From Eq. (3.28) and Table 10 of Ref. [350], we calculate the conservative constraints

$$\text{Re}\delta g_L^{e_r} \in [-8.5, 12.0] \cdot 10^{-4}, \quad \text{Re}\delta g_R^{e_r} \in [-5.4, 6.7] \cdot 10^{-4} \quad (3.56)$$

at 95% confidence from the fit results obtained using the large- m_t expansion. The expressions in Eq. (3.56) are conservative since we do not account for correlations between different operators but this does not affect our results in an important way. The results of the fit are sensitive to the interference between the SM and leptoquark contributions, hence only the real part of the $\delta g_I^{e_r}$ is constrained.

3.4 Results and discussion

Below we study the extent to which the experimental anomalies in $R_{D^{(*)}}$, the $b \rightarrow s$ transition and $(g-2)_\mu$ can be accommodated in light of the constraints presented in Sec. 3.3.2. We first consider each anomaly separately and then present the combined parameter space.

For all of the random scans in this section our Monte Carlo strategy proceeds as follows. We sample random real values of the free parameters x_{rs} for $r, s \neq 1$ and leptoquark masses in the range $\hat{m}_{S_1} \in [0.6, 5]$. Values are sampled from the region described in Eq. (3.37)—a necessary condition for the x_{rs} to respect the bound from $B \rightarrow K\nu\nu$, discussed in Sec. 3.3.2—and the perturbativity bound $|x_{rs}| \leq \sqrt{4\pi}$ is imposed at sampling. The values chosen for the right-handed couplings y_{rs} depend on the process studied, although we find that only the y_{2r} and y_{32} are important for our analysis. Two scans are

performed, here labelled I and II. Scan I explores the parameter space associated with the $b \rightarrow s$ anomalies and thus only contains the couplings featuring in Eq. (3.14), while scan II is intended to elucidate the parameter space associated with both the neutral-current and charged-current anomalies, hence y_{32} is included. An important difference between scans I and II is that the former allows $C_{LR}^{S_1} \neq 0$, although this comes at the expense of fewer points passing all of the constraints since the couplings y_{22} and y_{23} are heavily constrained by semileptonic charged-current processes discussed in Sec. 3.3.2. Explicitly, the parameters and respective ranges over which they are scanned are as follows.

Scan I. $6 \cdot 10^6$ points sampled from the region in Eq. (3.37) subject to

- $\hat{m}_{S_1} \in [0.6, 5]$,
- $|x_{rs}| \leq \sqrt{4\pi}$ for $r, s \neq 1$,
- $|y_{22}|, |y_{23}| \leq \sqrt{4\pi}$,
- All other couplings are set to zero.

Of the $6 \cdot 10^6$ points, only $\sim 5 \cdot 10^3$ pass all of the constraints.

Scan II. $6 \cdot 10^6$ points sampled from the region in Eq. (3.37) subject to

- $\hat{m}_{S_1} \in [0.6, 5]$,
- $|x_{rs}| \leq \sqrt{4\pi}$ for $r, s \neq 1$,
- $|y_{23}| \leq 0.05, |y_{32}| \leq \sqrt{4\pi}$,
- All other couplings, including y_{22} , are set to zero.

We will see from the results of scan I that $y_{22} \approx 0$ is preferred for $R_{K^{(*)}}$, hence we take it to vanish in scan II. The range $|y_{23}| \leq 0.05$ is motivated *a posteriori* by the fit to $(g - 2)_\mu$ and the avoidance of a number of constraints. These relaxed requirements on the y_{2r} mean that, of the $6 \cdot 10^6$ generated points, $\sim 3.7 \cdot 10^4$ pass all of the constraints.

For each of the points the relevant observables and operators R_D , R_{D^*} , $C_{LL}^{S_1}$ and $C_{LR}^{S_1}$ are calculated and then the associated coupling constants are filtered through the constraints considered, including $R_{K^*}^{vv} < 2.7$.

Our analysis mainly focuses on answering the following questions: (1) To what extent can the present leptoquark model explain $R_{K^{(*)}}$ while maintaining a SM-like $R_{D^{(*)}}$? (2) To what extent can it explain $R_{D^{(*)}}$ with a SM-like $R_{K^{(*)}}$? (3) How well can all of the anomalies be explained together? These questions are addressed below in the order given above. Throughout this discussion, the relative ease with which this leptoquark model can explain the tension in $(g - 2)_\mu$ is exploited to simplify our study. We do not include its calculation in our numerical scans, since the values of x_{23} and y_{23} required—namely, those satisfying Eq. (3.18)—are such that no constraints are encountered.

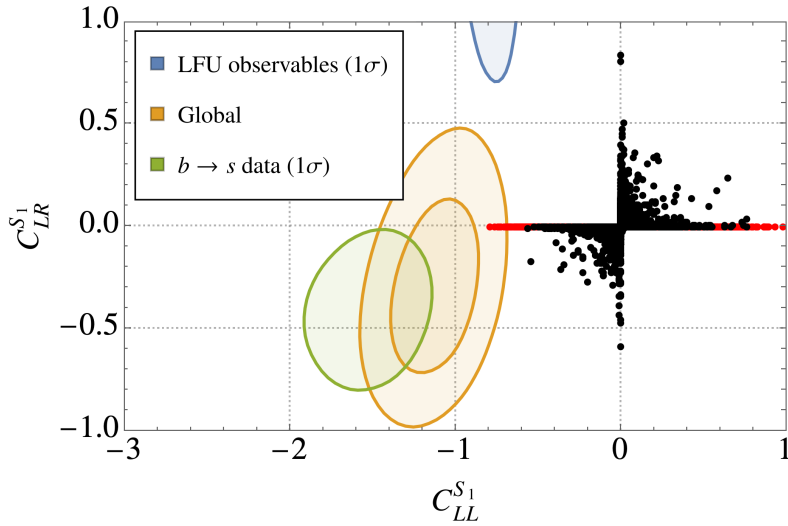
3.4.1 Flavour anomalies

Explaining the $b \rightarrow s$ data. In order for the leptoquark model to explain the measured tensions in the $b \rightarrow s$ transition the left-handed couplings of S_1 to the second and third generation of quarks are necessary to ensure a non-vanishing $C_{LL}^{S_1}$, a parameter space very heavily constrained by the limits from rare meson decays discussed in Sec. 3.3.2. The necessary condition Eq. (3.37) imposed by the bound on $R_{K^*}^{vv}$ can be combined with Eq. (3.14a) to give [226]

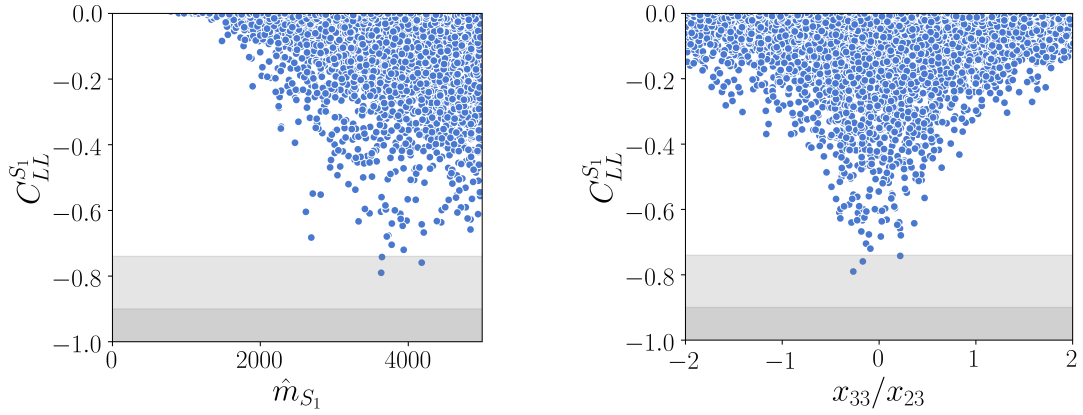
$$\sum_{i=1}^2 |z_{2r}|^2 + \left(1 - \frac{0.77}{\hat{m}_{S_1}^2}\right) |z_{23}|^2 \approx (|V_{us}|^2 + 1) |z_{22}|^2 + \left(1 - \frac{0.8}{\hat{m}_{S_1}^2}\right) |z_{23}|^2 \gtrsim -6C_{LL}^{S_1}. \quad (3.57)$$

It follows that $\mathcal{O}(1)$ couplings to the muon are necessary for the model to meet the benchmark $C_{LL}^{S_1} \approx -1.0$. For small leptoquark masses the model prefers a large $|z_{22}|$ since the top contribution is suppressed through destructive interference between the box diagrams in Fig. 3.3, however the limit from $D^0 \rightarrow \mu\mu$ [see Eq. (3.45)] prohibits such a scenario. Indeed, the analysis of Ref. [227] indicates that the constraint following from the LFU evident in $R_D^{\mu/e}$ also constitutes a very serious stumbling-block for the model's explanation of the $b \rightarrow s$ data for $m_{S_1} \lesssim 1$ TeV. We make progress by performing a random scan in which the leptoquark mass is allowed to vary up to 5 TeV—such large masses have the effect of lifting the suppression on the last term in Eq. (3.57) and permitting larger values for z_{22} according to Eq. (3.45). In addition to the x_{rs} , we turn on the y_{2r} with $r \neq 1$ in order to study the extent to which $C_{LR}^{S_1}$ can contribute. These define the parameters of scan I, introduced above, and we present the results of this scan along with those of scan II, for which $C_{LR} = 0$, in Fig. 3.8 and Fig. 3.9. Consistent with our comments in Section 3.3.2, we find that any phenomenologically viable explanation of the anomalous $b \rightarrow s$ data in this leptoquark model requires $m_{S_1} \gtrsim 2.5$ TeV. Additionally, constraints from the $\tau \rightarrow \mu$ flavour-changing observables require $|x_{32}| > |x_{33}|$ for large $|x_{32}|$. Although the benchmark value $C_{LL}^{S_1} \approx -1.0$ is unattainable in light of the constraints we have considered for a perturbative x_{23} , the model can reduce the tension with the $b \rightarrow s$ data to within $\sim 1.5\sigma$, a significant improvement on the SM. Points in parameter space implying such large, negative values for $C_{LL}^{S_1}$ also entail a vanishing C_{LR} .

Explaining $R_{D^{(*)}}$. We move on to consider the extent to which the leptoquark can explain the anomalies in the $b \rightarrow c$ transition. The fit presented in Fig. 3.2 suggests two scenarios for explaining the measured tensions in the $b \rightarrow c\ell\nu$ decays: (i) new physics only in C_V^{33} ; or (ii) new-physics in C_S^{33} and C_T^{33} , perhaps along with contributions in C_V^{33} . Possibility (i) is the region of parameter space considered in the model's original



(a) The results of scan I (black) and scan II (red) projected onto the $C_{LL}^{S_1}$ - $C_{LR}^{S_1}$ plane. The contours are those of Fig. 1.11 projected onto the chiral basis, originally from Ref. [13]. The blue contours represent the fit to only LFU observables, the green the fit to the other $b \rightarrow s$ data, while the global fit contours are shown in orange. The model can alleviate the tensions in LFU observables to just shy of the 1σ region, a significant improvement on the SM. In this region, $C_{LR}^{S_1} \approx 0$, implying a suppression of the y_{2r} . Agreement with only the LFU observables is not as good.



(b) A scatter plot showing the results of scan II projected onto the $C_{LL}^{S_1}$ - \hat{m}_{S_1} plane. Yellow points imply SM-like values for R_D and R_{D^*} . The constraints imposed by $D^0 \rightarrow \mu\mu$, $D^+ \rightarrow \pi^+\mu\mu$ and $Z \rightarrow \mu\bar{\mu}$ disfavor light leptoquark masses.

(c) A scatter plot of $C_{LL}^{S_1}$ against the ratio x_{33}/x_{23} for parameters subject to scan II. Again, yellow points correspond to SM-like R_D and R_{D^*} . A large, negative value for $C_{LL}^{S_1}$ requires $|x_{23}| > |x_{33}|$ to keep LFV $\tau \rightarrow \mu$ observables at bay.

Figure 3.8: The key results probing the extent to which the model can explain the tensions in $b \rightarrow s$ data. Significant improvement from the SM is possible for leptoquark masses between 3 and 5 TeV, $|x_{23}| > |x_{33}|$ and suppressed y_{2r} . The grey areas in (b) and (c) are the 1 and 2σ allowed regions for $C_{LL}^{S_1}$.

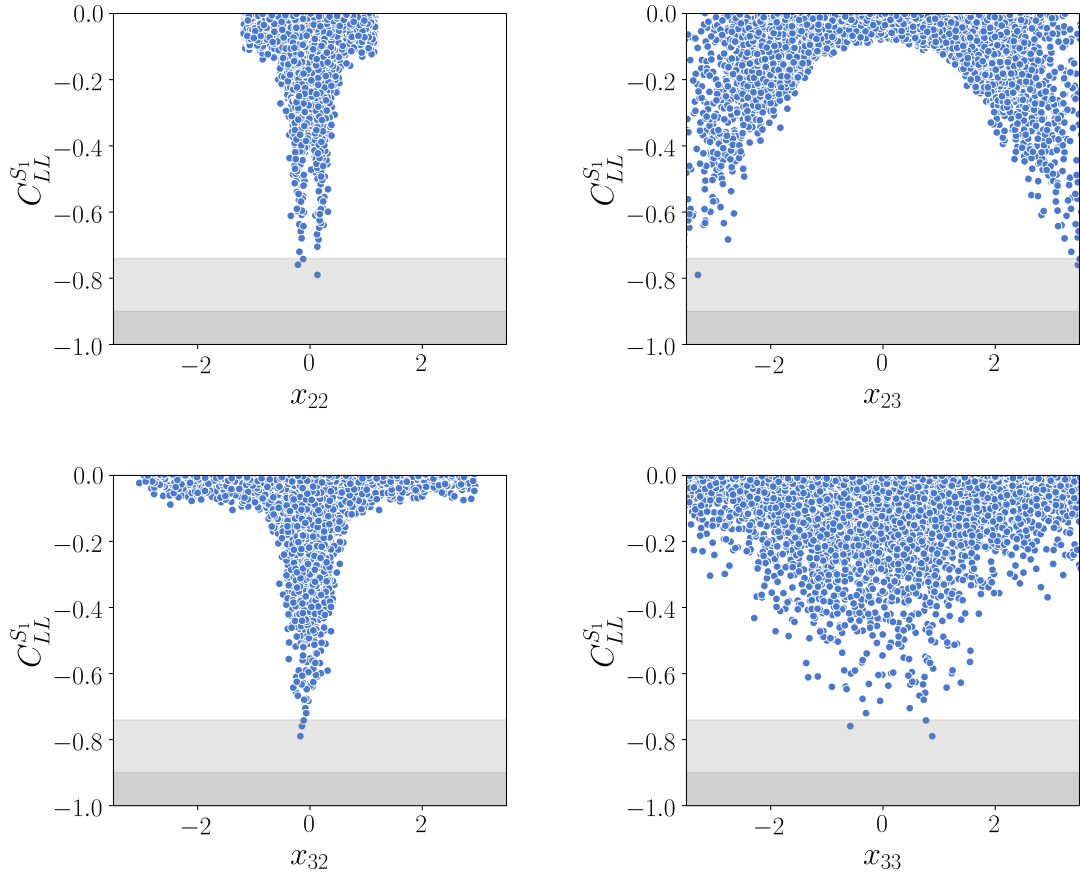


Figure 3.9: Slices through the parameter space investigated through scan II. The value of $C_{LL}^{S_1}$ is plotted against each Yukawa coupling scanned over. Plots against the x_{rs} contain points from scan II and hence 1 and 2σ regions for $C_{LL}^{S_1}$ can be specified since $C_{LR}^{S_1} = 0$; these are shaded grey. Large values of x_{23} are essential for an adequate explanation of the $b \rightarrow s$ data in this model, while small, but non-zero, values for x_{22} are necessary to allow $C_{LL}^{S_1}$ to be negative. The values of x_{23} required to explain the LFU observables to 2σ begin to impinge on the perturbativity constraint $|x_{23}| < \sqrt{4\pi}$. Only points implying SM-like $R_{D^{(*)}}$ are shown.

form. However, we emphasise that the conditions presented in Eq. (3.37) and Eq. (3.56) are sufficient to preclude that effects in C_V^{33} alone could be responsible for the enhancement of the $R_{D^{(*)}}$ ratios. The product $x_{32}^* x_{33}$ is heavily constrained from R_K^{VV} and $B_s - \bar{B}_s$ mixing, as indicated in Fig. 3.7. One could consider generating z_{23} , and therefore C_V^{33} , through quark mixing, thus making do only with a non-zero x_{33} and avoiding these constraints. This set-up, however, requires excessively large values of x_{33} to explain $R_{D^{(*)}}$, causing the leptoquark's contributions to the $Z\tau\bar{\tau}$ coupling to exceed current experimental limits—a result we illustrate in Fig. 3.10. In addition, we find the effects of lepton-flavour violation to be subdued, since such contributions add incoherently to the W -mediated SM processes, and thus entail couplings large enough to conflict with measurements of $B_s - \bar{B}_s$ mixing and precision electroweak observables. Scenario (ii) involves new physics in C_S^{rs} and C_T^{rs} . The most minimal approach here is to turn on only the bottom–tau–neutrino interaction x_{33} and the right-handed tau–charm coupling y_{32} . A non-zero x_{33} will generate C_V^{33} through quark-mixing. We find the coupling y_{32} to be weakly constrained by the precision electroweak measurements discussed earlier: in the limit $|y_{32}| \gg |y_{3(1,3)}|$, the bound

$$|y_{32}| < \frac{3.69 \hat{m}_{S_1}}{\sqrt{1 + 0.39 \ln \hat{m}_{S_1}}}, \quad (3.58)$$

follows from Eq. (3.56). In addition, small values of the muon–top coupling y_{23} will allow sizeable contributions to $(g-2)_\mu$ in the presence of $x_{23} \neq 0$ because of the top-mass enhancement in the mixed-chirality term of Eq. (3.17). This minimal texture involving only third-generation couplings to left-handed quarks comes with the additional benefit that the leptoquark can evade the constraints from measurements of $R_{K^*}^{VV}$ and $B_s - \bar{B}_s$ mixing. In fact, the only serious constraint is that arising from the modification of the $Z\tau\bar{\tau}$ coupling from a large x_{33} , a situation that can be remedied for $y_{32} \sim \mathcal{O}(1)$, allowing a good fit to the $R_{D^{(*)}}$ data for slightly smaller values of x_{33} . A sizeable y_{32} is thus a necessary requirement for this leptoquark model to explain the experimental anomalies in R_D and R_{D^*} . Note also that the measured tension in $(g-2)_\mu$ can be accommodated at the same time since the couplings involved are unimportant for $b \rightarrow c\tau\nu$. Saturating both x_{33} and y_{32} at the perturbativity bound $\sqrt{4\pi}$, we find that an explanation of $R_{D^{(*)}}$ loses viability at ~ 10 TeV.

In Fig. 3.11 we present the results of scan II in the $R_D - R_{D^*}$ plane, while Fig. 3.12 displays the values of the Yukawa couplings from the same scan that lead to interesting R_{D^*} values. Limits on the $B \rightarrow K^* VV$ rate and measurements of $B_s - \bar{B}_s$ mixing constrain the x_{r2} to be small, while large values for x_{33} and y_{32} are necessary since their product appears in the expressions for C_V^{33} , C_S^{33} and C_T^{33} . As discussed above, these large x_{33} values imply dangerous contributions to $Z \rightarrow \tau\tau$, causing few points to stray into the 1σ region. The model can, however, significantly reduce the tension in the $b \rightarrow c\tau\nu$ measurements in a large region of parameter space.

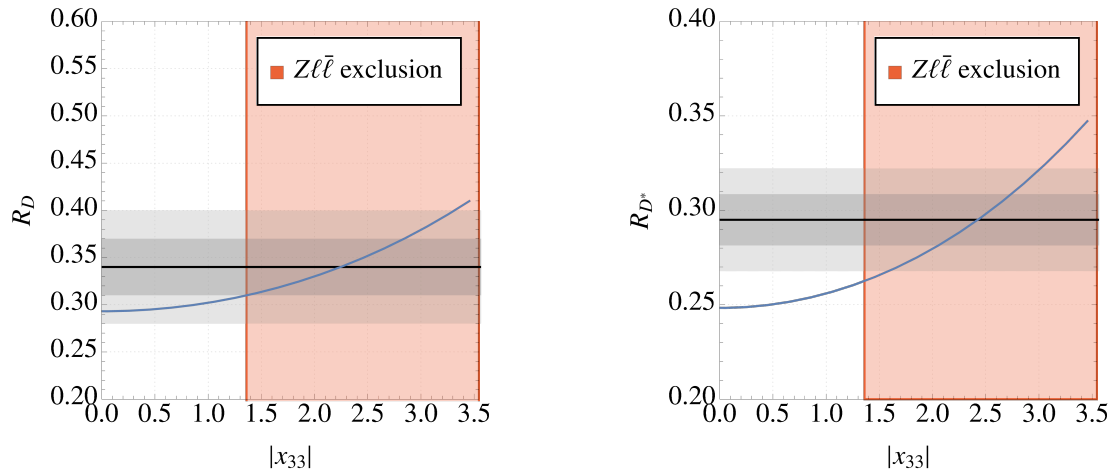


Figure 3.10: The solid blue lines represents the dependence of R_D (left) and $R_{D^{(*)}}$ (right) on $|x_{33}|$ when all other couplings are set to zero and $m_{S_1} = 1 \text{ TeV}$. A non-zero x_{33} generates a small z_{32} through the quark mixing of Eq. (3.4), although the $|x_{33}|$ values required to meet the anomalies become large enough to dangerously modify the $Z \rightarrow \tau\tau$ rate. The values of $|x_{33}|$ excluded by measurements of the $Z\tau\tau$ coupling are shaded red. The solid black line represents the central values of the measurements for R_D and $R_{D^{(*)}}$, and the grey areas are the 1 and 2σ regions.

Other $b \rightarrow c$ observables. The fit we present in Sec. 3.3.1 does not include the less-precisely measured observables $R_{J/\psi}$, $f_L^{D^*}$ and \mathcal{P}_τ^* , introduced in section 1.4.2. We instead use the preferred values from our fit to make predictions for these observables, concentrating on the scalar–tensor solution, since we find this to be the easiest to accommodate with the leptoquark. We note that this solution gives negligible efficiency variation from the SM for the measurement in the D^* mode [351] and displays a q^2 spectrum that agrees well with experiment [196].

In figure 3.13 we project the 2σ preferred region for C_{S_L} (see Table 3.1) onto combinations of $b \rightarrow c$ related observables to illustrate the ability of combined measurements to close in on this scenario. Were possible, we have also shown Belle II 50 ab^{-1} sensitivity [214] in grey centred around the SM prediction in black. Current measurements are shown in red with their 1σ errors in orange. With contributions in the scalar–tensor direction, the S_1 leptoquark’s contributions to $f_L^{D^*}$ are in the opposite direction to current measurements, although still within the 2σ region. If the central value of $f_L^{D^*}$ stays close to where it is, or moves down slightly, the model would then predict $\mathcal{P}_\tau \approx 0.4$, which compromises the potential mild improvement in $R_{J/\psi}$ the model can offer. This scenario leads to a SM-like \mathcal{P}_τ^* , but potentially large deviations in the $\mathcal{P}_\perp^{(*)}$ observables.

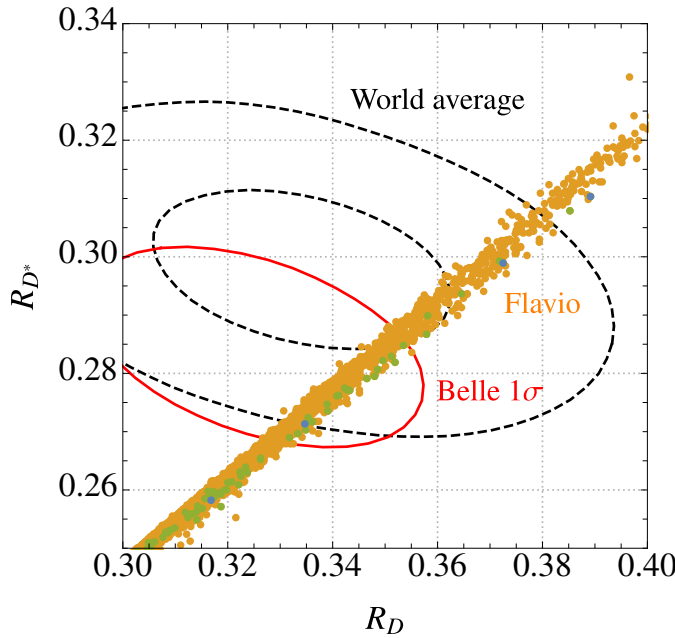


Figure 3.11: The results of scan II (orange points) presented as a scatter plot of R_D against R_{D^*} . The dashed black ellipses represent the 1 , 2 and 3σ contours from our fit with an assumed correlation $\rho = -0.2$, while the solid red curve indicates the 1σ allowed region implied by the Belle measurement from Ref. [15]. The green points place C_{LL} in the 3σ region of the fit of Ref. [13], while the blue points place C_{LL} within the 2σ region. It is clear that the anomalies in $b \rightarrow c\tau\nu$ can be well accommodated in this model, with relatively good agreement with the $b \rightarrow s$ data at the same time. Almost all of the points in the region of interest contribute along the scalar–tensor direction.

Explaining both the $b \rightarrow s$ data and $R_{D^{(*)}}$. In order to establish the full power of the model to explain both $R_{D^{(*)}}$ and the $B \rightarrow s$ data, we perform a complete scan over the 7-dimensional parameter space spanned by the leptoquark mass and the couplings x_r for $r, s \neq 1$, y_{23} and y_{32} —the parameters of scan II. Results from this scan have been presented above in Fig. 3.11, where the green and blue points project the results of scan II into C_{LL} – R_D – R_{D^*} space, where colour is used as the third axis. The green points imply $C_{LL} \in [-1.54, -0.58]$ (the 3σ region), while the blue points have $C_{LL} \in [-1.38, -0.74]$ (the 2σ region) [13]. This plot demonstrates a mild tension between $b \rightarrow s$ and $R_{D^{(*)}}$ in this leptoquark model: points lying within the 1σ region for C_{LL} keep $R_{D^{(*)}}$ SM-like. This can be attributed to the behaviour evident in Fig. 3.8c: large, negative values of $C_{LL}^{S_1}$ require $x_{33} \approx 0$, but x_{33} is essential to this model’s explanation of $R_{D^{(*)}}$, since it features in $C_{V,S,T}^{33}$. At best, we find that the model can explain all of the discrepant measurements to within 2σ , a striking level of consistency with all constraints and anomalies. In both

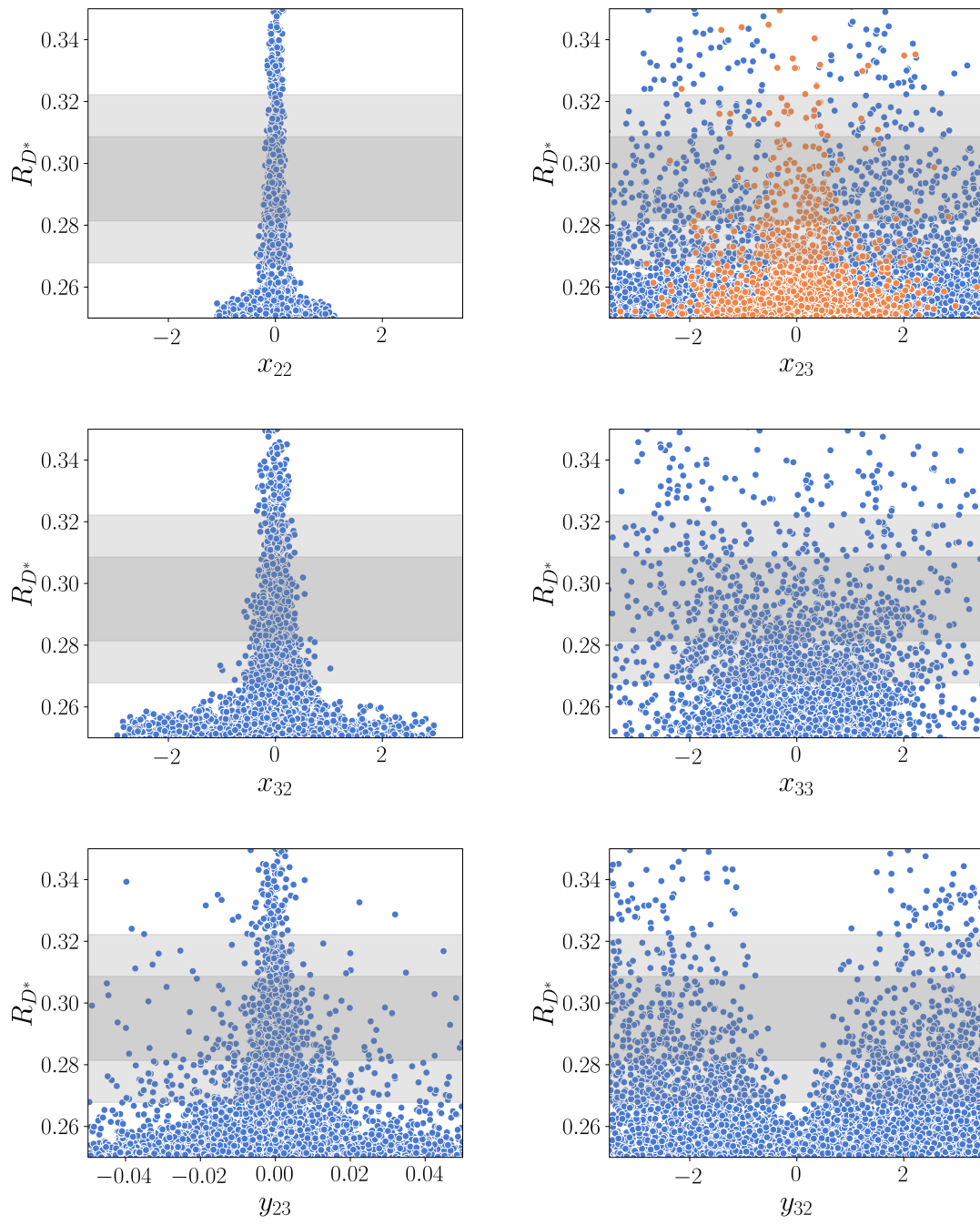


Figure 3.12: Slices through the parameter space of scan II shown against R_{D^*} . The grey bands correspond to the 1 and 2σ regions for the measurements to R_{D^*} . The orange points keep C_{LL} SM-like, while blue points show $> 1\%$ deviation in C_{LL} from the SM prediction. Large values x_{33} and y_{32} are necessary for an adequate explanation of R_{D^*} since these feature in C_S and C_T . Other left-handed couplings must be small to evade constraints from R_K^{VV} and $B_s - \bar{B}_s$ mixing. The results for R_D are qualitatively the same.

cases the $(g - 2)_\mu$ anomaly can also be accommodated.

3.5 Conclusions

We have reconsidered the potential of a scalar leptoquark $S_1 \sim (3, 1, -1/3)$ to explain recent B -physics anomalies: the LFU ratios $R_{K^{(*)}}$ and $R_{D^{(*)}}$, anomalies in branching ratio data and angular observables in the $b \rightarrow s$ transition, as well as the anomalous magnetic moment of the muon.

The leptoquark can reduce the tension in the $R_{D^{(*)}}$ observables to within 1σ of their current experimental values at the price of a sizeable coupling to the right-handed tau and charm quark. The explanation loses viability for masses above about 10 TeV. The leptoquark can also reduce the tensions in the $b \rightarrow s$ data, albeit at some expense to the explanation of $R_{D^{(*)}}$. Explicitly, the region of parameter space in which $R_{D^{(*)}}$ is accommodated to within 1σ implies C_{LL} values differing from the SM value by $< 1\%$, and coupling textures explaining the neutral-current anomalies to within 1σ keep $R_{D^{(*)}}$ within theoretical uncertainty from SM prediction. At best, we find that the model can accommodate the combined tensions in both the $b \rightarrow s$ and $b \rightarrow c$ transitions to within 2σ as well as eliminate the tension in $(g - 2)_\mu$, a remarkable feat for a single-particle extension of the SM.

A crucial new ingredient for this model's explanation of $R_{D^{(*)}}$ is the consideration of the area of parameter space in which the coupling y_{32} is large. The combination of right- and left-handed couplings induces scalar and tensor operators, which lift the chirality suppression of the B -meson decays and consequently produce a sizeable new-physics contribution. Moreover the tensor contribution resolves a possible tension induced by the scalar contribution to leptonic charmed B -meson decays, $B_c \rightarrow \tau\nu$. In our numerical scans we found that the right-handed Yukawa coupling y_{32} need take $\mathcal{O}(1)$ values, while the left-handed couplings x_{22} and x_{32} and the right-handed coupling y_{22} are required to be small. Interestingly, this model predicts a value of R_{D^*} slightly smaller than that suggested by current data, consistent with the Belle results. Future measurements of the asymmetry observable P_τ by Belle II can also test this model, which prefers $P_\tau \approx 0.4$, assuming the central values of $f_L^{D^*}$ and $R_{D^{(*)}}$ remain constant.

An explanation of $b \rightarrow s$ data requires $\mathcal{O}(1)$ couplings of the leptoquark to the muon, a scenario in conflict with the experimental measurements of the decays of the Z boson and D^0 mesons in the context of this leptoquark model. Moreover, the tension between the preferred value of C_{LL} and the lepton universality ratio $R_{D^{(*)}}^{\mu/e}$, pointed out in Ref. [227], is naturally relieved for leptoquark masses $m_{S_1} \gtrsim 1$ TeV. Consequently, the best fit to the $b \rightarrow s$ data (requiring large, negative values of $C_{LL}^{S_1}$) is obtained for large leptoquark masses of ~ 5 TeV with a large hierarchy between the left-handed couplings $|x_{32}| \gg |x_{33}|$ to avoid constraints from $\tau \rightarrow \mu$ LFV transitions.

Apart from the anomalies in lepton flavor universality ratios, the leptoquark can easily account for the anomalous magnetic moment of the muon by an appropriate choice of the product of couplings $y_{23}z_{23}$.

At a future 100 TeV proton–proton collider the pair-production cross section of the leptoquark will be substantially enhanced compared to the LHC with about 1 fb for a 5 TeV leptoquark [352] and thus will be able to probe most of the relevant parameter space for the B -physics anomalies studied here.

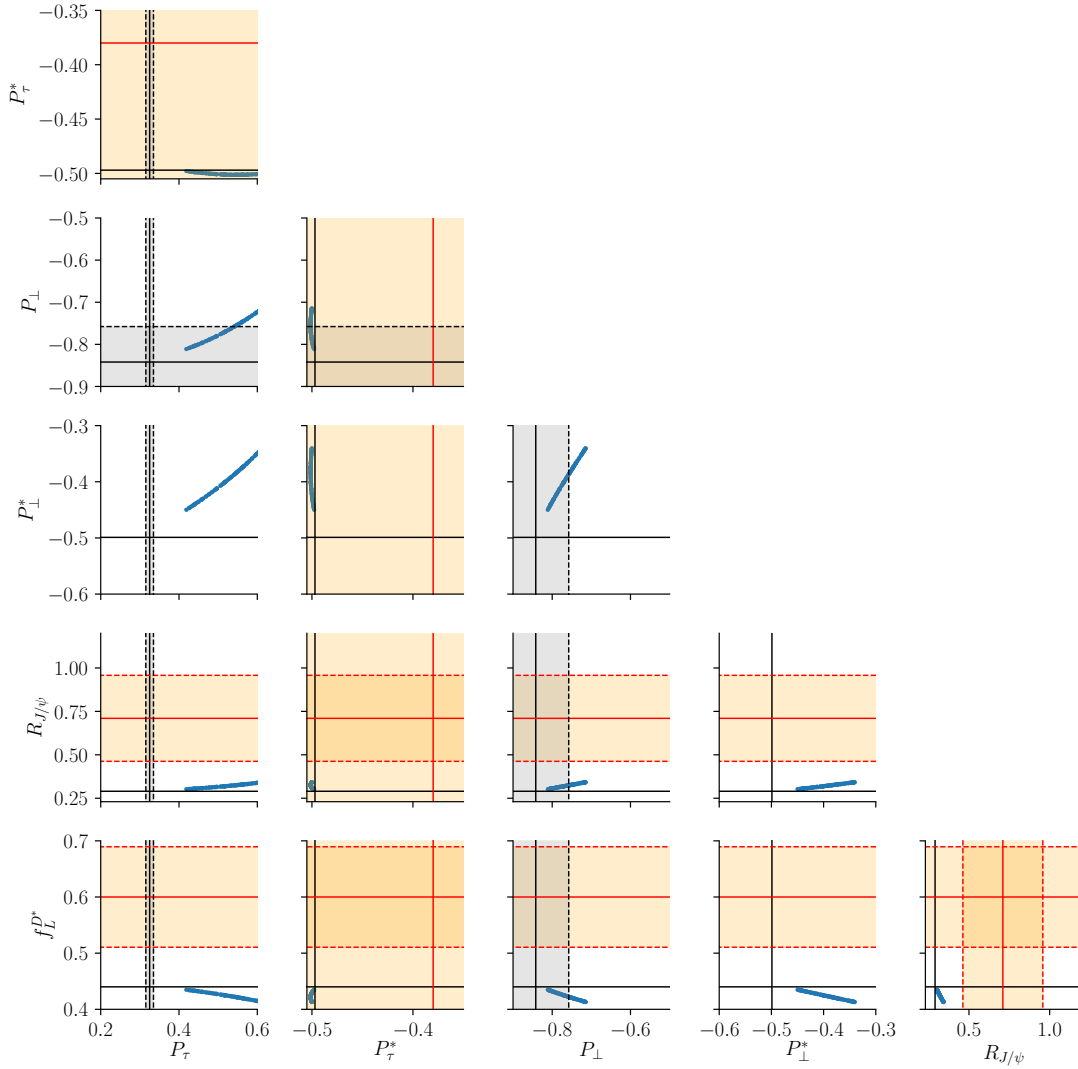


Figure 3.13: A grid plot of the various $b \rightarrow c$ related observables in addition to R_D and R_{D^*} considered in our analysis. Solid black lines represent the SM predictions around which the grey shaded regions are the Belle II 50 ab^{-1} sensitivities [214], bordered by the black dashed lines. Red lines are current measurements and orange regions are their 1σ errors. Where the Belle II sensitivity is unavailable we present only the SM prediction without a shaded region. The blue points explain $R_{D^{(*)}}$ to 2σ .

4

Models of neutrino mass and the flavour anomalies

This chapter is based on the publications ‘Reconsidering the One Leptoquark scenario: flavour anomalies and neutrino mass,’ written in collaboration with Yi Cai, Michael A. Schmidt, and Raymond R. Volkas [2], and ‘A near-minimal leptoquark model for reconciling flavour anomalies and generating radiative neutrino masses,’ written with Innes Bigaran and Raymond R. Volkas [3]. We explore the tantalising connection between models of radiative neutrino mass and explanations of the flavour anomalies. We consider two specific models, and conclude with more general comments about interesting models we choose from our model database. We exclusively use four-component spinor notation in this chapter.

4.1 Introduction

Taken together, the flavour anomalies paint a picture of new physics interacting more strongly with the second and third generations of SM fermions, introducing lepton flavour non-universality and FCNC interactions at energies not significantly higher than the electroweak scale. Interestingly, many of these phenomenological motifs arise naturally in radiative models of neutrino mass, hinting towards the attractive possibility of a common explanation for both phenomena.

In Chapter 2, we presented our model database containing all minimal tree-level

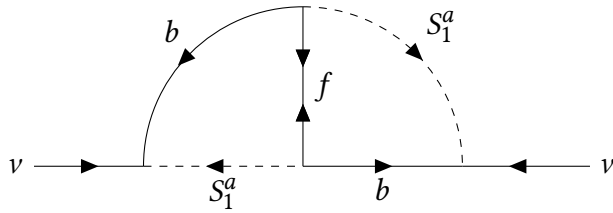


Figure 4.1: Two loop neutrino mass generation in the model of Ref. [16]. For simplicity we consider the case where the leptoquark S_1 couples significantly only to the third generation of quarks. At least two flavours of S_1 are required to meet the neutrino data.

$\Delta L = 2$ models. These give rise to neutrino masses at the loop level with exotic particle content that we have already seen is dominated by (scalar) leptoquarks. In the present chapter we explore the relationship between the flavour anomalies and models of radiative neutrino mass by (i) studying a radiative scenario containing the S_1 leptoquark in detail, (ii) building a more complex model involving an additional leptoquark, $S_3 \sim (3, 3, -\frac{1}{3})$, for a more precise explanation of the anomalies, and (iii) commenting more generally on a more systematic approach to studying the possible relationship between the anomalies and radiative models of Majorana neutrino mass.

Previous work has also considered radiative neutrino mass models whose particle content addresses the $b \rightarrow s$ anomalies, $R_{D^{(*)}}$, and $(g-2)_\mu$, e.g. [262, 286, 292, 300, 353–355]. In Refs. [286, 300] the flavour anomalies are explained through two light scalar or vector leptoquarks whose couplings to the SM Higgs doublet and fermions prohibit a consistent assignment of lepton number to the leptoquarks such that the symmetry is respected. Thus $U(1)_L$ is explicitly broken by two units and the neutrinos gain mass at the one-loop level [356], apart from the imposition of any additional symmetries¹. A general feature of such models is that large amounts of fine-tuning are required to suppress the neutrino mass to the required scale with at least one set of leptoquark–fermion couplings sizeable enough to explain the anomalies.

4.2 A minimal neutrino-mass scenario with S_1

In this section we incorporate the BN leptoquark into a two-loop neutrino mass model also containing the colour octet Majorana fermion $f \sim (8, 1, 0)$. The model can be derived as a tree-level completion of $\mathcal{O}_{11b} = LLQ\bar{d}Q\bar{d}$, in the notation of Table B.1. The model has been studied in detail apart from the anomalies in Ref. [16]. We summarise

¹Mass generation in Ref. [262] occurs at the two-loop level because the Yukawa couplings of one of the leptoquarks to the left-chiral fermions is turned off.

the key features of the model below, and point the reader to this paper for more detail.

Following Ref. [16] we couple the leptoquark S_1 to the Majorana fermion f in order to introduce the lepton-number violating terms $m_f f \bar{f}$ and $w_r \bar{d}_r f S_1$. The neutrino mass is proportional to the product of down-type quark mass matrices, which is dominated by the bottom quark mass. We do not consider the case where a strong hierarchy in the w_r undermines this dominance, and thus only the coupling to the third generation of quarks (w_3) is important for the neutrino mass generation. For this reason we set $w_{1,2} = 0$ to simplify the calculation of the neutrino mass. In this limit the neutrino mass matrix will have unit rank and an additional generation of the leptoquark s_1 is needed to satisfy current oscillation data. Replacing S_1 with ² $S_1^a = (S_1^1, S_1^2)$ in Eq. (3.1), small neutrino masses are generated through the two-loop graph shown in Fig. 4.1 and the neutrino mass is given by

$$M_{ij} \approx 4 \frac{m_f m_b^2}{(2\pi)^8} \sum_{a,b}^2 (x_{i3a} w_{3a}) I_{ab} (x_{j3b} w_{3b}), \quad (4.1)$$

where \mathbf{I} is the matrix of loop integrals in the leptoquark-generation space whose explicit form can be found in Ref. [16]. This expression for the mass matrix can be solved for the x_{r3a} through the Casas–Ibarra procedure [357] to give

$$x_{r3a} = \frac{(2\pi)^4}{2w_{3a}m_b\sqrt{m_f}} U_{rs}^* [\tilde{\mathbf{M}}^{1/2}]_{st} R_{tb} [\tilde{\mathbf{I}}^{-1/2} \mathbf{S}]_{ba}, \quad (4.2)$$

where tildes denote real and positive diagonal matrices, \mathbf{S} diagonalises the matrix \mathbf{I} and m_b is the mass of the bottom quark. We use the best-fit values from the NuFIT collaboration for the neutrino mixing angles and mass-squared differences [7, 358], shown in Fig. 1.2. The mass-squared differences fix the elements of $\tilde{\mathbf{M}}$, since the lightest neutrino in this model is almost massless. In the cases of normal and inverted neutrino mass hierarchy:

$$\mathbf{R}^{\text{NO}} = \begin{pmatrix} 0 & 0 \\ \cos \theta & -\sin \theta \\ \sin \theta & \cos \theta \end{pmatrix}, \quad \mathbf{R}^{\text{IO}} = \begin{pmatrix} \cos \theta & -\sin \theta \\ \sin \theta & \cos \theta \\ 0 & 0 \end{pmatrix}, \quad (4.3)$$

and $\theta \in \mathbb{C}$ parameterises the leptoquark–fermion Yukawa couplings through Eq. (4.2) in such a way that the correct pattern of neutrino masses and mixings is produced. Here we consider the region of parameter space where $m_{S_1^2}, m_f \gg m_{S_1^1}$ so that S_1^1 comes to be identified as the BN leptoquark, while S_1^2 and f are effectively divorced from the flavour anomalies. For this reason we refer to S_1^1 simply as S_1 and suppress the

²We highlight to the reader a redundancy in our notation: here we use a, b, \dots to label the leptoquark generations, not as colour indices, since these play no role in the discussion of this section.

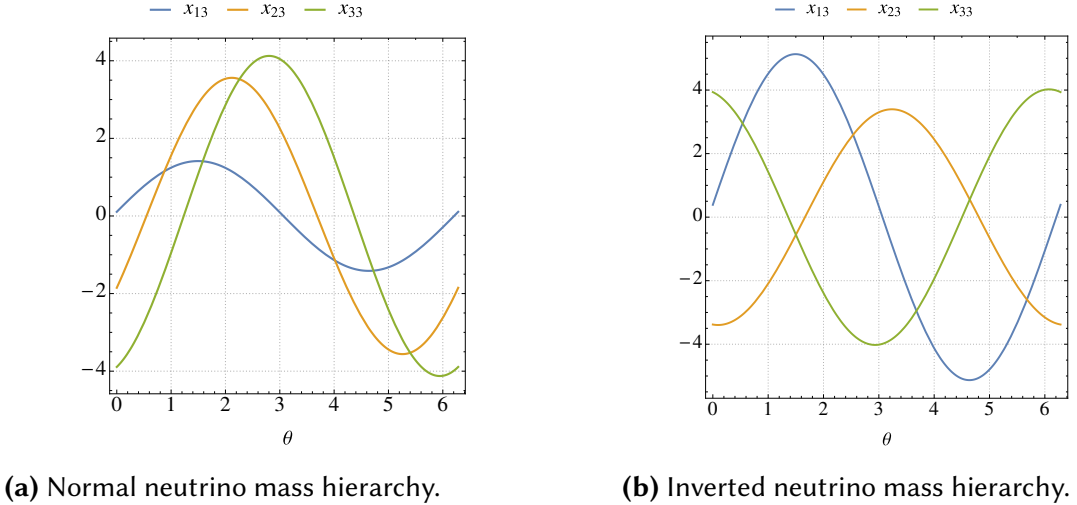


Figure 4.2: Plots of the relative sizes of the couplings of the leptoquark S_1^1 to the bottom quark and the r th neutrino flavour against θ , the Casas–Ibarra parameter, for $m_f = 25 \text{ TeV}$, $m_{S_1^2} = 20 \text{ TeV}$, $m_{S_1^1} = 4 \text{ TeV}$ and $w_3 = 0.003$. We only consider the case $\theta \in \mathbb{R}$ here.

leptoquark-flavour indices for the remainder of the discussion unless a distinction is necessary. The limit $m_{S_1^1} \ll m_{S_1^2}$ also allows for a simplification in the matrix product $\tilde{\mathbf{I}}^{-1/2}\mathbf{S}$ featuring in Eq. (4.2):

$$\tilde{\mathbf{I}}^{-1/2}\mathbf{S} \approx I_{11}^{-1/2} \begin{pmatrix} -i & i/\epsilon \\ 1 & \epsilon \end{pmatrix}, \quad (4.4)$$

where $\epsilon \equiv I_{12}/I_{11} \ll 1$. This flavour structure implies that its contribution to neutrino mixing is small, and thus the PMNS parameters are principally determined by the Yukawa couplings x_{r3a} . We exploit this relative insensitivity to m_f and $m_{S_1^2}$ to simplify our analysis in the following.

The decoupling of f and S_1^2 from the relevant flavour physics makes w_3 an effectively free parameter that acts as a lepton-flavour-blind scaling factor on the couplings of the leptoquark to the third generation of quarks, while θ governs their relative sizes for a given leptoquark flavour. We plot the x_{ij} against real θ values in Fig. 4.2 for the mass choices $m_f = 25 \text{ TeV}$, $m_{S_1^2} = 20 \text{ TeV}$ and $m_{S_1^1} = 4 \text{ TeV}$ with fixed $w_3 = 0.003$. Both the normal and inverted hierarchies are considered.

Both Fig. 4.2 and Eq. (4.2) indicate that, with the inclusion of neutrino mass, the couplings to the electron and electron-neutrino cannot be turned off *ad libitum*. Even a small electron coupling $z_{13} \neq 0$ can generate dangerous contributions to muon–electron conversion in nuclei in the presence of $z_{23} \neq 0$, necessary for the model to alleviate the tensions in the $b \rightarrow s$ transition. We plot the current limit from muon–electron

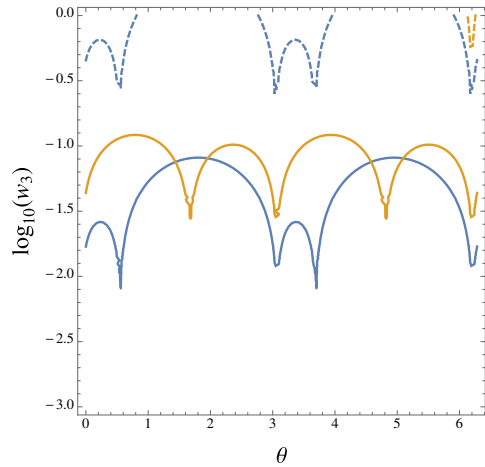


Figure 4.3: The figure shows the current (solid) and expected [17] (dashed) limits from muon–electron conversion in nuclei in the θ – w_3 plane for normal mass ordering (blue) and inverted ordering (orange). The region below each curve is ruled out. The dips at $\theta \approx 3.08$ and $\theta \approx 6.22$ stretch to negative infinity. Aside from accidental cancellation, the values $\theta \approx 3.08, 6.22$ ensure that the coupling to the electron vanishes. Only real values of θ are considered.

conversion experiments in gold nuclei $\text{Br}(\mu^{197}\text{Au} \rightarrow e^{197}\text{Au}) < 7.0 \cdot 10^{-13}$ [21] against θ and w_3 in Fig. 4.3 for both the normal and inverted hierarchies and a range of masses $m_{S_1^1}$. The prospective limit from the COMET experiment: $\text{Br} \sim 10^{-16}$ [17], is also shown. A fit to the neutrino oscillation data while respecting measurements of muon–electron conversion implies a fine-tuning in θ —or, equivalently, z_{31} —to arrange $|z_{31}| \ll |z_{33}|$, pushing the model into a very specific region of parameter space. The required $x_{31} \approx 0$ can be arranged with $\theta \approx 3.08 \pm n\pi$, fixing the ratio $x_{33}/x_{32} = 1.96$ for the normal neutrino mass hierarchy, and $x_{33}/x_{32} = -0.85$ for the inverted hierarchy. Comparison with Fig. 3.8c, however, indicates that neither of the aforementioned ratios can allow large contributions to C_{LL} in the correct direction, although the inverted hierarchy does slightly better than the normal mass ordering. This makes a combined explanation of the $b \rightarrow s$ anomalies and neutrino mass in this model problematic. If, instead, one required that this model explain $R_{D^{(*)}}$, $(g-2)_\mu$ and neutrino mass, the values of x_{33} required are compatible with both the normal and inverted hierarchies, and the model remains agnostic with respect to its preference.

Model 1	Model 2
$S_3 \sim (3, 3, -\frac{1}{3})$	$S_1 \sim (3, 1, -\frac{1}{3})$
$\chi_{L,R} \sim (3, 2, -\frac{5}{6})$	$\chi_{L,R} \sim (3, 2, -\frac{5}{6})$

Table 4.1: Particle content of two radiative models derived from dimension-seven operators identified in our model database [20] that contain S_1 and S_3 . Both models contain the vector-like quark $\chi_L + \chi_R$ whose components mix into the bottom quark.

4.3 A non-minimal model: S_1 and S_3

In the previous chapter it was shown that the BN scenario, although powerful given its simplicity, is restricted in its ability to adequately explain both the neutral- and charged-current anomalies. Additionally, the simple neutrino-mass embedding we study above is incompatible with an explanation of the neutral-current anomalies on account of LFV effects, which must be present in radiative neutrino-mass models. To further explore the extent to which these LFV effects can be circumnavigated in a model of neutrino mass and the flavour anomalies, we build a non-minimal model that also can better accommodate a simultaneous explanation of the $b \rightarrow s$ and $b \rightarrow c$ data.

It is known that a particularly simple model that can accommodate the neutral-current anomalies is that involving the scalar isovector leptoquark $S_3 \sim (3, 3, -\frac{1}{3})$ [273, 359]. The field mediates the $b \rightarrow s\mu\mu$ interaction at tree-level, and $C_{LL} \simeq -1.0$ can be accommodated in the face of almost no other constraints. It is also clear from Fig. 3.11 that the BN leptoquark with contributions along the scalar–tensor direction can explain $R_{D^{(*)}}$ to within the 1σ region of the combined fit. Thus, it seems sensible to construct a radiative neutrino-mass model containing both the S_1 and S_3 leptoquarks in the hope that the LFV bounds can be alleviated with the increased parameter choices. The operator analysis presented in Chapter 2, along with other similar approaches [95, 101, 104], finds two UV models derived from the dimension-seven operators $\mathcal{O}_{3a,b}$ that contain these fields, shown in Table 4.1. In the following we study the combined model that contains the three fields S_1 , S_3 and the vector-like fermion

$$\chi_{L,R} \sim (3, 2 - \frac{5}{6}) \tag{4.5}$$

with the intention that S_1 explain $R_{D^{(*)}}$ at tree-level, S_3 explain the $b \rightarrow s$ data at tree-level, and $\chi_{L,R}$ participate in the neutrino-mass mechanism. Our aim is to explore the extent to which this next-to-minimal model can accommodate neutrino masses, the flavour anomalies and bounds from LFV processes, as a representative example.

4.3.1 The model

The combination of models 1 and 2 of Table 4.1 provides a particle content of

$$\chi_L \sim (3, 2, -\frac{5}{6})_{(2,1)}, \chi_R \sim (3, 2, -\frac{5}{6})_{(1,2)}, S_1 \sim (3, 1, -\frac{1}{3})_S, S_3 \sim (3, 3, -\frac{1}{3})_S$$

for the model. The extension to the SM Lagrangian is $\Delta\mathcal{L} = \mathcal{L}_{\text{int}} + \mathcal{V}$, where

$$\mathcal{L}_{\text{int}} = m_\chi \bar{\hat{\chi}}_L \hat{\chi}_R + \hat{x}_d \bar{\hat{d}}_R H \hat{\chi}_L + (\hat{x}_1 S_1^\dagger - \hat{x}_3 S_3^\dagger) \hat{L} \hat{Q} + \hat{y} \hat{e}_R \hat{u}_R S_1 + (\hat{w}_1 S_1 - \hat{w}_3 S_3) \bar{\hat{\chi}}_R \hat{L} + \text{h.c.} \quad (4.6)$$

and the potential is

$$\begin{aligned} -\mathcal{V} = & \sum_{a \in \{1, 3\}} (m_{S_a}^2 |S_a|^2 + \lambda_a |S_a|^4 + \lambda_{Ha} |S_a|^2 |H|^2) + \lambda_{13} |S_1|^2 |S_3|^2 + \lambda'_{H3} |S_3 H|^2 \\ & + (\kappa H S_1 H^\dagger S_3^\dagger + \text{h.c.}) . \end{aligned} \quad (4.7)$$

Here again, we use hats to indicate interaction-eigenstate fields. Isospin, colour and flavour indices have been suppressed, and we use a to index the leptoquark types. The last term in the potential leads to a mixing between the S_1 and S_3 leptoquarks, governed by κ . We choose to set all quartic terms in the scalar potential to zero for simplicity, since they play no role in the neutrino mass or the anomalies. As this implies $\kappa = 0$ at least at tree-level, we show the leptoquarks as unhatted fields in Eqs. (4.6) and (4.7). Global $U(1)_B$ has been imposed on the Lagrangian to prevent the simultaneous presence of the diquark and lepton–quark couplings for both S_1 and S_3 , since these are together sufficient to mediate tree-level proton decay. The second term in \mathcal{L}_{int} leads to mixing between the down-type quarks and χ . For simplicity, we set the x_d coupling to the first two generations of down-type quarks to zero, *i.e.* $x_d^1 = x_d^2 = 0$, so that there is only mixing between χ and the bottom quark. We will see this to be motivated by the structure of the neutrino-mass matrix in Sec. 4.3.2. We choose to label the $SU(2)_L$ components of $\chi_{L,R}$

$$\hat{\chi}_X = \begin{pmatrix} \hat{B}_X \\ \hat{Y}_X \end{pmatrix}, \quad (4.8)$$

where $X \in \{L, R\}$. The fields $\hat{B}_{L,R}$ mix with the interaction-eigenstate bottom quark \hat{b}_X :

$$\begin{pmatrix} b_X \\ B_X \end{pmatrix} = \begin{pmatrix} \cos \theta_X & \sin \theta_X \\ -\sin \theta_X & \cos \theta_X \end{pmatrix}^\dagger \begin{pmatrix} \hat{b}_X \\ \hat{B}_X \end{pmatrix}, \quad (4.9)$$

forming the mass eigenstates B_X and b_X . The physical masses are given by

$$m_b^2 = m_b^2 - m_{bB}^2 \frac{m_\chi^2}{m_\chi^2 - m_b^2}, \quad m_B^2 = m_\chi^2 + m_{bB}^2 \frac{m_b^2}{m_\chi^2 - m_b^2}, \quad (4.10)$$

with $m_{bB} = x_d^3 v / \sqrt{2}$, $m_{\hat{b}} = y_b v / \sqrt{2}$, and

$$\theta_L = \sin^{-1} \frac{m_{bB} m_\chi}{m_\chi^2 - m_{\hat{b}}^2}, \quad \theta_R = \sin^{-1} \frac{m_{bB} m_{\hat{b}}}{m_\chi^2 - m_{\hat{b}}^2}. \quad (4.11)$$

Using the expressions given in Eq. (3.2), we move from the interaction to the charged-fermion mass basis. We again use $\check{\nu}_L$ to represent the weak-eigenstate neutrino fields. The pertinent parts of the Lagrangian are

$$\begin{aligned} \mathcal{L} \supset & x_1^{rs} \check{\nu}_L^r \hat{d}_L^s S_1^\dagger - [\mathbf{x}_1 \mathbf{V}^\dagger]^{rs} e_L^r u_L^s S_1^\dagger + y^{rs} e_R^r u_R^s S_1^\dagger + w_1^r (\bar{Y}_R e_L + \bar{B}_R \check{\nu}_L) S_1 \\ & + \frac{x_3^{rs}}{\sqrt{2}} \check{\nu}_L^r d_L^s S_3^{1/3} + \frac{1}{\sqrt{2}} [\mathbf{x}_3 \mathbf{V}^\dagger]^{rs} e_L^r u_L^s S_3^{1/3} + x_3^{rs} e_L^r \hat{d}_L^s S_3^{4/3} - [\mathbf{x}_3 \mathbf{V}^\dagger]^{rs} \check{\nu}_L^r u_L^s S_3^{-2/3} \\ & + w_3^r (\bar{Y}_R e_L^r - \bar{B}_R \check{\nu}_L^r) S_3^{-1/3} + w_3^r \bar{B}_R e_L^r S_3^{-2/3} + w_3^r \bar{Y}_R \check{\nu}_L^r S_3^{4/3} + \text{h.c.} \end{aligned} \quad (4.12)$$

and we have now dropped the hats, except on the $d^3 = b$ and B fields, since the mixing of Eq. (4.9) is still to be accounted for. We write flavour indices as superscripts here and in the remainder of this chapter in order to accommodate the leptoquark labels a on the coupling constants x_a and z_a . As in Chapter 3, we define

$$\mathbf{z}_a = \mathbf{x}_a \mathbf{V}^\dagger \quad (4.13)$$

with $a \in \{1, 3\}$ for the left-handed couplings of the leptoquarks to up-type quarks.

4.3.2 Neutrino mass

In this model there are two one-loop neutrino-mass mechanisms that are *a priori* active: one involving S_1 and $\chi_L + \chi_R$, the other involving S_3 and $\chi_L + \chi_R$. The neutrino-mass diagrams are shown in Fig. 4.4 in a generic way. There are also two-loop diagrams coming about from the closure of \mathcal{O}_8 , generated by the S_1 and $\chi_L + \chi_R$ model. Neutrino masses arising from \mathcal{O}_8 are very suppressed (see Tables 2.1 and B.1) and so we disregard these contributions as subdominant.

We calculate these one-loop diagrams in the mass-basis, finding

$$[\mathbf{m}_\nu]_{rs} = \frac{3m_B m_b}{16\pi^2} m_{bB} \sum_{a \in \{1, 3\}} (2 - \delta_{a3}) [x_a^{r3} w_a^s + (r \leftrightarrow s)] \frac{1}{m_B^2 - m_{S_a}^2} \log \frac{m_B}{m_{S_a}}, \quad (4.14)$$

in the sensible limit that $m_b \ll m_\chi$. The relative factor of 2 arises from the different group-theory factors relevant for each leptoquark. The mass matrix has rank 2 and therefore the model implies one almost massless neutrino. We have encountered this

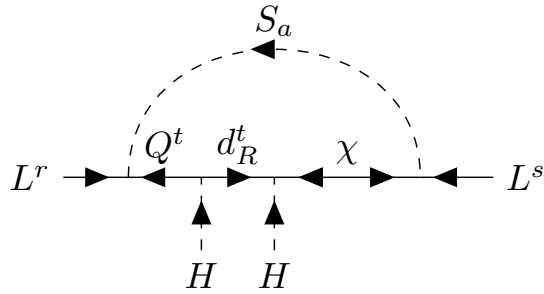


Figure 4.4: The one-loop neutrino-mass diagrams in the combined S_1 , S_3 and $\chi_L + \chi_R$ model, shown here in the unbroken phase. *A priori* there are two neutrino-mass mechanisms operating in this model: one with S_1 in the loop, and another with S_3 . It is clear from the diagram that the neutrino-mass matrix is proportional to the down-quark mass matrix.

mass-matrix structure before in Eqs. (2.62), and we apply the same Casas–Ibarra-like parametrisation of the Yukawa couplings:

$$\begin{aligned} x_a^{r3} &= \frac{\zeta}{\sqrt{2m_0(a)}} [\sqrt{m_2}\mathbf{u}_2^* + i\sqrt{m_3}\mathbf{u}_3^*]_r , \\ w_a^r &= \frac{1}{\zeta\sqrt{2m_0(a)}} [\sqrt{m_2}\mathbf{u}_2^* - i\sqrt{m_3}\mathbf{u}_3^*]_r , \end{aligned} \quad (4.15)$$

where

$$m_0(a) = (1 + \delta_{a1}) \frac{3m_b m_B}{16\pi^2} \frac{1}{m_B^2 - m_{S_a}^2} \log \frac{m_B}{m_{S_a}} , \quad (4.16)$$

and $\zeta \in \mathbb{C}$ is a free parameter.

Up to this point we have been general in our treatment of the neutrino mass in this model, keeping the leptoquark index a throughout. For the rest of our analysis we make the simplifying choice that $a = 3$, *i.e.* that only S_3 couples to $\chi_L + \chi_R$ and participates in the neutrino-mass mechanism. Our reasoning is as follows. The main goal of our study is to explore the extent to which bounds from LFV can be avoided in a model of neutrino-mass and the flavour anomalies. A key point is that the parametrisation of Eq. (4.15) does not allow x_a^{13} to be very small compared to x_a^{23} and x_a^{33} for any value of ζ . (This is a very different situation to that seen in Chapter 3, where specific values of the Casas–Ibarra parameter θ let the electron coupling vanish, at the cost of fixing the ratio of the muon and tau couplings to the leptoquark.) Our analysis of the S_1 leptoquark model showed that an adequate explanation of the $b \rightarrow c$ anomalies requires S_1 to live at scales of a few TeV. We anticipate that values of $|\zeta|$ sufficiently large to imply x_1^{33} sizeable enough to explain $R_{D^{(*)}}$, would also be too large to avoid muon–electron LFV

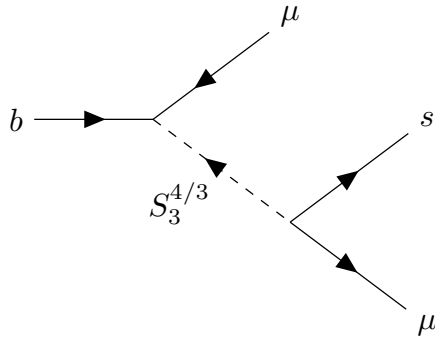


Figure 4.5: The figure shows the diagram through which the $|Q| = 4/3$ component of S_3 mediates the $b \rightarrow s\mu\mu$ decays.

bounds. Indeed, this has been shown in Ref. [3]. For this reason, we let only S_3 couple to $\chi_L + \chi_R$ and generate the neutrino masses. Thus, we expect an intimate connection in this model between the neutrino-mass parameters and those governing the $b \rightarrow s$ physics.

4.3.3 Flavour anomalies

Below we discuss the explanation of the flavour anomalies in our model. Specifically, we write down the leading-order contributions to C_9 and C_{10} , $R_{D^{(*)}}$, and $(g-2)_\mu$ from the particle content in the model. In summary, the dominant contributions are S_3 contributing to $C_9 = -C_{10}$ to explain the $b \rightarrow s$ data, and S_1 generating $C_S = -4C_T$ to solve the $R_{D^{(*)}}$ discrepancies. The S_1 leptoquark also participates in the usual top-mass-enhanced loop-level mechanism to explain $(g-2)_\mu$.

Neutral-current anomalies

As mentioned briefly above, the model is constructed so that S_3 can give the dominant contribution to $C_9 = -C_{10}$ [the direction characterised by new physics in the operator \mathcal{O}_{LL} of Eq. (3.13)]. The $|Q| = 4/3$ component of the isotriplet generates \mathcal{O}_{LL} at tree-level, through the diagram shown in Fig. 4.5. As discussed in detail in Chapter 3, S_1 contributes to the operators $\mathcal{O}_{LL} \sim \mathcal{O}_9 - \mathcal{O}_{10}$ and $\mathcal{O}_{LR} \sim \mathcal{O}_9 + \mathcal{O}_{10}$ at the loop level, with the relevant expressions given by Eq. (3.14). We take this contribution to be negligible, and concentrate on the tree-level generation of the operator through S_3 . Meeting the

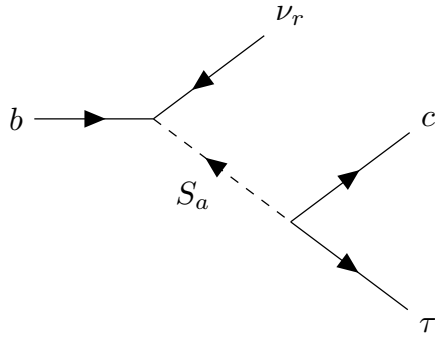


Figure 4.6: The leading-order diagrams contributing to R_D and R_{D^*} in our model. There are additional LNV diagrams that we ignore in our analysis.

best-fit value requires³

$$C_9 = -C_{10} = -\frac{\pi \cos(\theta_L)}{2\sqrt{2}G_F\alpha} \frac{1}{V_{tb}V_{ts}^*} \frac{x_3^{23}x_3^{22*}}{m_{S_3}^2} \approx -0.53, \quad (4.17)$$

corresponding to the choice of couplings

$$|x_3^{23}x_3^{22*}| \cos \theta_L \approx \left(\frac{m_{S_3}}{24 \text{ TeV}} \right)^2. \quad (4.18)$$

Note that the couplings above are derived from a global fit to real valued Wilson coefficients [13]. To ensure a $C_9 = -C_{10}$ consistent with this, we fix the value of C_9 such that $\text{Im } C_9 \approx 0$. This requires a constraint to be imposed on the Casas-Ibarra parametrisation, since Eq. (4.2) in general generates complex x_3^{23} , a point we elaborate on in Sec. 4.3.5.

Charged-current anomalies

There are a number of contributions to $b \rightarrow c\tau\nu_r$ diagrams in our model. Those which dominate are shown in Fig. 4.6: the ones mediated by the $|Q| = 1/3$ leptoquarks (of which one is present in the S_3 multiplet). The additional diagrams involve only S_3 and are lepton-number violating, and thus we expect them to be suppressed by the same combination of parameters required to render the neutrino masses sufficiently small. The diagrams in Fig. 4.6 imply the same set of Wilson coefficients discussed in earlier chapters, see e.g. Eq. (3.8). The neutrino flavour index r is left general since the process could be lepton-flavour violating, although only the vector contribution with

³Here and throughout this chapter, we use $C_{9,10}$ to represent the new-physics contribution to the muonic operator for brevity. We freely interchange between $C_{9,10}$ and $C_{9,10}^{\mu\mu}$, but we intend no difference between these.

a tau neutrino (*i.e.* C_V with $r = 3$) constructively interferes with the SM diagram. The contributions are

$$[C_S]_r = \frac{\sqrt{2} \cos \theta_L}{8G_F V_{cb}} \left(\frac{x_1^{r3} y_1^{32*}}{m_{S_1}^2} \right), \quad (4.19)$$

$$[C_V]_r = \frac{\sqrt{2} \cos \theta_L}{8G_F V_{cb}} \left(\frac{x_1^{r3} z_1^{32*}}{m_{S_1}^2} - \frac{x_3^{r3} z_3^{32*}}{2m_{S_3}^2} \right), \quad (4.20)$$

$$[C_T]_r = -\frac{1}{4} [C_S]_r. \quad (4.21)$$

We will often use the notation that $C_{S,V,T}$, written without an explicit index r , corresponds to $[C_{S,V,T}]_3$. In Chapter 3, we saw that contributions to the vector operator C_V could only be mild on account of constraints from $B \rightarrow K^*vv$ and \bar{B}_s - B_s mixing. These constraints are reassessed in this model to additionally account for the role of S_3 in Sec. 4.3.4, although the simplest approach is to fit $C_S = -4C_T$ to the best-fit value of Table 3.1: $C_S = -4C_T = 0.14$. This implies

$$x_1^{33} y_1^{32*} \cos \theta_L \approx \left(\frac{m_{S_1}}{1.6 \text{ TeV}} \right)^2, \quad (4.22)$$

although contributions to the vector operator are inevitable for both leptoquarks since $x_{1,3}^{33} \neq 0$, and z^{32} is therefore necessarily also non-zero on account of Eq. (4.13).

Anomalous magnetic moment of the muon

There are three diagrams contributing to the anomalous magnetic moment of the muon in this model. These are known results, *e.g.* [226, 268], and so we simply quote and interpret the results. The contributions are

$$a_\mu^{S_1} = \sum_r \frac{m_\mu m_{u_r}}{4\pi^2 m_{S_1}^2} \left(\frac{7}{4} - \ln \frac{m_{S_1}^2}{m_{u_r}^2} \right) \text{Re}(y^{2r} z_1^{2r}) - \frac{m_\mu^2}{32\pi^2 m_{S_1}^2} \left(\sum_r |z_1^{2r}|^2 + \sum_r |y^{2i}|^2 \right), \quad (4.23)$$

for S_1 [the same as Eq. (3.17) with the analogous notation for this model], and

$$a_\mu^{S_3} = -\frac{m_\mu^2}{32\pi^2 m_{S_3}^2} \sum_r |z_3^{2r}|^2, \quad (4.24)$$

for S_3 . The same-chirality terms are suppressed by $m_\mu^2/m_{S_a}^2$, and so negligibly small. This implies non-vanishing right-handed couplings for the S_1 leptoquark. This is the same situation as in Chapter 3, where it was found that the scalar-tensor solution to $R_{D(*)}$ could also accommodate the measured value of a_μ easily, since y^{23} is a free parameter unrelated to any other anomalies and relatively unconstrained.

4.3.4 Constraints

Below we discuss the constraints relevant to our model and the limits we require in our subsequent analysis. We restrict our main discussion to what we consider to be the minimal scenario to explain the B anomalies and $(g - 2)_\mu$. Here, the isotriplet leptoquark S_3 explains the neutral-current anomalies, while the $SU(2)_L$ singlet S_1 explains the charged-current anomalies with contributions to the scalar, tensor and vector operators. Minimally, this implies non-zero values for x_1^{33} and y^{32} . The top-mass enhancement evident in Eq. (4.23) means that only small values for the product of y^{23} and $z_1^{23} = x_1^{23}$ are required to explain the anomalous magnetic moment of the muon.

The S_3 leptoquark, which participates in the neutrino-mass generation, must have a non-zero Yukawa coupling to the electron, and this is the most important phenomenological consequence for the constraints we consider. This, together with the relation in Eq. (4.13), means that constraints from processes involving the first generation of SM fermions cannot be avoided completely. In fact, the hierarchy present in the leptoquark couplings to charged leptons is fixed by measured PMNS matrix elements, while the couplings to light quarks are suppressed by CKM matrix elements. Explicitly

$$\begin{aligned} z_3^{rs} &= x_3^{r3} V_{s3}^* \\ &= V_{s3}^* \frac{\zeta}{\sqrt{2m_0}} (\sqrt{m_2} u_{r2}^* + i\sqrt{m_3} u_{s3}^*) , \end{aligned} \quad (4.25)$$

where $m_0 = m_0(3)$ of Eq. (4.15). Of course, the Lagrangian in Eq. (4.12) contains many more parameters than these. For simplicity, we turn off any couplings not immediately related to the anomalies or neutrino mass. In reality these need only be small enough to respect any limits placed on them by experiment⁴.

The constraints presented in this section assume the following set of non-zero Yukawa couplings:

$$\mathbf{x}_1 = \begin{pmatrix} 0 & 0 & 0 \\ 0 & 0 & 0 \\ 0 & 0 & x_1^{33} \end{pmatrix}, \quad \mathbf{y} = \begin{pmatrix} 0 & 0 & 0 \\ 0 & 0 & y^{23} \\ 0 & y^{32} & 0 \end{pmatrix} \quad \text{and} \quad \mathbf{x}_3 = \begin{pmatrix} 0 & 0 & x_3^{13} \\ 0 & x_3^{22} & x_3^{23} \\ 0 & 0 & x_3^{33} \end{pmatrix}. \quad (4.26)$$

It is understood that $w_1^r = 0$, since we work in the regime where S_1 does not contribute to the neutrino mass. We discuss other Yukawa-coupling textures throughout this section where appropriate. Notably, we comment briefly on explaining $R_{D^{(*)}}$ with contributions only to the vector operator C_V , and the constraints associated with this scenario are presented in this section as well.

⁴Note that constraints from neutrinoless double beta decay are not explicitly considered in this analysis. The contributions are CKM suppressed and the couplings involved are exactly those involved in the neutrino-mass generation. As such, new-physics contributions from this model to this process are negligible.

This parameter space is explored in the context of the constraints implied by fits to the flavour anomalies and neutrino mass. We use a suite of computational machinery for most of the calculations, and this setup is discussed briefly below. Where appropriate we explicitly write out the dominant contributions to observables where we consider that this provides useful insight. Some observables are also calculated separate to these methods, and these are also discussed in detail below.

We use the computational frameworks SARAH [360, 361] and SPheno [361] to calculate Wilson coefficients, decay rates and a subset of the flavour observables, defined by FlavorKit [360], in our analysis. A full discussion of the underlying machinery and relation between these programs can be found in Ref. [362]. In addition, we use flavio [279] to calculate some flavour observables from the Wilson-coefficient output files of SPheno. This allows us to consider a broader range of flavour observables in our analysis. The renormalisation-group running of Wilson coefficients in flavio is implemented using the Wilson package [363].

Collider bounds

The ATLAS collaboration has dedicated searches for the heavy quarks B and Y . The most stringent limits come from searches for singly produced Y decaying to Wb , where a limit of $m_Y \gtrsim 1.85$ TeV is set with 95% confidence [364]. Limits on the B fermion come from searches for singly produced B decaying as $B \rightarrow Hb$ [365], or pair-produced B decays through $B \rightarrow Zb/Hb/Wt$ [366]. The latter search gives the more stringent limit of $m_B \gtrsim 1.34$ TeV. In our phenomenological analysis, we take m_χ to be much larger than these scales, safely avoiding the direct-production bounds.

Collider limits relevant for the scalar leptoquark S_1 are discussed in Sec. 3.2. Here we extend the discussion to S_3 as well. The $|Q| = 1/3$ component of S_3 contributes to the same decay channels as S_1 , that happen to be the most constraining. Thus, the direct-production limits quoted in Sec. 3.2 apply also to the S_3 leptoquark.

In our model couplings of third-generation quarks to the muon through S_3 are unavoidable. Here, limits from $t\bar{t}\mu\bar{\mu}$ searches can exclude leptoquark masses below 1.3 TeV, assuming $\text{Br}(S_a \rightarrow t\mu) \approx 100\%$ [367]. Additionally, since S_3 must couple the strange quark to the muon, dimuon-dijet searches are also potentially relevant. In this case, the limits can be as large as $m_{S_3} \gtrsim 1.5$ TeV [306, 368].

High- p_T dilepton production through the S_3 leptoquark has also been shown to provide interesting constraints and signatures for the leptoquarks in our model [222]. The leptoquark contributes to the processes $pp \rightarrow \ell\ell$ through tree-level t -channel graphs whose effects can alter the tail of the differential cross-sections for $pp \rightarrow \ell\ell$. We take the limits from Ref. [222] for the muon and tau modes derived from 36 fb^{-1} of ATLAS data at 13 TeV [369, 370]. We derive bounds on $bb \rightarrow ee$ and extract the 3000 fb^{-1} ATLAS sensitivity for the electron and muon modes from Ref. [371]. These bounds are shown

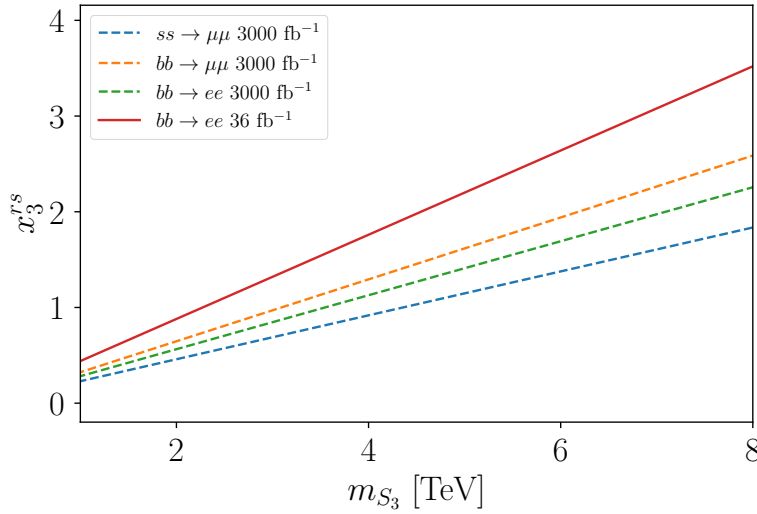


Figure 4.7: The figure shows the current (solid) and projected (dashed) upper limits on the couplings of the S_3 leptoquark to down-type quarks and charged leptons x_3^{rs} . The limits are from LHC searches in $pp \rightarrow \ell\ell$ high- p_T tails at 13 TeV from ATLAS [372], derived from Ref. [371]. The Yukawa coupling being constrained depends on the process. For example, $ss \rightarrow \mu\mu$ will constrain x_3^{22} .

in Fig. 4.7. We find that the limits on $cc \rightarrow ee$ and $uu \rightarrow ee$ give less stringent bounds on $|\zeta|$, and thus we do not include them in our numerical scans.

Fermion mixing

Of central importance in this model is the mixing generated by the terms $x_d^3 \bar{b}_R H \chi_L + \text{h.c.}$ between the b quark and the quark field χ_L . This mixing is a necessary ingredient for the violation of lepton number by S_3 , and plays a governing role in the overall scale of the neutrino mass $m_0 = m_0(3)$ according to Eq. (4.2). Its size also dictates the extent to which $\Delta L = 2$ neutrino final states are important to consider, for example in $B \rightarrow K^{(*)} \nu \nu$.

The mixing of the b with χ leads to new contributions to the oblique electroweak parameters S and T . These have been measured to high precision by LEP [373]. The mixing also leads to an alteration of the Zbb coupling at tree-level, for which global electroweak fits have suggested a small deviation from the SM value, e.g. [350]. The dominant contributions to these effects are encapsulated in the effective dimension-six Lagrangian generated by the heavy $\chi_L + \chi_R$ at the scales probed by experiment:

$$\mathcal{L}_{\chi}^{(6)} \supset \frac{C_{Hd}^{33}}{m_{\chi}^2} (H^\dagger i D_\mu H) (\bar{b}_R \gamma^\mu b_R) + \frac{C_{dH}^{33}}{m_{\chi}^2} \gamma_b (H^\dagger H) (\bar{Q}_3 b_R H). \quad (4.27)$$

The first operator modifies the electroweak precision observables discussed above and the second affects Higgs measurements and is currently poorly constrained. We take the 2σ bounds on the operator coefficient C_{Hd}^{33} from the electroweak fit performed in Ref. [350] $C_{Hd}^{33} \in [-0.38, 0.03]$ to derive

$$|x_d^3| \in [0.25, 0.87] \left(\frac{m_\chi}{\text{TeV}} \right). \quad (4.28)$$

This implies the bounds $\theta_R \in [0.06, 0.21]$ at 95% confidence, with central value $\theta_R \approx 0.16$. This agrees with Ref. [374] which studied the effects of the doublets $\chi_L + \chi_R$ and other vector-like quarks. The relation $\theta_L \approx \frac{m_b}{m_\chi} \theta_R$ from Eq. (4.11) implies the $\cos \theta_L$ factors appearing in Eq. (4.17) and Eq. (4.19)–(4.21) do not suppress the contributions to the anomalous observables⁵. Restricting this mixing to be small consequentially reduces the mass-splitting between the components of the exotic doublets $\chi_L + \chi_R$, such that $m_\chi \sim m_B \sim m_Y$ remains a valid approximation.

Lepton-flavour violation

Both leptoquarks contribute to lepton-flavour violating processes, although the diagrams involving both the left- and right-handed Yukawa couplings of S_1 are generally dominant due to the top-enhancement in expressions, see *e.g.* Ref. [16]. In our analysis we calculate LFV observables using the SARAH and SPheno pipeline discussed above. We present a summary of the processes we include in our phenomenological analysis along with the limits we impose in Table 4.2.

Z decays

The leptoquarks S_1 and S_3 will modify the Z coupling to leptons through one-loop diagrams involving SM quarks and the vector-like quark $\chi_L + \chi_R$. For the contributions involving leptoquarks and SM fermions we use the results of Ref. [375], which include corrections due to the external momenta of the Z . The additional diagrams with the vector-like quark in the loop are shown in Fig. 4.8. We find the contributions to the leptonic Z couplings from these to be

$$\delta g_L^{rs} = \frac{w_3^s w_3^{r*}}{768\pi^2 x(x-1)^4} [x_Z f(x) + x_Z^2 g(x)] \quad (4.29)$$

⁵This result is a stronger, and more general, constraint than that quoted from direct searches in Ref. [364], which suggests a 95% confidence interval of $\sin \theta_R \in [0.17, 0.55]$ for $m_\chi \sim 800$ GeV.

Process	Limit
$\text{Br}(\mu \rightarrow e\gamma)$	$< 4.2 \cdot 10^{-13}$
$\text{Br}(\mu \rightarrow 3e)$	$< 1.0 \cdot 10^{-12}$
$\frac{\sigma(\mu\text{Au} \rightarrow e\text{Au})}{\sigma(\mu\text{Au} \rightarrow \text{capture})}$	$< 7.0 \cdot 10^{-13}$
$\text{Br}(\tau \rightarrow e\gamma)$	$< 3.3 \cdot 10^{-8}$
$\text{Br}(\tau \rightarrow \mu\gamma)$	$< 4.4 \cdot 10^{-8}$
$\text{Br}(\tau \rightarrow 3\mu)$	$< 2.1 \cdot 10^{-8}$
$\text{Br}(\tau \rightarrow 3e)$	$< 2.7 \cdot 10^{-8}$

Table 4.2: The table shows the limits we take on the LFV processes considered in our analysis [21]. These are calculated using SARAH and SPheno.

where $x \equiv m_\chi^2/m_{S_3}^2$, $x_Z \equiv m_Z^2/m_{S_3}^2$ and the functions $f(x)$ and $g(x)$ are

$$\begin{aligned} f(x) = & 3x(x-1) \left[(4x^3 - 30x + 20) - (x-1)(19x^2 - 53x + 28) \log x \right] \\ & + 6x \cos^2 \theta_W (x-1) \left[(x-1)(x^2 - 17x + 10) + 2(x^3 + 6x - 4) \log x \right] \end{aligned} \quad (4.30)$$

$$\begin{aligned} g(x) = & 5(x-1)(x^3 - 5x^2 + 13x + 3) + 60x \log x \\ & + \cos^2 \theta_W [4(x-1)(x^3 - 5x^2 + 13x + 3) - 48x \log x] . \end{aligned} \quad (4.31)$$

The couplings w_3^ℓ are inversely proportional to ζ , and thus we expect these contributions to be suppressed when ζ and the χ - b mixing parameter x_d^3 are sizeable.

Charm-meson decays

Since couplings to up-type quarks and charged leptons cannot be avoided for the leptoquark that couples to χ , the physics of operators of the form $O_{rstu} \sim (u_r \Gamma u_s)(\ell_t \Gamma \ell_u)$ is important to study. Here, we consider the leptonic decays of the D^0 meson, since a sizeable coupling to the charm quark can assist in the explanation of the large effects seen in the charged current anomalies [345].

In Sec. 3.3.2 we saw that S_1 generates the entire spectrum of operators which can in principle contribute to the leptonic decays of the D^0 , since it interacts with both left- and right-chiral SM fermions. Concretely, the dimension-six Lagrangian of Eq. (3.40),

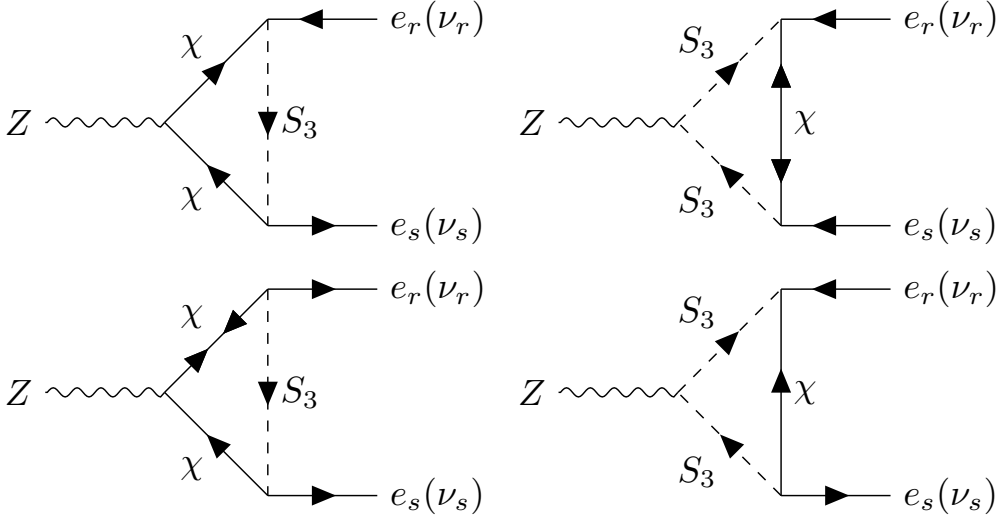


Figure 4.8: The figure shows the additional diagrams contributing to $Z \rightarrow e_r e_s$ and $Z \rightarrow \nu_r \nu_s$ involving both χ and S_3 in our model. In all cases, there are diagrams with B and Y in the loop with different charge states of S_3 .

repeated here in a slightly altered notation:

$$\begin{aligned} \mathcal{L}_{u_r u_s e_t e_u} = & \frac{4G_F}{\sqrt{2}} \left[C_{D,V_R}^{rstu} (\bar{u}_r \gamma_\mu P_R u_s) (\bar{e}_t \gamma^\mu P_R e_u) + C_{D,V_L}^{rstu} (\bar{u}_r \gamma_\mu P_L u_s) (\bar{e}_t \gamma^\mu P_L e_u) \right. \\ & + C_{D,T}^{rstu} (\bar{u}_r \sigma_{\mu\nu} P_R u_s) (\bar{e}_t \sigma^{\mu\nu} P_R e_u) + C_{D,S_L}^{rstu} (\bar{u}_r P_L u_s) (\bar{e}_t P_L e_u) \\ & \left. + C_{D,S_R}^{rstu} (\bar{u}_r P_R u_s) (\bar{e}_t P_R e_u) + \text{h.c.} \right], \end{aligned} \quad (4.32)$$

is generated with tree-level contributions from both leptoquarks:

$$C_{D,V_L}^{rstu} = \frac{1}{2\sqrt{2}G_F} \left(\frac{z_1^{ts} z_1^{ur*}}{2m_{S_1}^2} + \frac{z_3^{ts} z_3^{ur*}}{m_{S_3}^2} \right), \quad (4.33)$$

$$C_{D,V_R}^{rstu} = \frac{1}{4\sqrt{2}G_F} \frac{y^{ts*} y^{ur}}{m_{S_1}^2}, \quad (4.34)$$

$$C_{D,S_L}^{rstu} = \frac{1}{4\sqrt{2}G_F} \frac{z_1^{ts} y^{ur}}{m_{S_1}^2}, \quad (4.35)$$

$$C_{D,S_R}^{rstu} = \frac{1}{4\sqrt{2}G_F} \frac{y^{ts*} z_1^{ur*}}{m_{S_1}^2}, \quad (4.36)$$

$$C_{D,T}^{rstu} = -\frac{1}{4} C_{D,S_L}^{rstu}, \quad (4.37)$$

although in our phenomenological analysis only the relevant S_3 couplings are present.

As highlighted in Ref. [345], the strongest experimental constraints on these coefficients come from measurements of the process $D^0 \rightarrow \mu\mu$, for which Eq. (3.44) is relevant. We impose the experimental upper limit $\text{Br}(D^0 \rightarrow \mu\mu) < 7.6 \cdot 10^{-9}$ [344]. Contributions to the electronic mode from the vector operators are helicity suppressed and we ensure $|\gamma^{1r}| \ll 1$ in all numerical scans to avoid contributions to the electronic scalar and tensor operators.

Bottom-meson decays and mixing

Here we consider the decays $B \rightarrow K^{(*)}vv$ and constraints from $\bar{B}_s - B_s$ mixing, found to be very important constraints on the BN scenario for explaining R_D and R_{D^*} .

We saw in Sec. 3.3.2 that S_1 contributed to the decays $B \rightarrow K^{(*)}vv$ through contributions to a vector four-fermion operator. There are similar contributions to the same operator

$$\mathcal{O}_{vv}^{rs} = \frac{8G_F}{\sqrt{2}} \frac{\alpha}{4\pi} V_{tb} V_{ts}^* [\bar{v}_r \gamma_\mu P_L v_s] [\bar{s} \gamma^\mu P_L b], \quad (4.38)$$

also from S_3 in this case. That is:

$$C_{vv}^{rs} = \frac{\cos \theta_L}{2\sqrt{2} G_F V_{tb} V_{ts}^*} \frac{4\pi}{\alpha} \left(\frac{x_1^{r3} x_1^{s2*}}{m_{S_1}^2} + \frac{x_3^{r3} x_3^{s2*}}{2m_{S_3}^2} \right). \quad (4.39)$$

The presence of both contributions presents the possibility of arranging for a cancellation. This approach has been employed in the literature to recover an explanation of $b \rightarrow c$ data with only contributions to the vector operator [285]. We impose $R_{K^*}^{vv} < 2.7$, as in Sec. 3.3.2, in our numerical analysis.

The process of $B_s - \bar{B}_s$ mixing provides a complementary constraint on the same couplings involved in the $b \rightarrow svv$ processes. It was found in Chapter 3 that the process leads to a weaker constraint than $B \rightarrow Kv v$ and $B \rightarrow K^*vv$ for low S_1 masses, but becomes relevant for masses larger than a few TeV. In our model, we have contributions from both the isosinglet and isotriplet leptoquarks through box diagrams with neutrinos and charged leptons in the loop. These contribute to the operator C_1^{bs} ,

$$\mathcal{L}_{\Delta B=2} \supset C_1^{bs} (\bar{b} \gamma_\mu P_L s)(\bar{b} \gamma^\mu P_L s), \quad (4.40)$$

where colour indices are contracted within parentheses. The combination $C_{B_s} \exp 2i\phi_{B_s} = \Delta m_s^{\text{exp}} / \Delta m_s^{\text{SM}}$ is calculated using SPheno [361, 362, 376], and we impose the UTfit collaboration's result [347]

$$C_{B_s} = 1.110 \pm 0.090 \quad (4.41)$$

in our numerical scans. We will work with small imaginary parts for the couplings fixed by the neutrino mass and we maintain $\phi_{B_s} \approx 0$ for the phase, consistent with UTfit's result.

Summary of constraints

In Tables 4.2 and 4.3 we present summaries of the constraints of this section. The tables contain the observables we consider in our later phenomenological analysis as well as the limits we require.

4.3.5 Results and discussion

Below we explore the extent to which this model can accommodate the charged- and neutral-current anomalies, the anomalous magnetic moment of the muon and neutrino mass in light of the constraints presented in the previous section.

First, we review the minimal setup introduced at the beginning of Section 4.3.4 and present the results of our Monte Carlo analysis. We also comment briefly on non-minimal scenarios.

Monte Carlo analysis

In the minimal scenario the deviations in $R_{D^{(*)}}$ are explained by the isosinglet leptoquark S_1 with contributions in the direction $C_{S_L}(m_{S_1}) = -4C_T(m_{S_1})$, implying $\mathcal{O}(1)$ values for the couplings x_1^{33} and y^{32} [2, 222, 378]. Contributions to the vector operator are more heavily constrained since they necessarily imply large effects in $B \rightarrow K^{(*)}\nu\nu$ and $B_s - \bar{B}_s$ mixing, in the absence of any kind of cancellation. The S_1 particle also explains the anomalous magnetic moment of the muon with the values of y^{23} and $z_1^{23} = x_1^{23}$ fixed according to Eq. (4.23). The limits derived in Ref. [3] and sketched out in Sec. 4.3.2 suggest the extent to which S_1 can contribute to the generation of neutrino masses is small. Since we consider suppressed leptoquark mixing, this means there is no connection between the neutrino-mass mechanism and the anomalies in $R_{D^{(*)}}$ and $(g-2)_\mu$ in this model. For this reason, we fix m_{S_1} and the couplings involved in Eq. (4.23) and Eq. (4.19) to meet the respective central values to explain these deviations. Explicitly, the conditions

$$\text{Re}(x_1^{23}y^{23}) \approx \frac{0.004\hat{m}_{S_1}^2}{1 + \log \hat{m}_{S_1}} \quad \text{and} \quad x_1^{33}y^{32} \approx 2.7C_S\hat{m}_{S_1}^2, \quad (4.42)$$

[with \hat{m}_{S_1} defined as in Eq. (3.6)] are met with $m_{S_1} = 2\text{ TeV}$, $C_S = 0.14$, $x_3^{33} = 0.7$, $y^{32} = 2.15$, $y^{23} = 0.5$ and $x_1^{23} = 0.02$ in all results presented in this section. Many of

Process	Quantity	Requirement
$ss \rightarrow \mu\mu$	$ x_3^{22} $	$< 0.41m_{S_3}/\text{TeV}$ [222]
$bb \rightarrow \mu\mu$	$ x_3^{23} $	$< 0.58m_{S_3}/\text{TeV}$ [222]
$ss \rightarrow \tau\tau$	$ x_3^{32} $	$< 0.54m_{S_3}/\text{TeV}$ [222]
$bb \rightarrow \tau\tau$	$ x_3^{33} $	$< 0.80m_{S_3}/\text{TeV}$ [222]
$bb \rightarrow ee$	$ x_3^{13} $	$< 0.44m_{S_3}/\text{TeV}$ [371]
$Z \rightarrow bb$	C_{Hd}^{33}	$\in [-0.38, 0.03]$ [350]
$\tau \rightarrow \eta e$	Br	$< 9.2 \cdot 10^{-8}$
$\tau \rightarrow \pi e$	Br	$< 8.0 \cdot 10^{-8}$
$\tau \rightarrow \phi\mu$	Br	$< 8.4 \cdot 10^{-8}$
$Z \rightarrow e^\pm \mu^\mp$	Br	$< 7.5 \cdot 10^{-7}$
$Z \rightarrow e^\pm \tau^\mp$	Br	$< 9.8 \cdot 10^{-6}$
$Z \rightarrow \mu^\pm \tau^\mp$	Br	$< 1.2 \cdot 10^{-5}$
$Z \rightarrow e_r e_s$	g_L	$\in [-8.5, 12] \cdot 10^{-4}$
$Z \rightarrow e_r e_s$	g_R	$\in [-5.4, 6.7] \cdot 10^{-4}$
$Z \rightarrow \nu_r \nu_s$	N_ν	within 2.9840 ± 0.0164
$D^0 \rightarrow \mu\mu$	Br	$< 7.6 \cdot 10^{-9}$ [344]
$B^+ \rightarrow K^+ e^\pm \mu^\mp$	Br	$< 9.1 \cdot 10^{-8}$
$B^0 \rightarrow K^{0*} e^\pm \mu^\mp$	Br	$< 1.8 \cdot 10^{-7}$
$B_s \rightarrow \mu^\pm e^\mp$	Br	$< 5.4 \cdot 10^{-9}$
$B \rightarrow D \ell \nu$	$R_D^{\mu/e} = \frac{\text{Br}(B \rightarrow D \mu \nu)}{\text{Br}(B \rightarrow D e \nu)}$	within 0.995 ± 0.090 [329]
$B \rightarrow D^* \ell \nu$	$R_{D^*}^{e/\mu} = \frac{\text{Br}(B \rightarrow D^* e \nu)}{\text{Br}(B \rightarrow D^* \mu \nu)}$	within 1.04 ± 0.10 [319]
$B_s - \bar{B}_s$ mixing	C_{B_s}	$\in [0.942, 1.288]$ [347]
$B \rightarrow K \nu \nu$	$r_K^{\nu \nu} = \frac{\text{Br}}{\text{Br}_{\text{SM}}}$	< 3.9 [341]
$B \rightarrow K^* \nu \nu$	$r_{K^*}^{\nu \nu} = \frac{\text{Br}}{\text{Br}_{\text{SM}}}$	< 2.7 [341]
$b \rightarrow s\gamma$	Br	$\in [-0.17, 0.24]$ [377]
$B_c \rightarrow \tau\nu$	Br	$< 30\%$ [217]
$K \rightarrow \ell \nu$	$r_K^{\mu/e} = \frac{\text{Br}(K \rightarrow e \nu)}{\text{Br}(K \rightarrow \mu \nu)}$	within $(2.488 \pm 0.018) \cdot 10^{-5}$

Table 4.3: The table is a summary of the constraints considered in this section, not also mentioned in Table 4.2. In cases where opposite-sign lepton pairs can have differing flavour, we choose the observable with both combinations of signs averaged. For the rare tau decays not elsewhere referenced, we have included only those which we found gave most competitive constraints. Where citations are omitted the requirements are taken from Ref. [21].

the implications of explaining $R_{D^{(*)}}$ with $C_{S_L}(\Lambda) = -4C_T(\Lambda)$ have been discussed in the literature [213, 378, 379], and we have expanded on this in Sec. 3.4.

The isoscalar scalar S_3 explains the neutral-current anomalies and participates in the neutrino-mass generation. Thus, the couplings entering the expression for $C_9^{\mu\mu} = -C_{10}^{\mu\mu}$ [Eq. (4.17)] are fixed by the Casas–Ibarra parametrisation, itself following from the structure of the neutrino-mass matrix. A consequence of this is that the x_3^{r3} take complex values and in general $\text{Im}(C_9^{\mu\mu}) \neq 0$. Indeed, for $\zeta \in \mathbb{R}$ the imaginary part of $C_9^{\mu\mu}$ is much larger than the real part, since $\text{Re}(x_3^{23}) = \sqrt{m_2/m_3}\text{Im}(x_3^{23})$ from Eq. (4.15). Although $\text{Im}C_9^{\mu\mu} > \text{Re}C_9^{\mu\mu}$ may lead to an acceptable explanation of the $b \rightarrow s$ anomalies (see e.g. Appendix C of Ref. [160]), most fits in the literature assume $\text{Im}C_9^{\mu\mu} = 0$ and we aim to reproduce this in our model as well. The simplest way to do this is to assume $\arg \zeta \approx \pi/2$, so that ζ is mostly imaginary. This now implies $\text{Re}(x_3^{23}) = \sqrt{m_3/m_2}\text{Im}(x_3^{23})$, and so the muonic couplings of S_3 are mostly real.

One may worry that the central value of δ_{CP} (used in our numerical analysis) or a non-zero value for the Majorana phase α_2 will spoil the desired $\text{Im}C_9^{\mu\mu} \ll \text{Re}C_9^{\mu\mu}$. Using $\text{Im}C_9^{\mu\mu}/\text{Re}C_9^{\mu\mu} = \tan \arg C_9^{\mu\mu}$ as a measure of the relative size of imaginary part of $C_9^{\mu\mu}$, we find

$$\begin{aligned} \tan \arg C_9^{\mu\mu} &\approx -\cot \arg \zeta \\ &+ \sqrt{\frac{m_2}{m_3}} [0.085 \cos(\alpha_2 + \delta_{CP}) - 0.72 \cos \alpha_2] \csc^2 \arg \zeta + \mathcal{O}\left(\frac{m_2}{m_3}\right), \end{aligned} \quad (4.43)$$

for our model, derived from Eq. (4.15) and Eq. (4.17). This clarifies that the effects of the phases are subleading in $\sqrt{m_2/m_3}$. In figure 4.9 we plot $\text{Im}(x_3^{r3})/\text{Re}(x_3^{r3})$ for $r = 1, 2, 3$ as contours with varying $\arg \zeta$ and α_2 . This illustrates the behaviour discussed above but also investigates the effect on the other leptonic couplings. It is evident that the choice $\arg \zeta \approx \pi/2$ also leaves the tau coupling mostly real, although this cannot be said for the electron coupling where the dependence on α_2 is significant. We nevertheless proceed with the choice $\arg \zeta = \pi/2$ in our numerical analysis and account for the possibility of a large imaginary part in the coupling x_3^{13} .

To explore the extent to which this scenario can explain the flavour anomalies and neutrino mass, we perform a random scan over the 5 free parameters of the setup: $|\zeta|$, x_3^{22} , m_{S_3} , m_χ , α_2 . Random values are drawn uniformly over the intervals defined for these parameters in Table 4.4. Notably, the Yukawa coupling x_d^3 is fixed to $0.25m_\chi/\text{TeV}$, the lower edge of the 2σ region from Eq. (4.28) needed to explain the small discrepancy in $Z \rightarrow b\bar{b}$. We generate $2 \cdot 10^6$ points which are filtered through all of the constraints presented in section 4.3.4.

The leptoquark S_3 mediates highly-constraining processes of muon–electron conversion in nuclei at tree-level, and the couplings involved are directly related to those that explain the neutrino masses and the $b \rightarrow s$ anomalies.

We find that only about 12% of the points in our numerical scan are rejected on the basis of a constraint, but from among these almost all are disallowed because they

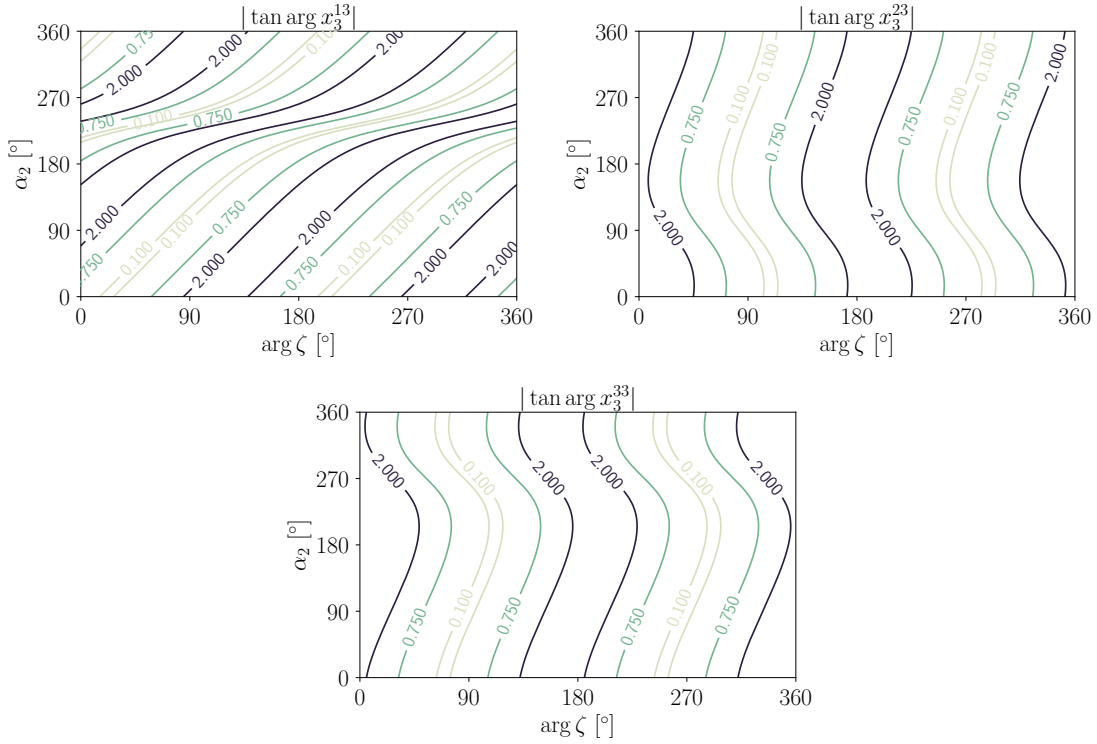


Figure 4.9: Contours of $|\tan \arg x_3^{r3}| = |\text{Im}(x_3^{r3})/\text{Re}(x_3^{r3})|$ with varying $\arg \zeta$ and Majorana phase α_2 . The index r enumerates over charged-lepton flavours. It is clear that the choice $\arg \zeta \approx \pi/2$ ensures $\text{Im}x_3^{r3} \ll \text{Re}x_3^{r3}$ for the muon and tau couplings ($r = 2, 3$). The ratio of the imaginary and real parts of the electron coupling ($r = 1$) varies significantly with α_2 . The Dirac phase and all other neutrino parameters have been set to their central values.

violate the muon–electron conversion bound given in Table 4.2. In Fig. 4.10 we present the results of our random scan with slices through the parameter space and various projections. We find that our model requires muon–electron conversion in Gold nuclei at a rate no less than $2 \cdot 10^{-13}$ to accommodate the preferred value of $C_9^{\mu\mu}$. The COMET [380–383] and Mu2e [384–386] experiments have projected sensitivities of $\text{Br}(\mu\text{Al} \rightarrow e\text{Al}) \lesssim 10^{-16}$ at 90% confidence⁶. These will provide an improvement on the current limit by four orders of magnitude, and will test and potentially falsify this scenario. Interestingly, our model cannot simultaneously avoid the muon–electron conversion bound and explain the $b \rightarrow s$ anomalies with a vanishing Majorana phase α_2 , a result made clear in Fig. 4.11a. There, it is also apparent that the constraint can be

⁶Although COMET and Mu2e will measure muon–electron conversion in Aluminium, we nevertheless display the result on the same plot since we find that the calculations in Gold and Aluminium differ by less than an order of magnitude.

Parameters	$ \zeta $	x_3^{22}	m_{S_3}	m_χ	α_2
Interval	$[1, 600]$	$[0, \sqrt{4\pi}]$	$[1, 30]$ TeV	$[1, 10]$ TeV	$[0, 2\pi]$

Table 4.4: The table shows the intervals from which the corresponding free parameters are randomly drawn for our Monte Carlo analysis. All other parameters are fixed, see the text for details.

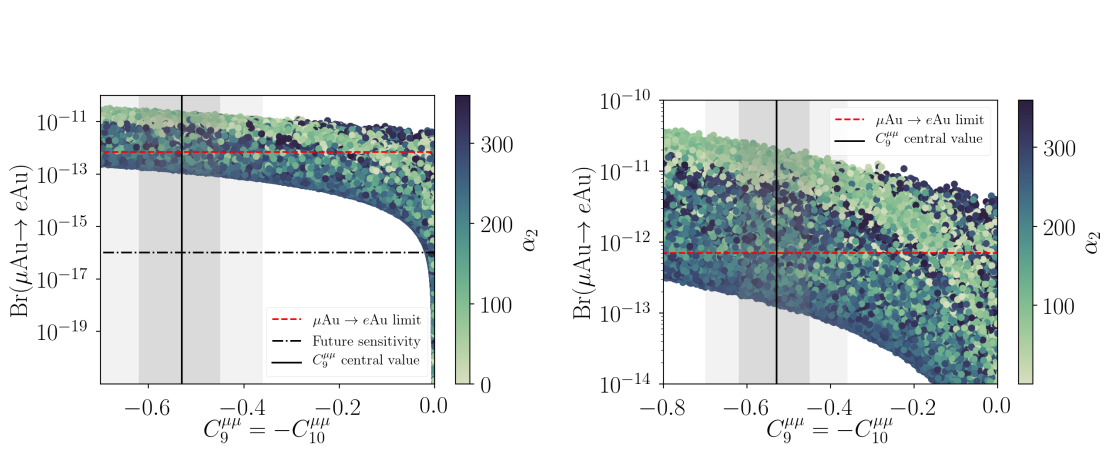


Figure 4.10: The results of the random scan projected onto $\text{Br}(\mu\text{Au} \rightarrow e\text{Au})$ and $C_9^{\mu\mu}$. All constraints except muon-electron conversion in Gold have been applied. The solid black line represents the central value of the fit of Ref. [13] to the anomalous $b \rightarrow s$ data, and the heavier and lighter shaded regions are the 1 and 2σ regions. The dashed red line corresponds to the current most stringent limit on $\text{Br}(\mu\text{Au} \rightarrow e\text{Au})$ from SINDRUM II [336] and the black dot-dashed line is a representation of the projected sensitivity of future experimental reach [380–386]. The plot on the right is an enlarged look at the interesting region of the plot on the left. The colour axis represents the value of the Majorana phase α_2 .

avoided for $100^\circ \lesssim \alpha_2 \lesssim 300^\circ$, a region that overlaps with that shown in Fig. 4.9, needed for a small imaginary part for the electron couplings x_3^{13} . We find that an additional two constraints cut into the parameter space significantly: bounds from $D^0 \rightarrow \mu\mu$ and the ATLAS measurement of $ss \rightarrow \mu\mu$. Our model predicts the $D^0 \rightarrow \mu\mu$ rate to be an order of magnitude larger than estimates of the SM contribution $\text{Br}(D^0 \rightarrow \mu\mu)_{\text{SM}} \sim 3 \cdot 10^{-13}$ [387] (see Fig. 4.11b), while the ATLAS 3000 fb^{-1} projected limit from $ss \rightarrow \mu\mu$ indicates that a non-observation would almost entirely rule out the model for low leptoquark masses (see Fig. 4.11c).

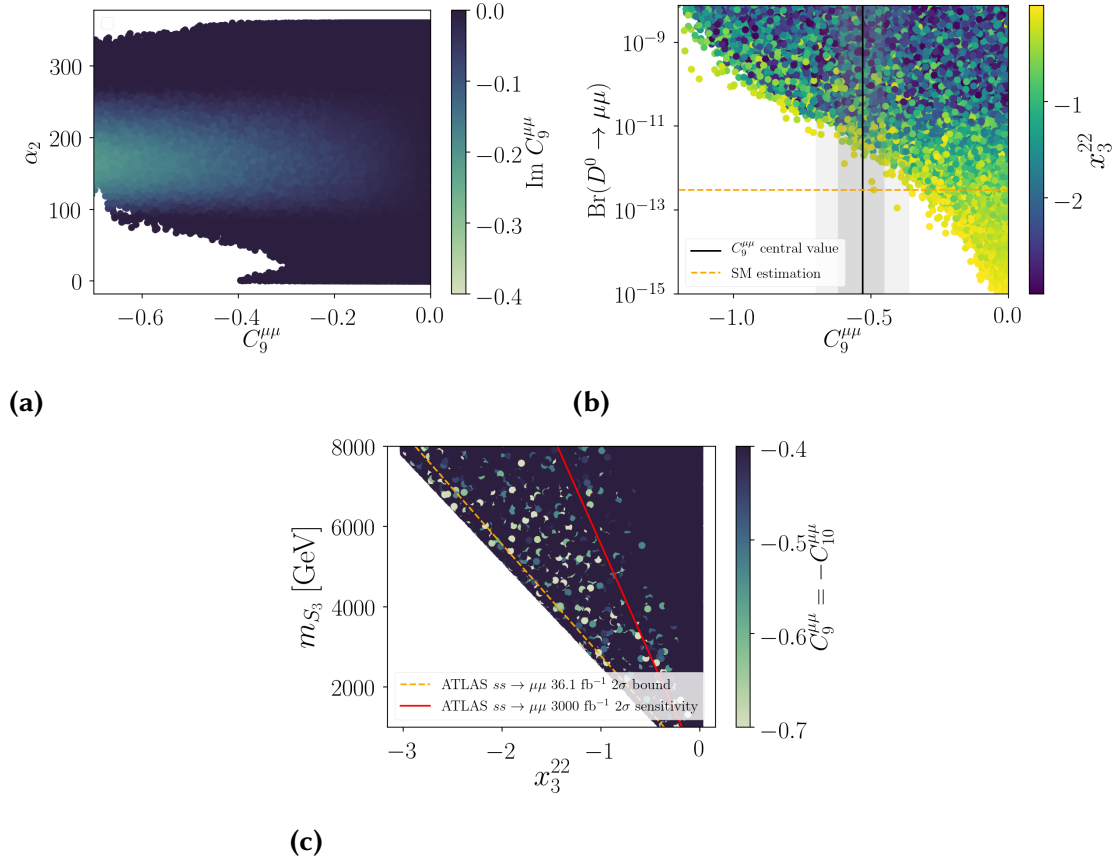


Figure 4.11: The other interesting results of our Monte Carlo analysis. (a) The relation between $C_9^{\mu\mu}$ and the Majorana phase α_2 . The points shown pass all of the constraints considered in our analysis. The colour axis represents the imaginary part of $C_9^{\mu\mu}$. The plot shows the preference away from a vanishing α_2 , driven by the constraint $\text{Br}(\mu\text{Au} \rightarrow e\text{Au})$, and the consistency of the available parameter space with a small imaginary part of $C_9^{\mu\mu}$. (b) The results of the random scan projected onto $\text{Br}(D^0 \rightarrow \mu\mu)$ and $C_9^{\mu\mu}$. Points shown pass all constraints. Our model predicts $\text{Br}(D^0 \rightarrow \mu\mu) \gtrsim 10^{-12}$, about an order of magnitude larger than the SM estimate from Ref. [387]. We note that our calculation is not valid below the dashed orange line since it only represents the new-physics contribution. (c) The plot shows the influence of the ATLAS $ss \rightarrow \mu\mu$ limits on the parameter space of our model. Coloured points lie in the 2σ region of the $b \rightarrow s$ fit we use. Dark blue points cannot explain the $b \rightarrow s$ data. The dashed orange line corresponds to the current ATLAS limit, while the solid red line is the 3000 fb^{-1} projection. The abrupt absence of points in the bottom left of the plot is due to the constraint $D^0 \rightarrow \mu\mu$.

Comments on explaining $R_{D^{(*)}}$ with the vector operator

In our analysis above we consider only contributions in the scalar–tensor direction to explain the charged-current anomalies in R_D and R_{D^*} , necessitating the inclusion of S_1 in this model to generate these contributions. This choice is made to avoid the dangerous contributions to $B \rightarrow K^{(*)}\nu\nu$, which necessarily exist in the presence of a large C_{V_L} . We explored two ways these constraints could be avoided in the context of our model:

1. As discussed previously in the literature [2, 287, 388], one way to avoid the constraints from $B \rightarrow K^{(*)}\nu\nu$ and $B_s - \bar{B}_s$ mixing is to explain the $R_{D^{(*)}}$ anomalies with a large x_1^{33} while ensuring $x_1^{32} \approx 0$. The coupling z_1^{32} required to explain $R_{D^{(*)}}$ is generated through Eq. (4.13), while keeping the strange-quark coupling to the neutrinos zero. Combining Eq. (4.13) and Eq. (4.20) with $x_1^{33} \gg x_3^{33}$ gives

$$C_V = \frac{\cos \theta_L}{4\sqrt{2}G_F V_{cb}} \frac{|x_1^{33}|^2 V_{ts}}{m_{S_1}^2}, \quad (4.44)$$

which implies $1.7 \lesssim |x_1^{33}|/(m_{S_1} \text{ TeV}) \lesssim 7.2$ for $\cos \theta_L \approx 1$ to explain $R_{D^{(*)}}$ according to our fit to C_V (see Table 3.1). We note here that even saturating the lower 2σ bound on C_V leads to contributions to $Z \rightarrow \tau\tau$ that disagree with experiment, despite the reduction of the global average driven by the latest Belle result.

2. Ref. [285] proposed that the $R_{D^{(*)}}$ anomalies could be explained through the vector operator by considering a cancellation between the S_1 and S_3 particles in this model to the processes $B \rightarrow K^{(*)}\nu\nu$. This was further studied in Ref. [389] and Ref. [390]. We have investigated this suggestion in considerable detail for this model, and could not find any parameter space that could simultaneously resolve the $R_{D^{(*)}}$ anomalies and be consistent with constraints from $B_s - \bar{B}_s$ mixing. Our findings are in agreement with Ref. [390]. We note that Ref. [390] proposed some lines of investigation, such as the use of complex-valued couplings constants, that could potentially alter this conclusion, but an investigation of such a scenario is beyond the scope of this study.

4.4 Radiative models explaining the flavour anomalies with leptoquarks

The success of the non-minimal model just studied is a promising indication for combined explanations of neutrino mass and the flavour anomalies. Fig. 2.14a suggests that the scalar leptoquarks S_1 and S_3 , there respectively denoted ω_1 and ζ , appear often in

models of radiative neutrino mass. Indeed, the appearance of both fields together in the non-minimal model studied above is somewhat *ad hoc*, since any one leptoquark is sufficient to violate lepton number by two units in the presence of χ . It would be attractive to therefore search for radiative models in which both S_1 and S_3 were necessary for the mechanism of lepton-number violation. Doing so would introduce an even tighter connection between all of the anomalies and the neutrino masses. As discussed briefly in Sec. 2.5.2, the leptoquark $R_2 \sim (3, 2, \frac{7}{6})$ can also explain the charged-current anomalies in a relatively unconstrained way. Our analysis of the exotics appearing in the model database indicates that it is the most common field to appear in radiative models. Again, this is clear from Fig. 2.14a, where R_2 is denoted Π_7 .

We search the filtered model database introduced in Chapter 2 for Lagrangians containing (i) S_1 and S_3 , or (ii) R_2 and S_3 , where all of these fields are required to couple as leptoquarks. We find 84 models for case (i) and 203 models for case (ii). All of the models are derived from dimension-eleven operators and contain more than three exotic fields, with the exception of four of the $R_2 + S_3$ models that require only one more scalar to violate lepton number. These models are summarized in Table 4.5, along with a small random sample from the remaining 283 models of cases (i) and (ii). The models tend to imply a large upper bound on the new-physics scale, since the operators from which they are derived tend to contain two L fields. This reduces the number of loops and SM-lepton mass insertions required in the operator closure. Models in which S_1 or R_2 couple to \bar{e} instead of L are in general filtered out by those models in which the leptoquark couplings to L feature in the $\Delta L = 2$ mechanism. This phenomenon is also seen and discussed in Sec. 2.5.2.

4.5 Conclusions

In this chapter we have begun to explore the connection between models of radiative neutrino mass and explanations of the flavour anomalies. We did this by first taking the BN scenario and embedding it into a simple two-loop model, first studied in Ref. [16], from the model database studied in Chapter 2. The tight connection between the neutrino-mass generation and the explanation of the anomalies means that the model cannot simultaneously explain the neutrino masses and the $b \rightarrow s$ data on account of $\tau \rightarrow \mu$ and $\mu \rightarrow e$ LFV observables. Specifically, bounds from muon-electron conversion in nuclei fix the ratio of the couplings x_{33} and x_{23} in the S_1 model, so that the large value of x_{23} required to generate $C_{LL} \approx -1$ (see Eq. (3.57)) leads to $\tau \rightarrow \mu\gamma$ and $\tau \rightarrow \mu\mu\mu$ rates incompatible with experiment. The fixing of x_{33}/x_{23} in this model is ultimately due to the fact that the coupling of S_1 to the electron cannot be avoided in the neutrino-mass model, and the structure of the mass matrix is such that one can ensure $x_{13} \approx 0$ at the cost of fixing x_{33}/x_{23} .

$S_3 +$ field content	Operators	Λ [TeV]
$R_2, (\mathbf{3}, \mathbf{1}, \frac{2}{3})_S$	71	$2 \cdot 10^7$
$R_2, (\mathbf{3}, \mathbf{3}, \frac{2}{3})_S$	71	$2 \cdot 10^7$
$R_2, (\mathbf{3}, \mathbf{4}, \frac{1}{6})_S$	71	$2 \cdot 10^7$
$R_2, (\mathbf{1}, \mathbf{4}, \frac{3}{2})_S$	71	$2 \cdot 10^7$
$R_2, (\mathbf{8}, \mathbf{1}, \mathbf{1})_S, (\mathbf{3}, \mathbf{1}, \frac{2}{3})_F$	$25c$	$4 \cdot 10^3$
$R_2, (\mathbf{8}, \mathbf{3}, \mathbf{1})_S, (\mathbf{3}, \mathbf{3}, \frac{2}{3})_F$	$25c$	$4 \cdot 10^3$
$R_2, (\mathbf{8}, \mathbf{2}, \frac{1}{2})_F, (\mathbf{8}, \mathbf{3}, \mathbf{0})_F$	$29c$	$2 \cdot 10^7$
$S_1, (\mathbf{3}, \mathbf{2}, \frac{1}{6})_F, (\bar{\mathbf{6}}, \mathbf{2}, \frac{1}{6})_S$	$25c$	$4 \cdot 10^3$
$S_1, (\bar{\mathbf{3}}, \mathbf{3}, \frac{1}{3})_F, (\bar{\mathbf{6}}, \mathbf{3}, \frac{2}{3})_S$	$47i$	$2 \cdot 10^7$
$S_1, (\mathbf{3}, \mathbf{3}, \frac{2}{3})_S, (\mathbf{3}, \mathbf{4}, \frac{1}{6})_F$	$40h$	$2 \cdot 10^7$

Table 4.5: The table shows a small sample of the 287 models of radiative neutrino mass that also contain either both of S_3 and R_2 or both of S_3 and S_1 . The first four models listed are the only ones of the 287 that contain only three fields in total. The models tend to have a high predicted scale since two L fields are generally present in the operators, reducing the number of loops and SM-lepton mass insertions required in the operator closure.

To address the limited success of this neutrino-mass model, we also studied a non-minimal scenario containing the leptoquark S_3 in addition to S_1 . Here, we were mainly interested in the extent to which bounds from muon–electron conversion could accommodate an explanation of the flavour anomalies in a neutrino-mass model. Although the S_3 explanation of the $b \rightarrow s$ anomalies is usually relatively unconstrained, introducing the neutrino-mass connection leads to a rich phenomenology wherein a value of C_{LL} compatible with an explanation of the neutral-current anomalies requires a muon–electron conversion rate in Gold nuclei of no less than $2 \cdot 10^{-13}$, within reach of the upcoming COMET and Mu2e experiments. The model also predicts a range for the Majorana phase α_2 of $100^\circ \lesssim \alpha_2 \lesssim 300^\circ$, and a rate for $D^0 \rightarrow \mu\mu$ an order of magnitude larger than the SM value.

The $S_1 + S_3$ model can successfully explain all of the flavour anomalies to within 1σ , while respecting all of the constraints we consider in our analysis. The model is non-minimal both in the sense that two fields explain the anomalies separately, but also in the sense that both of these fields are not necessary for lepton-number violation. A tighter connection between the neutrino mass and the flavour anomalies may be seen in a model in which all of the exotic multiplets play some role in the violation of lepton number. We find 287 such models that explain the $b \rightarrow s$ anomalies with S_3 and the $b \rightarrow c$ anomalies with one of S_1 or R_2 . There are four $S_3 + R_2$ models that contain only three exotic fields in total. From here the stage is set for a fuller exploration of these models and the exciting predictions they may imply for both neutrino and flavour physics.

5

The two-photon decay of a scalar-quirk bound state

This chapter is based on the publication ‘Explaining the 750 GeV diphoton excess with a coloured scalar charged under a new confining gauge interaction,’ written in collaboration with Robert Foot [1]. We use the extinct Greek letter \digamma (digamma) to represent a bound state of scalars charged under an unbroken $SU(N)$, whose two-photon decay is posited to explain the 750 GeV diphoton excess, which similarly went extinct. The explanation in terms of the $SU(N)$ bound state provides an especially simple explanation for the large production cross-section, which characterised the excess. Given the sensitivity of the diphoton channel to new physics, we hope that the conclusions of this paper still provide useful insight into how such a diphoton resonance might be explained economically. We note that this chapter is somewhat parenthetical to the earlier narrative of the thesis.

5.1 Introduction

An excess of events containing two photons with invariant mass near 750 GeV has been observed in 13 TeV proton–proton collisions by the ATLAS and CMS collaborations [391, 392]. The cross section $\sigma(pp \rightarrow \gamma\gamma)$ is estimated to be

$$\sigma(pp \rightarrow \gamma\gamma) = \begin{cases} (10 \pm 3) \text{ fb} & \text{ATLAS} \\ (6 \pm 3) \text{ fb} & \text{CMS} \end{cases} \quad (5.1)$$

and there is no evidence of any accompanying excess in the dilepton channel [393]. If we interpret this excess as the two photon decay of a single new particle of mass m then ATLAS data provide a hint of a large width: $\Gamma/m \sim 0.06$, while CMS data prefer a narrow width. Naturally, further data collected at the LHC should provide a clearer picture as to the nature of this excess.

There has been vast interest in the possibility that the diphoton excess results from physics beyond the SM. Most discussion has focused on models where the excess is due to a new scalar particle which subsequently decays into two photons *e.g.* Ref. [394]. The possibility that the new scalar particle is a bound state of exotic charged fermions has also been considered, *e.g.* Refs. [395–399]. Here we consider the case that the 750 GeV state is a non-relativistic bound state constituted by an exotic *scalar* particle χ and its antiparticle, charged under $SU(3)_c$ as well as a new unbroken non-abelian gauge interaction. Having χ be a scalar rather than a fermion is not merely a matter of taste: in such a framework a fermionic χ would lead to the formation of bound states which (typically) decay to two leptons more often than to photons; a situation which is not favoured by the data.

The bound state, which we denote \mathfrak{f} , can be produced through gluon–gluon fusion directly (*i.e.* at threshold $\sqrt{s_{gg}} \simeq M_{\mathfrak{f}}$) or indirectly via $gg \rightarrow \chi^\dagger \chi \rightarrow \mathfrak{f} + \text{soft quanta}$ (*i.e.* above \mathfrak{f} threshold: $\sqrt{s_{gg}} > M_{\mathfrak{f}}$). The indirect production mechanism can dominate the production of the bound state, which is an interesting feature of this kind of theory.

5.2 The model

We take the new confining unbroken gauge interaction to be $SU(N)$, and assume that, like $SU(3)_c$, it is asymptotically free and confining at low energies. However, the new $SU(N)$ dynamics is qualitatively different from QCD as all the matter particles [assumed to be in the fundamental representation of $SU(N)$] are taken to be much heavier than the confinement scale, Λ_N . In fact we here consider only one such matter particle, χ , so that $M_\chi \gg \Lambda_N$ is assumed. In this circumstance a $\chi^\dagger \chi$ pair produced at the LHC above the threshold $2M_\chi$ but below $4M_\chi$ cannot fragment into two jets. The $SU(N)$ string which connects them cannot break as there are no light $SU(N)$ -charged states available. This is in contrast to heavy quark production in QCD where light quarks can be produced out of the vacuum enabling the colour string to break. The produced $\chi^\dagger \chi$ pair can be viewed as a highly excited bound state, which de-excites by $SU(N)$ -ball and soft glueball/pion emission [400].

With the new unbroken gauge interaction assumed to be $SU(N)$ the gauge symmetry of the SM is extended to

$$SU(3)_c \otimes SU(2)_L \otimes U(1)_Y \otimes SU(N). \quad (5.2)$$

This kind of theory can arise naturally in models which feature large colour groups [401–403] and in models with leptonic colour [404–407] but was also considered earlier by Okun [408]. The notation *quirks* for heavy particles charged under an unbroken gauge symmetry (where $M_\chi \gg \Lambda_N$) was introduced in [400] where the relevant phenomenology was examined in some detail in a particular model¹. For convenience we borrow their nomenclature and call the new quantum number *hue* and the massless gauge bosons *huons* (\mathcal{H}).

The phenomenological signatures of the bound states (quirkonia) formed depend on whether the quirk is a fermion or boson. Here we assume that the quirk χ is a Lorentz scalar in light of previous work which indicated that bound states formed from a fermionic χ state would be expected to be observed at the LHC via decays of the spin-1 bound state into opposite-sign lepton pairs ($\ell^+\ell^-$) [400, 407]. In fact, this appears to be a serious difficulty in attempts to interpret the 750 GeV state as a bound state of fermionic quirk particles (such as those of Refs. [395–397]). The detailed consideration of a scalar χ appears to have been largely overlooked², perhaps due to the paucity of known elementary scalar particles. With the recent discovery of a Higgs-like scalar at 125 GeV [411, 412] it is perhaps worth examining signatures of scalar quirk particles. In fact, we point out here that the two photon decay is the most important experimental signature of bound states formed from electrically charged scalar quirks. Furthermore this explanation is only weakly constrained by current data and thus appears to be a simple and plausible option for the new physics suggested by the observed diphoton excess.

5.3 Explaining the excess

The scalar χ that we introduce transforms under the extended gauge group (Eq. 5.2) as

$$\chi \sim (3, 1, Y; \mathbf{N}), \quad (5.3)$$

where we use the normalisation $Q = Y/2$. The possibility that χ also transforms non-trivially under $SU(2)_L$ is interesting, however for the purposes of this letter we focus on the $SU(2)_L$ singlet case for definiteness. Since two-photon decays of non-relativistic quirkonium will be assumed to be responsible for the diphoton excess observed at the LHC, the mass of χ will need to be around 375 GeV.

We have assumed that χ is charged under $SU(3)_c$ so that it can be produced at tree-level through QCD-driven pair production. We present the production mechanisms in Fig. 5.1. To estimate the production cross section of the bound states, we first consider

¹Some other aspects of such models have been discussed over the years, including the possibility that the $SU(N)$ confining scale is low (\sim keV), a situation which leads to macroscopic strings [409].

²The idea has been briefly mentioned in recent literature [398, 410].

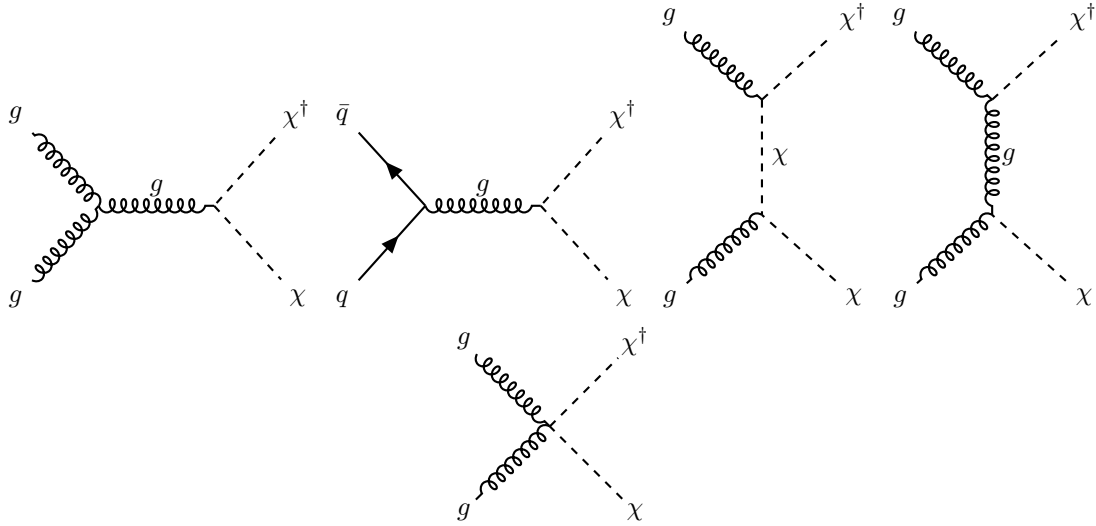


Figure 5.1: Tree-level pair production mechanisms for the scalar quirk χ .

Draft compiled on 2020/12/17 at 19:21:00

the indirect production mechanism which we expect to be dominant. Here, a $\chi^\dagger \chi$ pair is produced above threshold and de-excites emitting soft glueballs/pions and hueballs: $gg \rightarrow \chi^\dagger \chi \rightarrow f + \text{soft quanta}$. We first consider the case where the confinement scale of the new $SU(N)$ interaction is similar to that of QCD. What happens in this case can be adapted from the discussion in [400], where a fermionic quirk charged under an unbroken $SU(2)$ gauge interaction was considered. As already briefly discussed in the introduction, the $\chi^\dagger \chi$ pairs initially form a highly excited bound state, which subsequently de-excites in two stages. The first stage is the non-perturbative regime where the hue string is longer than Λ_N^{-1} . The second stage is characterised by a string scale significantly less than Λ_N^{-1} : the perturbative Coulomb region. Here the bound state can be characterised by the quantum numbers n and l . De-excitation continues until quirkonium is in a lowly excited state with $l \leq 1$ and n . Imagine first that de-excitation continued until the ground state ($n = 1, l = 0$) is reached. Given we are considering χ to be a scalar, the quirkonium ground state, f , will have spin 0, and is thus expected to decay into SM gauge bosons and huons. The cross section $\sigma(pp \rightarrow f \rightarrow \gamma\gamma)$ in this case is then

$$\sigma(pp \rightarrow \gamma\gamma) \approx \sigma(pp \rightarrow \chi^\dagger \chi) \times \text{Br}(f \rightarrow \gamma\gamma). \quad (5.4)$$

Since production is governed by QCD interactions, we can use the values of the pair production cross sections for stops/sbottoms in the limit of decoupled squarks and

gluinos [413]. For a χ mass of 375 GeV

$$\sigma(pp \rightarrow \chi^\dagger \chi) \approx \begin{cases} 2.6N \text{ pb} & \text{at } 13 \text{ TeV} \\ 0.5N \text{ pb} & \text{at } 8 \text{ TeV} \end{cases}. \quad (5.5)$$

The branching fraction is to leading order

$$\text{Br}(\varphi \rightarrow \gamma\gamma) \approx \frac{3NQ^4\alpha^2}{\frac{2}{3}N\alpha_s^2 + \frac{3}{2}C_N\alpha_N^2 + 3NQ^4\alpha^2}, \quad (5.6)$$

where $C_N \equiv (N^2 - 1)/(2N)$, α_N is the new $SU(N)$ interaction strength and we have neglected the small contribution of $\varphi \rightarrow Z\gamma/ZZ$ to the total width. Eq. (5.6) also neglects the decay to Higgs particles: $\varphi \rightarrow hh$, which arises from the Higgs potential portal term $\lambda_\chi \chi^\dagger \chi \phi^\dagger \phi$. Theoretically this rate is unconstrained given the dependence on the unknown parameter λ_χ , but could potentially be important. However, limits from resonant Higgs boson pair production derived from 13 TeV data: $\sigma(pp \rightarrow X \rightarrow hh \rightarrow bbbb) \lesssim 50 \text{ fb}$ at $M_X \approx 750 \text{ GeV}$ [414, 415] imply that the Higgs decay channel must indeed be subdominant (*c.f.* $\varphi \rightarrow gg, \mathcal{H}\mathcal{H}$).

The renormalised gauge coupling constants in Eq. (5.6) are evaluated at the renormalisation scale $\mu \sim M_\varphi/2$. Taking for instance the specific case of $N = 2$, $\alpha_N = \alpha_s \approx 0.10$ (at $\mu \sim M_\varphi/2$) gives

$$\sigma(pp \rightarrow \gamma\gamma) \approx 5 \left(\frac{Q}{1/2} \right)^4 \text{ fb at } 13 \text{ TeV}. \quad (5.7)$$

At $\sqrt{s} = 8 \text{ TeV}$ the cross section is around five times smaller. We present the cross section $\sigma(pp \rightarrow \varphi \rightarrow \gamma\gamma)$ for a range of masses M_φ and different combinations of Q and N in Fig. 5.2. The parameter choice $\alpha_N = \alpha_s$ and $\Lambda_N = \Lambda_{\text{QCD}}$ has been assumed. (The cross section is not highly sensitive to Λ_N , α_N so long as we are in the perturbative regime: $\Lambda_N \lesssim \Lambda_{\text{QCD}}$.) Evidently, for $N = 2$, a χ with electric charge $Q \approx 1/2$ is produced at approximately the right rate to explain the diphoton excess.

In practice de-excitation of the produced quirkonium does not always continue until the ground state is reached. In this case annihilations of excited states can also contribute. However those with $l = 0$ will decay in the same way as the ground state. The only difference is that the excited states will have a slightly larger mass (which we will estimate in a moment) due to the change in the binding energy. This detail could be important as it can effectively enlarge the observed width. Annihilation of excited states with non-zero orbital angular momentum could in principle also be important, however these are suppressed as the radial wavefunction vanishes at the origin: $R(0) = 0$ for $l \geq 1$. They are expected to de-excite predominately to $l = 0$ states rather than annihilate [400]. Nevertheless, for sufficiently large α_N the $l = 1$ annihilations: $\varphi \rightarrow \mu^+ \mu^-$ and $\varphi \rightarrow e^+ e^-$ could potentially be observable.

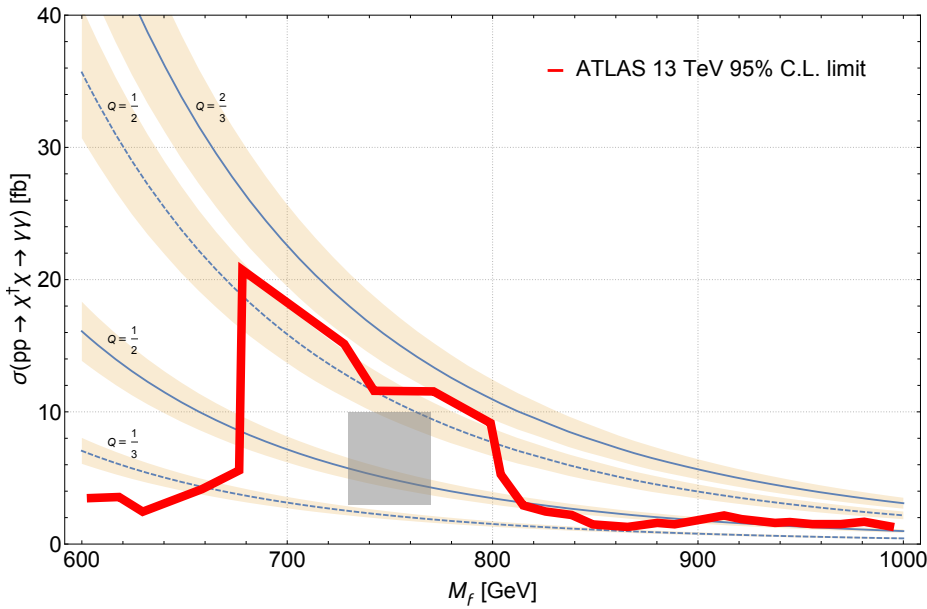


Figure 5.2: The cross section $\sigma(pp \rightarrow \chi \rightarrow \gamma\gamma)$ at 13 TeV for a range of quirkonium masses M_χ and charge assignments. Solid lines denote choices of $N = 2$ and dashed lines choices of $N = 5$. The rectangle represents the $\sigma \in [3, 10]$ fb indicative region accommodated by the ATLAS and CMS data. The solid red line is the ATLAS 13 TeV exclusion limit. Uncertainties reflect error associated with the parton distribution functions.

The $l = 0$ excited states can be characterised by the quantum number n with binding energies:

$$\frac{E_n}{M_\chi} = -\frac{1}{8n^2} \left[\frac{4}{3} \bar{\alpha}_s + C_N \bar{\alpha}_N + Q^2 \bar{\alpha} \right]^2. \quad (5.8)$$

The above formula was adapted from known results with quarkonium, e.g. [395] (and of course also the hydrogen atom). The coupling constants $\bar{\alpha}_s$, $\bar{\alpha}_N$ and $\bar{\alpha}$ are evaluated at a renormalisation scale corresponding to the mean distance between the particles which is of order the Bohr radius: $a_0 = 4/[(4\bar{\alpha}_s/3 + C_N \bar{\alpha}_N + Q^2 \bar{\alpha}) M_\chi]$. The bound state, described by the radial quantum number n has mass given by $M_\chi(n) = 2M_\chi + E_n$. Considering as an example $N = 2$ and $\bar{\alpha}_N = \bar{\alpha}_s = 0.15$, $\bar{\alpha} = 1/137$ we find the mass difference between the $n = 1$ and $n = 2$ states to be $\Delta M = (E_1 - E_2) \approx 0.01 M_\chi$. Larger mass splittings will be possible³ if $\bar{\alpha}_N > \bar{\alpha}_s$, although it has been shown in the context of fermionic quirk models that the phenomenology is substantially altered in this regime [396]. In

³Additional possibilities arise if χ transforms non-trivially under $SU(2)_L$, i.e. forming a representation N_L . The mass degeneracy of the multiplet will be broken at tree-level by Higgs potential terms along with

particular, the hueballs can become so heavy that the decays of the bound state into hueballs is kinematically forbidden.

In the above calculation of the bound state production cross section, we considered only the *indirect* production following pair production of $\chi^\dagger \chi$ above threshold. The bound state can also be produced directly: $gg \rightarrow f$, where $\sqrt{s_{gg}} \approx M_f$. The cross section of the ground state direct resonance production is

$$\sigma(pp \rightarrow f)_{DR} \approx \frac{C_{gg} K_{gg} \Gamma(f \rightarrow gg)}{s M_f}, \quad (5.9)$$

where C_{gg} is the appropriate parton luminosity coefficient and K_{gg} is the gluon NLO QCD K-factor. For $\sqrt{s} = 13$ TeV we take $C_{gg} \approx 2137$ [394] and $K_{gg} = 1.6$ [416]. The partial width $\Gamma(f \rightarrow gg)$ of the $n = 1, l = 0$ ground state is given by

$$\Gamma(f \rightarrow gg) = \frac{4}{3} M_f N \alpha_s^2 \frac{|R(0)|^2}{M_f^3}, \quad (5.10)$$

where the radial wavefunction at the origin for the ground state is:

$$\frac{|R(0)|^2}{M_f^3} = \frac{1}{16} \left[\frac{4}{3} \bar{\alpha}_s + C_N \bar{\alpha}_N + Q^2 \bar{\alpha} \right]^3. \quad (5.11)$$

Considering again the example of $N = 2$ and $\bar{\alpha}_N = \bar{\alpha}_s = 0.15$, $\bar{\alpha} = 1/137$ we find

$$\sigma(pp \rightarrow f)_{DR} \approx 0.40 \text{ pb} \quad \text{at 13 TeV}. \quad (5.12)$$

Evidently, the direct resonance production cross section is indeed expected to be subdominant, around 8% that of the indirect production cross section (Eq. 5.5)⁴.

We now comment on the regime where Λ_N is smaller than Λ_{QCD} . In fact, if the $SU(N)$ confining scale is only a little smaller than Λ_{QCD} then a light quark pair can form out of the vacuum, leading to a bound state of two QCD colour singlet states: $\chi \bar{q}$ and $\chi^\dagger q$. These colour singlet states would themselves be bound together by $SU(N)$ gauge interactions to form the $SU(N)$ singlet bound state. Since only $SU(N)$ interactions bind the two composite states ($\chi \bar{q}$ and $\chi^\dagger q$), it follows that $\frac{4}{3} \bar{\alpha}_s + C_N \bar{\alpha}_N + Q^2 \bar{\alpha} \rightarrow C_N \bar{\alpha}_N + (Q - Q_q)^2 \bar{\alpha}$ in Eqs. 5.8 and 5.11. Therefore if the confinement scale of $SU(N)$ is smaller than

electroweak radiative corrections. The net effect is that the predicted width of the $pp \rightarrow \gamma\gamma$ bump can be effectively larger as there are N_L distinct bound states, f^i , (of differing masses) which can each contribute to the decay width. Although each state is expected to have a narrow width, when smeared by the detector resolution the effect can potentially be a broad feature.

⁴If $\bar{\alpha}_N$ is sufficiently large, one can potentially have direct resonance production comparable or even dominating indirect production (such a scenario has been contemplated recently in [397, 398]). Naturally at such large $\bar{\alpha}_N$ the perturbative calculations become unreliable, and one would have to resort to non-perturbative techniques such as lattice computations.

that of QCD then the direct production rate becomes completely negligible relative to the indirect production mechanism. The rate of φ production is the same as that found earlier in Eq. 5.5, but the branching ratio to two photons is modified:

$$\text{Br}(\varphi \rightarrow \gamma\gamma) \simeq \frac{3NQ^4\alpha^2}{\frac{7}{3}N\alpha_s^2 + \frac{3}{2}C_N\alpha_N^2 + 3NQ^4\alpha^2}, \quad (5.13)$$

where, as before, we have neglected the small contribution of $\varphi \rightarrow Z\gamma/ZZ$ to the total width, and also the contribution from $\varphi \rightarrow hh$. In this regime somewhat larger values of Q can be accommodated, such as $Q = 5/6$ for $N = 2$ ⁵.

Notice that in the $\Lambda_N < \Lambda_{\text{QCD}}$ regime the size of the mass splittings between the excited states becomes small as $\frac{4}{3}\bar{\alpha}_S + C_N\bar{\alpha}_N + Q^2\bar{\alpha} \rightarrow C_N\bar{\alpha}_N + (Q - Q_q)^2\bar{\alpha}$ in Eq. 5.8. We therefore expect no effective width enhancement due to the excited state decays at the LHC in the small Λ_N regime. Of course a larger effective width is still possible if there are several nearly degenerate scalar quirk states, which, as briefly mentioned earlier, can arise if χ transforms nontrivially under $SU(2)_L$.

Other signatures

While the two photon decay channel of the bound state should be the most important signature, the dominant decay is expected to be via $\varphi \rightarrow gg$ and $\varphi \rightarrow \mathcal{H}\mathcal{H}$. The former process is expected to lead to dijet production while the latter will be an invisible decay. The dijet cross section is easily estimated:

$$\sigma(pp \rightarrow jj) \approx \begin{cases} 2.6N \times \text{Br}(\varphi \rightarrow gg) \text{ pb} & \text{at } 13 \text{ TeV} \\ 0.5N \times \text{Br}(\varphi \rightarrow gg) \text{ pb} & \text{at } 8 \text{ TeV} \end{cases}. \quad (5.14)$$

The limit from 8 TeV data is $\sigma(pp \rightarrow jj) \lesssim 2.5 \text{ pb}$ [418, 419]. If gluons dominate the φ decays (i.e. $\text{Br}(\varphi \rightarrow gg) \approx 1$) then this experimental limit is satisfied for $N \leq 5$. For sufficiently large α_N the invisible decay can be enhanced, thereby reducing $\text{Br}(\varphi \rightarrow gg)$. In this circumstance the bound on N from dijet searches would weaken.

The invisible decays $\varphi \rightarrow \mathcal{H}\mathcal{H}$ are not expected to lead to an observable signal at leading order for much of the parameter space of interest⁶. However, the bremsstrahlung

⁵Although it is perhaps too early to speculate on the possible role of χ in a more elaborate framework, we nevertheless remark here that particles fitting its description are required for spontaneous symmetry breaking of extended Pati–Salam type unified theories [417].

⁶Scalar quirk loops can mediate hueball decays into gluons and other SM bosons [400, 420, 421]. The decay rate is uncertain, depending on the non-perturbative hueball dynamics. However, if the hueballs are able to decay within the detector then they can lead to observable signatures including displaced vertices. This represents another possible collider signature of the model.

of a hard gluon from the initial state: $pp \rightarrow f g \rightarrow \mathcal{H} \mathcal{H} g$ can lead to a jet plus missing transverse energy signature. Current data are not expected to give stringent limits from such decay channels, however this signature could become important when a larger data sample is collected. Note though that the rate will become negligible in the limit that α_N becomes small. Also, in the small Λ_N regime, where the bound state is formed from $\chi \bar{q}$ and $\chi^\dagger q$, the two-body decay $f \rightarrow g\gamma$ (jet + photon) will also arise as in this case the scalar quirk pair is not necessarily in the colour singlet configuration. The decay rate at leading order is substantial:

$$\frac{\Gamma(f \rightarrow j\gamma)}{\Gamma(f \rightarrow \gamma\gamma)} = \frac{8\alpha_s}{3\alpha Q^2}. \quad (5.15)$$

Nevertheless, we estimate that this is still consistent with current data [422], but would be expected to become important when a larger data sample is collected.

Another important signature of the model will be the $pp \rightarrow f \rightarrow Z\gamma$ and $pp \rightarrow f \rightarrow ZZ$ processes. The rates of these decays, relative to $f \rightarrow \gamma\gamma$, are estimated to be:

$$\begin{aligned} \frac{\Gamma(f \rightarrow Z\gamma)}{\Gamma(f \rightarrow \gamma\gamma)} &= 2 \tan^2 \theta_W, \\ \frac{\Gamma(f \rightarrow ZZ)}{\Gamma(f \rightarrow \gamma\gamma)} &= \tan^4 \theta_W. \end{aligned} \quad (5.16)$$

If χ transforms non-trivially under $SU(2)_L$ then deviations from these predicted rates arise along with the tree-level decay $f \rightarrow W^+W^-$.

5.4 Conclusions

We have considered a charged scalar particle χ of mass around 375 GeV charged under both $SU(3)_c$ and a new confining gauge interaction (assigned to be $SU(N)$ for definiteness). These interactions confine $\chi^\dagger \chi$ into non-relativistic bound states whose decays into photons can explain the 750 GeV diphoton excess observed at the LHC. Taking the new confining group to be $SU(2)$, we found that the diphoton excess required χ to have electric charge approximately $Q \sim [\frac{1}{2}, 1]$. An important feature of our model is that the exotic particle χ has a mass much greater than the $SU(N)$ -confinement scale Λ_N . In the absence of light $SU(N)$ -charged matter fields this makes the dynamics of this new interaction qualitatively different to that of QCD: pair production of the scalars and the subsequent formation of the bound state dominates over direct bound state resonance production (at least in the perturbative regime where $\Lambda_N \lesssim \Lambda_{QCD}$). Since χ is a Lorentz scalar, decays of $\chi^\dagger \chi$ bound states to lepton pairs are naturally suppressed, and thus constraints from dilepton searches at the LHC can be ameliorated. This explanation

is quite weakly constrained by current searches and data from the forthcoming run at the LHC will be able to probe our scenario more fully. In particular, dijet, mono-jet, di-Higgs and jet + photon searches may be the most promising discovery channels.

6

Conclusions and Outlook

The strongest indication of physics beyond the Standard Model is the clear and overwhelming evidence for neutrino oscillations and the non-zero neutrino masses these observations imply. Unfortunately there are many viable scenarios for explaining the origin of mass and mixing in the neutrino sector, and it is not clear which models should receive more attention. The simplest tend to be far beyond the current or near-future reach of experiments, at least in their most motivated regions of parameter space. There are many non-minimal but testable models one can construct that explain the smallness of the neutrino masses in a satisfying way, although studying these models systematically has proven to be difficult. In this thesis we have mapped out the space of one very motivated class of such models: minimal models of Majorana neutrino mass. In doing so we hope to have provided a platform for various systematic studies, perhaps both phenomenological and experimental. We have also begun to explore the potential role these models might play in underlying the exciting but still illusive B -meson anomalies, whose connection to neutrino physics was an unexpected but welcome development that occurred in the course of this doctoral work.

In Chapter 2 we presented the algorithm and computational machinery we used to generate the roughly eleven thousand models that constitute our model database. Almost all of the models have the neutrinos picking up mass at loop level, and therefore the database is essentially one of radiative models of Majorana neutrino mass. Our analysis was built on lepton-number-violating effective operators, many of which appear for the first time in our study. The models are represented in a computational format designed to facilitate future automated phenomenological analysis, and we have made both the code we used to implement the algorithm as well as the database publicly avail-

able. We conducted a preliminary study on the basis of the database, finding a number of interesting models containing relatively few free parameters while predicting very low-scale new physics. We also investigated the structure of the neutrino-mass matrices of some novel models, including one derived from an operator containing derivatives, and a four-multiplet model incorporating a specific explanation of the flavour anomalies. The model database is a fantastic tool for identifying different motifs and patterns across the space of Majorana neutrino mass models. One important finding of our study was the preponderance of scalar leptoquarks in the completions.

The recent experimental hints of lepton flavour non-universality in neutral- and charged-current B decays have ignited interest in phenomenological models of scalar leptoquarks, since these have been identified as strong candidates that could underlie the discrepant measurements. In Chapter 3 we detailed a comprehensive study of a particularly simple such scenario, originally proposed in Ref. [226]. The so-called *one leptoquark* model presents the S_1 leptoquark as an economic explanation of both the $b \rightarrow s$ and $b \rightarrow c$ anomalies through related sets of Yukawa couplings to left-handed SM fermions. The results of our detailed phenomenological analysis of the model showed that its viability was compromised by a full consideration of its constraints. The ability of the leptoquark to explain the measured values of R_D and R_{D^*} remained, although in a previously unconsidered region of parameter space entailing Yukawa couplings to both left- and right-handed SM fermions. A combined explanation of both sets of anomalies was found to be possible, along with a mechanism to explain the discrepant value of the anomalous magnetic moment of the muon. In this combined scenario, we found that the $b \rightarrow s$ and $b \rightarrow c$ anomalies could be explained to within 2σ while also accommodating the measurement of $(g - 2)_\mu$, an impressive improvement on the SM for such a simple model.

The analysis we conducted on our model database suggests that there may be a connection between radiative models of neutrino mass and the flavour anomalies. This is a phenomenologically rich research direction that we have only begun to explore, and our work on this topic is described in Chapter 4. There, we studied two models of radiative neutrino mass involving scalar leptoquarks. The first contained the S_1 leptoquark; we explored the extent to which the pattern of neutrino masses and mixings observed could be reproduced in this model, while at the same time accommodating the flavour anomalies. We found that the structure of the mass matrix was such that the problematic coupling of S_1 to the electron could be arranged to be small at the cost of fixing the ratio of the tau-top S_1 coupling to the muon-top S_1 coupling. This implied very clear predictions of tau-muon LFV observables like $\tau \rightarrow \mu\gamma$ and $\tau \rightarrow \mu\mu\mu$ if the muon couplings were at all sizeable. Large couplings to the muon are necessary in this model to explain the $b \rightarrow s$ anomalies and so these could not be explained along with the neutrino masses without unacceptably large rates for $\tau \rightarrow \mu$ observables.

Given this simple model's limited success, we also considered a next-to-minimal scenario in which the mechanisms explaining the charged- and neutral-current anomalies

were somewhat divorced. The model we studied is a completion of a dimension-seven operator containing the S_3 leptoquark, known to provide a good explanation of the neutral-current anomalies, and the vector-like quark χ . We add S_1 to the model in order to incorporate the successes of the *one leptoquark* in explaining the anomalies in R_D , R_{D^*} and $(g - 2)_\mu$. In this model, the coupling to the electron could not be avoided on account of the structure of the neutrino-mass matrix. This implied a parameter space constrained most strongly by muon-electron LFV observables, the most important of which we found to be muon-electron conversion in nuclei. Interestingly, our analysis showed an intimate connection between the muon-electron conversion rate, the size of the $C_9^{bs\mu\mu} = -C_{10}^{bs\mu\mu}$ Wilson coefficients, and even the value of the Majorana phase α_2 . Excitingly, the model predicts a muon-electron conversion rate that will be observed or excluded by the next generation of experiments, along with a $D^0 \rightarrow \mu\mu$ rate an order of magnitude larger than the SM prediction. The model can successfully explain all of the discrepant measurements along with neutrino mass, showing that a combined explanation is possible.

We expect our model database to be a useful resource for exploring the connection radiative models might have to the flavour anomalies. To facilitate future work in this direction, we finished Chapter 4 with a selection of models from the database that contain particle content sufficient to explain the anomalies. These models predict a tighter connection between the anomalies and neutrino physics than seen in the next-to-minimal scenario studied above, since each field is necessary for the violation of lepton number.

We eagerly await the results of future measurements, particularly of the clean ratios R_K and R_{K^*} , to see what they may imply about these models and the connection to radiative neutrino mass going forward. Should they show that the anomalies were really some statistical or experimental effect, it would not be the first time this has happened. Indeed, in Chapter 5 a remarkably simple explanation of the 750 GeV diphoton excess was introduced, and this anomaly has since vanished. The model introduced a scalar field charged under a new confining $SU(N)$, the diphoton decay of whose bound state ζ explained the excess seen by ATLAS and CMS. An interesting feature of the model is that pair production of the scalar and the subsequent formation of the bound state dominates over the direct ζ production, since there are no light $SU(N)$ -charged states that can be produced from the vacuum to break the $SU(N)$ string.

This is perhaps a good example of scientific creativity and useful model building, albeit in response to spurious new physics. Should some or all of the flavour anomalies also go like ζ , we hope that the same can be said of our research connecting radiative neutrino masses and the flavour anomalies. Indeed, in this case the main results of this doctoral work will essentially remain unchanged: models explaining deviations in dimension-six four-fermion operators will always have some possible connection to models of radiative neutrino mass. Now that, subject to certain minimality assumptions, these have been catalogued in our model database, it remains for experimental-

ists to continue to probe the coefficients at dimension six, and for phenomenologists to continue to constrain and draw out predictions from the models.

A

Mathematical notation

Throughout this thesis we choose to label representations by their dimension, which we typeset in bold. Fields are labelled by their transformation properties under the Lorentz group and the SM gauge group $SU(3)_c \otimes SU(2)_L \otimes U(1)_Y$. All spinors are treated as two-component objects transforming as either $(2, 1)$ (left-handed) or $(1, 2)$ (right-handed) under the Lorentz group, written as $SU(2)_+ \otimes SU(2)_-$. The left-handed spinors carry undotted spinor indices $\alpha, \beta, \dots \in \{1, 2\}$, while the right-handed spinors carry dotted indices $\dot{\alpha}, \dot{\beta}, \dots \in \{\dot{1}, \dot{2}\}$. Wherever possible we attempt to conform to the conventions of Ref. [106] when working with spinor fields (see appendix G for the correspondence to four-component notation and appendix J for SM-fermion nomenclature). For objects carrying a single spacetime index V_μ we define

$$V_{\alpha\dot{\beta}} = \sigma_{\alpha\dot{\beta}}^\mu V_\mu \quad \text{and} \quad \bar{V}_{\dot{\alpha}\beta} = \bar{\sigma}_{\dot{\alpha}\beta}^\mu V_\mu . \quad (\text{A.1})$$

Note that in this notation

$$\square = \partial_\mu \partial^\mu = \frac{1}{2} \text{Tr}[\partial \bar{\partial}] = \frac{1}{2} \text{Tr}[\bar{\partial} \partial] , \quad (\text{A.2})$$

and we will often just use \square to represent the contraction of two covariant derivatives $D_\mu D^\mu$ where this is clear from context. For field-strength tensors, generically $X_{\mu\nu}$, we work with the irreducible representations (irreps) $X_{\alpha\beta}$ and $\bar{X}_{\dot{\alpha}\dot{\beta}}$, where

$$X_{\{\alpha\beta\}} = 2i[\sigma^{\mu\nu}]_\alpha^\gamma \epsilon_{\gamma\beta} X_{\mu\nu} \quad \text{and} \quad \bar{X}_{\{\dot{\alpha}\dot{\beta}\}} = 2i[\bar{\sigma}^{\mu\nu}]_{\dot{\beta}}^{\dot{\gamma}} \epsilon_{\dot{\alpha}\dot{\gamma}} X_{\mu\nu} , \quad (\text{A.3})$$

or the alternate forms with one raised and one lowered index. We also define

$$\phi_1 \tilde{D}^\mu \phi_2 = \frac{1}{2} [\phi_1 D^\mu \phi_2 - (D^\mu \phi_1) \phi_2] , \quad (\text{A.4})$$

for some fields ϕ_i . Where we use four-component spinor fields, we always simplify $\chi^C \psi$ (where χ^C is the charge-conjugate spinor) to $\chi \psi$ to avoid clutter.

Indices for $SU(2)_L$ (isospin) are taken from the middle of the Latin alphabet. These are kept lowercase for the fundamental representation for which $i, j, k, \dots \in \{1, 2\}$ and the indices of the adjoint are capitalised $I, J, K, \dots \in \{1, 2, 3\}$. Colour indices are taken from the beginning of the Latin alphabet and the same distinction between lowercase and uppercase letters is made. For both $SU(2)$ and $SU(3)$, a distinction between raised and lowered indices is maintained such that, for example, $(\psi^i)^\dagger = (\psi^\dagger)_i$ for an isodoublet field ψ . However, we often specialise to the case of only raised, symmetrised indices for $SU(2)$, and use a tilde to denote a conjugate field whose $SU(2)_L$ indices have been raised:

$$\tilde{\psi}^i \equiv \epsilon^{ij} \psi_j^\dagger. \quad (\text{A.5})$$

We adopt this notation from the usual definition of \tilde{H} , and note that throughout the paper we freely interchange between $\tilde{\psi}^i$ and ψ_i^\dagger . For the sake of tidiness, we sometimes use parentheses (...) to indicate the contraction of suppressed indices. Curly braces are reserved to indicate symmetrised indices \{\dots\} and square brackets enclose antisymmetrised indices [\dots], but this notation is avoided when the permutation symmetry between indices is clear. We use τ^I and λ^A for the Pauli and Gell-Mann matrices, and normalise the non-abelian vector potentials of the SM such that

$$(W_{\alpha\dot{\beta}})^i{}_j = \frac{1}{2}(\tau^I)^i{}_j W_{\alpha\dot{\beta}}^I \quad \text{and} \quad (G_{\alpha\dot{\beta}})^a{}_b = \frac{1}{2}(\lambda^A)^a{}_b G_{\alpha\dot{\beta}}^A. \quad (\text{A.6})$$

Flavour (or family) indices of the SM fermions are represented by the lowercase Latin letters $\{r, s, t, u, v, w\}$.

For the non-gauge degrees of freedom in the SM we capitalise isospin doublets (Q, L, H), while the left-handed isosinglets are written in lowercase with a bar featuring as a part of the name of the field ($\bar{u}, \bar{d}, \bar{e}$). The representations and hypercharges for the SM field content are summarised in Table A.1. Our definition of the SM gauge-covariant derivative is exemplified by

$$\bar{D}_{\dot{\alpha}\beta} Q_r^{\beta ai} = \left[\delta_b^a \delta_j^i (\bar{d}_{\dot{\alpha}\beta} + ig_1 Y_Q \bar{B}_{\dot{\alpha}\beta}) + ig_2 \delta_b^a (\bar{W}_{\dot{\alpha}\beta})^i{}_j + ig_3 \delta_j^i (\bar{G}_{\dot{\alpha}\beta})^a{}_b \right] Q_r^{\beta bj}. \quad (\text{A.7})$$

Note that the derivative implicitly carries $SU(2)_L$ and $SU(3)_c$ indices [explicit on the right-hand side of Eq. (A.7)] which are suppressed on the left-hand side to reduce clutter. Where appropriate we show these indices explicitly.

We represent the SM quantum numbers of fields as a 3-tuple $(C, I, Y)_L$, with C and I the dimension of the colour and isospin representations, Y the hypercharge of the field, and L an (often omitted) label of the Lorentz representation: S (scalar), F (fermion) or V (vector), although sometimes we use the irrep, e.g. $(2, 1)$. We normalise the hypercharge such that $Q = I_3 + Y$. Finally, for exotic fields that contribute to dimension-six operators at tree-level, we try and adopt names consistent with Table 3 of Ref. [22], which we reproduce here in Table A.2.

Field	$SU(3)_c \otimes SU(2)_L \otimes U(1)_Y$	$SU(2)_+ \otimes SU(2)_-$
$Q^{\alpha i}$	(3, 2, $\frac{1}{6}$)	(2, 1)
$L^{\alpha i}$	(1, 2, $-\frac{1}{2}$)	(2, 1)
\bar{u}_a^α	($\bar{3}$, 1, $-\frac{2}{3}$)	(2, 1)
\bar{d}_a^α	($\bar{3}$, 1, $\frac{1}{3}$)	(2, 1)
\bar{e}^α	(1, 1, 1)	(2, 1)
$(G_{\alpha\beta})_b^a$	(8, 1, 0)	(3, 1)
$(W_{\alpha\beta})_j^i$	(1, 3, 0)	(3, 1)
$B_{\alpha\beta}$	(1, 1, 0)	(3, 1)
H^i	(1, 2, $\frac{1}{2}$)	(1, 1)

Table A.1: The SM fields and their transformation properties under the SM gauge group G_{SM} and the Lorentz group. The final unbolded number in the 3-tuples of the G_{SM} column represents the $U(1)_Y$ charge of the field, normalised such that $Q = I_3 + Y$. For the fermions a generational index has been suppressed.

Name	S	S_1	S_2	φ	Ξ	Ξ_1	Θ_1	Θ_3
Irrep	(1, 1, 0)	(1, 1, 1)	(1, 1, 2)	(1, 2, $\frac{1}{2}$)	(1, 3, 0)	(1, 3, 1)	(1, 4, $\frac{1}{2}$)	(1, 4, $\frac{3}{2}$)
Name	ω_1	ω_2	ω_4	Π_1	Π_7	ζ		
Irrep	(3, 1, $\frac{1}{3}$)	(3, 1, $\frac{2}{3}$)	(3, 1, $\frac{4}{3}$)	(3, 2, $\frac{1}{6}$)	(3, 2, $\frac{7}{6}$)	(3, 3, $\frac{1}{3}$)		
Name	Ω_1	Ω_2	Ω_4	Y	Φ			
Irrep	(6, 1, $\frac{1}{3}$)	(6, 1, $\frac{2}{3}$)	(6, 1, $\frac{4}{3}$)	(6, 3, $\frac{1}{3}$)	(8, 2, $\frac{1}{2}$)			
Name	N	E	Δ_1	Δ_3	Σ	Σ_1		
Irrep	(1, 1, 0)	(1, 1, 1)	(1, 2, $\frac{1}{2}$)	(1, 2, $\frac{3}{2}$)	(1, 3, 0)	(1, 3, 1)		
Name	U	D	Q_1	Q_5	Q_7	T_1	T_2	
Irrep	(3, 1, $\frac{2}{3}$),	(3, 1, $\frac{1}{3}$)	(3, 2, $\frac{1}{6}$)	(3, 2, $-\frac{5}{6}$)	(3, 2, $\frac{7}{6}$)	(3, 3, $\frac{1}{3}$)	(3, 3, $\frac{2}{3}$)	

Table A.2: The table shows the exotic scalars (top) and vectorlike or Majorana fermions (bottom) contributing to the dimension-six SMEFT at tree-level [22]. We sometimes use the label of a field as presented in the table to represent its conjugate, although we always define the transformation properties each time a field is mentioned to avoid confusion. For the leptoquarks (second row), we add a prime to the field name presented here if the baryon-number assignment is such that only the diquark couplings are allowed.

B

Table of lepton-number-violating operators

Below we present the catalogue of $\Delta L = 2$ operators we use in our study. The operators are listed and labelled in a way consistent with the previous catalogues [84, 99], although we enforce that operators with the same field content carry the same numerical labels. This means that our listing may contain more $SU(2)_L$ structures for any numbered family of operators. Product operators as presented in the table must be read with care. This is just a convenient shorthand to represent the field-content of an operator and illustrate that isospin indices are internally contracted. For example, by writing $\mathcal{O}_{5b} = \mathcal{O}_1 Q^i \bar{d} \tilde{H}^j \epsilon_{ij}$, we do not mean to suggest that Lorentz indices must be contracted internally to \mathcal{O}_1 and the down-type Yukawa.

In each row we also provide information relevant to the number of completions. The number of unfiltered models (sets of field content) derived from the operator using our techniques is presented, along with the number that survive the democratic filtering procedure with the neutrino-mass filtering criterion. A sizeable number of operators end up with no completions that can play a dominant role in the physics of neutrino mass.

Other information relevant to the operators is also shown, including the number of loops required for the operator closure (the same as the number of loops appearing in the associated neutrino self-energy diagram) and the upper-bound on the scale of the new physics generating the operator at tree level, derived from the atmospheric lower bound on the mass of the heaviest neutrino. Operators for which a range is given for the number of loops are those that generate the dimension-seven or dimension-nine

analogues of the Weinberg operator. The additional Higgs fields in these diagrams can always be closed off, adding more loops to the neutrino self-energy while reducing the overall scale suppression. The contribution with the highest number of loops will dominate for scales $\Lambda \gtrsim 4\pi v$.

We remind the reader that our analysis does not include the number of unfiltered completions of \mathcal{O}_1''' . In this case, the number of filtered models comes from Ref. [103]. Other operators featuring a ‘–’ are non-explosive, *i.e.* they do not support tree-level topologies containing only scalars and fermions.

Table B.1: The table displays our listing of the $\Delta L = 2$ operators along with the number of completions before and after our model-filtering procedure, the number of loops in the neutrino self-energy diagram, and the upper bound on the new-physics scale associated with each operator. See the main text of the appendix for more information.

Labels	Operator	Models	Filtered	Loops	Λ [TeV]
1	$L^i L^j H^k H^l \cdot \epsilon_{ik} \epsilon_{jl}$	3	3	0	$6 \cdot 10^{11}$
2	$L^i L^j L^k \bar{e} H^l \cdot \epsilon_{ik} \epsilon_{jl}$	8	2	1	$4 \cdot 10^7$
3a	$L^i L^j Q^k \bar{d} H^l \cdot \epsilon_{ij} \epsilon_{kl}$	9	2	2	$2 \cdot 10^5$
3b	$L^i L^j Q^k \bar{d} H^l \cdot \epsilon_{ik} \epsilon_{jl}$	14	5	1	$9 \cdot 10^7$
4a	$L^i L^j \tilde{Q}^k \bar{u}^\dagger H^l \cdot \epsilon_{ik} \epsilon_{jl}$	5	0	1	$4 \cdot 10^9$
4b	$L^i L^j \tilde{Q}^k \bar{u}^\dagger H^l \cdot \epsilon_{ij} \epsilon_{kl}$	4	2	2	$10 \cdot 10^6$
5a	$L^i L^j Q^k \bar{d} H^l H^m \tilde{H}^n \cdot \epsilon_{il} \epsilon_{jn} \epsilon_{km}$	790	36	2	$6 \cdot 10^5$
5b	$\mathcal{O}_1 \cdot Q^i \bar{d} \tilde{H}^j \cdot \epsilon_{ij}$	492	14	1,2	$6 \cdot 10^5$
5c	$\mathcal{O}_{3a} \cdot H^i \tilde{H}^j \cdot \epsilon_{ij}$	509	0	2,3	$1 \cdot 10^3$
5d	$\mathcal{O}_{3b} \cdot H^i \tilde{H}^j \cdot \epsilon_{ij}$	799	16	1,2	$6 \cdot 10^5$
6a	$L^i L^j \tilde{Q}^k \bar{u}^\dagger H^l H^m \tilde{H}^n \cdot \epsilon_{il} \epsilon_{jn} \epsilon_{km}$	289	14	2	$2 \cdot 10^7$
6b	$\mathcal{O}_1 \cdot \tilde{Q}^i \bar{u}^\dagger \tilde{H}^j \cdot \epsilon_{ij}$	177	0	1,2	$2 \cdot 10^7$
6c	$\mathcal{O}_{4a} \cdot H^i \tilde{H}^j \cdot \epsilon_{ij}$	262	0	1,2	$2 \cdot 10^7$
6d	$\mathcal{O}_{4b} \cdot H^i \tilde{H}^j \cdot \epsilon_{ij}$	208	0	2,3	$6 \cdot 10^4$
7	$L^i \bar{e}^\dagger Q^j \tilde{Q}^k H^l H^m H^n \cdot \epsilon_{il} \epsilon_{jm} \epsilon_{kn}$	240	15	2	$2 \cdot 10^5$
8	$L^i \bar{e}^\dagger \bar{u}^\dagger \bar{d} H^j \cdot \epsilon_{ij}$	5	1	2,3	$2 \cdot 10^1$
9	$L^i L^j L^k L^l \bar{e} \bar{e} \cdot \epsilon_{ik} \epsilon_{jl}$	14	1	2	$3 \cdot 10^3$
10	$L^i L^j L^k \bar{e} Q^l \bar{d} \cdot \epsilon_{ik} \epsilon_{jl}$	50	1	2	$6 \cdot 10^3$
11a	$L^i L^j Q^k Q^l \bar{d} \bar{d} \cdot \epsilon_{ij} \epsilon_{kl}$	48	0	3	$4 \cdot 10^1$
11b	$L^i L^j Q^k Q^l \bar{d} \bar{d} \cdot \epsilon_{ik} \epsilon_{jl}$	72	16	2	$1 \cdot 10^4$
12a	$L^i L^j \tilde{Q}^k \tilde{Q}^l \bar{u}^\dagger \bar{u}^\dagger \cdot \epsilon_{ik} \epsilon_{jl}$	19	0	2	$2 \cdot 10^7$
12b	$L^i L^j \tilde{Q}^k \tilde{Q}^l \bar{u}^\dagger \bar{u}^\dagger \cdot \epsilon_{ij} \epsilon_{kl}$	17	4	3	$6 \cdot 10^4$
13	$L^i L^j L^k \bar{e} \tilde{Q}^l \bar{u}^\dagger \cdot \epsilon_{ik} \epsilon_{jl}$	12	0	2	$2 \cdot 10^5$
14a	$L^i L^j Q^k \tilde{Q}^l \bar{u}^\dagger \bar{d} \cdot \epsilon_{ij} \epsilon_{kl}$	29	1	3	$1 \cdot 10^3$

Labels	Operator	Models	Filtered	Loops	Λ [TeV]
14b	$L^i L^j Q^k \tilde{Q}^l \bar{u}^\dagger \bar{d} \cdot \epsilon_{ik} \epsilon_{jl}$	43	1	2	$6 \cdot 10^5$
15	$L^i L^j L^k \tilde{L}^l \bar{u}^\dagger \bar{d} \cdot \epsilon_{ik} \epsilon_{jl}$	12	1	3	$1 \cdot 10^3$
16	$L^i L^j \bar{e} \bar{e}^\dagger \bar{u}^\dagger \bar{d} \cdot \epsilon_{ij}$	13	1	3	$1 \cdot 10^3$
17	$L^i L^j \bar{u}^\dagger \bar{d} \bar{d}^\dagger \cdot \epsilon_{ij}$	18	12	3	$1 \cdot 10^3$
18	$L^i L^j \bar{u} \bar{u}^\dagger \bar{u}^\dagger \bar{d} \cdot \epsilon_{ij}$	22	8	3	$1 \cdot 10^3$
19	$L^i \bar{e}^\dagger Q^j \bar{u}^\dagger \bar{d} \bar{d} \cdot \epsilon_{ij}$	27	0	3,4	$2 \cdot 10^{-1}$
20	$L^i \bar{e}^\dagger \tilde{Q}^j \bar{u}^\dagger \bar{u}^\dagger \bar{d} \cdot \epsilon_{ij}$	27	3	3,4	$8 \cdot 10^{-1}$
21a	$L^i L^j L^k \bar{e} Q^l \bar{u} H^m H^n \cdot \epsilon_{il} \epsilon_{jm} \epsilon_{kn}$	3943	1	2,3	$2 \cdot 10^3$
21b	$L^i L^j L^k \bar{e} Q^l \bar{u} H^m H^n \cdot \epsilon_{ik} \epsilon_{jm} \epsilon_{ln}$	4080	4	3	$2 \cdot 10^3$
22a	$L^i L^j L^k \tilde{L}^l \bar{e} \bar{e}^\dagger H^m H^n \cdot \epsilon_{il} \epsilon_{jm} \epsilon_{kn}$	726	0	2	$2 \cdot 10^7$
22b	$\mathcal{O}_2 \cdot \tilde{L}^i \bar{e}^\dagger H^j \epsilon_{ij}$	931	0	2	$2 \cdot 10^7$
23a	$L^i L^j L^k \bar{e} \tilde{Q}^l \bar{d}^\dagger H^m H^n \cdot \epsilon_{il} \epsilon_{jm} \epsilon_{kn}$	780	0	2,3	$4 \cdot 10^1$
23b	$\mathcal{O}_2 \cdot \tilde{Q}^i \bar{d}^\dagger H^j \cdot \epsilon_{ij}$	969	0	2,3	$4 \cdot 10^1$
24a	$L^i L^j Q^k \bar{Q}^l \bar{d} \bar{d} H^m \tilde{H}^n \cdot \epsilon_{il} \epsilon_{jn} \epsilon_{km}$	9613	193	3	$9 \cdot 10^1$
24b	$L^i L^j Q^k \bar{Q}^l \bar{d} \bar{d} H^m \tilde{H}^n \cdot \epsilon_{im} \epsilon_{jn} \epsilon_{kl}$	6058	110	3	$9 \cdot 10^1$
24c	$\mathcal{O}_{3a} \cdot Q^i \bar{d} \tilde{H}^j \cdot \epsilon_{ij}$	6022	34	3,4	1
24d	$\mathcal{O}_{3b} \cdot Q^i \bar{d} \tilde{H}^j \cdot \epsilon_{ij}$	9616	211	2,3	$9 \cdot 10^1$
24e	$\mathcal{O}_{11a} \cdot H^i \tilde{H}^j \cdot \epsilon_{ij}$	3834	18	3,4	1
24f	$\mathcal{O}_{11b} \cdot H^i \tilde{H}^j \cdot \epsilon_{ij}$	5915	131	2,3	$9 \cdot 10^1$
25a	$L^i L^j Q^k \bar{Q}^l \bar{u} \bar{d} H^m H^n \cdot \epsilon_{im} \epsilon_{jn} \epsilon_{kl}$	5960	151	2,3	$4 \cdot 10^3$
25b	$\mathcal{O}_{3a} \cdot Q^i \bar{u} H^j \cdot \epsilon_{ij}$	5913	9	3,4	10
25c	$\mathcal{O}_{3b} \cdot Q^i \bar{u} H^j \cdot \epsilon_{ij}$	14036	470	2,3	$4 \cdot 10^3$
26a	$L^i L^j \tilde{L}^k \bar{e}^\dagger Q^l \bar{d} H^m H^n \cdot \epsilon_{ik} \epsilon_{jm} \epsilon_{ln}$	1600	0	3	$4 \cdot 10^1$
26b	$L^i L^j \tilde{L}^k \bar{e}^\dagger Q^l \bar{d} H^m H^n \cdot \epsilon_{im} \epsilon_{jn} \epsilon_{kl}$	1040	0	2,3	$4 \cdot 10^1$
26c	$\mathcal{O}_{3a} \cdot \tilde{L}^i \bar{e}^\dagger H^j \cdot \epsilon_{ij}$	1149	0	3	$4 \cdot 10^1$
26d	$\mathcal{O}_{3b} \cdot \tilde{L}^i \bar{e}^\dagger H^j \cdot \epsilon_{ij}$	1797	0	2,3	$4 \cdot 10^1$
27a	$L^i L^j Q^k \tilde{Q}^l \bar{d} \bar{d}^\dagger H^m H^n \cdot \epsilon_{ik} \epsilon_{jm} \epsilon_{ln}$	3851	164	2	$2 \cdot 10^7$
27b	$L^i L^j Q^k \tilde{Q}^l \bar{d} \bar{d}^\dagger H^m H^n \cdot \epsilon_{im} \epsilon_{jn} \epsilon_{kl}$	2226	74	2	$2 \cdot 10^7$
27c	$\mathcal{O}_{3a} \cdot \tilde{Q}^i \bar{d}^\dagger H^j \cdot \epsilon_{ij}$	2469	33	3	$6 \cdot 10^4$
27d	$\mathcal{O}_{3b} \cdot \tilde{Q}^i \bar{d}^\dagger H^j \cdot \epsilon_{ij}$	3443	165	2	$2 \cdot 10^7$
28a	$L^i L^j Q^k \tilde{Q}^l \bar{u}^\dagger \bar{d} H^m \tilde{H}^n \cdot \epsilon_{il} \epsilon_{jn} \epsilon_{km}$	4038	64	3	$4 \cdot 10^3$
28b	$L^i L^j Q^k \tilde{Q}^l \bar{u}^\dagger \bar{d} H^m \tilde{H}^n \cdot \epsilon_{im} \epsilon_{jn} \epsilon_{kl}$	4103	0	3,4	10
28c	$L^i L^j Q^k \tilde{Q}^l \bar{u}^\dagger \bar{d} H^m \tilde{H}^n \cdot \epsilon_{ik} \epsilon_{jn} \epsilon_{lm}$	4305	123	3	$4 \cdot 10^3$
28d	$\mathcal{O}_{3a} \cdot \tilde{Q}^i \bar{u}^\dagger \tilde{H}^j \cdot \epsilon_{ij}$	2749	7	3,4	10
28e	$\mathcal{O}_{3b} \cdot \tilde{Q}^i \bar{u}^\dagger \tilde{H}^j \cdot \epsilon_{ij}$	4304	90	2,3	$4 \cdot 10^3$
28f	$\mathcal{O}_{4a} \cdot Q^i \bar{d} \tilde{H}^j \cdot \epsilon_{ij}$	4039	74	2,3	$4 \cdot 10^3$
28g	$\mathcal{O}_{4b} \cdot Q^i \bar{d} \tilde{H}^j \cdot \epsilon_{ij}$	2748	14	3,4	10

Labels	Operator	Models	Filtered	Loops	Λ [TeV]
28 <i>h</i>	$\mathcal{O}_{14a} \cdot H^i \tilde{H}^j \cdot \epsilon_{ij}$	2701	10	3,4	10
28 <i>i</i>	$\mathcal{O}_{14b} \cdot H^i \tilde{H}^j \cdot \epsilon_{ij}$	4177	90	3	$4 \cdot 10^3$
29 <i>a</i>	$L^i L^j Q^k \tilde{Q}^l \bar{u} \bar{u}^\dagger H^m H^n \cdot \epsilon_{im} \epsilon_{jn} \epsilon_{kl}$	2226	267	2	$2 \cdot 10^7$
29 <i>b</i>	$L^i L^j Q^k \tilde{Q}^l \bar{u} \bar{u}^\dagger H^m H^n \cdot \epsilon_{ik} \epsilon_{jm} \epsilon_{ln}$	3846	498	2	$2 \cdot 10^7$
29 <i>c</i>	$\mathcal{O}_{4a} \cdot Q^i \bar{u} H^j \cdot \epsilon_{ij}$	3444	422	2	$2 \cdot 10^7$
29 <i>d</i>	$\mathcal{O}_{4b} \cdot Q^i \bar{u} H^j \cdot \epsilon_{ij}$	2468	64	3	$6 \cdot 10^4$
30 <i>a</i>	$L^i L^j \tilde{L}^k \bar{e}^\dagger \tilde{Q}^l \bar{u}^\dagger H^m H^n \cdot \epsilon_{ik} \epsilon_{jm} \epsilon_{ln}$	1772	0	3	$2 \cdot 10^3$
30 <i>b</i>	$L^i L^j \tilde{L}^k \bar{e}^\dagger \tilde{Q}^l \bar{u}^\dagger H^m H^n \cdot \epsilon_{im} \epsilon_{jn} \epsilon_{kl}$	1140	2	3	$2 \cdot 10^3$
30 <i>c</i>	$\mathcal{O}_{4a} \cdot \tilde{L}^i \bar{e}^\dagger H^j \cdot \epsilon_{ij}$	1776	2	2,3	$2 \cdot 10^3$
30 <i>d</i>	$\mathcal{O}_{4b} \cdot \tilde{L}^i \bar{e}^\dagger H^j \cdot \epsilon_{ij}$	1398	11	3	$2 \cdot 10^3$
31 <i>a</i>	$\mathcal{O}_{4a} \cdot \tilde{Q}^i \bar{d}^\dagger H^j \cdot \epsilon_{ij}$	3107	10	2,3	$4 \cdot 10^3$
31 <i>b</i>	$L^i L^j \tilde{Q}^k \tilde{Q}^l \bar{u}^\dagger \bar{d}^\dagger H^m H^n \cdot \epsilon_{im} \epsilon_{jn} \epsilon_{kl}$	1404	4	2,3	$4 \cdot 10^3$
31 <i>c</i>	$\mathcal{O}_{4b} \cdot \tilde{Q}^i \bar{d}^\dagger H^j \cdot \epsilon_{ij}$	1654	8	3,4	10
32 <i>a</i>	$L^i L^j \tilde{Q}^k \tilde{Q}^l \bar{u}^\dagger \bar{u}^\dagger H^m \tilde{H}^n \cdot \epsilon_{il} \epsilon_{jn} \epsilon_{km}$	2103	157	3	$2 \cdot 10^5$
32 <i>b</i>	$L^i L^j \tilde{Q}^k \tilde{Q}^l \bar{u}^\dagger \bar{u}^\dagger H^m \tilde{H}^n \cdot \epsilon_{im} \epsilon_{jn} \epsilon_{kl}$	1493	151	3	$2 \cdot 10^5$
32 <i>c</i>	$\mathcal{O}_{4a} \cdot \tilde{Q}^i \bar{u}^\dagger \tilde{H}^j \cdot \epsilon_{ij}$	2100	56	3	$2 \cdot 10^5$
32 <i>d</i>	$\mathcal{O}_{4b} \cdot \tilde{Q}^i \bar{u}^\dagger \tilde{H}^j \cdot \epsilon_{ij}$	1747	26	3,4	$4 \cdot 10^2$
32 <i>e</i>	$\mathcal{O}_{12a} \cdot H^i \tilde{H}^j$	1250	36	3	$2 \cdot 10^5$
32 <i>f</i>	$\mathcal{O}_{12b} \cdot H^i \tilde{H}^j$	1143	24	3,4	$4 \cdot 10^2$
33	$\mathcal{O}_1 \cdot \bar{e} e \bar{e}^\dagger \bar{e}^\dagger$	451	5	2	$2 \cdot 10^7$
34	$L^i \bar{e} \bar{e}^\dagger \bar{e}^\dagger Q^j \bar{d} H^k H^l \cdot \epsilon_{ik} \epsilon_{jl}$	1377	231	3	$4 \cdot 10^1$
35	$L^i \bar{e} \bar{e}^\dagger \bar{e}^\dagger \tilde{Q}^j \bar{u}^\dagger H^k H^l \cdot \epsilon_{ik} \epsilon_{jl}$	1126	15	3	$2 \cdot 10^3$
36	$\bar{e}^\dagger \bar{e}^\dagger Q^i Q^j \bar{d} \bar{d} H^k H^l \cdot \epsilon_{ik} \epsilon_{jl}$	970	208	4	$6 \cdot 10^{-5}$
37	$\bar{e}^\dagger \bar{e}^\dagger Q^i \tilde{Q}^j \bar{u}^\dagger \bar{d} H^k H^l \cdot \epsilon_{ik} \epsilon_{jl}$	2470	58	4,5,6,7	$4 \cdot 10^{-2}$
38	$\bar{e}^\dagger \bar{e}^\dagger \tilde{Q}^i \tilde{Q}^j \bar{u}^\dagger \bar{u}^\dagger H^k H^l \cdot \epsilon_{ik} \epsilon_{jl}$	3358	451	4	$1 \cdot 10^{-1}$
39 <i>a</i>	$\mathcal{O}_1 \cdot L^i L^j \tilde{L}^k \tilde{L}^l \cdot \epsilon_{ik} \epsilon_{jl}$	296	0	2	$2 \cdot 10^7$
39 <i>b</i>	$L^i L^j L^k L^l \tilde{L}^m \tilde{L}^n H^p H^q \cdot \epsilon_{il} \epsilon_{jl} \epsilon_{mp} \epsilon_{nq}$	220	6	2	$2 \cdot 10^7$
39 <i>c</i>	$L^i L^j L^k L^l \tilde{L}^m \tilde{L}^n H^p H^q \cdot \epsilon_{il} \epsilon_{jn} \epsilon_{kp} \epsilon_{mq}$	588	0	2	$2 \cdot 10^7$
39 <i>d</i>	$\mathcal{O}_1 \cdot L^i L^j \tilde{L}^k \tilde{L}^l \cdot \epsilon_{ij} \epsilon_{kl}$	324	0	2	$2 \cdot 10^7$
40 <i>a</i>	$L^i L^j L^k \tilde{L}^l Q^m \tilde{Q}^n H^p H^q \cdot \epsilon_{il} \epsilon_{jn} \epsilon_{kp} \epsilon_{mq}$	963	22	2	$2 \cdot 10^7$
40 <i>b</i>	$L^i L^j L^k \tilde{L}^l Q^m \tilde{Q}^n H^p H^q \cdot \epsilon_{il} \epsilon_{jp} \epsilon_{kq} \epsilon_{mn}$	729	25	2	$2 \cdot 10^7$
40 <i>c</i>	$L^i L^j L^k \tilde{L}^l Q^m \tilde{Q}^n H^p H^q \cdot \epsilon_{in} \epsilon_{jp} \epsilon_{kq} \epsilon_{lm}$	759	25	2	$2 \cdot 10^7$
40 <i>d</i>	$L^i L^j L^k \tilde{L}^l Q^m \tilde{Q}^n H^p H^q \cdot \epsilon_{ik} \epsilon_{jl} \epsilon_{mp} \epsilon_{nq}$	953	0	3	$6 \cdot 10^4$
40 <i>e</i>	$L^i L^j L^k \tilde{L}^l Q^m \tilde{Q}^n H^p H^q \cdot \epsilon_{il} \epsilon_{jm} \epsilon_{kp} \epsilon_{nq}$	1321	31	2	$2 \cdot 10^7$
40 <i>f</i>	$L^i L^j L^k \tilde{L}^l Q^m \tilde{Q}^n H^p H^q \cdot \epsilon_{ik} \epsilon_{jn} \epsilon_{lp} \epsilon_{mq}$	963	100	2	$2 \cdot 10^7$
40 <i>g</i>	$L^i L^j L^k \tilde{L}^l Q^m \tilde{Q}^n H^p H^q \cdot \epsilon_{im} \epsilon_{jn} \epsilon_{kp} \epsilon_{lq}$	1339	30	2	$2 \cdot 10^7$
40 <i>h</i>	$L^i L^j L^k \tilde{L}^l Q^m \tilde{Q}^n H^p H^q \cdot \epsilon_{ik} \epsilon_{jm} \epsilon_{lp} \epsilon_{nq}$	820	56	2	$2 \cdot 10^7$

Labels	Operator	Models	Filtered	Loops	Λ [TeV]
40 <i>i</i>	$L^i L^j L^k \tilde{L}^l Q^m \tilde{Q}^n H^p H^q \cdot \epsilon_{im} \epsilon_{jp} \epsilon_{kq} \epsilon_{ln}$	844	9	2	$2 \cdot 10^7$
40 <i>j</i>	$L^i L^j L^k \tilde{L}^l Q^m \tilde{Q}^n H^p H^q \cdot \epsilon_{ik} \epsilon_{jp} \epsilon_{ln} \epsilon_{mq}$	908	60	2	$2 \cdot 10^7$
40 <i>k</i>	$L^i L^j L^k \tilde{L}^l Q^m \tilde{Q}^n H^p H^q \cdot \epsilon_{ik} \epsilon_{jp} \epsilon_{lm} \epsilon_{nq}$	970	98	2	$2 \cdot 10^7$
40 <i>l</i>	$L^i L^j L^k \tilde{L}^l Q^m \tilde{Q}^n H^p H^q \cdot \epsilon_{ik} \epsilon_{jp} \epsilon_{lq} \epsilon_{mn}$	933	87	2	$2 \cdot 10^7$
41 <i>a</i>	$L^i L^j L^k \tilde{L}^l \bar{d} \bar{d}^\dagger H^m H^n \cdot \epsilon_{il} \epsilon_{jm} \epsilon_{kn}$	729	6	2	$2 \cdot 10^7$
41 <i>b</i>	$L^i L^j L^k \tilde{L}^l \bar{d} \bar{d}^\dagger H^m H^n \cdot \epsilon_{ik} \epsilon_{jm} \epsilon_{ln}$	933	71	2	$2 \cdot 10^7$
42 <i>a</i>	$L^i L^j L^k \tilde{L}^l \bar{u} \bar{u}^\dagger H^m H^n \cdot \epsilon_{il} \epsilon_{jm} \epsilon_{kn}$	729	21	2	$2 \cdot 10^7$
42 <i>b</i>	$L^i L^j L^k \tilde{L}^l \bar{u} \bar{u}^\dagger H^m H^n \cdot \epsilon_{ik} \epsilon_{jm} \epsilon_{ln}$	933	120	2	$2 \cdot 10^7$
43 <i>a</i>	$L^i L^j L^k \tilde{L}^l \bar{u}^\dagger \bar{d} H^m \tilde{H}^n \cdot \epsilon_{ik} \epsilon_{jn} \epsilon_{lm}$	1068	7	3,4	10
43 <i>b</i>	$L^i L^j L^k \tilde{L}^l \bar{u}^\dagger \bar{d} H^m \tilde{H}^n \cdot \epsilon_{il} \epsilon_{jm} \epsilon_{kn}$	1438	7	3,4	10
43 <i>c</i>	$L^i L^j L^k \tilde{L}^l \bar{u}^\dagger \bar{d} H^m \tilde{H}^n \cdot \epsilon_{ik} \epsilon_{jm} \epsilon_{ln}$	1068	8	3,4	10
43 <i>d</i>	$L^i L^j L^k \tilde{L}^l \bar{u}^\dagger \bar{d} H^m \tilde{H}^n \cdot \epsilon_{ik} \epsilon_{jl} \epsilon_{mn}$	1068	8	3,4	10
44 <i>a</i>	$L^i L^j \bar{e} \bar{e}^\dagger Q^k \tilde{Q}^l H^m H^n \cdot \epsilon_{il} \epsilon_{jm} \epsilon_{kn}$	1571	155	2	$2 \cdot 10^7$
44 <i>b</i>	$L^i L^j \bar{e} \bar{e}^\dagger Q^k \tilde{Q}^l H^m H^n \cdot \epsilon_{im} \epsilon_{jn} \epsilon_{kl}$	1016	91	2	$2 \cdot 10^7$
44 <i>c</i>	$L^i L^j \bar{e} \bar{e}^\dagger Q^k \tilde{Q}^l H^m H^n \cdot \epsilon_{ij} \epsilon_{km} \epsilon_{ln}$	1137	2	3	$6 \cdot 10^4$
44 <i>d</i>	$L^i L^j \bar{e} \bar{e}^\dagger Q^k \tilde{Q}^l H^m H^n \cdot \epsilon_{ik} \epsilon_{jm} \epsilon_{ln}$	1765	133	2	$2 \cdot 10^7$
45	$L^i L^j \bar{e} \bar{e}^\dagger \bar{d} \bar{d}^\dagger H^k H^l \cdot \epsilon_{ik} \epsilon_{jl}$	1016	81	2	$2 \cdot 10^7$
46	$L^i L^j \bar{e} \bar{e}^\dagger \bar{u} \bar{u}^\dagger H^k H^l \cdot \epsilon_{ik} \epsilon_{jl}$	1016	49	2	$2 \cdot 10^7$
47 <i>a</i>	$L^i L^j Q^k Q^l \tilde{Q}^m \tilde{Q}^n H^p H^q \cdot \epsilon_{im} \epsilon_{jn} \epsilon_{kp} \epsilon_{lq}$	1013	236	2	$2 \cdot 10^7$
47 <i>b</i>	$L^i L^j Q^k Q^l \tilde{Q}^m \tilde{Q}^n H^p H^q \cdot \epsilon_{im} \epsilon_{jp} \epsilon_{kn} \epsilon_{lq}$	2253	423	2	$2 \cdot 10^7$
47 <i>c</i>	$L^i L^j Q^k Q^l \tilde{Q}^m \tilde{Q}^n H^p H^q \cdot \epsilon_{ip} \epsilon_{jq} \epsilon_{km} \epsilon_{ln}$	1007	200	2	$2 \cdot 10^7$
47 <i>d</i>	$L^i L^j Q^k Q^l \tilde{Q}^m \tilde{Q}^n H^p H^q \cdot \epsilon_{il} \epsilon_{jn} \epsilon_{kp} \epsilon_{mq}$	2838	690	2	$2 \cdot 10^7$
47 <i>e</i>	$L^i L^j Q^k Q^l \tilde{Q}^m \tilde{Q}^n H^p H^q \cdot \epsilon_{in} \epsilon_{jp} \epsilon_{kl} \epsilon_{mq}$	1730	387	2	$2 \cdot 10^7$
47 <i>f</i>	$L^i L^j Q^k Q^l \tilde{Q}^m \tilde{Q}^n H^p H^q \cdot \epsilon_{ij} \epsilon_{kn} \epsilon_{lp} \epsilon_{mq}$	1702	60	3	$6 \cdot 10^4$
47 <i>g</i>	$L^i L^j Q^k Q^l \tilde{Q}^m \tilde{Q}^n H^p H^q \cdot \epsilon_{il} \epsilon_{jp} \epsilon_{kn} \epsilon_{mq}$	2796	530	2	$2 \cdot 10^7$
47 <i>h</i>	$L^i L^j Q^k Q^l \tilde{Q}^m \tilde{Q}^n H^p H^q \cdot \epsilon_{ij} \epsilon_{kp} \epsilon_{lq} \epsilon_{mn}$	924	46	3	$6 \cdot 10^4$
47 <i>i</i>	$L^i L^j Q^k Q^l \tilde{Q}^m \tilde{Q}^n H^p H^q \cdot \epsilon_{il} \epsilon_{jp} \epsilon_{kq} \epsilon_{mn}$	2078	369	2	$2 \cdot 10^7$
47 <i>j</i>	$L^i L^j Q^k Q^l \tilde{Q}^m \tilde{Q}^n H^p H^q \cdot \epsilon_{ip} \epsilon_{jq} \epsilon_{kl} \epsilon_{mn}$	902	183	2	$2 \cdot 10^7$
47 <i>k</i>	$L^i L^j Q^k Q^l \tilde{Q}^m \tilde{Q}^n H^p H^q \cdot \epsilon_{ik} \epsilon_{jl} \epsilon_{mp} \epsilon_{nq}$	1203	258	2	$2 \cdot 10^7$
47 <i>l</i>	$L^i L^j Q^k Q^l \tilde{Q}^m \tilde{Q}^n H^p H^q \cdot \epsilon_{ij} \epsilon_{kl} \epsilon_{mp} \epsilon_{nq}$	814	46	3	$6 \cdot 10^4$
48	$L^i L^j \bar{d} \bar{d} \bar{d}^\dagger \bar{d}^\dagger H^k H^l \cdot \epsilon_{ik} \epsilon_{jl}$	921	125	2	$2 \cdot 10^7$
49	$L^i L^j \bar{u} \bar{u}^\dagger \bar{d} \bar{d}^\dagger H^k H^l \cdot \epsilon_{ik} \epsilon_{jl}$	2086	384	2	$2 \cdot 10^7$
50 <i>a</i>	$L^i L^j \bar{u}^\dagger \bar{d} \bar{d} \bar{d}^\dagger H^k \tilde{H}^l \cdot \epsilon_{ik} \epsilon_{jl}$	2285	68	3,4	10
50 <i>b</i>	$\mathcal{O}_{17} \cdot H^i \tilde{H}^j \cdot \epsilon_{ij}$	1523	52	3,4	10
51	$L^i L^j \bar{u} \bar{u}^\dagger \bar{u}^\dagger H^k H^l \cdot \epsilon_{ik} \epsilon_{jl}$	921	225	2	$2 \cdot 10^7$
52 <i>a</i>	$L^i L^j \bar{u} \bar{u}^\dagger \bar{u}^\dagger \bar{d} H^k \tilde{H}^l \cdot \epsilon_{ik} \epsilon_{jl}$	2896	170	3,4	10
52 <i>b</i>	$\mathcal{O}_{18} \cdot H^i \tilde{H}^j \cdot \epsilon_{ij}$	1872	94	3,4	10

Labels	Operator	Models	Filtered	Loops	Λ [TeV]
53	$L^i L^j \bar{u}^\dagger \bar{u}^\dagger \bar{d} \bar{d} \tilde{H}^k \tilde{H}^l \cdot \epsilon_{ik} \epsilon_{jl}$	939	162	4,5,6	$2 \cdot 10^{-1}$
54a	$L^i \bar{e}^\dagger Q^j Q^k \tilde{Q}^l \bar{d} H^m H^n \cdot \epsilon_{il} \epsilon_{jm} \epsilon_{kn}$	2203	92	3	$4 \cdot 10^1$
54b	$L^i \bar{e}^\dagger Q^j Q^k \tilde{Q}^l \bar{d} H^m H^n \cdot \epsilon_{im} \epsilon_{jk} \epsilon_{ln}$	3393	89	3	$4 \cdot 10^1$
54c	$L^i \bar{e}^\dagger Q^j Q^k \tilde{Q}^l \bar{d} H^m H^n \cdot \epsilon_{im} \epsilon_{jk} \epsilon_{ln}$	2456	30	3	$4 \cdot 10^1$
54d	$L^i \bar{e}^\dagger Q^j Q^k \tilde{Q}^l \bar{d} H^m H^n \cdot \epsilon_{ik} \epsilon_{jm} \epsilon_{ln}$	3835	100	3	$4 \cdot 10^1$
55a	$L^i \bar{e}^\dagger Q^j \tilde{Q}^k \tilde{Q}^l \bar{u}^\dagger H^m H^n \cdot \epsilon_{il} \epsilon_{jm} \epsilon_{kn}$	3478	143	3	$2 \cdot 10^3$
55b	$L^i \bar{e}^\dagger Q^j \tilde{Q}^k \tilde{Q}^l \bar{u}^\dagger H^m H^n \cdot \epsilon_{im} \epsilon_{jl} \epsilon_{kn}$	3493	144	3	$2 \cdot 10^3$
55c	$L^i \bar{e}^\dagger Q^j \tilde{Q}^k \tilde{Q}^l \bar{u}^\dagger H^m H^n \cdot \epsilon_{im} \epsilon_{jn} \epsilon_{kl}$	2049	86	3	$2 \cdot 10^3$
55d	$L^i \bar{e}^\dagger Q^j \tilde{Q}^k \tilde{Q}^l \bar{u}^\dagger H^m H^n \cdot \epsilon_{ij} \epsilon_{km} \epsilon_{ln}$	2156	106	3	$2 \cdot 10^3$
56	$L^i \bar{e}^\dagger Q^j \bar{d} \bar{d}^\dagger H^k H^l \cdot \epsilon_{ik} \epsilon_{jl}$	2273	252	3	$4 \cdot 10^1$
57	$L^i \bar{e}^\dagger \tilde{Q}^j \bar{u}^\dagger \bar{d} \bar{d}^\dagger H^k H^l \cdot \epsilon_{ik} \epsilon_{jl}$	4251	481	3	$2 \cdot 10^3$
58	$L^i \bar{e}^\dagger \tilde{Q}^j \bar{u} \bar{u}^\dagger \bar{u}^\dagger H^k H^l \cdot \epsilon_{ik} \epsilon_{jl}$	2408	183	3	$2 \cdot 10^3$
59a	$L^i \bar{e}^\dagger Q^j \bar{u}^\dagger \bar{d} \bar{d} H^k \tilde{H}^l \cdot \epsilon_{ik} \epsilon_{jl}$	2638	65	3,4,5	$2 \cdot 10^{-1}$
59b	$\mathcal{O}_{19} \cdot H^i \tilde{H}^j \cdot \epsilon_{ij}$	2583	65	3,4,5	$2 \cdot 10^{-1}$
59c	$\mathcal{O}_8 \cdot Q^i \bar{d} \tilde{H}^j \cdot \epsilon_{ij}$	2639	42	4,5,6	$6 \cdot 10^{-2}$
60a	$L^i \bar{e}^\dagger \tilde{Q}^j \bar{u}^\dagger \bar{u}^\dagger \bar{d} H^k \tilde{H}^l \cdot \epsilon_{il} \epsilon_{jk}$	2687	35	4,5	$1 \cdot 10^{-1}$
60b	$\mathcal{O}_8 \cdot \tilde{Q}^i \bar{u}^\dagger \tilde{H}^j \cdot \epsilon_{ij}$	2687	121	3,4,5	$4 \cdot 10^{-1}$
60c	$\mathcal{O}_{20} \cdot H^i \tilde{H}^j \cdot \epsilon_{ij}$	2687	104	3,4,5	$4 \cdot 10^{-1}$
61a	$\mathcal{O}_1 \cdot L^i \bar{e} \tilde{H}^j \cdot \epsilon_{ij}$	382	0	1,2	$2 \cdot 10^5$
61b	$\mathcal{O}_2 \cdot H^i \tilde{H}^j \cdot \epsilon_{ij}$	408	0	1,2	$2 \cdot 10^5$
62a	$L^i L^j L^k L^l \bar{e} \bar{e} H^m \tilde{H}^n \cdot \epsilon_{il} \epsilon_{jm} \epsilon_{kn}$	1820	0	2,3	$2 \cdot 10^1$
62b	$\mathcal{O}_9 \cdot H^i \tilde{H}^j \cdot \epsilon_{ij}$	830	1	2,3	$2 \cdot 10^1$
63a	$L^i L^j L^k \bar{e} Q^l \bar{d} H^m \tilde{H}^n \cdot \epsilon_{ik} \epsilon_{jn} \epsilon_{lm}$	4619	12	3	$4 \cdot 10^1$
63b	$L^i L^j L^k \bar{e} Q^l \bar{d} H^m \tilde{H}^n \cdot \epsilon_{il} \epsilon_{jm} \epsilon_{kn}$	7216	77	2,3	$4 \cdot 10^1$
63c	$\mathcal{O}_2 \cdot Q^i \bar{d} \tilde{H}^j \cdot \epsilon_{ij}$	4621	49	2,3	$4 \cdot 10^1$
63d	$\mathcal{O}_{10} \cdot H^i \tilde{H}^j \cdot \epsilon_{ij}$	4590	45	2,3	$4 \cdot 10^1$
64a	$L^i L^j L^k \bar{e} \tilde{Q}^l \bar{u}^\dagger H^m \tilde{H}^n \cdot \epsilon_{il} \epsilon_{jm} \epsilon_{kn}$	1370	0	3	$2 \cdot 10^3$
64b	$L^i L^j L^k \bar{e} \tilde{Q}^l \bar{u}^\dagger H^m \tilde{H}^n \cdot \epsilon_{ik} \epsilon_{jn} \epsilon_{lm}$	1050	0	3	$2 \cdot 10^3$
64c	$\mathcal{O}_2 \cdot \tilde{Q}^i \bar{u}^\dagger \tilde{H}^j \cdot \epsilon_{ij}$	1049	0	2,3	$2 \cdot 10^3$
64d	$\mathcal{O}_{13} \cdot H^i \tilde{H}^j \cdot \epsilon_{ij}$	1008	0	3	$2 \cdot 10^3$
65a	$L^i L^j \bar{e} \bar{e}^\dagger \bar{u}^\dagger \bar{d} H^k \tilde{H}^l \cdot \epsilon_{ik} \epsilon_{jl}$	1925	17	3,4	10
65b	$\mathcal{O}_{16} \cdot H^i \tilde{H}^j \cdot \epsilon_{ij}$	1259	11	3,4	10
71	$\mathcal{O}_1 \cdot Q^i \bar{u} H^j \cdot \epsilon_{ij}$	396	9	2	$2 \cdot 10^7$
75	$\mathcal{O}_8 \cdot Q^i \bar{u} H^j \cdot \epsilon_{ij}$	3951	84	3	$4 \cdot 10^1$
76	$\bar{e}^\dagger \bar{e}^\dagger \bar{u}^\dagger \bar{u}^\dagger \bar{d} \bar{d}$	16	4	4,5,6	$2 \cdot 10^{-2}$
77	$\mathcal{O}_1 \cdot \tilde{L}^i \bar{e}^\dagger H^j \cdot \epsilon_{ij}$	156	0	2	$2 \cdot 10^5$
78	$\mathcal{O}_1 \cdot \tilde{Q}^i \bar{d}^\dagger H^j \cdot \epsilon_{ij}$	156	0	2	$6 \cdot 10^5$
1'	$\mathcal{O}_1 \cdot \tilde{H}^i H^j \cdot \epsilon_{ij}$	53	1	0,1	$4 \cdot 10^9$

Labels	Operator	Models	Filtered	Loops	Λ [TeV]
8'	$\mathcal{O}_8 \cdot \tilde{H}^i H^j \cdot \epsilon_{ij}$	301	4	2,3,4	1
1''	$\mathcal{O}_1 \cdot \tilde{H}^i H^j \tilde{H}^k H^l \cdot \epsilon_{ij} \epsilon_{kl}$	1893	6	0,1,2	$2 \cdot 10^7$
1'''	$\mathcal{O}_1 \cdot \tilde{H}^i H^j \tilde{H}^k H^l \tilde{H}^m H^n \cdot \epsilon_{ij} \epsilon_{kl} \epsilon_{mn}$	—	2	0,1,2	$2 \cdot 10^7$
7'	$\mathcal{O}_7 \cdot \tilde{H}^i H^j \cdot \epsilon_{ij}$	24951	374	2,3	$2 \cdot 10^3$
8''	$\mathcal{O}_8 \cdot \tilde{H}^i H^j \tilde{H}^k H^l \cdot \epsilon_{ij} \epsilon_{kl}$	19229	197	2,3,4,5	$7 \cdot 10^{-1}$
71'	$\mathcal{O}_{71} \cdot \tilde{H}^i H^j \cdot \epsilon_{ij}$	39331	446	2,3	$2 \cdot 10^5$
76'	$\mathcal{O}_{76} \cdot \tilde{H}^i H^j \cdot \epsilon_{ij}$	679	209	4,5,6,7	$4 \cdot 10^{-2}$
77'	$\mathcal{O}_{77} \cdot \tilde{H}^i H^j \cdot \epsilon_{ij}$	14598	0	1,2,3	$2 \cdot 10^3$
78'	$\mathcal{O}_{78} \cdot \tilde{H}^i H^j \cdot \epsilon_{ij}$	14644	1	2,3	$4 \cdot 10^3$
79a	$\mathcal{O}_{61a} \cdot \tilde{H}^i H^j \cdot \epsilon_{ij}$	31791	14	1,2,3	$2 \cdot 10^3$
79b	$\mathcal{O}_2 \cdot \tilde{H}^i H^j \tilde{H}^k H^l \cdot \epsilon_{ij} \epsilon_{kl}$	23931	14	1,2,3	$2 \cdot 10^3$
80a	$\mathcal{O}_{5a} \cdot \tilde{H}^i H^j \cdot \epsilon_{ij}$	72694	154	2,3	$4 \cdot 10^3$
80b	$\mathcal{O}_{5b} \cdot \tilde{H}^i H^j \cdot \epsilon_{ij}$	49108	371	1,2,3	$4 \cdot 10^3$
80c	$\mathcal{O}_{3a} \cdot \tilde{H}^i H^j \tilde{H}^k H^l \cdot \epsilon_{ij} \epsilon_{kl}$	31569	16	2,3,4	$1 \cdot 10^1$
80d	$\mathcal{O}_{3b} \cdot \tilde{H}^i H^j \tilde{H}^k H^l \cdot \epsilon_{ij} \epsilon_{kl}$	49505	367	1,2,3	$4 \cdot 10^3$
81a	$\mathcal{O}_{6a} \cdot \tilde{H}^i H^j \cdot \epsilon_{ij}$	26174	95	2,3	$2 \cdot 10^5$
81b	$\mathcal{O}_{6b} \cdot \tilde{H}^i H^j \cdot \epsilon_{ij}$	17298	18	1,2,3	$2 \cdot 10^5$
81c	$\mathcal{O}_{4a} \cdot \tilde{H}^i H^j \tilde{H}^k H^l \cdot \epsilon_{ij} \epsilon_{kl}$	15575	18	1,2,3	$2 \cdot 10^5$
81d	$\mathcal{O}_{4b} \cdot \tilde{H}^i H^j \tilde{H}^k H^l \cdot \epsilon_{ij} \epsilon_{kl}$	12400	41	2,3,4	$4 \cdot 10^2$
82	$L^i \tilde{L}^j \bar{e}^\dagger \bar{e}^\dagger \bar{u}^\dagger \bar{d} H^k H^l \cdot \epsilon_{ik} \epsilon_{jl}$	1151	56	3,4,5	$2 \cdot 10^{-1}$
D1	$(DL)^i L^j \bar{u}^\dagger \bar{d} \cdot \epsilon_{ij}$	—	—	3,4,5	$2 \cdot 10^{-1}$
D2a	$(DL)^i L^j (DH)^k H^l \cdot \epsilon_{ij} \epsilon_{kl}$	1	0	1	$2 \cdot 10^9$
D2b	$(DL)^i L^j (DH)^k H^l \cdot \epsilon_{il} \epsilon_{jk}$	3	3	0	$6 \cdot 10^{11}$
D2c	$(DL)^i L^j (DH)^k H^l \cdot \epsilon_{ik} \epsilon_{jl}$	3	3	0	$6 \cdot 10^{11}$
D3	$L^i \bar{e}^\dagger H^j H^k (DH)^l \cdot \epsilon_{ik} \epsilon_{jl}$	4	0	1	$4 \cdot 10^7$
D4a	$L^i L^j (DL)^k (D\bar{e}) H^l \cdot \epsilon_{ik} \epsilon_{jl}$	8	2	1	$4 \cdot 10^7$
D4b	$L^i L^j (DL)^k (D\bar{e}) H^l \cdot \epsilon_{ij} \epsilon_{kl}$	8	2	1	$4 \cdot 10^7$
D5a	$L^i L^j (DL)^k \tilde{L}^l H^m H^n \cdot \epsilon_{il} \epsilon_{jm} \epsilon_{kn}$	21	0	1	$4 \cdot 10^9$
D5b	$L^i L^j (DL)^k \tilde{L}^l H^m H^n \cdot \epsilon_{ik} \epsilon_{jm} \epsilon_{ln}$	30	4	1	$4 \cdot 10^9$
D5c	$L^i L^j (DL)^k \tilde{L}^l H^m H^n \cdot \epsilon_{ij} \epsilon_{km} \epsilon_{ln}$	30	4	1	$4 \cdot 10^9$
D5d	$L^i L^j (DL)^k \tilde{L}^l H^m H^n \cdot \epsilon_{im} \epsilon_{jn} \epsilon_{kl}$	21	0	1	$4 \cdot 10^9$
D6a	$L^i L^j \bar{e} \bar{e}^\dagger (DH)^k H^l \cdot \epsilon_{ik} \epsilon_{jl}$	30	2	1	$4 \cdot 10^9$
D6b	$L^i L^j \bar{e} \bar{e}^\dagger (DH)^k H^l \cdot \epsilon_{ij} \epsilon_{kl}$	16	0	2	$10 \cdot 10^6$
D7a	$(DL)^i L^j Q^k (D\bar{d}) H^l \cdot \epsilon_{ij} \epsilon_{kl}$	9	2	2	$2 \cdot 10^5$
D7b	$(DL)^i L^j Q^k (D\bar{d}) H^l \cdot \epsilon_{ik} \epsilon_{jl}$	14	5	1	$9 \cdot 10^7$
D7c	$(DL)^i L^j Q^k (D\bar{d}) H^l \cdot \epsilon_{il} \epsilon_{jk}$	14	5	1	$9 \cdot 10^7$
D8a	$L^i L^j Q^k \tilde{Q}^l (DH)^m H^n \cdot \epsilon_{in} \epsilon_{jk} \epsilon_{lm}$	53	11	1	$4 \cdot 10^9$
D8b	$L^i L^j Q^k \tilde{Q}^l (DH)^m H^n \cdot \epsilon_{in} \epsilon_{jl} \epsilon_{km}$	44	6	1	$4 \cdot 10^9$

Labels	Operator	Models	Filtered	Loops	Λ [TeV]
D8c	$L^i L^j Q^k \tilde{Q}^l (DH)^m H^n \cdot \epsilon_{ik} \epsilon_{jl} \epsilon_{mn}$	25	0	2	$10 \cdot 10^6$
D8d	$L^i L^j Q^k \tilde{Q}^l (DH)^m H^n \cdot \epsilon_{im} \epsilon_{jk} \epsilon_{ln}$	53	11	1	$4 \cdot 10^9$
D8e	$L^i L^j Q^k \tilde{Q}^l (DH)^m H^n \cdot \epsilon_{im} \epsilon_{jl} \epsilon_{kn}$	44	6	1	$4 \cdot 10^9$
D8f	$L^i L^j Q^k \tilde{Q}^l (DH)^m H^n \cdot \epsilon_{im} \epsilon_{jn} \epsilon_{kl}$	30	5	1	$4 \cdot 10^9$
D8g	$L^i L^j Q^k \tilde{Q}^l (DH)^m H^n \cdot \epsilon_{ij} \epsilon_{km} \epsilon_{ln}$	35	7	2	$10 \cdot 10^6$
D8h	$L^i L^j Q^k \tilde{Q}^l (DH)^m H^n \cdot \epsilon_{ij} \epsilon_{kn} \epsilon_{lm}$	35	7	2	$10 \cdot 10^6$
D8i	$L^i L^j Q^k \tilde{Q}^l (DH)^m H^n \cdot \epsilon_{ij} \epsilon_{kl} \epsilon_{mn}$	16	3	2	$10 \cdot 10^6$
D9a	$L^i L^j \bar{d} \bar{d}^\dagger (DH)^k H^l \cdot \epsilon_{ik} \epsilon_{jl}$	30	5	1	$4 \cdot 10^9$
D9b	$L^i L^j \bar{d} \bar{d}^\dagger (DH)^k H^l \cdot \epsilon_{ij} \epsilon_{kl}$	16	4	2	$10 \cdot 10^6$
D10a	$(DL)^i L^j \bar{u}^\dagger \bar{d} H^k \tilde{H}^l \cdot \epsilon_{il} \epsilon_{jk}$	56	13	2,3	$1 \cdot 10^3$
D10b	$(DL)^i L^j \bar{u}^\dagger \bar{d} H^k \tilde{H}^l \cdot \epsilon_{ij} \epsilon_{kl}$	36	7	2,3	$1 \cdot 10^3$
D10c	$(DL)^i L^j \bar{u}^\dagger \bar{d} H^k \tilde{H}^l \cdot \epsilon_{ik} \epsilon_{jl}$	56	13	2,3	$1 \cdot 10^3$
D11	$(DL)^i L^j (D\bar{u}^\dagger) (\bar{D}\bar{d}) \cdot \epsilon_{ij}$	—	—	2,3	$1 \cdot 10^3$
D12a	$L^i L^j \bar{u} \bar{u}^\dagger (DH)^k H^l \cdot \epsilon_{ik} \epsilon_{jl}$	30	5	1	$4 \cdot 10^9$
D12b	$L^i L^j \bar{u} \bar{u}^\dagger (DH)^k H^l \cdot \epsilon_{ij} \epsilon_{kl}$	16	4	2	$10 \cdot 10^6$
D13a	$(DL)^i L^j \tilde{Q}^k (D\bar{u}^\dagger) H^l \cdot \epsilon_{ij} \epsilon_{kl}$	4	2	2	$10 \cdot 10^6$
D13b	$(DL)^i L^j \tilde{Q}^k (D\bar{u}^\dagger) H^l \cdot \epsilon_{ik} \epsilon_{jl}$	5	0	1	$4 \cdot 10^9$
D14a	$L^i \bar{e}^\dagger Q^j \bar{d} (DH)^k H^l \cdot \epsilon_{ik} \epsilon_{jl}$	53	0	2	$6 \cdot 10^3$
D14b	$L^i \bar{e}^\dagger Q^j \bar{d} (DH)^k H^l \cdot \epsilon_{il} \epsilon_{jk}$	53	0	2	$6 \cdot 10^3$
D14c	$L^i \bar{e}^\dagger Q^j \bar{d} (DH)^k H^l \cdot \epsilon_{ij} \epsilon_{kl}$	27	0	2	$6 \cdot 10^3$
D15	$(DL)^i \bar{e}^\dagger (D\bar{u}^\dagger) \bar{d} H^j \cdot \epsilon_{ij}$	5	1	2,3	$2 \cdot 10^1$
D16a	$L^i \bar{e}^\dagger \tilde{Q}^j \bar{u}^\dagger (DH)^k H^l \cdot \epsilon_{ik} \epsilon_{jl}$	58	8	2	$2 \cdot 10^5$
D16b	$L^i \bar{e}^\dagger \tilde{Q}^j \bar{u}^\dagger (DH)^k H^l \cdot \epsilon_{il} \epsilon_{jk}$	58	8	2	$2 \cdot 10^5$
D16c	$L^i \bar{e}^\dagger \tilde{Q}^j \bar{u}^\dagger (DH)^k H^l \cdot \epsilon_{ij} \epsilon_{kl}$	27	4	2	$2 \cdot 10^5$
D17	$\bar{e}^\dagger \bar{e}^\dagger \bar{u}^\dagger \bar{d} (DH)^i H^j \cdot \epsilon_{ij}$	16	7	3,4	$2 \cdot 10^{-1}$
D18a	$(DL)^i L^j H^k H^l (DH)^m \tilde{H}^n \cdot \epsilon_{ik} \epsilon_{jm} \epsilon_{ln}$	53	1	0,1	$4 \cdot 10^9$
D18b	$(DL)^i L^j H^k H^l (DH)^m \tilde{H}^n \cdot \epsilon_{ik} \epsilon_{jl} \epsilon_{mn}$	53	1	0,1	$4 \cdot 10^9$
D18c	$(DL)^i L^j H^k H^l (DH)^m \tilde{H}^n \cdot \epsilon_{im} \epsilon_{jl} \epsilon_{kn}$	53	1	0,1	$4 \cdot 10^9$
D18d	$(DL)^i L^j H^k H^l (DH)^m \tilde{H}^n \cdot \epsilon_{ij} \epsilon_{km} \epsilon_{ln}$	24	1	1,2	$10 \cdot 10^6$
D18e	$(DL)^i L^j H^k H^l (DH)^m \tilde{H}^n \cdot \epsilon_{in} \epsilon_{jl} \epsilon_{km}$	34	0	1	$4 \cdot 10^9$
D18f	$(DL)^i L^j H^k H^l (DH)^m \tilde{H}^n \cdot \epsilon_{il} \epsilon_{jn} \epsilon_{km}$	34	0	1	$4 \cdot 10^9$
D19a	$(D^2 L)^i L^j (D^2 H)^k H^l \cdot \epsilon_{ij} \epsilon_{kl}$	1	0	1	$2 \cdot 10^9$
D19b	$(D^2 L)^i L^j (D^2 H)^k H^l \cdot \epsilon_{il} \epsilon_{jk}$	3	3	0	$6 \cdot 10^{11}$
D19c	$(D^2 L)^i L^j (D^2 H)^k H^l \cdot \epsilon_{ik} \epsilon_{jl}$	3	3	0	$6 \cdot 10^{11}$
D20	$L^i \bar{e}^\dagger H^j H^k H^l (DH)^m \tilde{H}^n \cdot \epsilon_{il} \epsilon_{jm} \epsilon_{kn}$	129	0	1,2	$2 \cdot 10^5$
D21	$(DL)^i (D\bar{e}^\dagger) H^j H^k (DH)^l \cdot \epsilon_{ik} \epsilon_{jl}$	2	0	1	$4 \cdot 10^7$
D22	$\bar{e}^\dagger \bar{e}^\dagger (DH)^i (DH)^j H^k H^l \cdot \epsilon_{ik} \epsilon_{jl}$	9	0	2	$3 \cdot 10^3$

Definition of Symbols and Acronyms

B

BSM Beyond the Standard Model

C

CC Charged current

CKM Cabibbo–Kobayashi–Maskawa

CP Charge parity

D

\digamma The Greek letter Digamma

E

EFT Effective Field Theory

EOM Equations of motion

F

FCNC Flavour changing neutral current

G

G_{SM} The SM gauge group

H

h.c. Hermitian conjugate

HS Hilbert series

I

IBP Integration by parts

IO Inverted ordering

L

LFU Lepton flavour universality

LFV Lepton flavour violation

LHC Large Hadron Collider

LNV Lepton number violation

LQ Leptoquark

N

NC Neutral current

NO Normal ordering

NP New physics

P

PMNS Pontecorvo–Maki–Nakagawa–Sakata

Q

QCD Quantum chromodynamics

S

S_1 The scalar leptoquark transforming as $(3, \mathbf{1}, -\frac{1}{3})$ under G_{SM}

S_3 The scalar leptoquark transforming as $(3, \mathbf{3}, -\frac{1}{3})$ under G_{SM}

SM Standard Model

SMEFT Standard Model Effective Field Theory

U

UV Ultraviolet

V

vev Vacuum expectation value

W

WET Weak Effective Field Theory

Bibliography

- [1] R. Foot and J. Gargalionis, *Explaining the 750 GeV diphoton excess with a colored scalar charged under a new confining gauge interaction*, *Phys. Rev. D* **94** (2016), no. 1 011703, [[arXiv:1604.06180](https://arxiv.org/abs/1604.06180)].
- [2] Y. Cai, J. Gargalionis, M. A. Schmidt, and R. R. Volkas, *Reconsidering the One Leptoquark solution: flavor anomalies and neutrino mass*, *JHEP* **10** (2017) 047, [[arXiv:1704.05849](https://arxiv.org/abs/1704.05849)].
- [3] I. Bigaran, J. Gargalionis, and R. R. Volkas, *A near-minimal leptoquark model for reconciling flavour anomalies and generating radiative neutrino masses*, *JHEP* **10** (2019) 106, [[arXiv:1906.01870](https://arxiv.org/abs/1906.01870)].
- [4] J. Gargalionis, I. Popa-Mateiu, and R. R. Volkas, *Radiative neutrino mass model from a mass dimension-11 $\Delta L = 2$ effective operator*, *JHEP* **03** (2020) 150, [[arXiv:1912.12386](https://arxiv.org/abs/1912.12386)].
- [5] J. Gargalionis and R. R. Volkas, *Exploding operators for Majorana neutrino masses and beyond*, [arXiv:2009.13537](https://arxiv.org/abs/2009.13537).
- [6] I. Esteban, M. Gonzalez-Garcia, M. Maltoni, T. Schwetz, and A. Zhou, *The fate of hints: updated global analysis of three-flavor neutrino oscillations*, [arXiv:2007.14792](https://arxiv.org/abs/2007.14792).
- [7] “Nufit 5.0 (2020).” www.nu-fit.org. Accessed: 2020-09-03.
- [8] LHCb Collaboration, R. Aaij et al., *Search for lepton-universality violation in $B^+ \rightarrow K^+ \ell^+ \ell^-$ decays*, *Phys. Rev. Lett.* **122** (2019), no. 19 191801, [[arXiv:1903.09252](https://arxiv.org/abs/1903.09252)].
- [9] Belle Collaboration, A. Abdesselam et al., *Test of lepton flavor universality in $B \rightarrow K \ell^+ \ell^-$ decays*, [arXiv:1908.01848](https://arxiv.org/abs/1908.01848).
- [10] BaBar Collaboration, J. Lees et al., *Measurement of Branching Fractions and Rate Asymmetries in the Rare Decays $B \rightarrow K^{(*)} l^+ l^-$* , *Phys. Rev. D* **86** (2012) 032012, [[arXiv:1204.3933](https://arxiv.org/abs/1204.3933)].

- [11] **Belle** Collaboration, A. Abdesselam et al., *Test of lepton flavor universality in $B \rightarrow K^* \ell^+ \ell^-$ decays at Belle*, [arXiv:1904.02440](https://arxiv.org/abs/1904.02440).
- [12] **LHCb** Collaboration, R. Aaij et al., *Test of lepton universality with $B^0 \rightarrow K^{*0} \ell^+ \ell^-$ decays*, *JHEP* **08** (2017) 055, [[arXiv:1705.05802](https://arxiv.org/abs/1705.05802)].
- [13] J. Aebrischer, W. Altmannshofer, D. Guadagnoli, M. Reboud, P. Stangl, and D. M. Straub, *B -decay discrepancies after Moriond 2019*, *Eur. Phys. J. C* **80** (2020), no. 3 252, [[arXiv:1903.10434](https://arxiv.org/abs/1903.10434)].
- [14] **HFLAV** Collaboration, Y. S. Amhis et al., *Averages of b -hadron, c -hadron, and τ -lepton properties as of 2018*, [arXiv:1909.12524](https://arxiv.org/abs/1909.12524). updated results and plots available at <https://hflav.web.cern.ch/>.
- [15] **Belle** Collaboration, A. Abdesselam et al., *Measurement of $\mathcal{R}(D)$ and $\mathcal{R}(D^*)$ with a semileptonic tagging method*, [arXiv:1904.08794](https://arxiv.org/abs/1904.08794).
- [16] P. W. Angel, Y. Cai, N. L. Rodd, M. A. Schmidt, and R. R. Volkas, *Testable two-loop radiative neutrino mass model based on an $LLQd^cQd^c$ effective operator*, *JHEP* **10** (2013) 118, [[arXiv:1308.0463](https://arxiv.org/abs/1308.0463)]. [Erratum: *JHEP*11,092(2014)].
- [17] **COMET** Collaboration, A. Kurup, *The COherent Muon to Electron Transition (COMET) experiment*, *Nucl. Phys. Proc. Suppl.* **218** (2011) 38–43.
- [18] W. Buchmuller and D. Wyler, *Effective Lagrangian Analysis of New Interactions and Flavor Conservation*, *Nucl. Phys. B* **268** (1986) 621–653.
- [19] B. Grzadkowski, M. Iskrzynski, M. Misiak, and J. Rosiek, *Dimension-Six Terms in the Standard Model Lagrangian*, *JHEP* **10** (2010) 085, [[arXiv:1008.4884](https://arxiv.org/abs/1008.4884)].
- [20] J. Gargalionis and R. R. Volkas, *Database of tree-level completions of lepton-number-violating effective operators*, Sept., 2020. The database of filtered models is packaged into our example code at <https://github.com/johngarg/neutrinomass>.
- [21] **Particle Data Group** Collaboration, C. Patrignani et al., *Review of Particle Physics*, *Chin. Phys. C* **40** (2016), no. 10 100001.
- [22] J. de Blas, J. C. Criado, M. Perez-Victoria, and J. Santiago, *Effective description of general extensions of the Standard Model: the complete tree-level dictionary*, *JHEP* **03** (2018) 109, [[arXiv:1711.10391](https://arxiv.org/abs/1711.10391)].
- [23] S. Glashow, *Partial Symmetries of Weak Interactions*, *Nucl. Phys.* **22** (1961) 579–588.

- [24] S. Weinberg, *A Model of Leptons*, *Phys. Rev. Lett.* **19** (1967) 1264–1266.
- [25] A. Salam, *Weak and Electromagnetic Interactions*, *Conf. Proc. C* **680519** (1968) 367–377.
- [26] G. ’t Hooft, *Renormalization of Massless Yang-Mills Fields*, *Nucl. Phys. B* **33** (1971) 173–199.
- [27] S. Glashow, J. Iliopoulos, and L. Maiani, *Weak Interactions with Lepton-Hadron Symmetry*, *Phys. Rev. D* **2** (1970) 1285–1292.
- [28] D. J. Gross and F. Wilczek, *Ultraviolet Behavior of Nonabelian Gauge Theories*, *Phys. Rev. Lett.* **30** (1973) 1343–1346.
- [29] B. Pontecorvo, *Mesonium and anti-mesonium*, *Sov. Phys. JETP* **6** (1957) 429.
- [30] Z. Maki, M. Nakagawa, and S. Sakata, *Remarks on the unified model of elementary particles*, *Prog. Theor. Phys.* **28** (1962) 870–880.
- [31] A. Y. Smirnov, *Solar neutrinos: Oscillations or No-oscillations?*, [arXiv:1609.02386](https://arxiv.org/abs/1609.02386).
- [32] J. N. Bahcall and R. K. Ulrich, *Solar models, neutrino experiments, and helioseismology*, *Rev. Mod. Phys.* **60** (Apr, 1988) 297–372.
- [33] S. Turck-Chieze, S. Cahen, M. Casse, and C. Doom, *Revisiting the Standard Solar Model*, *APJ* **335** (Dec., 1988) 415.
- [34] J. N. Bahcall and M. H. Pinsonneault, *Standard solar models, with and without helium diffusion, and the solar neutrino problem*, *Rev. Mod. Phys.* **64** (Oct, 1992) 885–926.
- [35] J. N. Bahcall, M. H. Pinsonneault, and G. J. Wasserburg, *Solar models with helium and heavy-element diffusion*, *Rev. Mod. Phys.* **67** (Oct, 1995) 781–808.
- [36] D. R. Morrison, *Review of solar models and solar neutrino experiments, Part. World* **3** (1992), no. 1 30–39.
- [37] R. Davis, *Solar neutrinos. ii. experimental*, *Phys. Rev. Lett.* **12** (Mar, 1964) 303–305.
- [38] Kamiokande-II Collaboration, K. Hirata et al., *Observation of B-8 Solar Neutrinos in the Kamiokande-II Detector*, *Phys. Rev. Lett.* **63** (1989) 16.
- [39] Kamiokande-II Collaboration, K. Hirata et al., *Results from one thousand days of real time directional solar neutrino data*, *Phys. Rev. Lett.* **65** (1990) 1297–1300.

- [40] GALLEX Collaboration, W. Hampel et al., *GALLEX solar neutrino observations: Results for GALLEX IV*, *Phys. Lett. B* **447** (1999) 127–133.
- [41] SAGE Collaboration, J. Abdurashitov et al., *Measurement of the solar neutrino capture rate with gallium metal*, *Phys. Rev. C* **60** (1999) 055801, [[astro-ph/9907113](#)].
- [42] SNO Collaboration, Q. Ahmad et al., *Measurement of the rate of $\nu_e + d \rightarrow p + p + e^-$ interactions produced by 8B solar neutrinos at the Sudbury Neutrino Observatory*, *Phys. Rev. Lett.* **87** (2001) 071301, [[nucl-ex/0106015](#)].
- [43] SNO Collaboration, Q. Ahmad et al., *Direct evidence for neutrino flavor transformation from neutral current interactions in the Sudbury Neutrino Observatory*, *Phys. Rev. Lett.* **89** (2002) 011301, [[nucl-ex/0204008](#)].
- [44] Kamiokande-II Collaboration, K. Hirata et al., *Observation of a small atmospheric muon-neutrino / electron-neutrino ratio in Kamiokande*, *Phys. Lett. B* **280** (1992) 146–152.
- [45] R. Becker-Szendy et al., *Neutrino measurements with the IMB detector*, *Nucl. Phys. B Proc. Suppl.* **38** (1995) 331–336.
- [46] Super-Kamiokande Collaboration, Y. Fukuda et al., *Evidence for oscillation of atmospheric neutrinos*, *Phys. Rev. Lett.* **81** (1998) 1562–1567, [[hep-ex/9807003](#)].
- [47] F. von Feilitzsch and N. Schmitz, eds., *Neutrino physics and astrophysics. Proceedings, 20th International Conference, Neutrino 2002, Munich, Germany, May 25-30, 2002*, vol. 118, 2003.
- [48] M. Shiozawa, “Experimental results on atmospheric neutrinos in Super-Kamiokande-I.” *Neutrino 2002*, 2002.
- [49] Super-Kamiokande Collaboration, M. Smy, *Solar neutrino precision measurements using all 1496 days of Super-Kamiokande I data*, *Nucl. Phys. B Proc. Suppl.* **118** (2003) 25–32, [[hep-ex/0208004](#)].
- [50] C. Giganti, S. Lavignac, and M. Zito, *Neutrino oscillations: The rise of the PMNS paradigm*, *Prog. Part. Nucl. Phys.* **98** (2018) 1–54, [[arXiv:1710.00715](#)].
- [51] F. Capozzi, E. Di Valentino, E. Lisi, A. Marrone, A. Melchiorri, and A. Palazzo, *Global constraints on absolute neutrino masses and their ordering*, *Phys. Rev. D* **95** (2017), no. 9 096014, [[arXiv:2003.08511](#)]. [Addendum: *Phys.Rev.D* 101, 116013 (2020)].

- [52] KamLAND Collaboration, K. Eguchi et al., *First results from KamLAND: Evidence for reactor anti-neutrino disappearance*, *Phys. Rev. Lett.* **90** (2003) 021802, [[hep-ex/0212021](#)].
- [53] T2K Collaboration, K. Abe et al., *Measurements of neutrino oscillation in appearance and disappearance channels by the T2K experiment with 6.6×10^{20} protons on target*, *Phys. Rev. D* **91** (2015), no. 7 072010, [[arXiv:1502.01550](#)].
- [54] MINOS Collaboration, J. Evans, *The MINOS Experiment: Results and Prospects*, *Adv. High Energy Phys.* **2013** (2013) 182537, [[arXiv:1307.0721](#)].
- [55] NOvA Collaboration, P. Adamson et al., *Measurement of the neutrino mixing angle θ_{23} in NOvA*, *Phys. Rev. Lett.* **118** (2017), no. 15 151802, [[arXiv:1701.05891](#)].
- [56] Double Chooz Collaboration, F. Ardellier et al., *Double Chooz: A Search for the neutrino mixing angle theta(13)*, [hep-ex/0606025](#).
- [57] RENO Collaboration, J. Ahn et al., *RENO: An Experiment for Neutrino Oscillation Parameter θ_{13} Using Reactor Neutrinos at Yonggwang*, [arXiv:1003.1391](#).
- [58] Daya Bay Collaboration, F. An et al., *The Detector System of The Daya Bay Reactor Neutrino Experiment*, *Nucl. Instrum. Meth. A* **811** (2016) 133–161, [[arXiv:1508.03943](#)].
- [59] C. Jarlskog, *Commutator of the quark mass matrices in the standard electroweak model and a measure of maximal CP nonconservation*, *Phys. Rev. Lett.* **55** (Sep, 1985) 1039–1042.
- [60] R. Shrock, *New Tests For, and Bounds On, Neutrino Masses and Lepton Mixing*, *Phys. Lett. B* **96** (1980) 159–164.
- [61] KATRIN Collaboration, M. Aker et al., *Improved Upper Limit on the Neutrino Mass from a Direct Kinematic Method by KATRIN*, *Phys. Rev. Lett.* **123** (2019), no. 22 221802, [[arXiv:1909.06048](#)].
- [62] KATRIN Collaboration, M. Aker et al., *First operation of the KATRIN experiment with tritium*, *Eur. Phys. J. C* **80** (2020), no. 3 264, [[arXiv:1909.06069](#)].
- [63] J. Schechter and J. Valle, *Neutrinoless Double beta Decay in $SU(2) \times U(1)$ Theories*, *Phys. Rev. D* **25** (1982) 2951.
- [64] E. Takasugi, *Can the Neutrinoless Double Beta Decay Take Place in the Case of Dirac Neutrinos?*, *Phys. Lett. B* **149** (1984) 372–376.

- [65] M. Hirsch, S. Kovalenko, and I. Schmidt, *Extended black box theorem for lepton number and flavor violating processes*, *Phys. Lett. B* **642** (2006) 106–110, [[hep-ph/0608207](#)].
- [66] M. J. Dolinski, A. W. Poon, and W. Rodejohann, *Neutrinoless Double-Beta Decay: Status and Prospects*, *Ann. Rev. Nucl. Part. Sci.* **69** (2019) 219–251, [[arXiv:1902.04097](#)].
- [67] DARWIN Collaboration, F. Agostini et al., *Sensitivity of the DARWIN observatory to the neutrinoless double beta decay of ^{136}Xe* , [arXiv:2003.13407](#).
- [68] GERDA Collaboration, M. Agostini et al., *Probing Majorana neutrinos with double- β decay*, *Science* **365** (2019) 1445, [[arXiv:1909.02726](#)].
- [69] Planck Collaboration, N. Aghanim et al., *Planck 2018 results. VI. Cosmological parameters*, [arXiv:1807.06209](#).
- [70] P. Minkowski, $\mu \rightarrow e\gamma$ at a rate of one out of 10^9 muon decays?, *Physics Letters B* **67** (1977), no. 4 421 – 428.
- [71] T. Yanagida, *Horizontal gauge symmetry and masses of neutrinos*, *Conf. Proc. C7902131* (1979) 95–99.
- [72] M. Gell-Mann, P. Ramond, and R. Slansky, *Complex Spinors and Unified Theories*, *Conf. Proc. C790927* (1979) 315–321, [[arXiv:1306.4669](#)].
- [73] R. N. Mohapatra and G. Senjanović, *Neutrino mass and spontaneous parity nonconservation*, *Phys. Rev. Lett.* **44** (Apr, 1980) 912–915.
- [74] S. L. Glashow, *The Future of Elementary Particle Physics*, *NATO Sci. Ser. B* **61** (1980) 687.
- [75] M. Magg and C. Wetterich, *Neutrino Mass Problem and Gauge Hierarchy*, *Phys. Lett.* **94B** (1980) 61–64.
- [76] J. Schechter and J. W. F. Valle, *Neutrino masses in $su(2) \otimes u(1)$ theories*, *Phys. Rev. D* **22** (Nov, 1980) 2227–2235.
- [77] G. Lazarides, Q. Shafi, and C. Wetterich, *Proton lifetime and fermion masses in an $so(10)$ model*, *Nuclear Physics B* **181** (1981), no. 2 287 – 300.
- [78] C. Wetterich, *Neutrino Masses and the Scale of B-L Violation*, *Nucl. Phys. B* **187** (1981) 343–375.
- [79] R. N. Mohapatra and G. Senjanović, *Neutrino masses and mixings in gauge models with spontaneous parity violation*, *Phys. Rev. D* **23** (Jan, 1981) 165–180.

- [80] R. Foot, H. Lew, X. G. He, and G. C. Joshi, *Seesaw Neutrino Masses Induced by a Triplet of Leptons*, *Z. Phys.* **C44** (1989) 441.
- [81] A. Zee, *A Theory of Lepton Number Violation, Neutrino Majorana Mass, and Oscillation*, *Phys. Lett.* **93B** (1980) 389. [Erratum: *Phys. Lett.* **95B**, 461(1980)].
- [82] A. Zee, *Quantum Numbers of Majorana Neutrino Masses*, *Nucl. Phys.* **B264** (1986) 99–110.
- [83] K. S. Babu, *Model of ‘Calculable’ Majorana Neutrino Masses*, *Phys. Lett.* **B203** (1988) 132–136.
- [84] A. de Gouvea and J. Jenkins, *A Survey of Lepton Number Violation Via Effective Operators*, *Phys. Rev.* **D77** (2008) 013008, [[arXiv:0708.1344](https://arxiv.org/abs/0708.1344)].
- [85] ATLAS Collaboration, G. Aad et al., *Search for doubly-charged Higgs bosons in like-sign dilepton final states at $\sqrt{s} = 7$ TeV with the ATLAS detector*, *Eur. Phys. J. C* **72** (2012) 2244, [[arXiv:1210.5070](https://arxiv.org/abs/1210.5070)].
- [86] ATLAS Collaboration, G. Aad et al., *Search for anomalous production of prompt same-sign lepton pairs and pair-produced doubly charged Higgs bosons with $\sqrt{s} = 8$ TeV pp collisions using the ATLAS detector*, *JHEP* **03** (2015) 041, [[arXiv:1412.0237](https://arxiv.org/abs/1412.0237)].
- [87] ATLAS Collaboration, M. Aaboud et al., *Search for doubly charged Higgs boson production in multi-lepton final states with the ATLAS detector using proton–proton collisions at $\sqrt{s} = 13$ TeV*, *Eur. Phys. J. C* **78** (2018), no. 3 199, [[arXiv:1710.09748](https://arxiv.org/abs/1710.09748)].
- [88] CMS Collaboration, S. Chatrchyan et al., *A Search for a Doubly-Charged Higgs Boson in pp Collisions at $\sqrt{s} = 7$ TeV*, *Eur. Phys. J. C* **72** (2012) 2189, [[arXiv:1207.2666](https://arxiv.org/abs/1207.2666)].
- [89] CMS Collaboration, *Search for a doubly-charged Higgs boson with $\sqrt{s} = 8$ TeV pp collisions at the CMS experiment*, .
- [90] CMS Collaboration, *A search for doubly-charged Higgs boson production in three and four lepton final states at $\sqrt{s} = 13$ TeV*, .
- [91] L. Wolfenstein, *A Theoretical Pattern for Neutrino Oscillations*, *Nucl. Phys. B* **175** (1980) 93–96.
- [92] S. M. Boucenna, S. Morisi, and J. W. F. Valle, *The low-scale approach to neutrino masses*, *Adv. High Energy Phys.* **2014** (2014) 831598, [[arXiv:1404.3751](https://arxiv.org/abs/1404.3751)].

- [93] Y. Cai, J. Herrero-García, M. A. Schmidt, A. Vicente, and R. R. Volkas, *From the trees to the forest: a review of radiative neutrino mass models*, *Front.in Phys.* **5** (2017) 63, [[arXiv:1706.08524](#)].
- [94] Y. Farzan, S. Pascoli, and M. A. Schmidt, *Recipes and Ingredients for Neutrino Mass at Loop Level*, *JHEP* **03** (2013) 107, [[arXiv:1208.2732](#)].
- [95] F. Bonnet, M. Hirsch, T. Ota, and W. Winter, *Systematic study of the d=5 Weinberg operator at one-loop order*, *JHEP* **07** (2012) 153, [[arXiv:1204.5862](#)].
- [96] D. Aristizabal Sierra, A. Degee, L. Dorame, and M. Hirsch, *Systematic classification of two-loop realizations of the Weinberg operator*, *JHEP* **03** (2015) 040, [[arXiv:1411.7038](#)].
- [97] R. Cepedello, R. M. Fonseca, and M. Hirsch, *Systematic classification of three-loop realizations of the Weinberg operator*, *JHEP* **10** (2018) 197, [[arXiv:1807.00629](#)].
- [98] R. Cepedello, M. Hirsch, and J. Helo, *Loop neutrino masses from d = 7 operator*, *JHEP* **07** (2017) 079, [[arXiv:1705.01489](#)].
- [99] K. S. Babu and C. N. Leung, *Classification of effective neutrino mass operators*, *Nucl. Phys.* **B619** (2001) 667–689, [[hep-ph/0106054](#)].
- [100] P. W. Angel, N. L. Rodd, and R. R. Volkas, *Origin of neutrino masses at the lhc: $\Delta l = 2$ effective operators and their ultraviolet completions*, *Phys. Rev. D* **87** (Apr, 2013) 073007.
- [101] Y. Cai, J. D. Clarke, M. A. Schmidt, and R. R. Volkas, *Testing Radiative Neutrino Mass Models at the LHC*, *JHEP* **02** (2015) 161, [[arXiv:1410.0689](#)].
- [102] F. Bonnet, D. Hernandez, T. Ota, and W. Winter, *Neutrino masses from higher than d=5 effective operators*, *JHEP* **10** (2009) 076, [[arXiv:0907.3143](#)].
- [103] G. Anamiati, O. Castillo-Felisola, R. M. Fonseca, J. C. Helo, and M. Hirsch, *High-dimensional neutrino masses*, *JHEP* **12** (2018) 066, [[arXiv:1806.07264](#)].
- [104] C. Klein, M. Lindner, and S. Ohmer, *Minimal Radiative Neutrino Masses*, *JHEP* **03** (2019) 018, [[arXiv:1901.03225](#)].
- [105] C. Klein, M. Lindner, and S. Vogl, *Radiative neutrino masses and successful SU(5) unification*, *Phys. Rev. D* **100** (2019), no. 7 075024, [[arXiv:1907.05328](#)].
- [106] H. K. Dreiner, H. E. Haber, and S. P. Martin, *Two-component spinor techniques and Feynman rules for quantum field theory and supersymmetry*, *Phys. Rept.* **494** (2010) 1–196, [[arXiv:0812.1594](#)].

- [107] B. Henning, X. Lu, and H. Murayama, *How to use the Standard Model effective field theory*, *JHEP* **01** (2016) 023, [[arXiv:1412.1837](#)].
- [108] I. Brivio and M. Trott, *The Standard Model as an Effective Field Theory*, *Phys. Rept.* **793** (2019) 1–98, [[arXiv:1706.08945](#)].
- [109] L. Lehman and A. Martin, *Hilbert Series for Constructing Lagrangians: expanding the phenomenologist’s toolbox*, *Phys. Rev.* **D91** (2015) 105014, [[arXiv:1503.07537](#)].
- [110] B. Henning, X. Lu, T. Melia, and H. Murayama, *Hilbert series and operator bases with derivatives in effective field theories*, *Commun. Math. Phys.* **347** (2016), no. 2 363–388, [[arXiv:1507.07240](#)].
- [111] L. Lehman and A. Martin, *Low-derivative operators of the Standard Model effective field theory via Hilbert series methods*, *JHEP* **02** (2016) 081, [[arXiv:1510.00372](#)].
- [112] B. Henning, X. Lu, T. Melia, and H. Murayama, 2, 84, 30, 993, 560, 15456, 11962, 261485, ...: *Higher dimension operators in the SM EFT*, *JHEP* **08** (2017) 016, [[arXiv:1512.03433](#)]. [Erratum: JHEP09,019(2019)].
- [113] B. Henning, X. Lu, T. Melia, and H. Murayama, *Operator bases, S-matrices, and their partition functions*, *JHEP* **10** (2017) 199, [[arXiv:1706.08520](#)].
- [114] A. Kobach, *Baryon Number, Lepton Number, and Operator Dimension in the Standard Model*, *Phys. Lett. B* **758** (2016) 455–457, [[arXiv:1604.05726](#)].
- [115] J. Aebischer et al., *WCxf: an exchange format for Wilson coefficients beyond the Standard Model*, *Comput. Phys. Commun.* **232** (2018) 71–83, [[arXiv:1712.05298](#)].
- [116] E. E. Jenkins, A. V. Manohar, and P. Stoffer, *Low-Energy Effective Field Theory below the Electroweak Scale: Operators and Matching*, *JHEP* **03** (2018) 016, [[arXiv:1709.04486](#)].
- [117] J. Aebischer, M. Fael, C. Greub, and J. Virto, *B physics Beyond the Standard Model at One Loop: Complete Renormalization Group Evolution below the Electroweak Scale*, *JHEP* **09** (2017) 158, [[arXiv:1704.06639](#)].
- [118] E. E. Jenkins, A. V. Manohar, and P. Stoffer, *Low-Energy Effective Field Theory below the Electroweak Scale: Anomalous Dimensions*, *JHEP* **01** (2018) 084, [[arXiv:1711.05270](#)].

- [119] J. Aebischer, A. Crivellin, M. Fael, and C. Greub, *Matching of gauge invariant dimension-six operators for $b \rightarrow s$ and $b \rightarrow c$ transitions*, *JHEP* **05** (2016) 037, [[arXiv:1512.02830](https://arxiv.org/abs/1512.02830)].
- [120] G. Buchalla, A. J. Buras, and M. E. Lautenbacher, *Weak decays beyond leading logarithms*, *Rev. Mod. Phys.* **68** (1996) 1125–1144, [[hep-ph/9512380](https://arxiv.org/abs/hep-ph/9512380)].
- [121] C. Arzt, *Reduced effective Lagrangians*, *Phys. Lett. B* **342** (1995) 189–195, [[hep-ph/9304230](https://arxiv.org/abs/hep-ph/9304230)].
- [122] H. Georgi, *On-shell effective field theory*, *Nucl. Phys. B* **361** (1991) 339–350.
- [123] J. Gasser and H. Leutwyler, *Chiral Perturbation Theory to One Loop*, *Annals Phys.* **158** (1984) 142.
- [124] J. Gasser and H. Leutwyler, *Chiral Perturbation Theory: Expansions in the Mass of the Strange Quark*, *Nucl. Phys. B* **250** (1985) 465–516.
- [125] A. De Rujula, M. Gavela, P. Hernandez, and E. Masso, *The Selfcouplings of vector bosons: Does LEP-1 obviate LEP-2?*, *Nucl. Phys. B* **384** (1992) 3–58.
- [126] J. Chisholm, *Change of variables in quantum field theories*, *Nuclear Physics* **26** (1961), no. 3 469 – 479.
- [127] S. Kamefuchi, L. O’Raifeartaigh, and A. Salam, *Change of variables and equivalence theorems in quantum field theories*, *Nucl. Phys.* **28** (1961) 529–549.
- [128] P. Divakaran, *Equivalence theorems and point transformations in field theory*, *Nuclear Physics* **42** (1963) 235–246.
- [129] M. Bergere and Y.-M. P. Lam, *Equivalence Theorem and Faddeev-Popov Ghosts*, *Phys. Rev. D* **13** (1976) 3247–3255.
- [130] H. Sharatchandra, *The equivalence theorem is subtle*, *Annals of Physics* **116** (1978), no. 2 408 – 418.
- [131] A. Salam and J. Strathdee, *Equivalent formulations of massive vector field theories*, *Phys. Rev. D* **2** (Dec, 1970) 2869–2876.
- [132] R. Kallosh and I. Tyutin, *The Equivalence theorem and gauge invariance in renormalizable theories*, *Yad. Fiz.* **17** (1973) 190–209.
- [133] H. Lehmann, K. Symanzik, and W. Zimmermann, *On the formulation of quantized field theories*, *Nuovo Cim.* **1** (1955) 205–225.
- [134] P. Pouliot, *Molien function for duality*, *JHEP* **01** (1999) 021, [[hep-th/9812015](https://arxiv.org/abs/hep-th/9812015)].

- [135] S. Benvenuti, B. Feng, A. Hanany, and Y.-H. He, *Counting BPS Operators in Gauge Theories: Quivers, Syzygies and Plethystics*, *JHEP* **11** (2007) 050, [[hep-th/0608050](#)].
- [136] F. Dolan, *Counting BPS operators in N=4 SYM*, *Nucl. Phys. B* **790** (2008) 432–464, [[arXiv:0704.1038](#)].
- [137] A. Hanany, E. E. Jenkins, A. V. Manohar, and G. Torri, *Hilbert Series for Flavor Invariants of the Standard Model*, *JHEP* **03** (2011) 096, [[arXiv:1010.3161](#)].
- [138] E. E. Jenkins and A. V. Manohar, *Algebraic Structure of Lepton and Quark Flavor Invariants and CP Violation*, *JHEP* **10** (2009) 094, [[arXiv:0907.4763](#)].
- [139] A. Hanany and R. Kalveks, *Highest Weight Generating Functions for Hilbert Series*, *JHEP* **10** (2014) 152, [[arXiv:1408.4690](#)].
- [140] A. Hanany, N. Mekareeya, and G. Torri, *The Hilbert Series of Adjoint SQCD*, *Nucl. Phys. B* **825** (2010) 52–97, [[arXiv:0812.2315](#)].
- [141] R. Feger and T. W. Kephart, *LieART—A Mathematica application for Lie algebras and representation theory*, *Comput. Phys. Commun.* **192** (2015) 166–195, [[arXiv:1206.6379](#)].
- [142] T. Ma, J. Shu, and M.-L. Xiao, *Standard Model Effective Field Theory from On-shell Amplitudes*, [arXiv:1902.06752](#).
- [143] B. Henning and T. Melia, *Constructing effective field theories via their harmonics*, *Phys. Rev. D* **100** (2019), no. 1 016015, [[arXiv:1902.06754](#)].
- [144] H.-L. Li, Z. Ren, J. Shu, M.-L. Xiao, J.-H. Yu, and Y.-H. Zheng, *Complete Set of Dimension-8 Operators in the Standard Model Effective Field Theory*, [arXiv:2005.00008](#).
- [145] H.-L. Li, Z. Ren, M.-L. Xiao, J.-H. Yu, and Y.-H. Zheng, *Complete Set of Dimension-9 Operators in the Standard Model Effective Field Theory*, [arXiv:2007.07899](#).
- [146] Muon g-2 Collaboration, G. Bennett et al., *Final Report of the Muon E821 Anomalous Magnetic Moment Measurement at BNL*, *Phys. Rev. D* **73** (2006) 072003, [[hep-ex/0602035](#)].
- [147] T. Blum, A. Denig, I. Logashenko, E. de Rafael, B. L. Roberts, T. Teubner, and G. Venanzoni, *The Muon (g-2) Theory Value: Present and Future*, [arXiv:1311.2198](#).

- [148] R. Parker, C. Yu, W. Zhong, B. Estey, and H. Mæller, *Measurement of the fine-structure constant as a test of the standard model*, *Science* **360** (04, 2018) 191–195.
- [149] LHCb Collaboration, R. Aaij et al., *Differential branching fractions and isospin asymmetries of $B \rightarrow K^{(*)}\mu^+\mu^-$ decays*, *JHEP* **06** (2014) 133, [[arXiv:1403.8044](#)].
- [150] LHCb Collaboration, R. Aaij et al., *Angular analysis and differential branching fraction of the decay $B_s^0 \rightarrow \phi\mu^+\mu^-$* , *JHEP* **09** (2015) 179, [[arXiv:1506.08777](#)].
- [151] CMS Collaboration Collaboration, *Measurement of properties of B_s0 to mu+mu- decays and search for $B0$ to mu+mu- with the CMS experiment*, Tech. Rep. CMS-PAS-BPH-16-004, CERN, Geneva, 2019.
- [152] LHCb Collaboration, R. Aaij et al., *First Evidence for the Decay $B_s^0 \rightarrow \mu^+\mu^-$* , *Phys. Rev. Lett.* **110** (2013), no. 2 021801, [[arXiv:1211.2674](#)].
- [153] LHCb Collaboration, R. Aaij et al., *Measurement of the $B_s^0 \rightarrow \mu^+\mu^-$ branching fraction and effective lifetime and search for $B^0 \rightarrow \mu^+\mu^-$ decays*, *Phys. Rev. Lett.* **118** (2017), no. 19 191801, [[arXiv:1703.05747](#)].
- [154] ATLAS Collaboration, M. Aaboud et al., *Study of the rare decays of B_s^0 and B^0 mesons into muon pairs using data collected during 2015 and 2016 with the ATLAS detector*, *JHEP* **04** (2019) 098, [[arXiv:1812.03017](#)].
- [155] LHCb Collaboration, R. Aaij et al., *Differential branching fraction and angular analysis of $\Lambda_b^0 \rightarrow \Lambda\mu^+\mu^-$ decays*, *JHEP* **06** (2015) 115, [[arXiv:1503.07138](#)]. [Erratum: *JHEP* 09, 145 (2018)].
- [156] F. Kruger, L. M. Sehgal, N. Sinha, and R. Sinha, *Angular distribution and CP asymmetries in the decays $\bar{B} \rightarrow K^-\pi^+e^-e^+$ and $\bar{B} \rightarrow \pi^-\pi^+e^-e^+$* , *Phys. Rev. D* **61** (2000) 114028, [[hep-ph/9907386](#)]. [Erratum: *Phys. Rev. D* 63, 019901 (2001)].
- [157] U. Egede and J. Serrano, *Rare b-hadron decays*, *Comptes Rendus Physique* **21** (2020), no. 1 93–106.
- [158] T. Blake, M. Gersabeck, L. Hofer, S. Jäger, Z. Liu, and R. Zwicky, *Round table: Flavour anomalies in $b \rightarrow sl+l-$ processes*, *EPJ Web Conf.* **137** (2017) 01001, [[arXiv:1703.10005](#)].
- [159] A. Bharucha, D. M. Straub, and R. Zwicky, *$B \rightarrow V\ell^+\ell^-$ in the Standard Model from light-cone sum rules*, *JHEP* **08** (2016) 098, [[arXiv:1503.05534](#)].
- [160] W. Altmannshofer and D. M. Straub, *New physics in $b \rightarrow s$ transitions after LHC run 1*, *Eur. Phys. J. C* **75** (2015), no. 8 382, [[arXiv:1411.3161](#)].

- [161] R. R. Horgan, Z. Liu, S. Meinel, and M. Wingate, *Calculation of $B^0 \rightarrow K^{*0} \mu^+ \mu^-$ and $B_s^0 \rightarrow \phi \mu^+ \mu^-$ observables using form factors from lattice QCD*, *Phys. Rev. Lett.* **112** (2014) 212003, [[arXiv:1310.3887](#)].
- [162] C. Bobeth, M. Gorbahn, T. Hermann, M. Misiak, E. Stamou, and M. Steinhauser, *$B_{s,d} \rightarrow l^+ l^-$ in the Standard Model with Reduced Theoretical Uncertainty*, *Phys. Rev. Lett.* **112** (2014) 101801, [[arXiv:1311.0903](#)].
- [163] G. Hiller and F. Krüger, *More model-independent analysis of $b \rightarrow s$ processes*, *Phys. Rev. D* **69** (2004) 074020, [[hep-ph/0310219](#)].
- [164] B. Capdevila, A. Crivellin, S. Descotes-Genon, J. Matias, and J. Virto, *Patterns of New Physics in $b \rightarrow s \ell^+ \ell^-$ transitions in the light of recent data*, [arXiv:1704.05340](#).
- [165] B. Capdevila, S. Descotes-Genon, J. Matias, and J. Virto, *Assessing lepton-flavour non-universality from $B \rightarrow K^* \ell \ell$ angular analyses*, *JHEP* **10** (2016) 075, [\[arXiv:1605.03156\]](#).
- [166] C. Bobeth, G. Hiller, and G. Piranishvili, *Angular distributions of $\bar{B} \rightarrow \bar{K} \ell^+ \ell^-$ decays*, *JHEP* **12** (2007) 040, [[arXiv:0709.4174](#)].
- [167] P. Koppenburg, Z. Dolezal, and M. Smizanska, *Rare decays of b hadrons*, *Scholarpedia* **11** (2016) 32643, [[arXiv:1606.00999](#)].
- [168] A. Ali, T. Mannel, and T. Morozumi, *Forward backward asymmetry of dilepton angular distribution in the decay $b \rightarrow s l^+ l^-$* , *Phys. Lett. B* **273** (1991) 505–512.
- [169] U. Egede, T. Hurth, J. Matias, M. Ramon, and W. Reece, *New observables in the decay mode $\bar{B}_d \rightarrow \bar{K}^{*0} l^+ l^-$* , *JHEP* **11** (2008) 032, [[arXiv:0807.2589](#)].
- [170] S. Descotes-Genon, T. Hurth, J. Matias, and J. Virto, *Optimizing the basis of $B \rightarrow K^* ll$ observables in the full kinematic range*, *JHEP* **05** (2013) 137, [\[arXiv:1303.5794\]](#).
- [171] LHCb Collaboration, R. Aaij et al., *Measurement of Form-Factor-Independent Observables in the Decay $B^0 \rightarrow K^{*0} \mu^+ \mu^-$* , *Phys. Rev. Lett.* **111** (2013) 191801, [\[arXiv:1308.1707\]](#).
- [172] LHCb Collaboration, R. Aaij et al., *Measurement of CP-Averaged Observables in the $B^0 \rightarrow K^{*0} \mu^+ \mu^-$ Decay*, *Phys. Rev. Lett.* **125** (2020), no. 1 011802, [\[arXiv:2003.04831\]](#).
- [173] Belle Collaboration, S. Wehle et al., *Lepton-Flavor-Dependent Angular Analysis of $B \rightarrow K^* \ell^+ \ell^-$* , *Phys. Rev. Lett.* **118** (2017), no. 11 111801, [[arXiv:1612.05014](#)].

- [174] ATLAS Collaboration, M. Aaboud et al., *Angular analysis of $B_d^0 \rightarrow K^* \mu^+ \mu^-$ decays in pp collisions at $\sqrt{s} = 8$ TeV with the ATLAS detector*, *JHEP* **10** (2018) 047, [[arXiv:1805.04000](#)].
- [175] CMS Collaboration, A. M. Sirunyan et al., *Measurement of angular parameters from the decay $B^0 \rightarrow K^{*0} \mu^+ \mu^-$ in proton-proton collisions at $\sqrt{s} = 8$ TeV*, *Phys. Lett. B* **781** (2018) 517–541, [[arXiv:1710.02846](#)].
- [176] S. Descotes-Genon, L. Hofer, J. Matias, and J. Virto, *On the impact of power corrections in the prediction of $B \rightarrow K^* \mu^+ \mu^-$ observables*, *JHEP* **12** (2014) 125, [[arXiv:1407.8526](#)].
- [177] A. Khodjamirian, T. Mannel, A. Pivovarov, and Y.-M. Wang, *Charm-loop effect in $B \rightarrow K^{(*)} \ell^+ \ell^-$ and $B \rightarrow K^* \gamma$* , *JHEP* **09** (2010) 089, [[arXiv:1006.4945](#)].
- [178] M. Algueró, B. Capdevila, A. Crivellin, S. Descotes-Genon, P. Masjuan, J. Matias, M. Novoa Brunet, and J. Virto, *Emerging patterns of New Physics with and without Lepton Flavour Universal contributions*, *Eur. Phys. J. C* **79** (2019), no. 8 714, [[arXiv:1903.09578](#)]. [Addendum: *Eur.Phys.J.C* **80**, 511 (2020)].
- [179] A. Arbey, T. Hurth, F. Mahmoudi, D. M. Santos, and S. Neshatpour, *Update on the $b \rightarrow s$ anomalies*, *Phys. Rev. D* **100** (2019), no. 1 015045, [[arXiv:1904.08399](#)].
- [180] M. Ciuchini, A. M. Coutinho, M. Fedele, E. Franco, A. Paul, L. Silvestrini, and M. Valli, *New Physics in $b \rightarrow s \ell^+ \ell^-$ confronts new data on Lepton Universality*, *Eur. Phys. J. C* **79** (2019), no. 8 719, [[arXiv:1903.09632](#)].
- [181] S. Descotes-Genon, J. Matias, and J. Virto, *Understanding the $B \rightarrow K^* \mu^+ \mu^-$ Anomaly*, *Phys. Rev. D* **88** (2013) 074002, [[arXiv:1307.5683](#)].
- [182] W. Altmannshofer and D. M. Straub, *Implications of $b \rightarrow s$ measurements*, in *50th Rencontres de Moriond on EW Interactions and Unified Theories*, pp. 333–338, 3, 2015. [arXiv:1503.06199](#).
- [183] S. Descotes-Genon, L. Hofer, J. Matias, and J. Virto, *Global analysis of $b \rightarrow s \ell \ell$ anomalies*, *JHEP* **06** (2016) 092, [[arXiv:1510.04239](#)].
- [184] BaBar Collaboration, J. Lees et al., *Evidence for an excess of $\bar{B} \rightarrow D^{(*)} \tau^- \bar{\nu}_\tau$ decays*, *Phys. Rev. Lett.* **109** (2012) 101802, [[arXiv:1205.5442](#)].
- [185] BaBar Collaboration, J. Lees et al., *Measurement of an Excess of $\bar{B} \rightarrow D^{(*)} \tau^- \bar{\nu}_\tau$ Decays and Implications for Charged Higgs Bosons*, *Phys. Rev. D* **88** (2013), no. 7 072012, [[arXiv:1303.0571](#)].

- [186] **Belle** Collaboration, M. Huschle et al., *Measurement of the branching ratio of $\bar{B} \rightarrow D^{(*)}\tau^-\bar{\nu}_\tau$ relative to $\bar{B} \rightarrow D^{(*)}\ell^-\bar{\nu}_\ell$ decays with hadronic tagging at Belle*, *Phys. Rev. D* **92** (2015), no. 7 072014, [[arXiv:1507.03233](#)].
- [187] **Belle** Collaboration, S. Hirose et al., *Measurement of the τ lepton polarization and $R(D^*)$ in the decay $\bar{B} \rightarrow D^*\tau^-\bar{\nu}_\tau$* , *Phys. Rev. Lett.* **118** (2017), no. 21 211801, [[arXiv:1612.00529](#)].
- [188] **Belle** Collaboration, S. Hirose et al., *Measurement of the τ lepton polarization and $R(D^*)$ in the decay $\bar{B} \rightarrow D^*\tau^-\bar{\nu}_\tau$ with one-prong hadronic τ decays at Belle*, *Phys. Rev. D* **97** (2018), no. 1 012004, [[arXiv:1709.00129](#)].
- [189] **LHCb** Collaboration, R. Aaij et al., *Measurement of the ratio of branching fractions $\mathcal{B}(\bar{B}^0 \rightarrow D^{*+}\tau^-\bar{\nu}_\tau)/\mathcal{B}(\bar{B}^0 \rightarrow D^{*+}\mu^-\bar{\nu}_\mu)$* , *Phys. Rev. Lett.* **115** (2015), no. 11 111803, [[arXiv:1506.08614](#)]. [Erratum: *Phys. Rev. Lett.* **115**, 159901 (2015)].
- [190] **LHCb** Collaboration, R. Aaij et al., *Measurement of the ratio of the $B^0 \rightarrow D^{*-}\tau^+\nu_\tau$ and $B^0 \rightarrow D^{*-}\mu^+\nu_\mu$ branching fractions using three-prong τ -lepton decays*, *Phys. Rev. Lett.* **120** (2018), no. 17 171802, [[arXiv:1708.08856](#)].
- [191] **LHCb** Collaboration, R. Aaij et al., *Test of Lepton Flavor Universality by the measurement of the $B^0 \rightarrow D^{*-}\tau^+\nu_\tau$ branching fraction using three-prong τ decays*, *Phys. Rev. D* **97** (2018), no. 7 072013, [[arXiv:1711.02505](#)].
- [192] D. Bigi and P. Gambino, *Revisiting $B \rightarrow D\ell\nu$* , *Phys. Rev. D* **94** (2016), no. 9 094008, [[arXiv:1606.08030](#)].
- [193] F. U. Bernlochner, Z. Ligeti, M. Papucci, and D. J. Robinson, *Combined analysis of semileptonic B decays to D and D^* : $R(D^{(*)})$, $|V_{cb}|$, and new physics*, *Phys. Rev. D* **95** (2017), no. 11 115008, [[arXiv:1703.05330](#)]. [Erratum: *Phys. Rev. D* **97**, 059902 (2018)].
- [194] D. Bigi, P. Gambino, and S. Schacht, *$R(D^*)$, $|V_{cb}|$, and the Heavy Quark Symmetry relations between form factors*, *JHEP* **11** (2017) 061, [[arXiv:1707.09509](#)].
- [195] S. Jaiswal, S. Nandi, and S. K. Patra, *Extraction of $|V_{cb}|$ from $B \rightarrow D^{(*)}\ell\nu$ and the Standard Model predictions of $R(D^{(*)})$* , *JHEP* **12** (2017) 060, [[arXiv:1707.09977](#)].
- [196] M. Freytsis, Z. Ligeti, and J. T. Ruderman, *Flavor models for $\bar{B} \rightarrow D^{(*)}\tau\bar{\nu}$* , *Phys. Rev. D* **92** (2015), no. 5 054018, [[arXiv:1506.08896](#)].
- [197] **LHCb** Collaboration, R. Aaij et al., *Measurement of the ratio of branching fractions $\mathcal{B}(B_c^+ \rightarrow J/\psi\tau^+\nu_\tau)/\mathcal{B}(B_c^+ \rightarrow J/\psi\mu^+\nu_\mu)$* , *Phys. Rev. Lett.* **120** (2018), no. 12 121801, [[arXiv:1711.05623](#)].

- [198] A. Yu. Anisimov, I. M. Narodetsky, C. Semay, and B. Silvestre-Brac, *The B_c meson lifetime in the light front constituent quark model*, *Phys. Lett.* **B452** (1999) 129–136, [[hep-ph/9812514](#)].
- [199] V. V. Kiselev, *Exclusive decays and lifetime of B_c meson in QCD sum rules*, [hep-ph/0211021](#).
- [200] M. A. Ivanov, J. G. Korner, and P. Santorelli, *Exclusive semileptonic and nonleptonic decays of the B_c meson*, *Phys. Rev.* **D73** (2006) 054024, [[hep-ph/0602050](#)].
- [201] E. Hernandez, J. Nieves, and J. M. Verde-Velasco, *Study of exclusive semileptonic and non-leptonic decays of B_c in a nonrelativistic quark model*, *Phys. Rev.* **D74** (2006) 074008, [[hep-ph/0607150](#)].
- [202] T. Huang and F. Zuo, *Semileptonic B_c decays and charmonium distribution amplitude*, *Eur. Phys. J.* **C51** (2007) 833–839, [[hep-ph/0702147](#)].
- [203] W. Wang, Y.-L. Shen, and C.-D. Lu, *Covariant Light-Front Approach for $B(c)$ transition form factors*, *Phys. Rev.* **D79** (2009) 054012, [[arXiv:0811.3748](#)].
- [204] A. Issadykov and M. A. Ivanov, *The decays $B_c \rightarrow J/\psi + \bar{l}v_l$ and $B_c \rightarrow J/\psi + \pi(K)$ in covariant confined quark model*, *Phys. Lett.* **B783** (2018) 178–182, [[arXiv:1804.00472](#)].
- [205] W.-F. Wang, Y.-Y. Fan, and Z.-J. Xiao, *Semileptonic decays $B_c \rightarrow (\eta_c, J/\Psi)l\nu$ in the perturbative QCD approach*, *Chin. Phys.* **C37** (2013) 093102, [[arXiv:1212.5903](#)].
- [206] A. K. Alok, D. Kumar, J. Kumar, S. Kumbhakar, and S. U. Sankar, *New physics solutions for R_D and R_{D^*}* , *JHEP* **09** (2018) 152, [[arXiv:1710.04127](#)].
- [207] A. Azatov, D. Bardhan, D. Ghosh, F. Sgarlata, and E. Venturini, *Anatomy of $b \rightarrow c\tau\nu$ anomalies*, *JHEP* **11** (2018) 187, [[arXiv:1805.03209](#)].
- [208] X.-Q. Hu, S.-P. Jin, and Z.-J. Xiao, *Semileptonic decays $B_c \rightarrow (\eta_c, J/\psi)l\bar{\nu}_l$ in the "PQCD + Lattice" approach*, [arXiv:1904.07530](#).
- [209] D. Leljak, B. Melic, and M. Patra, *On lepton flavour universality in semileptonic $B_c \rightarrow \eta_c, J/\psi$ decays*, [arXiv:1901.08368](#).
- [210] K. Azizi, Y. Sarac, and H. Sundu, *Lepton flavour universality violation in semileptonic tree level weak transitions*, [arXiv:1904.08267](#).
- [211] C. Murgui, A. Peñuelas, M. Jung, and A. Pich, *Global fit to $b \rightarrow c\tau\nu$ transitions*, [arXiv:1904.09311](#).

- [212] Belle Collaboration, A. Abdesselam et al., *Measurement of the D^{*-} polarization in the decay $B^0 \rightarrow D^{*-} \tau^+ \nu_\tau$* , in *10th International Workshop on the CKM Unitarity Triangle (CKM 2018) Heidelberg, Germany, September 17-21, 2018*, 2019. [arXiv:1903.03102](https://arxiv.org/abs/1903.03102).
- [213] P. Asadi, M. R. Buckley, and D. Shih, *Asymmetry Observables and the Origin of $R_{D^{(*)}}$ Anomalies*, *Phys. Rev.* **D99** (2019), no. 3 035015, [[arXiv:1810.06597](https://arxiv.org/abs/1810.06597)].
- [214] R. Alonso, J. Martin Camalich, and S. Westhoff, *Tau properties in $B \rightarrow D\bar{\nu}$ from visible final-state kinematics*, *Phys. Rev.* **D95** (2017), no. 9 093006, [[arXiv:1702.02773](https://arxiv.org/abs/1702.02773)].
- [215] X.-Q. Li, Y.-D. Yang, and X. Zhang, *Revisiting the one leptoquark solution to the $R(D^{(*)})$ anomalies and its phenomenological implications*, *JHEP* **08** (2016) 054, [[arXiv:1605.09308](https://arxiv.org/abs/1605.09308)].
- [216] A. Akeroyd and C.-H. Chen, *Constraint on the branching ratio of $B_c \rightarrow \tau\bar{\nu}$ from LEP1 and consequences for $R(D^{(*)})$ anomaly*, *Phys. Rev. D* **96** (2017), no. 7 075011, [[arXiv:1708.04072](https://arxiv.org/abs/1708.04072)].
- [217] R. Alonso, B. Grinstein, and J. Martin Camalich, *Lifetime of B_c^- Constrains Explanations for Anomalies in $B \rightarrow D^{(*)}\tau\bar{\nu}$* , *Phys. Rev. Lett.* **118** (2017), no. 8 081802, [[arXiv:1611.06676](https://arxiv.org/abs/1611.06676)].
- [218] M. Blanke, A. Crivellin, S. de Boer, T. Kitahara, M. Moscati, U. Nierste, and I. Nišandžić, *Impact of polarization observables and $B_c \rightarrow \tau\bar{\nu}$ on new physics explanations of the $b \rightarrow c\tau\bar{\nu}$ anomaly*, *Phys. Rev. D* **99** (2019), no. 7 075006, [[arXiv:1811.09603](https://arxiv.org/abs/1811.09603)].
- [219] D. Bardhan and D. Ghosh, *B -meson charged current anomalies: The post-Moriond 2019 status*, *Phys. Rev. D* **100** (2019), no. 1 011701, [[arXiv:1904.10432](https://arxiv.org/abs/1904.10432)].
- [220] Y. Sakaki, M. Tanaka, A. Tayduganov, and R. Watanabe, *Testing leptoquark models in $\bar{B} \rightarrow D^{(*)}\tau\bar{\nu}$* , *Phys. Rev. D* **88** (2013), no. 9 094012, [[arXiv:1309.0301](https://arxiv.org/abs/1309.0301)].
- [221] M. Jung and D. M. Straub, *Constraining new physics in $b \rightarrow c\ell\bar{\nu}$ transitions*, *JHEP* **01** (2019) 009, [[arXiv:1801.01112](https://arxiv.org/abs/1801.01112)].
- [222] A. Angelescu, D. Bećirević, D. Faroughy, and O. Sumensari, *Closing the window on single leptoquark solutions to the B -physics anomalies*, *JHEP* **10** (2018) 183, [[arXiv:1808.08179](https://arxiv.org/abs/1808.08179)].
- [223] Z.-R. Huang, Y. Li, C.-D. Lu, M. A. Paracha, and C. Wang, *Footprints of New Physics in $b \rightarrow c\ell\bar{\nu}$ Transitions*, *Phys. Rev. D* **98** (2018), no. 9 095018, [[arXiv:1808.03565](https://arxiv.org/abs/1808.03565)].

- [224] Muon g-2 Collaboration, A. Chapelain, *The Muon g-2 experiment at Fermilab*, EPJ Web Conf. 137 (2017) 08001, [[arXiv:1701.02807](https://arxiv.org/abs/1701.02807)].
- [225] M. Davier, A. Hoecker, B. Malaescu, and Z. Zhang, *Reevaluation of the Hadronic Contributions to the Muon g-2 and to alpha(MZ)*, Eur. Phys. J. C71 (2011) 1515, [[arXiv:1010.4180](https://arxiv.org/abs/1010.4180)]. [Erratum: Eur. Phys. J.C72,1874(2012)].
- [226] M. Bauer and M. Neubert, *Minimal Leptoquark Explanation for the $R_{D^{(*)}}$, R_K , and $(g - 2)_\mu$ Anomalies*, Phys. Rev. Lett. 116 (2016), no. 14 141802, [[arXiv:1511.01900](https://arxiv.org/abs/1511.01900)].
- [227] D. Bećirević, N. Košnik, O. Sumensari, and R. Zukanovich Funchal, *Palatable Leptoquark Scenarios for Lepton Flavor Violation in Exclusive $b \rightarrow s\ell_1\ell_2$ modes*, JHEP 11 (2016) 035, [[arXiv:1608.07583](https://arxiv.org/abs/1608.07583)].
- [228] J. Gargalionis, “neutrinomass.” <https://github.com/johngarg/neutrinomass>, 2020.
- [229] R. M. Fonseca, *Enumerating the operators of an effective field theory*, [arXiv:1907.12584](https://arxiv.org/abs/1907.12584).
- [230] L. Lehman, *Extending the Standard Model Effective Field Theory with the Complete Set of Dimension-7 Operators*, Phys. Rev. D90 (2014), no. 12 125023, [[arXiv:1410.4193](https://arxiv.org/abs/1410.4193)].
- [231] A. De Gouvêa, W.-C. Huang, J. König, and M. Sen, *Accessible Lepton-Number-Violating Models and Negligible Neutrino Masses*, Phys. Rev. D 100 (2019), no. 7 075033, [[arXiv:1907.02541](https://arxiv.org/abs/1907.02541)].
- [232] O. Catà and T. Mannel, *Linking lepton number violation with B anomalies*, [arXiv:1903.01799](https://arxiv.org/abs/1903.01799).
- [233] B. Gripaios and D. Sutherland, *DEFT: A program for operators in EFT*, JHEP 01 (2019) 128, [[arXiv:1807.07546](https://arxiv.org/abs/1807.07546)].
- [234] J. C. Criado, *BasisGen: automatic generation of operator bases*, Eur. Phys. J. C79 (2019), no. 3 256, [[arXiv:1901.03501](https://arxiv.org/abs/1901.03501)].
- [235] R. M. Fonseca, *Calculating the renormalisation group equations of a SUSY model with Susyno*, Comput. Phys. Commun. 183 (2012) 2298–2306, [[arXiv:1106.5016](https://arxiv.org/abs/1106.5016)].
- [236] R. M. Fonseca, *The Sym2Int program: going from symmetries to interactions*, J. Phys. Conf. Ser. 873 (2017), no. 1 012045, [[arXiv:1703.05221](https://arxiv.org/abs/1703.05221)].

- [237] U. Banerjee, J. Chakrabortty, S. Prakash, and S. U. Rahaman, *Characters and Group Invariant Polynomials of (Super)fields: Road to "Lagrangian"*, [arXiv:2004.12830](https://arxiv.org/abs/2004.12830).
- [238] C. Arzt, M. B. Einhorn, and J. Wudka, *Patterns of deviation from the standard model*, *Nucl. Phys.* **B433** (1995) 41–66, [[hep-ph/9405214](https://arxiv.org/abs/hep-ph/9405214)].
- [239] M. B. Einhorn and J. Wudka, *The Bases of Effective Field Theories*, *Nucl. Phys.* **B876** (2013) 556–574, [[arXiv:1307.0478](https://arxiv.org/abs/1307.0478)].
- [240] P. W. Angel, N. L. Rodd, and R. R. Volkas, *Origin of neutrino masses at the LHC: $\Delta L = 2$ effective operators and their ultraviolet completions*, *Phys. Rev.* **D87** (2013), no. 7 073007, [[arXiv:1212.6111](https://arxiv.org/abs/1212.6111)].
- [241] J. Herrero-García and M. A. Schmidt, *Neutrino mass models: New classification and model-independent upper limits on their scale*, *Eur. Phys. J. C* **79** (2019), no. 11 938, [[arXiv:1903.10552](https://arxiv.org/abs/1903.10552)].
- [242] U. Banerjee, J. Chakrabortty, S. Prakash, S. U. Rahaman, and M. Spannowsky, *Effective Operator Bases for Beyond Standard Model Scenarios: An EFT compendium for discoveries*, [arXiv:2008.11512](https://arxiv.org/abs/2008.11512).
- [243] F. del Aguila, A. Aparici, S. Bhattacharya, A. Santamaria, and J. Wudka, *A realistic model of neutrino masses with a large neutrinoless double beta decay rate*, *JHEP* **05** (2012) 133, [[arXiv:1111.6960](https://arxiv.org/abs/1111.6960)].
- [244] F. del Aguila, A. Aparici, S. Bhattacharya, A. Santamaria, and J. Wudka, *Effective Lagrangian approach to neutrinoless double beta decay and neutrino masses*, *JHEP* **06** (2012) 146, [[arXiv:1204.5986](https://arxiv.org/abs/1204.5986)].
- [245] J. Herrero-Garcia, N. Rius, and A. Santamaria, *Higgs lepton flavour violation: UV completions and connection to neutrino masses*, *JHEP* **11** (2016) 084, [[arXiv:1605.06091](https://arxiv.org/abs/1605.06091)].
- [246] N. Craig, M. Jiang, Y.-Y. Li, and D. Sutherland, *Loops and Trees in Generic EFTs*, [arXiv:2001.00017](https://arxiv.org/abs/2001.00017).
- [247] S. S. Law and K. L. McDonald, *The simplest models of radiative neutrino mass*, *Int. J. Mod. Phys. A* **29** (2014) 1450064, [[arXiv:1303.6384](https://arxiv.org/abs/1303.6384)].
- [248] X.-G. He, *Is the Zee model neutrino mass matrix ruled out?*, *Eur. Phys. J. C* **34** (2004) 371–376, [[hep-ph/0307172](https://arxiv.org/abs/hep-ph/0307172)].

- [249] A. Meurer, C. P. Smith, M. Paprocki, O. Čertík, S. B. Kirpichev, M. Rocklin, A. Kumar, S. Ivanov, J. K. Moore, S. Singh, T. Rathnayake, S. Vig, B. E. Granger, R. P. Muller, F. Bonazzi, H. Gupta, S. Vats, F. Johansson, F. Pedregosa, M. J. Curry, A. R. Terrel, v. Roučka, A. Saboo, I. Fernando, S. Kulal, R. Cimrman, and A. Scopatz, *Sympy: symbolic computing in python*, *PeerJ Computer Science* **3** (Jan., 2017) e103.
- [250] G. Butler, ed., *Fundamental Algorithms for Permutation Groups*. Springer Berlin Heidelberg, 1991.
- [251] L. R. U. Manssur, R. Portugal, and B. F. Svaiter, *Group-theoretic approach for symbolic tensor manipulation*, *International Journal of Modern Physics C* **13** (Sep, 2002) 859–879.
- [252] T. Hahn, *Generating Feynman diagrams and amplitudes with FeynArts 3*, *Comput. Phys. Commun.* **140** (2001) 418–431, [[hep-ph/0012260](#)].
- [253] G. Csardi and T. Nepusz, *The igraph software package for complex network research*, *InterJournal Complex Systems* (2006) 1695.
- [254] T. igraph Core Team, *igraph*, Apr., 2020.
- [255] S. Horvát, *Igraph/m*, Apr., 2020. Please go to the GitHub repository to download an immediately usable version of this software.
- [256] A. A. Hagberg, D. A. Schult, and P. J. Swart, *Exploring network structure, dynamics, and function using networkx*, in *Proceedings of the 7th Python in Science Conference* (G. Varoquaux, T. Vaught, and J. Millman, eds.), (Pasadena, CA USA), pp. 11 – 15, 2008.
- [257] J. C. Criado, *MatchingTools: a Python library for symbolic effective field theory calculations*, *Comput. Phys. Commun.* **227** (2018) 42–50, [[arXiv:1710.06445](#)].
- [258] S. Das Bakshi, J. Chakrabortty, and S. K. Patra, *CoDEx: Wilson coefficient calculator connecting SMEFT to UV theory*, *Eur. Phys. J. C* **79** (2019), no. 1 21, [[arXiv:1808.04403](#)].
- [259] M. Krebber and H. Barthels, *MatchPy: Pattern Matching in Python*, *Journal of Open Source Software* **3** (June, 2018) 2.
- [260] M. Krebber, *Non-linear associative-commutative many-to-one pattern matching with sequence variables*, 2017.

- [261] I. Esteban, M. Gonzalez-Garcia, A. Hernandez-Cabezudo, M. Maltoni, and T. Schwetz, *Global analysis of three-flavour neutrino oscillations: synergies and tensions in the determination of θ_{23} , δ_{CP} , and the mass ordering*, *JHEP* **01** (2019) 106, [[arXiv:1811.05487](#)].
- [262] K. S. Babu and J. Julio, *Two-Loop Neutrino Mass Generation through Leptoquarks*, *Nucl. Phys.* **B841** (2010) 130–156, [[arXiv:1006.1092](#)].
- [263] K. Babu, P. B. Dev, S. Jana, and A. Thapa, *Non-Standard Interactions in Radiative Neutrino Mass Models*, *JHEP* **03** (2020) 006, [[arXiv:1907.09498](#)].
- [264] M. Duerr, M. Lindner, and A. Merle, *On the Quantitative Impact of the Schechter-Valle Theorem*, *JHEP* **06** (2011) 091, [[arXiv:1105.0901](#)].
- [265] K. Babu, S. Nandi, and Z. Tavartkiladze, *New Mechanism for Neutrino Mass Generation and Triply Charged Higgs Bosons at the LHC*, *Phys. Rev. D* **80** (2009) 071702, [[arXiv:0905.2710](#)].
- [266] O. Popov, M. A. Schmidt, and G. White, *R_2 as a single leptoquark solution to $R_{D^{(*)}}$ and $R_{K^{(*)}}$* , *Phys. Rev. D* **100** (2019), no. 3 035028, [[arXiv:1905.06339](#)].
- [267] K. Babu, P. B. Dev, S. Jana, and A. Thapa, *Unified Framework for B-Anomalies, Muon $g - 2$, and Neutrino Masses*, [arXiv:2009.01771](#).
- [268] I. Doršner, S. Fajfer, A. Greljo, J. F. Kamenik, and N. Košnik, *Physics of leptoquarks in precision experiments and at particle colliders*, *Phys. Rept.* **641** (2016) 1–68, [[arXiv:1603.04993](#)].
- [269] D. Bećirević, B. Panes, O. Sumensari, and R. Zukanovich Funchal, *Seeking leptoquarks in IceCube*, *JHEP* **06** (2018) 032, [[arXiv:1803.10112](#)].
- [270] D. Bećirević and O. Sumensari, *A leptoquark model to accommodate $R_K^{\text{exp}} < R_K^{\text{SM}}$ and $R_{K^*}^{\text{exp}} < R_{K^*}^{\text{SM}}$* , [arXiv:1704.05835](#).
- [271] I. Bigaran and R. R. Volkas, *Getting chirality right: single scalar leptoquark solution/s to the $(g - 2)_{e,\mu}$ puzzle*, [arXiv:2002.12544](#).
- [272] I. Doršner, S. Fajfer, and S. Saad, *$\mu \rightarrow e\gamma$ selecting scalar leptoquark solutions for the $(g - 2)_{e,\mu}$ puzzles*, [arXiv:2006.11624](#).
- [273] G. Hiller and M. Schmaltz, *R_K and future $b \rightarrow s\ell\ell$ physics beyond the standard model opportunities*, *Phys. Rev. D* **90** (2014) 054014, [[arXiv:1408.1627](#)].
- [274] B. Gripaios, M. Nardecchia, and S. A. Renner, *Composite leptoquarks and anomalies in B-meson decays*, *JHEP* **05** (2015) 006, [[arXiv:1412.1791](#)].

- [275] G. Hiller and I. Nisandzic, *R_K and R_{K^*} beyond the standard model*, *Phys. Rev. D* **96** (2017), no. 3 035003, [[arXiv:1704.05444](#)].
- [276] I. Doršner, S. Fajfer, D. A. Faroughy, and N. Košnik, *Saga of the two GUT leptoquarks in flavor universality and collider searches*, [arXiv:1706.07779](#).
- [277] J. M. Arnold, B. Fornal, and M. B. Wise, *Simplified models with baryon number violation but no proton decay*, *Phys. Rev. D* **87** (2013) 075004, [[arXiv:1212.4556](#)].
- [278] M. Gustafsson, J. M. No, and M. A. Rivera, *Predictive Model for Radiatively Induced Neutrino Masses and Mixings with Dark Matter*, *Phys. Rev. Lett.* **110** (2013), no. 21 211802, [[arXiv:1212.4806](#)]. [Erratum: Phys.Rev.Lett. 112, 259902 (2014)].
- [279] D. M. Straub, *flavio: a Python package for flavour and precision phenomenology in the Standard Model and beyond*, [arXiv:1810.08132](#).
- [280] R. Alonso, B. Grinstein, and J. Martin Camalich, *Lepton universality violation and lepton flavor conservation in B-meson decays*, *JHEP* **10** (2015) 184, [[arXiv:1505.05164](#)].
- [281] D. Bećirević, S. Fajfer, N. Košnik, and O. Sumensari, *Leptoquark model to explain the B-physics anomalies, R_K and R_D* , *Phys. Rev. D* **94** (2016), no. 11 115021, [[arXiv:1608.08501](#)].
- [282] S. M. Boucenna, A. Celis, J. Fuentes-Martin, A. Vicente, and J. Virto, *Non-abelian gauge extensions for B-decay anomalies*, *Phys. Lett. B* **760** (2016) 214–219, [[arXiv:1604.03088](#)].
- [283] S. M. Boucenna, A. Celis, J. Fuentes-Martin, A. Vicente, and J. Virto, *Phenomenology of an $SU(2) \times SU(2) \times U(1)$ model with lepton-flavour non-universality*, *JHEP* **12** (2016) 059, [[arXiv:1608.01349](#)].
- [284] L. Calibbi, A. Crivellin, and T. Ota, *Effective Field Theory Approach to $b \rightarrow s\ell\ell^{(\prime)}$, $B \rightarrow K(*)\nu\bar{\nu}$ and $B \rightarrow D(*)\tau\nu$ with Third Generation Couplings*, *Phys. Rev. Lett.* **115** (2015) 181801, [[arXiv:1506.02661](#)].
- [285] A. Crivellin, D. Müller, and T. Ota, *Simultaneous Explanation of $R(D^{(*)})$ and $b \rightarrow s\mu^+\mu^-$: The Last Scalar Leptoquarks Standing*, [arXiv:1703.09226](#).
- [286] F. F. Deppisch, S. Kulkarni, H. Päs, and E. Schumacher, *Leptoquark patterns unifying neutrino masses, flavor anomalies, and the diphoton excess*, *Phys. Rev. D* **94** (2016), no. 1 013003, [[arXiv:1603.07672](#)].

- [287] N. G. Deshpande and X.-G. He, *Consequences of R-parity violating interactions for anomalies in $\bar{B} \rightarrow D^{(*)}\tau\bar{\nu}$ and $b \rightarrow s\mu^+\mu^-$* , *Eur. Phys. J.* **C77** (2017), no. 2 134, [[arXiv:1608.04817](#)].
- [288] S. Fajfer and N. Košnik, *Vector leptoquark resolution of R_K and $R_{D^{(*)}}$ puzzles*, *Phys. Lett.* **B755** (2016) 270–274, [[arXiv:1511.06024](#)].
- [289] F. Feruglio, P. Paradisi, and A. Pattori, *Revisiting Lepton Flavor Universality in B Decays*, *Phys. Rev. Lett.* **118** (2017), no. 1 011801, [[arXiv:1606.00524](#)].
- [290] F. Feruglio, P. Paradisi, and A. Pattori, *On the Importance of Electroweak Corrections for B Anomalies*, [arXiv:1705.00929](#).
- [291] E. Megias, M. Quiros, and L. Salas, *Lepton-flavor universality violation in $R_{D^{(*)}}$ and R_K from warped space*, [arXiv:1703.06019](#).
- [292] O. Popov and G. A. White, *One Leptoquark to unify them? Neutrino masses and unification in the light of $(g-2)_\mu$, $R_{D^{(*)}}$ and R_K anomalies*, [arXiv:1611.04566](#).
- [293] D. Bećirević, S. Fajfer, and N. Košnik, *Lepton flavor nonuniversality in $b \rightarrow s\ell^+\ell^-$ processes*, *Phys. Rev.* **D92** (2015), no. 1 014016, [[arXiv:1503.09024](#)].
- [294] A. J. Buras and J. Girrbach, *Left-handed Z' and Z FCNC quark couplings facing new $b \rightarrow s\mu^+\mu^-$ data*, *JHEP* **12** (2013) 009, [[arXiv:1309.2466](#)].
- [295] R. Gauld, F. Goertz, and U. Haisch, *On minimal Z' explanations of the $B \rightarrow K^*\mu^+\mu^-$ anomaly*, *Phys. Rev.* **D89** (2014) 015005, [[arXiv:1308.1959](#)].
- [296] S. L. Glashow, D. Guadagnoli, and K. Lane, *Lepton Flavor Violation in B Decays?*, *Phys. Rev. Lett.* **114** (2015) 091801, [[arXiv:1411.0565](#)].
- [297] G. Hiller and M. Schmaltz, *Diagnosing lepton-nonuniversality in $b \rightarrow s\ell\ell$* , *JHEP* **02** (2015) 055, [[arXiv:1411.4773](#)].
- [298] F. Mahmoudi, S. Neshatpour, and J. Virto, *$B \rightarrow K^*\mu^+\mu^-$ optimised observables in the MSSM*, *Eur. Phys. J.* **C74** (2014), no. 6 2927, [[arXiv:1401.2145](#)].
- [299] E. Megias, G. Panico, O. Pujolas, and M. Quiros, *A Natural origin for the LHCb anomalies*, *JHEP* **09** (2016) 118, [[arXiv:1608.02362](#)].
- [300] H. Päs and E. Schumacher, *Common origin of R_K and neutrino masses*, *Phys. Rev.* **D92** (2015), no. 11 114025, [[arXiv:1510.08757](#)].
- [301] S. Sahoo and R. Mohanta, *Leptoquark effects on $b \rightarrow sv\bar{v}$ and $B \rightarrow K\ell^+\ell^-$ decay processes*, *New J. Phys.* **18** (2016), no. 1 013032, [[arXiv:1509.06248](#)].

- [302] S. Sahoo and R. Mohanta, *Study of the rare semileptonic decays $B_d^0 \rightarrow K^* \ell^+ \ell^-$ in scalar leptoquark model*, *Phys. Rev.* **D93** (2016), no. 3 034018, [[arXiv:1507.02070](#)].
- [303] D. Aristizabal Sierra, F. Staub, and A. Vicente, *Shedding light on the $b \rightarrow s$ anomalies with a dark sector*, *Phys. Rev.* **D92** (2015), no. 1 015001, [[arXiv:1503.06077](#)].
- [304] I. de Medeiros Varzielas and G. Hiller, *Clues for flavor from rare lepton and quark decays*, *JHEP* **06** (2015) 072, [[arXiv:1503.01084](#)].
- [305] S. de Boer and G. Hiller, *Flavor and new physics opportunities with rare charm decays into leptons*, *Phys. Rev.* **D93** (2016), no. 7 074001, [[arXiv:1510.00311](#)].
- [306] CMS Collaboration, A. M. Sirunyan et al., *Search for pair production of second-generation leptoquarks at $\sqrt{s} = 13$ TeV*, *Phys. Rev. D* **99** (2019), no. 3 032014, [[arXiv:1808.05082](#)].
- [307] ATLAS Collaboration, M. Aaboud et al., *Searches for third-generation scalar leptoquarks in $\sqrt{s} = 13$ TeV pp collisions with the ATLAS detector*, *JHEP* **06** (2019) 144, [[arXiv:1902.08103](#)].
- [308] B. Dumont, K. Nishiwaki, and R. Watanabe, *LHC constraints and prospects for S_1 scalar leptoquark explaining the $\bar{B} \rightarrow D^{(*)}\tau\bar{\nu}$ anomaly*, *Phys. Rev.* **D94** (2016), no. 3 034001, [[arXiv:1603.05248](#)].
- [309] D. Bardhan, P. Byakti, and D. Ghosh, *A closer look at the R_D and R_{D^*} anomalies*, *JHEP* **01** (2017) 125, [[arXiv:1610.03038](#)].
- [310] D. Choudhury, A. Kundu, S. Nandi, and S. K. Patra, *Unified resolution of the $R(D)$ and $R(D^*)$ anomalies and the lepton flavor violating decay $h \rightarrow \mu\tau$* , *Phys. Rev.* **D95** (2017), no. 3 035021, [[arXiv:1612.03517](#)].
- [311] S. Bhattacharya, S. Nandi, and S. K. Patra, *Looking for possible new physics in $B \rightarrow D^{(*)}\tau\nu_\tau$ in light of recent data*, *Phys. Rev.* **D95** (2017), no. 7 075012, [[arXiv:1611.04605](#)].
- [312] S. Bhattacharya, S. Nandi, and S. K. Patra, *Optimal-observable analysis of possible new physics in $B \rightarrow D^{(*)}\tau\nu_\tau$* , *Phys. Rev.* **D93** (2016), no. 3 034011, [[arXiv:1509.07259](#)].
- [313] MILC Collaboration, J. A. Bailey et al., *$B \rightarrow D\ell\nu$ form factors at nonzero recoil and $|V_{cb}|$ from 2+1-flavor lattice QCD*, *Phys. Rev.* **D92** (2015), no. 3 034506, [[arXiv:1503.07237](#)].

- [314] Heavy Flavor Averaging Group Collaboration, Y. Amhis et al., *Averages of B-Hadron, C-Hadron, and tau-lepton properties as of early 2012*, [arXiv:1207.1158](https://arxiv.org/abs/1207.1158).
- [315] BaBar Collaboration, B. Aubert et al., *Determination of the form-factors for the decay $B^0 \rightarrow D^{*-} \ell^+ \nu_\ell$ and of the CKM matrix element $|V_{cb}|$* , *Phys. Rev.* **D77** (2008) 032002, [[arXiv:0705.4008](https://arxiv.org/abs/0705.4008)].
- [316] BaBar Collaboration, B. Aubert et al., *Measurements of the Semileptonic Decays $\bar{B} \rightarrow D \ell \bar{\nu}$ and $\bar{B} \rightarrow D^* \ell \bar{\nu}$ Using a Global Fit to $D \rightarrow X \ell \bar{\nu}$ Final States*, *Phys. Rev.* **D79** (2009) 012002, [[arXiv:0809.0828](https://arxiv.org/abs/0809.0828)].
- [317] Belle Collaboration, K. Abe et al., *Measurement of $BR(\bar{B}_0 \rightarrow D^+ \ell^- \bar{n}\bar{u})$ and determination of $|V_{cb}|$* , *Phys. Lett.* **B526** (2002) 258–268, [[hep-ex/0111082](https://arxiv.org/abs/hep-ex/0111082)].
- [318] Belle Collaboration, W. Dungel et al., *Measurement of the form factors of the decay $B_0 \rightarrow D^* - \ell^+ n\bar{u}$ and determination of the CKM matrix element $|V_{cb}|$* , *Phys. Rev.* **D82** (2010) 112007, [[arXiv:1010.5620](https://arxiv.org/abs/1010.5620)].
- [319] Belle Collaboration, A. Abdesselam et al., *Precise determination of the CKM matrix element $|V_{cb}|$ with $\bar{B}^0 \rightarrow D^{*+} \ell^- \bar{\nu}_\ell$ decays with hadronic tagging at Belle*, [arXiv:1702.01521](https://arxiv.org/abs/1702.01521).
- [320] I. Doršner, S. Fajfer, N. Košnik, and I. Nišandžić, *Minimally flavored colored scalar in $\bar{B} \rightarrow D^{(*)} \tau \bar{\nu}$ and the mass matrices constraints*, *JHEP* **11** (2013) 084, [[arXiv:1306.6493](https://arxiv.org/abs/1306.6493)].
- [321] K. G. Chetyrkin, J. H. Kuhn, and M. Steinhauser, *RunDec: A Mathematica package for running and decoupling of the strong coupling and quark masses*, *Comput. Phys. Commun.* **133** (2000) 43–65, [[hep-ph/0004189](https://arxiv.org/abs/hep-ph/0004189)].
- [322] M. Misiak, *The $b \rightarrow se^+e^-$ and $b \rightarrow sy$ decays with next-to-leading logarithmic QCD corrections*, *Nucl. Phys.* **B393** (1993) 23–45. [Erratum: *Nucl. Phys.* **B439**, 461(1995)].
- [323] A. Djouadi, T. Kohler, M. Spira, and J. Tutas, *(e b), (e t) type leptoquarks at e p collider*, *Z. Phys.* **C46** (1990) 679–686.
- [324] D. Chakraverty, D. Choudhury, and A. Datta, *A Nonsupersymmetric resolution of the anomalous muon magnetic moment*, *Phys. Lett.* **B506** (2001) 103–108, [[hep-ph/0102180](https://arxiv.org/abs/hep-ph/0102180)].
- [325] K.-m. Cheung, *Muon anomalous magnetic moment and leptoquark solutions*, *Phys. Rev.* **D64** (2001) 033001, [[hep-ph/0102238](https://arxiv.org/abs/hep-ph/0102238)].

- [326] S. Aoki et al., *Review of lattice results concerning low-energy particle physics*, *Eur. Phys. J.* **C77** (2017), no. 2 112, [[arXiv:1607.00299](#)].
- [327] **Belle** Collaboration, A. Sibidanov et al., *Search for $B^- \rightarrow \mu^- \bar{\nu}_\mu$ Decays at the Belle Experiment*, *Phys. Rev. Lett.* **121** (2018), no. 3 031801, [[arXiv:1712.04123](#)].
- [328] **Belle** Collaboration, A. Zupanc et al., *Measurements of branching fractions of leptonic and hadronic D_s^+ meson decays and extraction of the D_s^+ meson decay constant*, *JHEP* **09** (2013) 139, [[arXiv:1307.6240](#)].
- [329] **Belle** Collaboration, R. Glattauer et al., *Measurement of the decay $B \rightarrow D \ell \nu_\ell$ in fully reconstructed events and determination of the Cabibbo-Kobayashi-Maskawa matrix element $|V_{cb}|$* , *Phys. Rev. D* **93** (2016), no. 3 032006, [[arXiv:1510.03657](#)].
- [330] V. Cirigliano and I. Rosell, $\pi/K \rightarrow e \bar{\nu}_e$ branching ratios to $O(e^2 p^4)$ in Chiral Perturbation Theory, *JHEP* **10** (2007) 005, [[arXiv:0707.4464](#)].
- [331] M. Finkemeier, *Radiative corrections to π_{l2} and K_{l2} decays*, [hep-ph/9501286](#).
- [332] W. Buchmuller and D. Wyler, *Constraints on SU(5) Type Leptoquarks*, *Phys. Lett.* **B177** (1986) 377–382.
- [333] S. Davidson, D. C. Bailey, and B. A. Campbell, *Model independent constraints on leptoquarks from rare processes*, *Z. Phys. C* **61** (1994) 613–644, [[hep-ph/9309310](#)].
- [334] **BaBar** Collaboration, B. Aubert et al., *Searches for Lepton Flavor Violation in the Decays $\tau^+ \rightarrow e^+ \gamma$ and $\tau^+ \rightarrow \mu^+ \gamma$* , *Phys. Rev. Lett.* **104** (2010) 021802, [[arXiv:0908.2381](#)].
- [335] **Belle** Collaboration, Y. Miyazaki et al., *Search for Lepton-Flavor-Violating tau Decays into a Lepton and a Vector Meson*, *Phys. Lett.* **B699** (2011) 251–257, [[arXiv:1101.0755](#)].
- [336] **SINDRUM II** Collaboration, W. H. Bertl et al., *A Search for muon to electron conversion in muonic gold*, *Eur. Phys. J.* **C47** (2006) 337–346.
- [337] W. Altmannshofer, A. J. Buras, D. M. Straub, and M. Wick, *New strategies for New Physics search in $B \rightarrow K^* \nu \bar{\nu}$, $B \rightarrow K \nu \bar{\nu}$ and $B \rightarrow X_s \nu \bar{\nu}$ decays*, *JHEP* **04** (2009) 022, [[arXiv:0902.0160](#)].
- [338] A. J. Buras, F. Schwab, and S. Uhlig, *Waiting for precise measurements of $K^+ \rightarrow \pi^+ \nu \bar{\nu}$ and $K_L \rightarrow \pi^0 \nu \bar{\nu}$* , *Rev. Mod. Phys.* **80** (2008) 965–1007, [[hep-ph/0405132](#)].
- [339] G. Buchalla and A. J. Buras, *The rare decays $K \rightarrow \pi \nu \bar{\nu}$, $B \rightarrow X \nu \bar{\nu}$ and $B \rightarrow l^+ l^-$: An Update*, *Nucl. Phys.* **B548** (1999) 309–327, [[hep-ph/9901288](#)].

- [340] M. Misiak and J. Urban, *QCD corrections to FCNC decays mediated by Z penguins and W boxes*, *Phys. Lett.* **B451** (1999) 161–169, [[hep-ph/9901278](#)].
- [341] **Belle** Collaboration, J. Grygier et al., *Search for $B \rightarrow h\nu\bar{\nu}$ decays with semileptonic tagging at Belle*, *Phys. Rev. D* **96** (2017), no. 9 091101, [[arXiv:1702.03224](#)]. [Addendum: Phys.Rev.D 97, 099902 (2018)].
- [342] G. Kumar, *Constraints on a scalar leptoquark from the kaon sector*, *Phys. Rev.* **D94** (2016), no. 1 014022, [[arXiv:1603.00346](#)].
- [343] **BNL-E949** Collaboration, A. V. Artamonov et al., *Study of the decay $K^+ \rightarrow \pi^+ \nu\bar{\nu}$ in the momentum region $140 < P_\pi < 199$ MeV/c*, *Phys. Rev.* **D79** (2009) 092004, [[arXiv:0903.0030](#)].
- [344] **LHCb** Collaboration, R. Aaij et al., *Search for the rare decay $D^0 \rightarrow \mu^+ \mu^-$* , *Phys. Lett.* **B725** (2013) 15–24, [[arXiv:1305.5059](#)].
- [345] S. Fajfer and N. Košnik, *Prospects of discovering new physics in rare charm decays*, *Eur. Phys. J.* **C75** (2015), no. 12 567, [[arXiv:1510.00965](#)].
- [346] **LHCb** Collaboration, R. Aaij et al., *Search for $D_s^+ \rightarrow \pi^+ \mu^+ \mu^-$ and $D_s^+ \rightarrow \pi^- \mu^+ \mu^+$ decays*, *Phys. Lett.* **B724** (2013) 203–212, [[arXiv:1304.6365](#)].
- [347] **UTfit** Collaboration, M. Bona et al., *Model-independent constraints on $\Delta F = 2$ operators and the scale of new physics*, *JHEP* **03** (2008) 049, [[arXiv:0707.0636](#)].
- [348] R. Fleischer, *Flavour Physics and CP Violation: Expecting the LHC*, in *High-energy physics. Proceedings, 4th Latin American CERN-CLAF School, Vina del Mar, Chile, February 18-March 3, 2007*, pp. 105–157, 2008. [arXiv:0802.2882](#).
- [349] T. Inami and C. S. Lim, *Effects of Superheavy Quarks and Leptons in Low-Energy Weak Processes $K_L \rightarrow \mu\bar{\mu}$, $K^+ \rightarrow \pi^+\nu\bar{\nu}$ and $K^0 \leftrightarrow \bar{K}^0$* , *Prog. Theor. Phys.* **65** (1981) 297. [Erratum: Prog. Theor. Phys.65,1772(1981)].
- [350] M. Ciuchini, E. Franco, S. Mishima, and L. Silvestrini, *Electroweak Precision Observables, New Physics and the Nature of a 126 GeV Higgs Boson*, *JHEP* **08** (2013) 106, [[arXiv:1306.4644](#)].
- [351] **Belle** Collaboration, Y. Sato et al., *Measurement of the branching ratio of $\bar{B}^0 \rightarrow D^{*+} \tau^- \bar{\nu}_\tau$ relative to $\bar{B}^0 \rightarrow D^{*+} \ell^- \bar{\nu}_\ell$ decays with a semileptonic tagging method*, *Phys. Rev.* **D94** (2016), no. 7 072007, [[arXiv:1607.07923](#)].
- [352] N. Arkani-Hamed, T. Han, M. Mangano, and L.-T. Wang, *Physics opportunities of a 100 TeV proton-proton collider*, *Phys. Rept.* **652** (2016) 1–49, [[arXiv:1511.06495](#)].

- [353] K. Cheung, T. Nomura, and H. Okada, *Testable radiative neutrino mass model without additional symmetries and explanation for the $b \rightarrow s\ell^+\ell^-$ anomaly*, *Phys. Rev.* **D94** (2016), no. 11 115024, [[arXiv:1610.02322](#)].
- [354] K. Cheung, T. Nomura, and H. Okada, *A Three-loop Neutrino Model with Leptoquark Triplet Scalars*, *Phys. Lett. B* **768** (2017) 359–364, [[arXiv:1701.01080](#)].
- [355] K. Cheung, T. Nomura, and H. Okada, *Three-loop neutrino mass model with a colored triplet scalar*, *Phys. Rev.* **D95** (2017), no. 1 015026, [[arXiv:1610.04986](#)].
- [356] D. Aristizabal Sierra, M. Hirsch, and S. G. Kovalenko, *Leptoquarks: Neutrino masses and accelerator phenomenology*, *Phys. Rev.* **D77** (2008) 055011, [[arXiv:0710.5699](#)].
- [357] J. A. Casas and A. Ibarra, *Oscillating neutrinos and $\mu \rightarrow e\gamma$* , *Nucl. Phys.* **B618** (2001) 171–204, [[hep-ph/0103065](#)].
- [358] I. Esteban, M. C. Gonzalez-Garcia, M. Maltoni, I. Martinez-Soler, and T. Schwetz, *Updated fit to three neutrino mixing: exploring the accelerator-reactor complementarity*, *JHEP* **01** (2017) 087, [[arXiv:1611.01514](#)].
- [359] G. Kumar, C. Hati, J. Orloff, and A. M. Teixeira, *Reconciling B-meson Anomalies, Neutrino Masses and Dark Matter*, in *16th Conference on Flavor Physics and CP Violation (FPCP 2018) Hyderabad, INDIA, July 14-18, 2018*, 2018. [arXiv:1811.10927](#).
- [360] W. Porod, F. Staub, and A. Vicente, *A Flavor Kit for BSM models*, *Eur. Phys. J.* **C74** (2014), no. 8 2992, [[arXiv:1405.1434](#)].
- [361] W. Porod and F. Staub, *SPheno 3.1: Extensions including flavour, CP-phases and models beyond the MSSM*, *Comput. Phys. Commun.* **183** (2012) 2458–2469, [[arXiv:1104.1573](#)].
- [362] A. Vicente, *Computer tools in particle physics*, [arXiv:1507.06349](#).
- [363] J. Aebischer, J. Kumar, and D. M. Straub, *Wilson: a Python package for the running and matching of Wilson coefficients above and below the electroweak scale*, *Eur. Phys. J.* **C78** (2018), no. 12 1026, [[arXiv:1804.05033](#)].
- [364] ATLAS Collaboration, M. Aaboud et al., *Search for single production of vector-like quarks decaying into Wb in pp collisions at $\sqrt{s} = 13$ TeV with the ATLAS detector*, *JHEP* **05** (2019) 164, [[arXiv:1812.07343](#)].

- [365] ATLAS Collaboration Collaboration, *Search for single production of a vector-like B quark decaying into a bottom quark and a Higgs boson which decays into a pair of photons*, Tech. Rep. ATLAS-CONF-2018-024, CERN, Geneva, Jul, 2018.
- [366] ATLAS Collaboration, M. Aaboud et al., *Combination of the searches for pair-produced vector-like partners of the third-generation quarks at $\sqrt{s} = 13$ TeV with the ATLAS detector*, *Phys. Rev. Lett.* **121** (2018), no. 21 211801, [[arXiv:1808.02343](#)].
- [367] CMS Collaboration, A. M. Sirunyan et al., *Search for leptoquarks coupled to third-generation quarks in proton-proton collisions at $\sqrt{s} = 13$ TeV*, *Phys. Rev. Lett.* **121** (2018), no. 24 241802, [[arXiv:1809.05558](#)].
- [368] ATLAS Collaboration, M. Aaboud et al., *Searches for scalar leptoquarks and differential cross-section measurements in dilepton-dijet events in proton-proton collisions at a centre-of-mass energy of $\sqrt{s} = 13$ TeV with the ATLAS experiment*, [arXiv:1902.00377](#).
- [369] ATLAS Collaboration, M. Aaboud et al., *Search for additional heavy neutral Higgs and gauge bosons in the ditau final state produced in 36 fb^{-1} of pp collisions at $\sqrt{s} = 13$ TeV with the ATLAS detector*, *JHEP* **01** (2018) 055, [[arXiv:1709.07242](#)].
- [370] ATLAS Collaboration, M. Aaboud et al., *Search for new high-mass phenomena in the dilepton final state using 36 fb^{-1} of proton-proton collision data at $\sqrt{s} = 13$ TeV with the ATLAS detector*, *JHEP* **10** (2017) 182, [[arXiv:1707.02424](#)].
- [371] A. Greljo and D. Marzocca, *High- p_T dilepton tails and flavor physics*, *Eur. Phys. J.* **C77** (2017), no. 8 548, [[arXiv:1704.09015](#)].
- [372] ATLAS Collaboration Collaboration, *Search for new high-mass phenomena in the dilepton final state using 36.1 fb^{-1} of proton-proton collision data at $\sqrt{s} = 13$ TeV with the ATLAS detector*, Tech. Rep. ATLAS-CONF-2017-027, CERN, Geneva, Apr, 2017.
- [373] ALEPH, DELPHI, L3, OPAL, SLD, LEP Electroweak Working Group, SLD Electroweak Group, SLD Heavy Flavour Group Collaboration, S. Schael et al., *Precision electroweak measurements on the Z resonance*, *Phys. Rept.* **427** (2006) 257–454, [[hep-ex/0509008](#)].
- [374] J. A. Aguilar-Saavedra, R. Benbrik, S. Heinemeyer, and M. Pérez-Victoria, *Handbook of vectorlike quarks: Mixing and single production*, *Phys. Rev.* **D88** (2013), no. 9 094010, [[arXiv:1306.0572](#)].

- [375] P. Arnan, D. Bećirević, F. Mescia, and O. Sumensari, *Probing low energy scalar leptoquarks by the leptonic W and Z couplings*, *JHEP* **02** (2019) 109, [[arXiv:1901.06315](https://arxiv.org/abs/1901.06315)].
- [376] W. Porod, *SPheno, a program for calculating supersymmetric spectra, SUSY particle decays and SUSY particle production at e+ e- colliders*, *Comput. Phys. Commun.* **153** (2003) 275–315, [[hep-ph/0301101](https://arxiv.org/abs/hep-ph/0301101)].
- [377] Heavy Flavor Averaging Group (HFAG) Collaboration, Y. Amhis et al., *Averages of b-hadron, c-hadron, and τ -lepton properties as of summer 2014*, [arXiv:1412.7515](https://arxiv.org/abs/1412.7515).
- [378] F. Feruglio, P. Paradisi, and O. Sumensari, *Implications of scalar and tensor explanations of $R_{D^{(*)}}$* , *JHEP* **11** (2018) 191, [[arXiv:1806.10155](https://arxiv.org/abs/1806.10155)].
- [379] A. K. Alok, D. Kumar, S. Kumbhakar, and S. Uma Sankar, *Impact of D^* polarization measurement on solutions to R_D - R_{D^*} anomalies*, [arXiv:1903.10486](https://arxiv.org/abs/1903.10486).
- [380] A. Kurup, *The coherent muon to electron transition (comet) experiment*, *Nuclear Physics B - Proceedings Supplements* **218** (2011), no. 1 38 – 43. Proceedings of the Eleventh International Workshop on Tau Lepton Physics.
- [381] COMET Collaboration, Y. G. Cui et al., *Conceptual design report for experimental search for lepton flavor violating mu- - e- conversion at sensitivity of 10^{-16} with a slow-extracted bunched proton beam (COMET)*, .
- [382] COMET Collaboration, C. Wu, *Search for Muon to Electron Conversion at J-PARC*, *Nucl. Part. Phys. Proc.* **287-288** (2017) 173–176.
- [383] COMET Collaboration, G. Adamov et al., *COMET Phase-I Technical Design Report*, [arXiv:1812.09018](https://arxiv.org/abs/1812.09018).
- [384] Mu2e Collaboration, L. Bartoszek et al., *Mu2e Technical Design Report*, [arXiv:1501.05241](https://arxiv.org/abs/1501.05241).
- [385] Mu2e Collaboration, G. Pezzullo, *Mu2e: A Search for Charged Lepton Flavor Violation in $\bar{\nu}N \rightarrow eN$ Conversion with a Sensitivity $< 10^{-16}$* , *PoS ICHEP2018* (2019) 583.
- [386] Mu2e Collaboration, R. Bonventre, *Searching for muon to electron conversion: The Mu2e experiment at Fermilab*, *SciPost Phys. Proc.* **1** (2019) 038.
- [387] G. Burdman, E. Golowich, J. L. Hewett, and S. Pakvasa, *Rare charm decays in the standard model and beyond*, *Phys. Rev.* **D66** (2002) 014009, [[hep-ph/0112235](https://arxiv.org/abs/hep-ph/0112235)].

- [388] W. Altmannshofer, P. S. Bhupal Dev, and A. Soni, *$R_{D^{(*)}}$ anomaly: A possible hint for natural supersymmetry with R -parity violation*, *Phys. Rev.* **D96** (2017), no. 9 095010, [[arXiv:1704.06659](https://arxiv.org/abs/1704.06659)].
- [389] D. Buttazzo, A. Greljo, G. Isidori, and D. Marzocca, *B-physics anomalies: a guide to combined explanations*, *JHEP* **11** (2017) 044, [[arXiv:1706.07808](https://arxiv.org/abs/1706.07808)].
- [390] D. Marzocca, *Addressing the B-physics anomalies in a fundamental Composite Higgs Model*, *JHEP* **07** (2018) 121, [[arXiv:1803.10972](https://arxiv.org/abs/1803.10972)].
- [391] *Search for resonances decaying to photon pairs in 3.2fb^{-1} of pp collisions at $\sqrt{s} = 13\text{ TeV}$ with the ATLAS detector*, Tech. Rep. ATLAS-CONF-2015-081, CERN, Geneva, Dec, 2015.
- [392] CMS Collaboration, *Search for new physics in high mass diphoton events in proton-proton collisions at 13 TeV*.
- [393] *Search for new phenomena in the dilepton final state using proton-proton collisions at $\sqrt{s} = 13\text{ TeV}$ with the ATLAS detector*, Tech. Rep. ATLAS-CONF-2015-070, CERN, Geneva, Dec, 2015.
- [394] R. Franceschini, G. F. Giudice, J. F. Kamenik, M. McCullough, A. Pomarol, R. Rattazzi, M. Redi, F. Riva, A. Strumia, and R. Torre, *What is the $\gamma\gamma$ resonance at 750 GeV?*, *JHEP* **03** (2016) 144, [[arXiv:1512.04933](https://arxiv.org/abs/1512.04933)].
- [395] Y. Kats and M. J. Strassler, *Resonances from QCD bound states and the 750 GeV diphoton excess*, *JHEP* **05** (2016) 092, [[arXiv:1602.08819](https://arxiv.org/abs/1602.08819)]. [Erratum: *JHEP* 07, 044 (2016)].
- [396] D. Curtin and C. B. Verhaaren, *Quirky Explanations for the Diphoton Excess*, *Phys. Rev. D* **93** (2016), no. 5 055011, [[arXiv:1512.05753](https://arxiv.org/abs/1512.05753)].
- [397] J. F. Kamenik and M. Redi, *Back to 1974: The \mathcal{Q} -onium*, *Phys. Lett. B* **760** (2016) 158–163, [[arXiv:1603.07719](https://arxiv.org/abs/1603.07719)].
- [398] P. Ko, C. Yu, and T.-C. Yuan, *Probing a new strongly interacting sector via composite diboson resonances*, *Phys. Rev. D* **95** (2017), no. 11 115034, [[arXiv:1603.08802](https://arxiv.org/abs/1603.08802)].
- [399] N. D. Barrie, A. Kobakhidze, S. Liang, M. Talia, and L. Wu, *Heavy Leptonium as the Origin of the 750 GeV Diphoton Excess*, [arXiv:1604.02803](https://arxiv.org/abs/1604.02803).
- [400] E. D. Carlson, L. J. Hall, U. Sarid, and J. W. Burton, *Cornering color SU(5)*, *Phys. Rev. D* **44** (1991) 1555–1568.

- [401] R. Foot, O. F. Hernandez, and T. G. Rizzo, *SU(5)-c COLOR MODEL SIGNATURES AT HADRON COLLIDERS*, *Phys. Lett. B* **246** (1990) 183–187.
- [402] R. Foot, *Top quark forward-backward asymmetry from $SU(N_c)$ color*, *Phys. Rev. D* **83** (2011) 114013, [[arXiv:1103.1940](#)].
- [403] T. Gherghetta, N. Nagata, and M. Shifman, *A Visible QCD Axion from an Enlarged Color Group*, *Phys. Rev. D* **93** (2016), no. 11 115010, [[arXiv:1604.01127](#)].
- [404] R. Foot and H. Lew, *QUARK - LEPTON SYMMETRIC MODEL*, *Phys. Rev. D* **41** (1990) 3502.
- [405] R. Foot, H. Lew, and R. Volkas, *Phenomenology of quark - lepton symmetric models*, *Phys. Rev. D* **44** (1991) 1531–1546.
- [406] R. Foot and R. Volkas, *Generalised leptonic colour*, *Phys. Lett. B* **645** (2007) 345–350, [[hep-ph/0607047](#)].
- [407] J. D. Clarke, R. Foot, and R. R. Volkas, *Quark-lepton symmetric model at the LHC*, *Phys. Rev. D* **85** (2012) 074012, [[arXiv:1112.3405](#)].
- [408] L. Okun, *THETA PARTICLES*, *Nucl. Phys. B* **173** (1980) 1–12.
- [409] J. Kang and M. A. Luty, *Macroscopic Strings and ‘Quirks’ at Colliders*, *JHEP* **11** (2009) 065, [[arXiv:0805.4642](#)].
- [410] P. Agrawal, J. Fan, B. Heidenreich, M. Reece, and M. Strassler, *Experimental Considerations Motivated by the Diphoton Excess at the LHC*, *JHEP* **06** (2016) 082, [[arXiv:1512.05775](#)].
- [411] ATLAS Collaboration, G. Aad et al., *Observation of a new particle in the search for the Standard Model Higgs boson with the ATLAS detector at the LHC*, *Phys. Lett. B* **716** (2012) 1–29, [[arXiv:1207.7214](#)].
- [412] CMS Collaboration, S. Chatrchyan et al., *Observation of a New Boson at a Mass of 125 GeV with the CMS Experiment at the LHC*, *Phys. Lett. B* **716** (2012) 30–61, [[arXiv:1207.7235](#)].
- [413] C. Borschensky, M. Krämer, A. Kulesza, M. Mangano, S. Padhi, T. Plehn, and X. Portell, *Squark and gluino production cross sections in pp collisions at $\sqrt{s} = 13, 14, 33$ and 100 TeV*, *Eur. Phys. J. C* **74** (2014), no. 12 3174, [[arXiv:1407.5066](#)].
- [414] *Search for pair production of Higgs bosons in the $b\bar{b}b\bar{b}$ final state using proton-proton collisions at $\sqrt{s} = 13$ TeV with the ATLAS detector*, Tech. Rep. ATLAS-CONF-2016-017, CERN, Geneva, Mar, 2016.

-
- [415] CMS Collaboration Collaboration, *Search for resonant pair production of Higgs bosons decaying to two bottom quark-antiquark pairs in proton-proton collisions at 13 TeV*, Tech. Rep. CMS-PAS-HIG-16-002, CERN, Geneva, 2016.
- [416] R. Harlander and P. Kant, *Higgs production and decay: Analytic results at next-to-leading order QCD*, *JHEP* **12** (2005) 015, [[hep-ph/0509189](#)].
- [417] R. Foot, H. Lew, and R. Volkas, *Models of extended Pati-Salam gauge symmetry*, *Phys. Rev. D* **44** (1991) 859. [Erratum: *Phys. Rev. D* **47**, 1272 (1993)].
- [418] ATLAS Collaboration, G. Aad et al., *Search for new phenomena in the dijet mass distribution using $p - p$ collision data at $\sqrt{s} = 8$ TeV with the ATLAS detector*, *Phys. Rev. D* **91** (2015), no. 5 052007, [[arXiv:1407.1376](#)].
- [419] CMS Collaboration, V. Khachatryan et al., *Search for narrow resonances decaying to dijets in proton-proton collisions at $\sqrt(s) = 13$ TeV*, *Phys. Rev. Lett.* **116** (2016), no. 7 071801, [[arXiv:1512.01224](#)].
- [420] J. E. Juknevich, D. Melnikov, and M. J. Strassler, *A Pure-Glue Hidden Valley I. States and Decays*, *JHEP* **07** (2009) 055, [[arXiv:0903.0883](#)].
- [421] J. E. Juknevich, *Pure-glue hidden valleys through the Higgs portal*, *JHEP* **08** (2010) 121, [[arXiv:0911.5616](#)].
- [422] ATLAS Collaboration, G. Aad et al., *Search for new phenomena with photon+jet events in proton-proton collisions at $\sqrt{s} = 13$ TeV with the ATLAS detector*, *JHEP* **03** (2016) 041, [[arXiv:1512.05910](#)].